K^+ signatures in the ProtoDUNE-SP detector at CERN

Thesis submitted for the Degree of Doctor of Philosophy

Author:

Miguel Ángel García Peris

Director:

Dr. Anselmo Cervera Villanueva

Universitat de València

Programa Oficial de Doctorado en Física

Instituto de Física Corpuscular (UV-CSIC)
Departamento de Física Atómica, Molecular y Nuclear

May 2023

The work on this thesis has been developed at the *Intituto de Física Corpuscular* (IFIC), affiliated with the UV and CSIC, and it has been possible thanks to the ACIF programme for the training of research personnel awarded by the *Generalitat Valenciana* and the *Fondo Social Europeo*.

Preface

During the last two decades neutrinos have turned high energy physics upside down due to their strange nature. The discovery of their oscillations between leptonic flavour implies that they are massive particles, contrary to the description of the Standard Model of particles physics. This evidences the existence of some unknown regime of physics beyond it. Tens of experiments have tried to characterize the oscillation phenomenon, but being neutrinos so complicated to detect has made this a very challenging task. Indeed, there are still some parameters with deep physics consequences that have not been determined precisely enough, amongst which δ_{CP} outstands. It is a phase quantifying how differently neutrinos and antineutrinos oscillate, and a value of this phase different from zero could be one of the ingredients to explain the baryon asymmetry present in our Universe; or, in other words, it could be an explanation for the existence of the Universe itself.

Current experiments have excluded the zero value with a confidence level up to 3σ. However, it is widely assumed that even combining the data from all those experiments, a discovery (5σ) will not be possible. Consequently, a new generation of experiment was proposed during the last decade, with improved techniques and sensitivities, so that neutrinos could be studied further. Examples of this new generation are JUNO, Hyper-Kamiokande and DUNE.

Apart from oscillations, there are other questions regarding neutrinos that are seeking for an answer. The absolute value of their masses is still unknown, and their upper bounds are much lower than those of any other fermion of the Standard Model. We do not know neither what is the hierarchy of their massive states, nor if they are Majonara particles, which would imply a violation of the leptonic number conservation. All things considered, and having in mind that the LHC is slowly turning into a precision test bench for the Standard Model, it is clear that neutrino physics is the key point of high energy physics in the next decade.

Or at least, this was my feeling when I was about to start my research career

in 2017. It was at that time when I joined the experimental neutrino physics group at IFIC for my Master Thesis. All my work since then has been devoted to DUNE and its prototypes at CERN. I liked the idea of working in an upcoming experiment with a very strong prototyping programme, because this would allow me to work in the different stages of a particle physics experiment: simulation, design, prototyping, testing, installation, commissioning and data analysis. And it has been this way.

My Master Thesis was focused on the calibration and installation of the Static Temperature Gradient Monitor of ProtoDUNE-SP, a gigantic thermometer able to measure the vertical temperature gradient inside the eight meters tall cryostat, with an unprecedented precision close to the mili-kelvin. Two weeks after the defence I started my PhD moving to CERN for five months, for the commissioning of ProtoDUNE-SP. During this first year my work was mainly focused on the study of the cryogenic instrumentation of the experiment, particularly the analysis of temperature data. For this work, the collaboration gave me the opportunity to present the talk 'Cryogenic Instrumentation at ProtoDUNE' in the ICHEP2020 conference. A brief summary of the results obtained is presented in Chapter 3. As a result of this work, the technology used for ProtoDUNE was accepted as baseline for DUNE FD1 temperature monitoring system. Two publications, one about the novel calibration procedure demonstrating the mili-kelving capabilities of the system, and another one about the entire ProtoDUNE-SP temperature monitoring system, will be released soon.

In 2019, IFIC's neutrino group joined the DUNE's Photon Detection Consortium along with other Spanish institutions. Then I started to work closely with the engineers of the NEXT neutrino-less double beta-decay experiment at IFIC to understand silicon photomultipliers and to prepare an experimental set-up to test them under cryogenic conditions. We were key players in the SiPM down-selection procedure, in which different sensor models from two different vendors, HPK and FBK, were tested to choose the one best fitting DUNE's needs. At IFIC I was in charge of receiving, testing, analysing and sharing the results with the other involved institutions. This process took almost a year, from Summer 2020 to Summer 2021. Two scientific papers are currently being prepared to present the results obtained, and I am a leading author of one of them. The results obtained at IFIC in this context are presented in detail in Chapter 4.

Continuing with the PDS activities, in 2022 I was awarded a grant to stay at CERN for seven months and participate in the installation of the PDS of ProtoDUNE-HD, a second phase of the ProtoDUNE-SP prototype. The activities developed involved the assembly of the PDS optical modules, the installation and testing in the APAs and the cold box, the study of the DAPHNE readout,

and the final installation in the cryostat. My initial contributions became leading tasks when I was appointed coordinator of the installation. These activities are briefly commented in the last section of Chapter 4.

Coming back in time a little bit, at the beginning of 2021 I started to work on the analysis that gives name to this thesis. Working on the PDS made me discover DUNEs capabilities beyond neutrino oscillations. In particular, proton decay searches, which constitutes one of the main research topics of giant neutrino experiments, as DUNE or HK. Indeed, the PDS is crucial for proton decay, as will be explained later, and kaons are crucial to investigate this phenomenon in DUNE. I entirely developed the secondary kaon selection presented here, and the subsequent analysis of the energy loss per unit length (including the evaluation of the systematic uncertainties). Thanks to this work, the capabilities of the Single-Phase LArTPC detector technology to identify low energy kaons have been demonstrated, which is of outmost importance for proton decay searches in DUNE. A publication is in preparation with the obtained results. A measurement of the secondary kaon production cross-section has been left for a future exercise. In addition to the analysis carried out, I have closely worked with my supervisor, Anselmo Cervera, on the adaptation of the HighLAND analysis framework to ProtoDUNE-SP.

* * *

Working in DUNE has allowed me to work on the different stages of a particle physics experiment, and hence, to use a broad set of analysis and hardware tools. The analysis presented in this dissertation has been mostly developed with the aforementioned HighLAND framework, which is a high-level analysis software that covers from data retrieving and reduction to graphic drawing utilities, passing through event selections, corrections and propagation of systematic uncertainties; with LArSoft, the DUNE simulation and reconstruction software, and with ROOT. I have also had the opportunity to work with GEANT4 to modestly participate in the preparation of a numerical simulation of the X-ARAPUCA device, and to use COMSOL and SOLIDWORKS to develop and simulate the Temperature Gradient Monitor and its exposure to electric fields. Focusing on the hardware, I have also worked with the LabView programme to automatize the different devices I used during the SiPM characterization: the oscilloscope, the power supplies, the pulse generator, the Keithley picoammeter, etc. Finally, during the installation of ProtoDUNE-HD, I learnt how to use the scissor-lift, which I consider to be one of the biggest successes of my PhD due to my horrible fear of heights.

* * *

This dissertation is organized in nine chapters. Chapter 1 presents an overview of neutrino physics and the proton decay phenomenon, and motivates the necessity of a new generation of experiments, as DUNE. The DUNE experiment is reviewed in Chapter 2, while Chapter 3 provides a detailed description of ProtoDUNE-SP, including the studies related to the cryogenic instrumentation in which I was involved. The activities regarding DUNE's Photon Detection System, specifically the SiPM down-selection and the installation in ProtoDUNE-HD, are summarized in Chapter 4. The analysis of stopping kaons in ProtoDUNE-SP is presented in Chapters 5, 6, 7 and 8. Finally, Chapter 9 concludes.

Summary

Introduction

Neutrinos

Neutrinos are the second most abundant particle in the Universe, yet the less understood. They are charge-less leptons that only interact via weak interaction and with a mass so low that they are described as massless by the Standard Model (SM) of particle physics. Consequently, detecting neutrinos constitutes a very challenging task since their interaction cross-section is ridiculously low. There are three families of neutrinos, each of them associated to a charged lepton: the electron neutrino to the electron, the muon neutrino to the muon, and the tau neutrino to the tau. Due to lepton number conservation, neutrinos (or antineutrinos) are generated in pairs with their associated charged anti-lepton (or lepton). In the same way, when they interact with the matter, they generate the associated charged lepton in the final state. Identifying this lepton enables to characterize the neutrino responsible of the reaction.

One of the most interesting facts about neutrinos is their ability to oscillate between leptonic flavours. Their flavour states do not correspond to their massive states, which are the ones with a well-defined time evolution. Consequently, a flavour state originated at $t = 0$ has a non-zero probability of being detected as a different flavour after some time has passed. This phenomenon has been measured using different sources of neutrinos: solar, atmospheric, reactor and accelerator neutrinos. It can be described by expressing the flavour states as a linear combination of the massive states

$$|\nu_\alpha\rangle = \sum_{k=1}^{3} U^*_{\alpha k} |\nu_k\rangle, \tag{1}$$

where U is the PMNS matrix, that can be parametrized as

$$U = \begin{pmatrix} 1 & 0 & 0 \\ 0 & c_{23} & s_{23} \\ 0 & s_{23} & c_{23} \end{pmatrix} \begin{pmatrix} c_{13} & 0 & s_{13}e^{-i\delta_{CP}} \\ 0 & 1 & 0 \\ -s_{13}e^{i\delta_{CP}} & 0 & c_{13} \end{pmatrix} \begin{pmatrix} c_{12} & s_{12} & 0 \\ -s_{12} & c_{12} & 0 \\ 0 & 0 & 1 \end{pmatrix}, \quad (2)$$

where c_{ij} and s_{ij} refer to cosine and sine of θ_{ij}, respectively, and θ_{ij} is the mixing angle between flavour states; and δ_{CP} is a complex phase known as Charge-Parity violation phase, which measures how differently neutrinos and antineutrinos oscillate. Given an initial flavour α, the probability of detecting a different flavour β at a time t is described by

$$\begin{aligned} P_{\nu_\alpha \to \nu_\beta}(L,E) = \delta_{\alpha\beta} - 4\sum_{k>j} \mathcal{R}\left[U^*_{\alpha k}U_{\beta k}U_{\alpha j}U^*_{\beta j}\right] \sin^2\left(\frac{\Delta m^2_{kj}L}{4E}\right) \\ +2\sum_{k>j} \mathcal{I}\left[U^*_{\alpha k}U_{\beta k}U_{\alpha j}U^*_{\beta j}\right] \sin\left(\frac{\Delta m^2_{kj}L}{2E}\right), \end{aligned} \quad (3)$$

where L is the distance between the origin of the neutrino and the detector, E is the energy of the neutrino, Δm_{kj} is the mass difference between massive neutrino states k and j, and $\mathcal{R}$ and $\mathcal{I}$ refer to real and imaginary parts of the matrix elements enclosed, respectively. With this, neutrino oscillations are described by three mixing angles (θ_{12},θ_{23} and θ_{31}), a CP violation phase (δ_{CP}) and the two squared mass differences (Δm^2_{12} and Δm^2_{23}).

Several points need to be highlighted regarding this phenomenon. First, neutrinos can only oscillate if they are massive particles, so its discovery has constituted the first proof of physics beyond the SM, which considers neutrinos as massless. Furthermore, giving mass to neutrinos is not straightforward from the theoretical point of view, and it generates the appearance of new concepts as Majorana particles, sterile neutrinos, the see-saw mechanism, etc. Second, the oscillation probability depends on the absolute value of the mass squared difference of the massive states, meaning that we do not have enough information to infer which is the absolute mass of the neutrinos and what is their ordering from lighter to heavier. Third, a value of δ_{CP} different from zero could provide an explanation to the baryon asymmetry currently observed in the Universe. In the very early stages of the Big Bang, equal amounts of matter and antimatter were created, and in the same way, they should have been annihilated. However, the Universe we live in today is made exclusively out of matter. Why so? What happened with the antimatter? This is the so-called baryon asymmetry for which neutrinos may be an answer if they and their antiparticles oscillate differently enough.

Due to their strong physics implications, neutrino oscillations have been thoroughly studied during the last twenty years using different neutrino sources, establishing as a result the three-flavour neutrino paradigm presented above. Experiments measuring solar neutrinos, as SNO, have characterized θ_{12} and Δm^2_{12}. θ_{23} and Δm^2_{23} have been measured by atmospheric neutrino experiments, as Super-Kamiokande, and by accelerator neutrino experiments, as T2K and NOνA. Accelerator experiments have also, along with reactor experiments as Double Chooz or Daya Bay, measured θ_{13}. Finally, the δ_{CP} zero value has been excluded at 3σ level by accelerator experiments. However, it is already known that even combining all of the available and achievable data from current detectors this would not be enough to reach the 5σ level. The same applies to the θ_{23}, for which it is unknown if it is below, above or equal to 45°; and to the mass ordering. For this reason, a new generation of neutrino experiments with more advanced technologies and higher sensitivities has been proposed, formed by Hyper-Kamiokande, JUNO and DUNE.

GUTs and Proton Decay

Aside from oscillations, the fact that neutrinos are massive particles imply that the SM is incomplete, and that it must exist a higher energy level theory of which the SM is just a low energy approximation. Great Unification Theories (GUTs) aim to be such theory, by bringing together all three interactions (electromagnetic, weak and strong) at sufficiently high energies; in the same way as it was found that the electromagnetic and weak interactions were unified at the electroweak scale. These theories predict a wide range of phenomena, but most of them are out of reach with the current technology since they involve very high energies. There are some exceptions, as the creation of new particles *on-shell* in the LHC, and proton decay.

The decay of the proton is a forbidden process in the SM due to baryon number conservation[1]. However, if the unification of forces predicted by GUTs truly happens, it implies that quarks and leptons are unified too, and consequently the baryon number is no longer a conserved quantity and the proton decay can happen. This hypothetical process has two preferred channels: $p \to e^+\pi^0$ and $p \to K^+\bar{\nu}$, the first one mostly predicted by non-supersymmetric GUTs and the second one by supersymmetric GUTs.

Although no evidence for this process has been observed so far, upper limits have been set by experiments, which has allowed discarding some of those models. These measurements have been obtained mainly by Super-Kamiokande,

[1]Fortunately, we would not be here otherwise.

which has good sensitivity for channels involving pions in the final states. However, it does not perform as well in channels with kaons in the final states since their very low momentum is below the Cerenkov threshold. On the contrary, the emerging Liquid Argon Time Projection Chamber technology (LArTPC) —that is going to be used by DUNE— has access to the full proton decay chain for channels involving kaons, improving the sensitivities achievable by water Cerenkov detectors.

DUNE

DUNE, which stands for Deep Underground Neutrino Experiment, is an upcoming long-baseline neutrino experiment located in the United States. In this kind of experiments a neutrino beam originated in an accelerator is characterized by two detectors. The Near Detector (ND) measures the properties of the unoscillated beam and the Far Detector (FD), located at a distance such that the oscillation is maximum, measures the oscillated beam. By comparing both measurements information from the oscillation parameters can be obtained. The neutrino beam is generated by colliding a proton beam against a target, generating multiple $\pi^{\pm}$. These are focused into a decay pipe, where they decay mostly to $\mu^{\pm}$ and $\nu\mu/\bar{\nu}_{\mu}$. The resulting $\mu + \nu_{\mu}$ beam is made collide again against a thick target meant to stop muons, forming the final neutrino beam.

Particularly, the measurement of δ_{CP} is done by comparing the measured oscillation probability of ν_{μ} and $\bar{\nu}_{\mu}$. However, here a not yet considered phenomenon comes into play: neutrino oscillations are not the same in vacuum and matter. L is usually of the order of hundreds of kilometres, meaning that neutrinos travel through the Earth before reaching the Far Detector. The Earth is made out of matter (electrons, protons and neutrons), so the probability of neutrinos and antineutrinos to interact along their trip from one detector to another is different. Consequently, this effect needs to be disentangled from the Charge-Parity violation effect. There are two different approaches to do so:

- Using a 'short' baseline so that matter effects are negligible. This requires to have a low and well-defined energy neutrino beam (below 1 GeV). This method is used by T2K and will be used by HK.

- Using a 'very long' baseline and a high and wide energy neutrino beam (between 1 and 10 GeV), so that matter effects are so clear they can be disentangled. This method, which has the advantage to resolve the neutrino mass ordering problem, will be used by DUNE.

DUNE's neutrino beam will be generated in Fermilab, where the Near Detector will be located too. Its Far Detector will be located in the Sandford Underground Research Facility (SURF), 1300 km away from the origin of the beam and 1.5 km underground. Due to the high and wide energy spectrum of the beam, neutrinos can undergo every possible process when interacting with nuclei: quasi-elastic scattering, nuclear resonance and deep inelastic scattering; meaning that very different topologies and final state particles are expected in this experimental approach. Neutrino information can only be inferred from the outcoming products of their reactions, so a detector technology with excellent tracking and calorimetric capabilities is needed: the LArTPC. DUNE's Far Detector will be formed by four enormous modular LArTPCs, each one of them enclosed in a monolithic cryostat that will keep the cryogenic liquid at 87 K.

This emerging technology has been tested and validated is the past by different experiments as LArIAT, MicroBooNE and ICARUS, and more recently by ProtoDUNE-SP. Its outstanding performance and the very low background provided by the underground location of DUNE allows to expand its physics programme beyond neutrino oscillations to include multi-messenger astronomy, proton decay searches and a wide range of beyond SM topics.

Liquid Argon Time Projection Chamber Technology

A Time Projection Chamber (TPC) consists of an "active volume" enclosed by two parallel planes, the anode and the cathode. These two planes are exposed to a potential difference, such that an electric field is generated going from the anode to the cathode. When a neutrino interacts with the medium, charged particle are generated. These ionize the medium's atoms between the planes, freeing electrons that drift towards the anode, where they are collected. This allows for a two-dimensional (2D) reconstruction in the plane perpendicular to the drift direction. If the time at which the neutrino interacts with the detector (the t_0) is known, it can be used along with the electron drift velocity, which depends in the electric field magnitude, to infer the coordinate in the drift direction, providing the final three-dimensional (3D) reconstruction of the event. Moreover, the amount of released electrons is proportional to the energy deposited by the charged particle, allowing for a calorimetry measurement.

This calorimetry measurement is fundamental in DUNE for particle identification. DUNE LArTPCs will not be exposed to any magnetic field, so different particle species can only be distinguished by means of their energy loss profile.

The mean energy loss is well described by the Bethe-Bloch formula:

$$\langle -\frac{dE}{dx} \rangle = Kz^2 \frac{Z}{A} \frac{1}{\beta^2} \left[\ln \left(\frac{2m_e c^2 \beta^2 \gamma^2 W_{max}}{I^2} \right) - \beta^2 - \frac{\delta(\beta\gamma)}{2} \right], \tag{4}$$

from which it can be observed that, for particles with the same electric charge (z), the energy loss depends on their velocity (β). This implies that particles with the same energy but different mass lose energy differently. What is typically done in other particle physics experiments is to represent this energy loss as a function of the momentum of the particle. However, in DUNE's LArTPCs the momentum can not be measured, so what is done is to represent the energy loss of a track as a function of its residual range, which is defined as the distance from a point of the track to its end point. Thus, different particle species have different $\frac{dE}{dx}$ versus residual range profiles, and comparing the measured profile of a track with the expected profiles of the different particle enables particle identification. This process is detailed in Section 2.4.1.1.

In the first Far Detector Module, FD1, known as Horizontal Drift, there will be three anode planes and two cathode planes, all of them disposed vertically, following the sequence of A-C-A-C-A. Thus, the module will have three different drift volumes of 3.6 meters wide. An electric potential of -180 kV will be needed to generate an electric field of 500 V/cm, granting electrons a drift velocity of $\sim$1.6 mm/µs. An additional field cage will surround the remaining open faces of the detector, granting homogeneity to the electric field up to a level of 1%. The anode planes will be formed by the so-called Anode Plane Assembly (APA), a stainless-steel frame 6.1 m high, 2.3 m wide and 76 mm thick over which four bronze wire planes are bounded. These wire planes are the ones responsible of collecting the electrons and providing the information for the tracking. This is achieved by disposing the first two planes, known as induction planes, at different rotated angles with respect to the vertical axis; and the third one, known as collection plane, parallel to the vertical axis. The induction planes generate bipolar induction signals when charge is passing through, whilst the collection plane generates unipolar signals when the charge is collected. Coincidences in the three planes of wires are used to determine the spatial coordinates of the event. The last wire plane is grounded to protect the other three planes from electrical problems. 150 APAs will be used in the first FD module.

Liquid argon was selected as target material for several reasons. First, because being a noble element implies having a very low electronegativity, meaning that ionization electrons will not be trapped again by surrounding argon atoms. Second, because it has a relatively heavy nucleus, increasing the interaction probability of neutrinos. Third, because it is a fantastic scintillator: argon emits more

than 20000 photons peaked at 127 nm per MeV deposited, and it is transparent to them. Consequently, detecting this scintillation light (that takes nanoseconds to reach the anode planes) allows to determine the t_0 for non beam events. Fourth, and last, because conforming 1% of the atmosphere, it is the cheapest of all noble elements.

Photon Detection System

As can be deduced from previous lines, apart from the LArTPC, DUNE's FD has a complementary light detection system (the Photon Detection System, PDS), whose objective is twofold: first, to measure the t_0 for non-beam events, and second, to provide a complementary energy reconstruction based on this light collection.

As indicated earlier, the t_0 permits the three-dimensional reconstruction of the events. When doing neutrino beam physics, this time is given by the beam trigger, which means that the PDS is not needed for oscillation physics. However, when doing non-beam physics, only LAr scintillation light can be used to infer the t_0. This is fundamental since many of the non-beam physics (as proton decay searches) rely on a proper fiducialization of the detector volume, vertex identification, and charge attenuation corrections (which depends on the drift coordinate). In addition, the PDS can improve the reconstruction, sensitivity and resolution of the experiment, since its independent energy measurement provides a redundancy that can be used to enhance TPC performance and to better control systematic uncertainties. In other words, in order to make DUNE a multi-purpose experiment, a proper PDS is needed.

DUNE's PDS is based in the photon-trapping X-ARAPUCA technology. An X-ARAPUCA cell consists of a wavelength shifting (WLS) bar, on top of which a short-pass dichroic filter with a sharp cut-off at 400 nm is placed. The external surface of this filter has an evaporation of PTP. On the other side of the WLS bar a reflective foil is located. Finally, several silicon photomultipliers (SiPM)s, which are read as a single electronic channel, are attached to the WLS material. When 127 nm argon scintillation light reaches the PTP evaporation, it is absorbed and re-emitted at 350 nm, meaning that it can pass through the dichroic filter and reach the bar. There, it is shifted again to about 430 nm, and gets trapped inside by total internal reflection until it is collected by one of the SiPMs, which has its maximum photon detection efficiency at that wavelength. In case of a photon escaping the WLS plate, it is reflected back to the bar by the dichroic filter or the reflective foil, having a second chance to be detected.

The geometry of these cells can be tailored to fit different needs. In the

case of DUNE's FD1, the photon-trapping cells (known as SuperCells) have dimensions of 487 mm × 93 mm × 3.5 mm, they are covered by six 78 mm × 93 mm dichroic filters and they have attached 48 SiPMs, which conform a unique electronic channel. Four of these devices are assembled together in a single mechanical structure of 2092 mm × 118 mm × 23 mm which is inserted horizontally inside an APA, behind the wire planes. This is the only location that has 'optical' access to the inner volume of the detector (since the wire planes are transparent) and that has a zero electric potential.

During the last years different R&D lines have been developed to optimize the X-ARAPUCA design. One of the main tasks was finding the most appropriate SiPM model considering DUNE physics requirements. Two different manufacturers, Hamamatsu Photonics (HPK) and Fondazione Bruno Kessler (FBK), developed dedicated photo-sensor models that were thoughtfully tested in cryogenic conditions in different institutions. This characterization involved absolute measurements of the gain, the signal-to-noise ratio, the dark current rate (DCR) and the correlated noise probability (optical cross-talk and after-pulsing); and tests for cryogenic reliability by exposing the sensors to controlled thermal cycles. After those tests it was found that, in general, HPK models performed better than FBK's, and also that larger cell pitch models presented larger gain and SNR values without a significant increase of DCR, thus being preferred. Lastly, it was observed that larger quenching resistance models were likely to have less correlated noise probability. The contribution of IFIC neutrino group during this process is detailed in Chapter 4.

The decision of using the X-ARAPUCA technology as baseline for the PDS was taken after the results obtained in ProtoDUNE-SP, the largest DUNE's prototype built and operated to date. The final PDS modules that will be used in DUNE's FD1 are being tested first in ProtoDUNE-HD, where they have been successfully installed and will be commissioned in the near future. An overview of the installation procedure can be found in Section 4.6. ProtoDUNE-HD constitutes the second iteration of ProtoDUNE-SP, and it is meant to be a 'module 0' for the FD1.

ProtoDUNE-SP

ProtoDUNE-SP was the first of the DUNE prototypes operated at the CERN Neutrino Platform. Even though the LArTPC technology had been previously used by other experiments, it had never been used at a scale as big as DUNE is planning to. The ProtoDUNE programme was proposed as a set of large

demonstrators for DUNE technology. The first iteration of ProtoDUNE consisted of two prototypes, ProtoDUNE-SP and ProtoDUNE-DP, meant to be a test-bench of the Single-Phase and Dual-Phase technologies, respectively. They were hosted by two similar cryostats with internal dimensions of $8\times8\times8$ m^3. In the case of the Single-Phase detector, its goals were

- Prototype and validate the production, delivery and installation procedures of the detector components.
- Validate the detector performance of the SP technology.
- Accumulate sufficiently large test-beam data samples to understand and calibrate the response of the detector to different particle species and to perform physics analysis.
- Ensure the long-term operational stability of the detector.

It consisted of two back to back LArTPCs sharing a central cathode made of heavily resistive materials, in such a way than the electron drift direction was opposite in each drift volume. The left open faces of the detector were covered by a field cage made of aluminium bars connected by means of resistive divider chains that provided the necessary voltage gradient along the drift direction. Two ground planes were located below and on top of the detector, to prevent the generation of electric discharges to the cryogenic system or the gas phase. Each anode plane was formed by three APAs, and each APA hosted 10 optical modules similar to the X-ARAPUCA aforementioned. The whole TPC hung from the inner ceiling of the corrugated cryostat. In order to decrease the energy loss of particles coming from the beam, a beam plug penetrated the cryostat and the detector up to five centimetres inside the field cage. Due to its disposition, beam particles only passed through one of the active volumes, being this one known as beam side and the other as non beam side. Finally, two cosmic ray taggers were located vertically outside the cryostat so that cosmic rays passing through the detector parallel to the APAs could be identified. Overall, ProtoDUNE-SP prototyped the design of all detector components at a scale of 1:1, and the argon mass at a scale of 1:20.

Apart from the detector, ProtoDUNE-SP had a complex recirculation and purification system, responsible of reducing the impurities concentration at least to 100 ppt oxygen equivalent. Three different purification loops were used, one for the liquid phase and two for the gas phase, that made the argon pass through different filters and then injected it back by four pipes deployed below the TPC at a temperature 0.4 K warmer than the average temperature of LAr inside the

cryostat. These favoured the convective movements of the 0.77 ktons of liquid argon and avoided stratification of impurities. Moreover, a set of different cryogenic instrumentation devices were installed at different locations in the cryostat to constantly monitor the status and quality of the argon. These included purity monitors and the temperature monitoring system among others. The study of these apparatus has allowed to understand that huge cryostats are very sensitive systems, in which every variable needs to be under control so that physics results are not compromised. IFIC has been heavily involved in the development and study of ProtoDUNE-SP cryogenic instrumentation, and some of the most important findings are presented in Section 3.3.

ProtoDUNE-SP was successfully installed, commissioned and exposed to a charged particle beam during The Summer and Fall of 2018. Later, it took cosmic rays data until The Summer of 2020, when its decommissioning started. During that time, the excellent capabilities of the LArTPC technology were highlighted, and the feasibility of bringing it to DUNE's scale demonstrated.

Secondary Kaon Analysis

One of the main DUNE's physics goals is searching for the hypothetical proton decay process. LArTPCs are specially good for identifying the proposed decay modes with kaons in the final states because they have access to the full decay chain of this process. On the contrary, water Cerenkov detectors can not detect the kaon since its low momentum is below the Cerenkov threshold. Among the different proton decay modes involving kaons, $p \rightarrow K^+\bar{\nu}$ has the largest branching ratio. In this channel, the only visible signal is the one of the K^+, with a very well-defined momentum of 340 MeV/c. The main kaon decay channel is $K^+ \rightarrow \mu^+\nu_\mu$ (64%), so the expected signal of this process in DUNE is a low-momentum track compatible with a kaon originated within the fiducial volume of the detector, followed by a low-momentum muon. The dominant background is generated by neutrino charged current quasi-elastic interactions, $\nu_\mu n \rightarrow p\mu^-$. When the muon happens to have a momentum similar to the 237 MeV/c expected for the K^+ decay at rest and it is not captured by a nucleus, it is indistinguishable from the one resulting from $p \rightarrow K^+\bar{\nu}$ followed by $K^+ \rightarrow \mu^+\nu_\mu$. So the discrimination between signal and background relies on two factors: first, the ability to differentiate kaons and protons, and second, the direction of the hadronic track.

Consequently, one of the most interesting studies to be done with ProtoDUNE-SP data was to demonstrate the capabilities of the LArTPC technology to iden-

tify low momentum kaons, so that the simulation of those particles and the sensitivity studies in which they are involved are validated. Unfortunately, during the beam runs of ProtoDUNE-SP almost no low energy kaons were produced. Instead, the secondary kaon selection developed and presented in Chapter 5 accomplished to select a sufficiently large sample of low energy kaons among the different secondary particles generated in hadronic reactions of higher energy. This selection is based in the main decay channel of the kaon, $K^+ \rightarrow \mu^+\nu_\mu$. Being this a two-body decay, the kinematics of the muon are very well-defined and they are used to isolate the kaon parent. Using all 6 and 7 GeV/c beam momentum runs a sample of 1200 kaon candidates with a 50% purity has been obtained. They have been used to demonstrate that the LArTPC technology can efficiently differentiate between kaons and protons by studying their energy loss profile as function of their residual range, hence proving the viability of proton decay searches in DUNE's far detectors.

The selected sample has been used also to study the simulation of the energy loss for these particles by means of the so-called Coherent Fit approach described in Chapter 6. The two-dimensional plot of $\frac{dE}{dx}$ as a function of residual range is divided in residual range slices (one-dimensional $\frac{dE}{dx}$ histograms), so that signal and background contributions can be considered. They both are described by means of a Landau-Gaussian convolution, whose different parameters are expressed as continuous functions of the residual range. In this way, a single maximum likelihood minimization procedure can be applied to all histograms simultaneously, maximizing the use of information between slices and decreasing the effect of the not-so-abundant statistics.

After the evaluation of systematic uncertainties presented in Chapter 7, it has been found that apparently the simulation is underestimating the energy loss of kaons for very low momentum. This information can be used now as a new systematic uncertainty to be considered in analysis involving kaons, as for a example a measurement of their production cross-section, which will be the next step to follow. Further studies, specially related with ion recombination, which constitutes the main source of systematic uncertainty of the $\frac{dE}{dx}$ measurement, are needed to confirm this effect. Finally, regarding the selected sample of low energy kaons, it has been observed that in the simulation they are produced with a slightly larger initial momentum, giving place to longer kaon tracks.

Resumen

Introducción

Neutrinos

[2] Los neutrinos son la segunda partícula más abundante del universo, y aun así es la que menos comprendemos. Se trata de leptones sin carga eléctrica que solo interaccionan mediante la fuerza débil, y con una masa tan pequeña que se consideran sin masa en el Modelo Estándar (SM) de física de partículas. Por ello, su sección eficaz de reacción es increíblemente baja y detectarlos puede llegar a ser una tarea verdaderamente complicada. Sabemos que hay tres familias de neutrinos, cada una de ellas asociada a un leptón cargado: el neutrino electrónico, asociado al electrón; el neutrino muónico, al muón; y el neutrino tau, al tau. Debido a la conservación del número leptónico, los neutrinos (o antineutrinos) se generan siempre junto a su anti-leptón (o leptón) cargado. De la misma forma, cuando un neutrino interacciona con el medio, el leptón cargado asociado se crea como resultado de la reacción. Dado que no podemos observar los neutrinos directamente debido a que no tienen carga eléctrica, para caracterizarlos hemos de ser capaces de identificar los leptones asociados en las diferentes reacciones en las que puedan participar.

Una de las características más interesantes de los neutrinos es su capacidad para cambiar su sabor leptónico mientras se desplazan. Esto es debido a que sus autoestados de sabor no se corresponden con sus autoestados de masa, que son los autoestados propios del hamiltoniano y, por tanto, con evolución temporal definida. En consecuencia, un autoestado de sabor bien definido en $t = 0$ tiene una probabilidad diferente de cero de ser detectado como otro sabor después de que pase cierto tiempo. Este fenómeno, conocido como "oscilaciones de neutrinos", se ha observado mediante el estudio de neutrinos solares, atmosféri-

[2] Nunca me imaginé que escribir científicamente en castellano fuese a costarme tanto. Prometo que he intentando castellanizar lo mejor posible todos los conceptos, pero pido perdón por adelantado por los gazapos que puedan encontrar.

cos, generados en reactores nucleares y creados artificialmente en aceleradores. Matemáticamente, esto se puede entender si expresamos los autoestados de sabor como una combinación lineal de los estados de masa

$$|\nu_\alpha\rangle = \sum_{k=1}^{3} U^*_{\alpha k}|\nu_k\rangle, \tag{5}$$

donde U es la matriz PMNS, que puede parametrizarse como

$$U = \begin{pmatrix} 1 & 0 & 0 \\ 0 & c_{23} & s_{23} \\ 0 & s_{23} & c_{23} \end{pmatrix} \begin{pmatrix} c_{13} & 0 & s_{13}e^{-i\delta_{CP}} \\ 0 & 1 & 0 \\ -s_{13}e^{i\delta_{CP}} & 0 & c_{13} \end{pmatrix} \begin{pmatrix} c_{12} & s_{12} & 0 \\ -s_{12} & c_{12} & 0 \\ 0 & 0 & 1 \end{pmatrix}, \tag{6}$$

con c_{ij} y s_{ij} simbolizando el coseno y el seno de θ_{ij}, respectivamente, y θ_{ij} el ángulo de mezcla entre los autoestados de masa i y j; y donde δ_{CP} es una fase compleja conocida como "fase de violación de la simetría Carga-Paridad", la cual cuantifica la diferencia en la oscilación entre los neutrinos y los antineutrinos. Dado un sabor leptónico inicial α, la probabilidad de observar un sabor diferente β tras un tiempo transcurrido t viene dada por

$$\begin{aligned} P_{\nu_\alpha \to \nu_\beta}(L,E) = \delta_{\alpha\beta} - 4\sum_{k>j} \mathcal{R}\left[U^*_{\alpha k}U_{\beta k}U_{\alpha j}U^*_{\beta j}\right] \sin^2\left(\frac{\Delta m^2_{kj}L}{4E}\right) \\ +2\sum_{k>j} \mathcal{I}\left[U^*_{\alpha k}U_{\beta k}U_{\alpha j}U^*_{\beta j}\right] \sin\left(\frac{\Delta m^2_{kj}L}{2E}\right), \end{aligned} \tag{7}$$

donde L es la distancia entre el origen del neutrino y el lugar donde se quiere caracterizar, E se corresponde con su energía, Δm_{kj} es la diferencia de masas entre los autoestados de masa k y j, y $\mathcal{R}$ y $\mathcal{I}$ se refieren a la parte real y la parte imaginaria de los elementos de matriz encerrados, respectivamente. Así pues, las ocilaciones de neutrinos se describen mediante tres ángulos de mezcla (θ_{12},θ_{23} y θ_{31}), una fase de violación CP (δ_{CP}) y dos diferencias cuadráticas de masa (Δm^2_{12} Δm^2_{23}).

Llegados a este punto, es necesario destacar varios aspectos sobre el fenómeno de las oscilaciones de neutrinos. En primer lugar, la oscilación de los neutrinos solo puede explicarse si son partículas masivas, así que el descubrimiento de este comportamiento ha supuesto la primera prueba de física más allá del Modelo Estándar, que los describe con masa cero. Además, incluir la masa de los neutrinos en el SM no es trivial, ya que genera la aparición de una gran variedad de nuevos conceptos como partículas de Majorana, neutrinos estériles y el mecanismo del balancín. En segundo lugar, la probabilidad de oscilación depende de la diferencia de masas de los estados masivos al cuadrado, por lo que no se tiene

información ni de la medida absoluta de las masas de los neutrinos ni de su jerarquía. Finalmente, un valor del δ_{CP} diferente de cero podría ser una explicación a la asimetría bariónica presente en nuestro Universo.

La generación de materia a partir de energía solo puede suceder si se crean exactamente las mismas cantidades de materia y de antimateria. El mismo proceso puede suceder de forma inversa, en el cual idénticas proporciones de materia y antimateria pueden aniquilarse para dar lugar a energía. De la misma forma, las mismas cantidades de materia y antimanteria tuvieron que generarse en los primeros instantes del Universo durante el Big Bang. No obstante, el mundo actual en el que vivimos está compuesto exclusivamente de materia y la antimateria solo existe de manera residual. Cabe preguntarse: ¿cómo habiéndose generado las mismas cantidades de materia y antimateria, estas no se han aniquilado recíprocamente? ¿Qué pasó en esos primeros instantes para que una pequeña parte de la materia sobreviviese a la aniquilación, y diera lugar posteriormente al Universo en el que vivimos? Esta cuestión es conocida como asimetría bariónica del universo, y se piensa que un valor suficientemente grande de δ_{CP} puede explicarla.

Las oscilaciones de neutrinos han sido concienzudamente estudiadas en los últimos veinte años debido a sus profundas implicaciones físicas, dando como resultado el paradigma de tres sabores ya presentado. Los experimentos dedicados al estudio de neutrinos solares, como SNO, han podido medir θ_{12} y Δm^2_{12}. Por otro lado, θ_{23} y Δm^2_{23} se han estudiado en experimentos centrados en neutrinos atmosféricos, como Super-Kamiokande, y en experimentos basados en haces de neutrinos generados en aceleradores, como T2K y NOνA. Estos últimos también han medido, junto con experimentos de reactores nucleares como Double Chooz y Daya Bay, el valor de θ_{13}. Por último, el valor nulo de δ_{CP} se ha excluido con una confianza de 3σ por experimentos de aceleradores. No obstante, en la actualidad sabemos que el nivel de confianza 5σ no se alcanzaría ni con la combinación de los datos tomados ni por tomar de todos los experimentos de esta generación. Lo mismo aplica al parámetro θ_{23}, del cual no se sabe si está por encima, por debajo, o es igual a 45°; y a la jerarquía de masas. Por ello, con el objetivo de alcanzar la precisión necesaria, se ha propuesto una nueva generación de experimentos que alcanzarán su plenitud en la próxima década, formada por Hyper-Kamiokande, JUNO y, en especial, DUNE.

Teorías de Gran Unificación y la Desintegración del Protón

El hecho de que los neutrinos tengan masa implica que el SM es una teoría incompleta, de lo que se deduce que tiene que existir otro modelo (del cual el Modelo Estándar sea una aproximación de baja energía) capaz de explicar las cosas que este no puede. Las teorías de gran unificación (GUTs, por sus siglas en inglés) son un conjunto de modelos que aspiran a ello, caracterizadas por predecir la unificación de las fuerzas electromagnética, débil y fuerte a altas escalas de energía; de la misma forma que las interacciones electromagnética y debil son unificadas en la escala electrodébil. Estas teorías tienen una gran variedad fenomenológica a altas energías que no podemos aspirar a testear en un futuro próximo. No obstante, también disponen de una serie de predicciones a baja energía accesibles a día de hoy, como la creación de partículas virtuales en reacciones del LHC o la desintegración del protón.

La desintegración del protón es un proceso prohibido por la conservación del número bariónico del Modelo Estándar[3]. No obstante, si la unificación de fuerzas predicha por las GUTs fuese cierta, el número bariónico no sería una cantidad conservada a causa de la unificación de cuarcs y leptones, dando lugar así a la desintegración del protón. Las diferentes GUTs pueden dividirse en dos grandes grupos: las no supersímetricas, las cuales favorecen el canal $p \to e^+\pi^0$ para dicho hipotético proceso; y las supersimétricas, que favorecen el canal $p \to K^+\bar{\nu}$.

A pesar de la amplia búsqueda que se ha hecho de este proceso durante años, todavía no se ha encontrado ninguna evidencia del mismo. Sí que han podido ponerse límites superiores a su vida media. Casi todos ellos han sido obtenidos por Super-Kamiokande, el cual tiene muy buena sensibilidad para explorar los canales preferidos por teorías no supersimétricas. Sin embargo, aunque también ha sido capaz de poner límites superiores a los canales que contienen kaones como resultado de la desintegración, su sensibilidad es bastante peor dado que el bajo momento del kaón lo hace invisible a los detectores de Cerenkov. Por contra, la nueva tecnología de detección de partículas conocida como "Cámara de Proyección Temporal de Argón Líquido" (LArTPC por sus siglas en inglés), piedra angular del proyecto DUNE, tiene acceso a la cadena completa de la desintegración del protón a kaones cargados, mejorando sustancialmente la sensibilidad esperada de los experimentos basados en detectores de Cerenkov.

[3]Afortunadamente. No estaríamos aquí de no ser así.

DUNE

DUNE, (*Deep Underground Neutrino Experiment*)[4] es un futuro experimento de física de neutrinos que estará localizado en Estados Unidos. Será uno de los conocidos como experimentos de larga distancia, en los cuales un haz de neutrinos generado en un acelerador se caracteriza en dos puntos distintos: primero, junto al origen del haz, por lo cual el flujo de neutrinos puede medirse antes de que empiece a oscilar; y segundo, a una distancia L del origen tal que el valor L/E maximiza la probabilidad de oscilación. El primer punto de medida se conoce como "Detector Cercano" y el segundo como "Detector Lejano". Al comparar las medidas en ambos detectores se obtiene información sobre los parámetros que describen las oscilaciones. El haz de neutrinos se genera mediante la colisión de un haz de protones contra un blanco, lo cual genera $\pi^{\pm}$ que se focalizan en una linea de desintegración. Ahí, los piones decaen en $\mu^{\pm}$ y $\nu_{\mu}/\bar{\nu}_{\mu}$ antes de colisionar contra un muro encargado de frenar a los muones y dejar pasar solo a los neutrinos.

En particular, la medida de δ_{CP} se consigue mediante el estudio de la probabilidad de oscilación del haz formado por neutrinos muónicos y el haz formado por antineutrinos muónicos. Esto, que en principio parece fácil, tiene una complicación extra de la cual todavía no se ha hablado: los conocidos como "efectos de materia". La distancia entre los dos puntos de medida es de cientos de kilómetros, por lo que el haz de neutrinos atraviesa la corteza terrestre en su camino entre detectores. Dado que la Tierra está hecha de materia (protones, neutrones y electrones) la probabilidad de interacción de neutrinos y antineutrinos es distinta. Por ello, si se quiere medir con precisión δ_{CP}, es necesario desentralazar este efecto de los efectos de materia. Hay dos manera diferentes de hacer esto:

- Bien usando un rango "corto", de manera que los efectos de materia son despreciables. Esto implica que la energía de los neutrinos tiene que ser pequeña (por debajo de 1 GeV) y bien definida. Este es el método usado por T2K y el que utilizará T2HK.

- O bien recurriendo a un rango "muy largo" y un espectro de energía alto y amplio, de manera que los efectos de materia sean tan evidentes que puedan ser fácilmente considerados. Este es el método en el que se basa DUNE.

[4]Una traducción aproximada del término al castellano sería "Experimento de Neutrinos a Gran Profundidad".

El haz de neutrinos de DUNE se generará en Fermilab, donde también estará ubicado el Detector Cercano. Por otro lado, el Detector Lejano se localizará en la Instalación de Investigación Subterránea de Sandford, a 1300 kilómetros de distancia del origen del haz y 1.5 kilómetros bajo tierra. Debido a la alta y dispersa energía del haz de neutrinos, estos pueden sufrir cualquier tipo de interacción cuando colisionen con los átomos del medio del detector lejano: dispersión cuasi-elástica, resonancia nuclear y dispersión inelástico profundo. Por ende, se espera encontrar una gran variedad de topologías y especies de partículas en dicho detector. Dado que la única forma de caracterizar el neutrino que ha reaccionado es mediante el estudio de los productos de su reacción, DUNE necesita utilizar una tecnología de detección con excelentes capacidades calorimétricas y de reconstrucción de eventos, y este es el caso de la LArTPC. El Detector Lejano de DUNE estará formado por cuatro gigantescas cámaras de proyección temporal de argón líquido modulares, cada una de ellas dentro de un criostato capaz de mantener el argón a 87 K.

Esta novedosa tecnología se ha utilizado en el pasado en otros experimentos como LArIAT, MicroBooNE e ICARUS y, más recientemente, en Proto-DUNE-SP. Todos estos experimentos han demostrado el increíble rendimiento de este tipo de detector. Esto, junto con los bajos niveles de fondo esperados a 1.5 kilómetros de profundidad, hacen del Detector Lejano de DUNE una localización ideal para desarrollar un amplio programa de física más allá de las osciolaciones de neutrinos, que incluya astronomía multi-mensajero, la búsqueda de la desintegración del protón y diversos temas de física más allá del Modelo Estándar.

La Cámara de Proyección Temporal de Argón Líquido

La tecnología LArTPC consiste en una Cámara de Proyección Temporal cuyo medio activo es argón líquido. Una TPC está formada por dos planos paralelos, uno de los cuales hace de ánodo y el otro de cátodo. Se aplica una diferencia de potencial entre ambos planos, de manera que se genere un campo eléctrico cuyas líneas vayan del ánodo al cátodo. Cuando un neutrino interacciona con el medio, se generan partículas cargadas que ionizan los átomos de argón. Los electrones liberados empiezan a derivar hacia el ánodo debido al campo eléctrico, donde son recolectados. Esto permite una reconstrucción bidimensional del evento en el plano perpendicular a la dirección de deriva. Finalmente, si conocemos el momento en el que neutrino interaccionó con el detector (comúnmente llamado t_0), dado que la velocidad de deriva de los electrones es sabida, se puede inferir la coordenada restante en la dirección de deriva para completar la reconstrucción tridimensional de la topología del suceso. Adicionalmente, dado que la cantidad

de electrones de ionización producidos por las partículas cargadas es proporcional a la energía que estas pierden al interaccionar con el medio, la LArTPC permite realizar una medida de la calorimetría de las diferentes partículas.

Esta calorimetría es fundamental para DUNE, puesto que de ella depende la identificación de especies de partículas. Dado que el detector no está expuesto a campos magnéticos, la única manera de distinguir diferentes especies es comparando sus pérdidas de energía por unidad de longitud. Esta magnitud se puede describir mediante la fórmula de Bethe-Bloch

$$\langle -\frac{dE}{dx} \rangle = K z^2 \frac{Z}{A} \frac{1}{\beta^2} \left[\ln \left(\frac{2 m_e c^2 \beta^2 \gamma^2 W_{max}}{I^2} \right) - \beta^2 - \frac{\delta(\beta\gamma)}{2} \right], \tag{8}$$

donde puede observarse que, para partículas con la misma carga z, la pérdida de energía depende de su velocidad (β). Así pues, partículas con la misma energía pero con masas distintas pierden energía de manera diferente. Lo que suele hacerse en otros tipos de experimentos es representar esta pérdida en función del momento de la partícula, pero ya que el momento no puede medirse en la LArTPC por la ausencia de campos magnéticos, esta variable se intercambia por el conocido como rango residual. El rango residual de una traza se define como la distancia de un punto de la traza hasta el final de la misma. Se puede deducir que una misma traza tiene diferentes rangos residuales, uno para cada uno de los puntos de su trayectoria. En consecuencia, diferentes tipos de partículas tienen diferentes perfiles de $\frac{dE}{dx}$ en función del rango residual, y comparando los diferentes perfiles se puede discernir qué tipo de partícula ha generado cada una de las trazas del evento. Este proceso se describe con mayor detalle en la Sección 2.4.1.1.

En el primer módulo del Detector Lejano de DUNE, FD1, conocido como módulo de Deriva Horizontal, habrá tres planos de ánodos y dos planos de cátodos, dispuestos según la secuencia A-C-A-C-A. Por tanto, este módulo contará con tres volúmenes de deriva diferente, cada uno de ellos con 3.6 metros de anchura. La diferencia de potencial entre ánodos y cátodos será de -180 kV, lo cual generará un campo eléctrico en el volumen activo de 500 V/cm, y hará a los electrones derivar con una velocidad de $\sim$1.6 mm/µs. El resto de caras del detector estarán cubiertas por una jaula de campo[5], responsable de homogeneizar el campo eléctrico dentro del volumen activo con una precisión de un 1%. Los unidad mínima a partir de la cual se forman los planos de ánodos es conocida como *Anode Plane Assembly* (APA), una estructura de acero inoxidable de 6.1 m de alto, 2.3 m largo and 76 mm de ancho sobre la que se bobinan cuatro planos de hilos. Estos hilos son los encargados de recolectar los electrones y proveer información para

[5]Esta me ha dolido.

la reconstrucción bidimensional de los eventos, lo que se consigue rotando cada uno de los dos primeros planos, llamados de inducción, un cierto ángulo con respecto a la vertical. Después, el tercer plano, denominado de recolección, se coloca paralelo a la vertical. Cuando los electrones pasan a través de los dos primeros planos generan señales bipolares mediante inducción electromagnética, mientras que al ser recolectados por el tercer plano generan señales monopolares. Posteriormente, se buscan coincidencias entre los hilos de los diferentes planos que han dado señal, lo que permite la reconstrucción espacial de los eventos. El cuarto plano de hilos está conectado a tierra para proteger a los otros tres de posibles problemas eléctricos.

La decisión de utilizar argón líquido como medio activo se debió a diferentes motivos. En primer lugar, porque al ser un elemento noble tiene una electronegatividad muy baja, lo cual significa que en general los electrones ionizados no son atrapados por otros átomos cercanos. En segundo lugar, porque el argón es un elemento relativamente pesado, lo cual aumenta las probabilidades de interación de los neutrinos con el medio. En tercer lugar, porque el argón es un centelleador excelente: emite más de 20000 fotones alrededor de 127 nm por cada MeV de energía depositado. Y no solo eso, sino que además es transparente a su propia luz de centelleo. Por tanto, esta luz (que tarda nanosegundos en llegar a los ánodos) puede utilizarse para determinar el t_0 de los eventos que no hayan sido generados por el haz. En cuarto y último lugar, porque su coste es relativamente accesible.

El Sistema de Fotodetección

Como puede deducirse de lo expuesto anteriormente, además de la TPC, el Detector Lejano de DUNE contará con un sistema de fotodetección complementario (PDS por sus siglas en inglés) con dos objetivos: proporcionar un t_0 para sucesos no generados por el haz, y proveer una medida de la calorimetría complementaria basada en la luz detectada.

Como se ha comentado, el t_0 es necesario para la reconstrucción tridimensional de los eventos. Cuando se quieren estudiar los neutrinos generados en el acelerador, el t_0 es conocido, por lo que el PDS no es realmente necesario para ello. Por otro lado, si lo que se pretende es hacer estudios de física sin el haz (como la búsqueda de la desintegración del protón), la única forma de obtener un t_0 es mediante la detección de la luz de centelleo. Esto es fundamental porque este tipo de física requiere una buena fiducialización del volumen activo del detector, una correcta identificación de los vértices y de las correcciones por atenuación, las cuales a su vez dependen de la coordenada en la dirección de deriva. Adi-

cionalmente, el PDS es capaz de mejorar el rendimiento de la TPC ya que puede proveer información redundante que se podrá utilizar para corregir y mejorar su funcionamiento, especialmente a bajas energías. En otras palabras, es necesario tener un sistema de fotodetección apropiado para expandir los resultados físicos de DUNE más allá de las oscilaciones.

Dicho sistema se basa en la tecnología conocida como X-ARAPUCA, que trata de detectar fotones atrapándolos por reflexión total. Una celda X-ARAPUCA consiste en una barra de un material capaz de desplazar la longitud de onda de los fotones incidentes (material WLS, por sus siglas en inglés), sobre la cual se coloca un filtro dicroico que refleja la luz con una longitud de onda por encima de los 400 nm. Este filtro tiene una evaporación externa de PTP. En el otro lado del material WLS se coloca una lámina reflectora. Finalmente, a dicho material se acoplan varios fotomultiplicadores de silicio (SiPM) sumados en un único canal electrónico. Cuando la luz de centelleo del argón (127 nm) llega a la evaporación de PTP, es absorbida y reemitida a 350 nm, por lo que puede pasar a través del filtro dicroico y llegar al material WLS. Ahí es absorbido una vez más y reemitido a aproximadamente 430 nm, que es la longitud de onda para la cual los SiPMs tienen la máxima eficiencia de detección. Estos fotones quedan atrapados por reflexión total dentro del material WLS hasta que son detectador por los SiPMs. Por contra, si los fotones logran escapar, son reflejados o bien por el filtro dicroico o bien por la lámina reflectora de vuelta al material WLS, pudiendo así ser detectados de nuevo.

La geometría de estas celdas puede ser ajustada para distintas necesidades. En el caso del FD1, estas celdas son conocidas como Súper-Celdas, tienen unas dimensiones de 487 mm $\times$ 93 mm $\times$ 3.5 mm, están cubiertas por seis filtros dicroicos de 78 mm $\times$ 93 mm y llevan acopladas 48 SiPMs medidos mediante un único canal electrónico. Cuatro Súper-Celdas se ensamblan mecánicamente en una única estructura de 2092 mm $\times$ 118 mm $\times$ 23 mm para formar un módulo óptico que es insertado horizontalmente dentro de las APAs ya descritas. De esta manera, los módulos ópticos pueden "ver" el interior del volumen activo (ya que los planos de hilos son transparentes a la luz) y además se encuentrán en el único lugar del detector cuyo potencial eléctrico es nulo.

Durante los últimos años se han desarrollado diferentes líneas de investigación con el objetivo de optimizar el diseño del X-ARAPUCA. Una de las principales tareas era encontrar el módelo de SiPM más apropiado para trabajar en las condiciones de DUNE (a 87 K) y que fuera acorde a sus requisitos físicos. Por ello, dos fabricantes distintos, Hamamatsu Photonics (HPK) y Fondazione Bruno Kessler (FBK), diseñaron modelos específicos que fueron evaluados en condiciones criogénicas en diferentes instituciones, entre ellas el IFIC. Estos es-

tudios incluían la medida de la ganancia y el ratio señal-ruido, la corriente oscura y el ruido correlacionado (*cross-talk* óptico y *after-pulsing*); junto con otros de resistencia a condiciones extremas mediante ciclos criogénicos controlados. Tras todos ellos se observó que, en términos generales, los sensores de HPK tenían mejores prestaciones que los de FBK, y que los sensores con mayor tamaño de píxel presentaban mayores valores de ganancia y relación señal-ruido sin un aumento significativo de corriente oscura y ruido correlacionado, motivos por los que son los mejor valorados. Finalmente, también se observó que los sensores con una mayor resistencia de extinción aparentemente tenían una menor probabilidad de mostrar eventos debidos al ruido correlacionado. Los estudios llevados a cabo en el IFIC durante más de un año se detallan en el Capítulo 4.

La decisión de utilizar la tecnología X-ARAPUCA como referencia para el sistema de fotodetección de DUNE se tomó en base a los resultados obtenidos en el experimento ProtoDUNE-SP, el mayor prototipo de DUNE construido y operado hasta la fecha. Algunos de los módulos finales que se usarán en el Detector Lejano de DUNE se han instalados en ProtoDUNE-HD, y su funcionamiento será objeto de inminentes estudios. ProtoDUNE-HD es la segunda iteración de ProtoDUNE-SP, cuyo objetivo es ser un "módulo 0" del FD1: está compuesto en su totalidad por piezas que serán usadas posteriormente en Sandford.

ProtoDUNE-SP

ProtoDUNE-SP ha sido el primero de los prototipos de DUNE construidos en el programa ProtoDUNE. A pesar de que la tecnología LArTPC había sido utilizada anterioremente en otros experimentos, nunca se había puesto en práctica a una escala tan grande como la que DUNE está planeando. Por ello se propuso el desarrollo del programa ProtoDUNE, cuyo objeto es construir prototipos de una escala intermedia entre lo que hecho anteriormente y lo que se pretende hacer, de forma que se demostrase la capacidad de superar los diversos desafíos tecnológicos. La primera iteración de ProtoDUNE consistió en dos prototipos distintos: ProtoDUNE-SP y ProtoDUNE-DP, cada uno de los cuales testeaba un modelo distinto de LArTPC, de fase única y de fase doble, respectivamente. Cada uno estaba contenido en un criostato con dimensiones internas de aproximadamente $8{\times}8{\times}8$ m^3. En el caso de ProtoDUNE-SP, sus objetivos eran:

- Prototipar y validar los procedimientos de producción, envío e instalación de los diferentes componentes del detector.
- Validar las capacidades de detección de la tecnología de fase única.

- Acumular grandes cantidades de datos con el haz de partículas para entender y calibrar la respuesta del detector a distintos tipos de partículas y para realizar análisis físicos de interés.
- Asegurar la estabilidad operacional del detector a largo plazo.

ProtoDUNE-SP consistía en dos LArTPCs que compartían el cátodo central de manera que la dirección de deriva en un volumen era opuesta a la del otro. Dicho cátodo estaba compuestos de materiales altamente resistivos para evitar descargas dieléctricas del argón. Las caras descubiertas del detector estaban ocupadas por una jaula de campo, formada por barras de aluminio conectadas mediante cadenas divisorias resistivas, que generaban el gradiente de potencial eléctrico necesario para homogeneizar el campo eléctrico en el volumen activo. Tanto la parte superior como la inferior del detector estaban cubiertas por planos conectados a tierra de tal forma que el sistema criogénico así como la fase gaseosa estaban protegidos de posibles descargas. Cada uno de los dos ánodos estaba formado por tres APAs, que contenían diez módulos ópticos similares a los X-ARAPUCA ya presentados. El detector en su conjunto colgaba del techo del criostato. Por otro lado, con el fin de reducir la pérdida de energía de las partículas del haz antes de llegar al volumen activo del detector, una penetración especial llena de nitrógeno gaseoso facilitaba la entrada de las partículas dentro del criostato. Debido a la disposición del haz, solo uno de los dos volúmenes de la TPC era atravesado por las partículas. Finalmente, dos planos identificadores de rayos cósmicos se situaban en el exterior del criostato para reconocer rayos cósmicos cruzando el detector paralelamente a los ánodos. En total, ProtoDUNE-SP prototipaba los componentes del FD1 de DUNE en una escala de 1:1 con una cantidad de argón líquido veinte veces menor.

Además del propio detector, ProtoDUNE-SP tenía un complejo sistema criogénico responsable de la recirculación y la purificación del argón, con el objetivo de reducir las impurezas hasta 100 ppt de oxígeno equivalente. El sistema contaba con tres circuitos diferenciados para ello, uno para la fase líquida y dos para la fase gas. En ellos el argón pasaba por una serie de filtros antes de volver a ser inyectado por cuatro tuberías situadas debajo de la TPC a una temperatura 0.4 K más caliente que la temperature media del argón dentro del criostato. Esto favorecía los movimientos convectivos de las 0.77 kilotoneladas de argón líquido y evitaba la estratificación vertical de las impurezas. Adicionalmente, una serie de diversos aparatos conocidos como instrumentación criogénica, localizados en diferentes puntos dentro del criostato, se encargaban de monitorizar constantemente el estado, la calidad y las dinámicas del argón. Entre ellos destacan los monitores de pureza y los sistema de monitorización de temperaturas. El estudio

de estos dispositivos ha permitido entender cuán sensible puede ser un criostato de estas magnitudes, por lo que todas las variables necesitan estar controladas para no comprometer los objetivos físicos del experimento. El IFIC ha estado muy involucrado en el desarrollo y el análisis de la instrumentación criogénica, y se puede leer un resumen de estos estudios en la Sección 3.3.

ProtoDUNE-SP fue instalado, testeado y expuesto a un haz de partículas cargadas durante el verano y otoño de 2018. Posteriormente, operó tomando datos de rayos cósmicos hasta el verano de 2020, momento en que se dio comienzo a su desmantelación. Durante este tiempo se demostró tanto las excelentes capacidades de la tecnología LArTPC como la viabilidad de operarla a la escala requerida por DUNE.

Análisis de Kaones Secundarios

Como ya se ha mencionado más arriba, uno de los principales objetivos de DUNE es realizar búsquedas de la hipotética desintegración del protón. Sus LArTPCs son especialmente útiles para estudiar los canales con kaones cargados en los estados finales, ya que tienen acceso a toda la cadena de desintegración (a diferencia de los detectores de Cerenkov, en los que el kaón está por lo general por debajo del umbral de detección). El canal más favorecido de estos procesos es $p \to K^+\bar{\nu}$, en el cual la única señal visible dentro del detector es la del K^+, que tiene un momento inicial perfectamente definido a 340 MeV/c. Su principal canal de desintegración es $K^+ \to \mu^+\nu_\mu$ (64%), por lo que la señal esperada de la desintegración del protón en DUNE es una traza de bajo momento compatible con un kaón, originada de manera descorrelacionada dentro del volumen activo del detector, seguida de una traza de bajo momento del muón resultado de su desintegración. El fondo dominante de este proceso viene dado por dispersión cuasi-elástica de neutrinos mediante corrientes cargadas, $\nu_\mu n \to p\mu^-$. Si el muón generado en este proceso tiene un momento similar a los 237 MeV/c esperados del resultante de la desintegración del kaón y no es capturado por núcleos cercanos, ambos son indistinguibles (ya que la TPC no puede medir el signo de la carga de las partículas que la atraviesan al no haber campos magnéticos). Por ello, la capacidad de discriminar entre señal y fondo depende primero de la capacidad para diferenciar kaones y protones en función de cómo interaccionan con el argón; y, segundo, de la dirección de la traza hadrónica.

Consecuentemente, uno de los estudios más interesantes que se esperaba desarrollar con los datos tomados en ProtoDUNE-SP tenía como objeto demostrar la capacidad de la LArTPC para identificar kaones de baja energía, de man-

era que la simulación de estas partículas y los estudios de sensibilidad en los que estuvieran envueltas se validasen. Lamentablemente, apenas se produjeron kaones de baja energía durante la toma de datos con haz. En su lugar, decidimos desarrollar la selección de kaones secundarios presentada en el Capítulo 5, que ha conseguido aislar una población suficientemente significativa de K^+ de bajo momento mediante su búsqueda entre las partículas secundarias resultado de reacciones hadrónicas de alta energía. Dicha selección se basa en la desintegración principal del kaón, $K^+ \to \mu^+\nu_\mu$. Dado que se trata de una desintegración a dos cuerpos, la cinemática del muón está muy bien definida y ha permitido aplicar una serie de cortes muy restrictivos. Usando toda la estadística disponible a 6 y 7 GeV/c de momento del haz se han obtenido 1200 candidatos a kaón con una pureza del 50%, que se han utilizado para demostrar la capacidad de la LArTPC para diferenciarlos eficientemente de los protones en base a su perfil de pérdida de energía por unidad de longitud en función del rango residual de las trazas, probando así la viabilidad de realizar búsquedas de la desintegración del protón en el detector lejano de DUNE.

Adicionalmente, la población seleccionada ha sido utilizada para estudiar la simulación de pérdida de energía de los kaones en argón mediante el método conocido como "Ajuste Coherente" descrito en el Capítulo 6. En él, la gráfica bidimensional del $\frac{dE}{dx}$ en función del rango residual se divide en secciones de rango residual, de manera que se obtinen distribuciones unidimensionales de $\frac{dE}{dx}$ en los que señal y fondo pueden ser considerados de manera independiente. Ambas contribuciones se describen mediante una convulición de una función de Landau y una Gaussiana, cuyos parámetros son expresados como funciones continuas del rango residual. Esto permite ajustar todos los histogramas unidimensionales en un único proceso de minimización (basado en un método de máxima verosimilitud). De esta forma, el uso de información entre histogramas es maximizado y el efecto de la escasa estadística reducido.

Tras la evaluación de los errores sistemáticos presentada en el Capítulo 7, se ha observado que aparentemente la simulación está subestimando la pérdida de energía de los kaones para muy bajo momento. Este resultado puede usarse ahora como una nueva fuente de errores sistemáticos en futuros análisis basados en kaones, como por ejemplo en la medida de su sección eficaz de producción, lo que constituiría el siguiente paso de este análisis. Por otro lado, solo cuando se hayan desarrollado más estudios que verifiquen dicha discrepancia, especialmente relacionados con el proceso de recombinación ya que este es la mayor fuente de incertidumbre sistemática de la medida, esta podrá ajustarse dentro del proceso de simulación. Para terminar, respecto a la cinemática de los kaones seleccionados, se ha podido observar que la simulación sobreestimaba tanto su longitud

xxx

como su momento inicial.

Agradecimientos

A lo largo de estos cinco años he dedicado mucho tiempo a pensar en el momento de escribir esta pequeña parte de la tesis doctoral, sobretodo durante los últimos meses. Era algo que me relajaba, que me hacía pensar que, aunque el camino estuviese siendo duro, tendría un final. Que me ayudaba a reconocer y valorar a las personas que son importantes en mi día a día, y sin las cuales no podría haber llegado hasta aquí. Ese momento ha llegado por fin, y aun habiendo pensado miles de veces en todos a los que quería nombrar y lo que quería decir de ellos, estoy seguro de que más de uno se me va a olvidar, o de que las palabras que les dedique no van a hacer justicia a todo el agradecimiento que quiero mostrarles. Sin más, empecemos.

En primer lugar, me gustaría empezar dándole las gracias a mi director de tesis, Anselmo, por haberme dado la oportunidad de realizar este trabajo, por haberme guiado y aconsejado durante los casi siete años que nos conocemos, tanto a nivel personal como profesional; y, por encima de todo, por haberme ayudado a confiar en mí mismo cuando yo más flaqueaba. No negaré que en algún que otro momento me han dado ganas de tirarle a la cabeza todas las cajas de corcho que guarda en el laboratorio a causa de su inexorable necesidad de dejarlo todo para el último momento. Pero, a pesar de eso, puedo decir que más que un supervisor en un amigo en el que sé que podré contar si algún día me da por construirme una casa.

Asimismo, me gustaría agradecer la ayuda y el consejo al resto de séniors del grupo de neutrinos del IFIC con los que he tenido el placer de coincidir durante todos estos años: Justo, Michel, Laura, Nadia, Neus y Pau. También a mis compañeros estudiantes, con los que, aun sin haber compartido todo este camino, he tenido la posibilidad de aprender, reirme y desconectar de vez en cuando: Jordi, Julio, Hamza y Mirald; y a los dos Albertos, con quienes he compartido el camino desde el máster hasta aquí. También me gustaría agradecerle a Marc, a Manu y a Jorge todo lo que me han enseñado de electrónica, que es prácticamente todo lo que sé. Finalmente, me gustaría agradecer la ayuda constante a los

miembros de la secretaría del IFIC, sin los cuales no habría sido capaz de superar el primer trámite burocrático: Luis, Jose, Tere, Marisa, Amparo y Sole.

Haber participado en una colaboración internacional como DUNE me ha dado la oportunidad de trabajar con gente de otras instituciones y/o paises, a las que también me gustaría mostrar mi agradecimiento. De todas ellas, me gustaría empezar por Inés, quien no ha dudado en apretarme las tuercas cuando ha sido necesario. *I would also like to acknowledge my dear friend Dave Warner, to whom I still owe a beer for his unmeasurable help and for using my pictures when talking about the installation of ProtoDUNE-HD (I always feel proud about that!). Finally, I would also like to thank the people from the DUNE collaboration that have helped me by listening to my presentations and giving me suggestions, and by answering my unaccountable questions in Slack: Tingjun Yan, Heng-Ye Liao, Leigh Whitehead, Richie Diurba and Jake Calcutt, among others.*

Compartir las penurias del doctorado es un caldo de cultivo fantástico para que broten las amistades más maravillosas que se puedan imaginar. Quisiera agradecerle a Masha, mi compañera de laboratorio, de doctorado y de director de tesis, todas las aventuras que hemos pasado, todas las cenas y cervezas que hemos compartido para arreglar nuestros *breakdowns* y todas las charlas en las que nos hemos desfogado poniendo verde a nuestro supervisor (Anselmo, tú no puedes leer esto). Quién me iba a decir a mí el primer día que nos conocimos que acabaría llevándote en coche a la puerta de la iglesia en el día de tu boda. No sé qué camino nos depara la vida a cada uno, pero no te quepa duda de que siempre habrá un sitio para ti en el Ford Fiesta de Gran Capacidad.

Ejemplo de amistades creadas en el ojo del huracán son también las que comparto con Manuel, Niccolò y Vikas, con quienes tuve el honor de participar en la instalación de ProtoDUNE-HD. Este ha sido sin duda uno de los momentos más emocionantes (y estresantes) de mi doctorado, pero tengo claro que si pude superarlo fue por compartirlo con vosotros. No negaré que me ilusiona y horroriza a partes iguales pensar en repetir nuestra hazaña en el *Far Detector*. Por todo ello, *grazie mille*.

Por suerte, no todas las amistades surgen "a roca y piedra". Hay algunas que brotan cuando todavía eres demasiado pequeño para entender las palabras del Maestro Sho-Hai *no puedo no querer dejar de amar a mis hermanos*. Esta frase, como no podía ser de otra manera, me hace acordarme de los tres mejores amigos que alguien como yo puede tener: Álvaro, Nacho y Ricky (por orden alfabético y sin orden de preferencia). Gracias por todas las anécdotas que comparto con cada uno de vosotros, por haberme acompañado durante prácticamente toda mi vida y por haberme ayudado a llenarla de felicidad. Es innegable que una de las aficiones que más hemos compartido estos últimos años han sido los videojuegos,

y no puedo nombrarlos y dejar de mencionar aquí a otros integrantes del canal de Discord *Roleo Gitano* (del cual los tres anteriores forman parte) con los que tantas horas he compartido: Fede, Borja y mi primo Álex. Gracias por tantas noches de vicio en la Grieta del Invocador, por tantas raids en Customs con bajas por fuego amigo, y por tantos ARAMs consecutivos con la excusa de "es que no podemos irnos a dormir con una derrota". No os quepa duda de que si hubiese tenido unos horarios decentes habría acabado la tesis un par de años antes, pero no me lo habría pasado tan bien. Además, que sepáis que por muy molestos que seáis a veces, tengo muchas ganas de escuchar los comentarios de los próximos días, que van a ser muy parecidos a "mucho doctor en física pero sigue sin esquivar los *skill-shots*". El tiempo pasa y nos hacemos mayores, pero espero siempre poder encontrar un rato para desconectar de la seriedad de la vida jugando con todos vosotros. Quisiera, antes de cerrar este párrafo, acordarme también de mi amiga Nuria, a quien le agradezco todos los veranos en el Mareny en los que hemos compartido más cubatas y chupitos de los que puedo recordar (literalmente).

Dicen que los amigos son la familia que se elige. No tengo muy claro si elegí o no a mis amigos, pero lo que está claro es que no elegí a mi familia. También tengo claro que, si me dieran a elegir ahora, no la cambiaría por nada del mundo. Gracias a mis primos, mis tíos, mis abuelos y, especialmente, a mis padres. Gracias por haber estado ahí desde siempre, por haber confiado en que era capaz de hacer lo que fuera que me propusiese, por apoyarme en mis (a veces) incomprensibles decisiones y por haberos sentido siempre orgullosos de mí, a pesar de nunca haber tenido muy claro qué es lo que hacía. Gracias, porque día a día me habeís guiado hasta convertirme en lo que soy, y si estoy aquí es por vosotros.

Para acabar, me gustaría dedicarle este último párrafo a Andrea, mi pareja, quien me ha acompañado en el camino de añadir un nuevo doctorado a mi colección, anteriormente formado sólo por el Doctorado en la Universidad de la Calle. Andrea, gracias por haber sido mi apoyo incondicional durante todo este proceso, por sentirte siempre tan orgullosa de mí sin ningún tipo de contamplaciones, por pelear por levantarme el ánimo cada vez que pensaba que estaba harto o que no podía más y por empujarme a seguir investigando a pesar de que eso signifique que tengamos que empezar a coger aviones pronto con tal de estar juntos. Gracias sobretodo porque, aun sin haber estado aquí desde el principio de este trabajo, has acabado por darle un sentido que no creía que pudiera encontrarle.

Contents

Preface **i**

Summary **v**

Resumen **xvii**

Agradecimientos **xxxi**

List of Figures **xxxix**

List of Tables **lii**

List of Abbreviations and Acronyms **lv**

1 Neutrino physics and Beyond **1**

1.1 History of Neutrinos 1

1.1.1 A Desperate Remedy 1

1.1.2 The Discovery 3

1.1.3 1, 2 and... 3? 3

1.2 Neutrino oscillations 5

1.2.1 The Solar Neutrino Problem 5

1.2.2 The Atmospheric Problem 7

1.2.3 The Discovery of Oscillations 8

1.2.4 Theoretical Framework 9

1.2.5 Neutrino masses 12

1.2.6 CP violation 13

1.2.7 Matter effects 14

1.2.8 Experiments and Parameters 14

1.3 Neutrinos in the Standard Model 17

1.3.1 Great Unification Theories and Proton Decay 21

1.4 Neutrino Interactions 22

2 The DUNE Experiment **25**
2.1 Overview . . . 25
2.2 DUNE Physics . . . 27
2.2.1 Neutrino Oscillations Physics . . . 27
2.2.2 Proton Decay Searches . . . 28
2.2.3 Supernova Searches . . . 30
2.2.4 BSM and Low Engery Physics . . . 31
2.3 Near Detector . . . 32
2.4 Far Detector . . . 34
2.4.1 Liquid Argon Time Projection Chamber Technology . . . 34
2.4.1.1 Particle Identification . . . 39
2.4.2 Photon Detection System . . . 40
2.5 The ProtoDUNE Programme . . . 45

3 The ProtoDUNE-SP Detector at CERN **47**
3.1 Overview and goals . . . 47
3.2 The Detector . . . 48
3.2.1 The LArTPC . . . 49
3.2.2 The Photon Detection System . . . 50
3.2.3 Cosmic Ray Tagger . . . 51
3.3 Cryogenic System and Instrumentation . . . 52
3.3.1 Purity Monitors . . . 53
3.3.2 Temperature Monitoring System . . . 55
3.4 Beam Line . . . 61
3.4.1 Test Beam of ProtoDUNE-SP . . . 61
3.5 Data Acquisition, Timing and Trigger . . . 63
3.6 Event Reconstruction . . . 65
3.7 Event Simulation . . . 68
3.8 Detector Calibration . . . 69
3.8.1 Space Charge Effect . . . 70
3.8.2 Charge Attenuation . . . 73
3.8.3 Detector Non-Uniformities . . . 74
3.8.4 Energy Calibration . . . 75
3.9 ProtoDUNE-SP Performance Summary . . . 76

4 SiPM Characterization for DUNE's Far Detector **79**
4.1 Silicon Photomultipliers . . . 80
4.1.1 SiPMs Characteristics . . . 81
4.2 Down-selection . . . 83

4.2.1 SiPM Models . . . 84
4.2.2 Validation procedure . . . 85
4.3 Experimental set-up . . . 86
4.4 Measurements . . . 89
4.4.1 Breakdown Voltage and Quenching Resistance . . . 89
4.4.2 Gain . . . 89
4.4.3 Uncorrelated and Correlated Noise . . . 93
4.4.4 Cryogenic Cycles . . . 96
4.5 Results . . . 97
4.5.1 25-batch HPK . . . 97
4.5.2 250-batch HPK . . . 100
4.5.3 250-batch FBK . . . 101
4.5.4 Down-selection Result . . . 102
4.6 Installation in ProtoDUNE-HD . . . 106

5 Secondary K^+ selection in ProtoDUNE-SP 111
5.1 Motivation . . . 111
5.2 Stopping K^+ in ProtoDUNE-SP . . . 113
5.3 Event Selection . . . 113
5.3.1 Beam Particle cuts . . . 114
5.3.2 Candidate existance . . . 116
5.3.3 Candidate's daughter cuts . . . 117
5.3.4 Candidate cuts . . . 119
5.3.5 Selection Result . . . 123
5.3.6 Efficiency and Purity . . . 124
5.3.7 Summary of the selection . . . 124
5.3.8 Event Displays . . . 127
5.4 ProtoDUNE-SP Kaon PID Capabilities . . . 131

6 Detailed study of K^+ energy loss 133
6.1 Residual Range slices . . . 134
6.2 Coherent Fit . . . 135
6.2.1 Parametric Functions . . . 136
6.2.1.1 Signal Parametrization . . . 136
6.2.1.2 Background Parametrization . . . 138
6.2.1.3 What-Is-Left Parametrization . . . 138
6.2.2 Minimization Procedure . . . 140
6.2.3 Fit Algorithm . . . 142
6.3 Fit Results . . . 142

6.3.1 $\sigma_{S,L}$ Coherent Fuction . . . 145
6.3.2 $\sigma_{S,G}$ Coherent Fuction . . . 145
6.3.3 μ_S Coherent Fuction . . . 147
6.3.4 Likelihood Weight . . . 152
6.3.5 Signal and Background: combined result . . . 152
6.4 Fit Stability . . . 154

7 Evaluation of Systematic Uncertainties 157
7.1 Effect of Systematic Uncertainties . . . 157
7.2 Propagation Models . . . 159
7.2.1 Efficiency-like systematics . . . 159
7.2.2 Normalisation systematics . . . 161
7.2.3 Reconstructed observable variation . . . 161
7.3 Calorimetric calibration . . . 161
7.3.1 Space Charge Effect on calibration constants . . . 163
7.3.2 Electron lifetime effect on calibration constants . . . 164
7.3.3 SCE and Electron Lifetime combined effect . . . 166
7.3.4 Error Propagation . . . 169
7.4 Recombination . . . 171
7.4.1 Error Propagation . . . 172
7.5 Space charge geometric effect . . . 173
7.5.1 Error Propagation . . . 174
7.6 Broken Tracks on APAs borders . . . 175
7.6.1 Efficiency Measurement with a Control Sample . . . 177
7.6.2 Weight Assignment . . . 180
7.6.3 Error Propagation . . . 181
7.7 Beam Particle Selection Efficiency . . . 182
7.7.1 Error Propagation . . . 184
7.8 Beam Particle Species normalisation . . . 184
7.8.1 Error Propagation . . . 186
7.9 Beam Momentum normalisation . . . 187
7.9.1 Error Propagation . . . 189

8 Results 191
8.1 Secondary Kaon Selection . . . 191
8.1.1 Evaluation of systematic uncertainties . . . 191
8.1.2 Signal and Background Distributions . . . 193
8.1.3 K^+ Distributions . . . 194
8.1.4 μ^+ Distributions . . . 194

8.2 Results on $\frac{dE}{dx}$ Characterization 196
8.2.1 Evaluation of Systematic Uncertainties 196
8.3 Future Prospects 199

9 Conclusions **201**

A Fits to histograms **205**

Bibliography **221**

List of Figures

1.1 Beta decay spectrum of Radium [2]. 2
1.2 Reactions following the pp chain (image from [11]). 6
1.3 Neutrino flux for the different endings of the pp chain (image from [12]). 6
1.4 Double ratio for atmospheric ν_μ and ν_e for different experiments (image from [21]). The double ratio consists on the ratio between the ν_μ/ν_e ratios for data and MC, in such a way that systematic uncertainties of the different experiments are cancelled and the comparison is easier. 8
1.5 Muon an tau solar neutrino flux as a function of electron neutrino flux. The intersection of bands indicates that the combined flux results are consistent with neutrino flavour transformation. Figure from [23]. . 9
1.6 Zenith angle distributions of μ-like and e-like events for sub-GeV and multi-GeV data sets. The hatched regions show the MC expectation for no oscillations. The bold line is the best-fit expectation for $\nu_\mu \leftrightarrow \nu_\tau$ oscillations. Figure from [24]. 10
1.7 ν_μ oscillation probability as a function of the ratio L/E for different neutrino species. After the first maximum, an interference effect can be observed. 12
1.8 Schematic view of normal and inverted mass ordering for neutrinos. The color represents the flavour composition of each mass state. Figure from [28]. 13
1.9 Feynman diagrams of the four interactions neutrinos can undergo with the target. Top: Neutral currents. Bottom: Charged currents. . 22
1.10 Predictions and measurements for neutrino nucleon cross-sections [80]. The three channels, QE, RES and DIS are shown, and the total cross-section as well. Top: ν_μ. Bottom: $\bar{\nu}_\mu$. 24

2.1 Schematic view of DUNE experiment and its locations. 26

2.2 Probability of oscillation from muon flavour to electron flavour for neutrinos (left) and antineutrinos (right), assuming different values of δ_{CP} and normal mass ordering. Image from [88]. 28
2.3 Sensitivity to the neutrino mass ordering (left) and CP violation (right) as a function of the true value of δ_{CP} for several exposures. The solid lines shows the median sensitivity while the width of the band represents 1σ of variations of statistics, systematics and oscillations parameters. Figure from [90]. 29
2.4 Left: Simulated event with a proton decay with a kaon (green) and the muon resulting from its decay (red). Right: Simulated CCQE background event with an outgoing proton (green) and a muon (red). The topology of both events is the same. The x-axis corresponds to the wire number whereas the y-axis corresponds to the readout time. Figure from [92]. 30
2.5 Neutrino spectrum of a supernova as a function of time for different cases: no oscillations (blue), oscillations with matter effects and normal ordering (red), oscillations with matter effects and inverted ordering (green). Figure from [88]. 31
2.6 Schematic view of DUNE's ND. Three consecutive detectors, NDLAr, TMS, and SAND, are exposed to the neutrino beam. The first two can be moved off axis with the PRISM system. Figure from [73]. . . 33
2.7 Schematic view of the principle of operation of a LArTPC. Ionization electrons drift towards the anode plane, where they generate signals in the three layers of wires. This information is used for the two-dimensional reconstruction of the event, which is ultimately completed with the t_0 information provided by the beam trigger or the detected photons. Figure from [83]. 37
2.8 Rotated view of an APA and its different wire planes. U and V are the induction planes, and are rotated with respect to the vertical axis. X is the collection plane and runs parallel to the vertical axis. Figure from [83]. 37
2.9 Cross section view of the FD1 module. The dimensions of the APA and CPA structures are 58.2 m long into the page and 12.0 m high. Each drift volume is approximately 3.6 m wide. 38
2.10 Diagram showing the residual range concept. 40
2.11 Theoretical dE/dx profile for different particle species as a function of the residual range. 40
2.12 Scheme of scintillation light production in argon. Figure from [83]. . 41

2.13 Schematic representation of a single sided X-ARAPUCA operating principle, assuming a 400 nm sharp cut-off in the dichroic filter. Figure from [83]. 43
2.14 Detailed exploded view of X-ARAPUCA supercell. Figure from [83]. 44
2.15 Full optical module that is inserted inside an APA. It is a mechanical structure combining four different SC. Figure from [83]. 45

3.1 View of the Neutrino Platform. In the front of the picture the cryostat of ProtoDUNE-SP can be observed. In the left back part, the cryostat of ProtoDUNE-DP is present too. Image from [112]. 48
3.2 Schematic view of ProtoDUNE-SP TPC detector components. Image from [105]. 51
3.3 Schematic view of ProtoDUNE-SP recirculating and purifying system. Image from [110]. 53
3.4 Diagram of ProtoDUNE-SP inner cryostat and some cryogenic instrumentation. In green, the location of the cameras is highlighted; In yellow, temperature sensors; in red, purity monitors. 54
3.5 Representation of a purity monitor. Image from [86]. 54
3.6 Electron lifetime measured by the three PrMs as a function of time from September 18 until February 2020. At the beginning, the purity was low because recirculation had not started yet. Later dips represent recirculation studies and pump stoppages. The bands represent the uncertainty of the measurements. Image from [110]. 55
3.7 Static T-Gradient Monitor installed inside ProtoDUNE-SP cryostat. 56
3.8 Comparison between the vertical temperature gradient measured in ProtoDUNE-SP by the Static T-Gradient Monitor and the CFD's prediction. The red band represents the CFD uncertainty, the data error point account for statistical and systematic uncertainties. Discrepancies are evident. 57
3.9 Relative temperature distribution measured at $y = 40$ cm plane with respect to the bottom sensor of the Static T-Gradient. The four sensors on the left ($x \approx -3$ m) were the ones on top of the pipes outlet, below the beam side APAs; the ones in the middle ($x \approx 0$ m) were the ones below the CPAs plane; and the ones on the right ($x \approx 3$ m) the ones below the non-beam side APAs plane, where the extraction pump was located. A gradient of ~ 20 mK was measured between the sensors below the cathode and the sensors closer to the pump. The colors are used so that temperatures and differences are understood easily. 58

3.10 Vertical temperature gradient measured by the Static T-Gradient Monitor during the filling process of ProtoDUNE-SP. In red, the measurement before LAr was sprayed from the top of the cryostat; in blue, the measurement after the spraying started. 59

3.11 Left: maximum temperature gradient measured by the Static T-Gradient Monitor during almost a year. The spikes were caused by recirculation stoppages. Right: projection of the plot in the left. Each entry corresponds to a data readout done each few seconds. 59

3.12 Overview of the accidental stoppage of the recirculating and purifying system of ProtoDUNE-SP at the end of October 2018. In the top plot, temperature (red) and electron lifetime (blue) are displayed. In the bottom plot, the normalized argon flow is represented. All three magnitudes are presented as a function of time. It can be observed how, after the LAr inflow was stopped on 29/10, there was an instantaneous drop of temperatures. This stoppage lasted for a day, when a new lifetime measurement was done and the problem was identified. A proper monitoring of temperature profiles would have helped to recognize this issue much earlier, avoiding loosing half of the electron lifetime. 60

3.13 Top: schematic view of the H4 beam line, its monitors and magnets. Bottom: diagram of how XBPF can be used to compute particle momentum. Images from [110]. 62

3.14 Particles' time of flight against reconstructed momentum for several ProtoDUNE-SP beam runs. Red curves represent predictions for the different particles species. Image from [110]. 63

3.15 Example of a reconstructed waveform on a single wire fitted to three Gauss functions. Image from [110]. 66

3.16 Diagram showing how the pitch of a hit is estimated. 70

3.17 Projections of the end position of reconstructed t_0-tagged cosmic rays in the xy plane (left) and zx plane (right). In absence of SCE, projections should lay over TPC boundaries, represented as black dashed lines in the plots. Image from [110]. 71

3.18 Data distortions normal to the top detector face (upper left), bottom detector face (upper right), upstream detector face (bottom left) and downstream detector face (bottom right) for data. Colour scale represents the distortion in cm. Image from [110]. 73

3.19 MC spatial distortions normal to the top detector face (upper left), bottom detector face (upper right), upstream detector face (bottom left) and downstream detector face (bottom right). Colour scale represents the distortion in cm. Image from [110]. 74

4.1 Left: schematic cross-section view of an APD. When there is incident photon in the photodiodes active area, with energy greater than the band gap energy, valence electrons are excited. They are accelerated in the depletion area towards the N-layer, generating a current flow. Image from [160]. Right: schematic view of the pixels forming an SiPM. Each of them has a quenching resistor. All of them share the same cathode and anode, thus the signal of the SiPM is the sum of the signals of every cell. Image from [161]. 81

4.2 Left: individual SiPM. Right: six-SiPM board. 84

4.3 Average single photoelectron signal for each SiPM model tested at IFIC at 50% PDE. 85

4.4 Left: black box hosting the electronic boards. Originally both boards should have been placed inside the box, but a problem with the feedthroughs made it necessary to locate the amplifier outside the box. Right: black box inside the cork box, filled with LN_2 and ready to take measurements. An optical fibre was inserted through the cork box and the black box to illuminate the SiPMs when necessary. . . . 87

4.5 Top: SiPM hosting board used during the 25-batch tests. Although it could fit up to eight SiPMs, only one channel was used during the down-selection. Bottom: differential amplifier to which the first board was connected. 88

4.6 IV curve with reverse bias. Bottom plot shows variation rate of the current. 90

4.7 IV curve with forward bias at room temperature of a LQR75 SiPM. 90

4.8 Recorded waveforms with the light source activated. It can be seen the nice performance offered by the electronic boards developed at IFIC, with very clean and fast signals with single photoelectron sensitivity and almost no underflow. 91

4.9 Charge histogram from a LQR 75 µm SiPM at 50% PDE. The first peak corresponds to the pedestal (the width of the baseline in the absence of signals), and the subsequent peaks to a single photoelectron, two photoelectrons, and so on. The red line represents a fit to the model described by the equations 4.5 and 4.5. 92

4.10 AP candidate. The identification of the peaks was done with the ROOT library TSpectrum. 93

4.11 Correlated plot distribution. The AP events are the ones on the left box, the XT candidates the ones in the big box, and all of them contribute to the DCR. 94

4.12 Top-left: DCR measured for the six LQR 75µm SiPMs. No clear trend with the PDE was observed for any of them. Top-right: Delay time distribution for a correlated noise measurement. Bottom: delay time of each event with respect to the previous event. Valleys are associated to the so-called burst phenomena. 95

4.13 Rate distribution (inverse of the delay time) fitted to a Landau distribution plus a constant. The peak corresponding to the burst contribution does not appear because of the axis range. 96

4.14 Temperature profile during some cryogenic cycles. 96

4.15 HPK characterization after the thermal cycles. Each point corresponds to the average of all SiPMs of each model, and the error corresponds to the standard deviation. Top left: gain. Top right: SNR_F. Mid left: total DCR. Mid right: DCR subtracting burst component. Bottom left: XT probability. Bottom right: AP probability. 98

4.16 IV characterization for the 120 LQR50µm tested at IFIC. Top left: breakdown voltage at room temperature and comparison with vendor's information. Top right: quenching resistance at room temperature. The red band represents the measurement provided by the vendor with the associated uncertainty. Bottom left: variation of the breakdown voltage at LN_2 temperature before and after thermal cycles. Bottom right: variation for the quenching resistance at room temperature before and after thermal cycles. Bin width has been chosen to represent set-up sensitivity. 101

4.17 IV difference before and after thermal cycles for the FBK sensors tested at IFIC. Top left: breakdown voltage difference for ST sensors. Top right: quenching resistance difference for ST sensors. Bottom left: breakdown voltage difference for TT sensors. Top right: quenching resistance difference for TT sensors. 103

4.18 FBK characterization after the thermal cycles. LQR50µm results are also presented for reference. Each point corresponds to the average of all SiPMs of each model, and the error corresponds to the standard deviation. Top left: gain. Top right: SNR_F. Mid left: total DCR. Mid right: DCR subtracting burst component. Bottom left: XT probability. Bottom right: AP probability. 104

4.19 Left: working group assembling the optical modules. Right: installation of the dichroic filters with the PTP evaporation. 106

4.20 Left, insertion of the modules in an APA. Right, module inside the APA frame, behind the wire planes. 107

4.21 APA completely instrumented about to be tested in the cold box. . 108

4.22 Installation of the APAs inside the cryostat. Top left: cold cables installation. Top right: cable trail installation. Bottom: flange installation. 109

4.23 ProtoDUNE-HD beam drift volume completely instrumented. 110

5.1 Diagram of proton decay signal (left), and the main source of background, (right). 112

5.2 Beam particle momentum measured by the beam instrumentation for 6 GeV/c runs and MC. The plotted category correspond to the true beam particle. 116

5.3 Number of candidates per event. The category plotted represents the particle specie of the true beam particle. 117

5.4 Daughter object type. Zero corresponds to unknown, 1 to shower, 2 to track. The category plotted represents the particle specie of the true particle associated to the daughter of the candidate. The discrepancy in the relative proportion between tracks and showers is due to the broken tracks between APAs overestimation in the MC simulation. 118

5.5 χ^2 distribution under muon hypothesis for candidates' daughters. . . 119

5.6 Momentum by range under muon hypothesis for candidates' daughters. 119

5.7 Daughter angular distribution with respect to candidate end direction. 120

5.8 Top: Diagram showing background formed by miss-reconstructed inelastic interactions. Bottom: Distance between daughter and candidate. 121

5.9 Top: Kaon candidates χ^2 distribution under kaon hypothesis. Two peaks are clearly distinguishable, the one in the left corresponding to the stopping kaons (signal), and the one in the right corresponding to the background. 121
5.10 $\frac{dE}{dx}$ distribution as a function of the residual range. Top: Data. Bottom: MC. The up-going population corresponds to the selected stopping kaons, whereas the flat distribution corresponds to the background. 122
5.11 Left: initial momentum of the stopping kaons sample computed using calorimetry information. The red line represents the initial momentum of a kaon resulting of a proton decay. Right: same distribution, but the category plotted represents the particle specie of the primary MC beam particle. 124
5.12 Evolution of purity and efficiency as a function of the applied cuts during the event selection. 125
5.13 Diagram of the two different topologies of the signal events. 127
5.14 Kaon candidate event display. The candidate is in the bottom right of the image. 128
5.15 Kaon candidate event display. The candidate is a long track crossing the detector and ending in the right side of the image. 128
5.16 Kaon candidate event display. The candidate is the middle large track going from left to right. It can also be observed the effect of the electron diverters, splitting the tree long tracks. 129
5.17 Kaon candidate event display. At the wire $\sim$ 250, there is a vertex with four outgoing particles. The longest one is the candidate, forming the hook described above. 130
5.18 Kaon candidate event display. The candidate tracks starts approximately at the wire 400 and ends in the 700. 130
5.19 χ^2_{prot} for stopping protons, kaons and muons. 131

6.1 $\frac{dE}{dx}$ distribution for different residual ranges. The top two plots correspond to the RR slice between 1 and 3 cm; the bottom two plots to the slice between 9 and 11 cm. The right peak corresponds to the stopping kaon population, and the left one to the background. The histogram has been normalized in such a way that the sum of all of the entries is 1. The RR slice width of 2 cm has been chosen so that a compromise is found between statistics and resolution. 134
6.2 $\frac{dE}{dx}$ distribution for residual range between 31 and 33 cm fitted to a sum of two Landau-Gaus distributions. Left: MC. Right: Data . . . 135

6.3 Signal distribution for different residual range slices. The big peak corresponds to the real contributions, whereas the left distribution of points are caused by reconstructed errors and miss-associated cosmic rays' hits. The red line corresponds to a double Landau-Gauss fit. . . 137
6.4 Dependence of the Landau-Gauss parameters with the residual range. The error bar is given by the fit result. The red line represents the chosen parametrization, given by the equations 6.1, 6.2 and 6.3. . . . 138
6.5 Background distribution for different residual range slices. The red line corresponds to a Landau-Gauss (plus constant) fit. The constant is added to take into account the homogeneous layer of counts covering all the X-axis, which would have strongly driven the fit otherwise. 139
6.6 (Almost non) dependence of the Landau-Gauss parameters with the residual range. The error bar is given by the fit result. 140
6.7 σ_L dependence for the what-is-left contribution. 141
6.8 Coherent Fit result for the slice corresponding to residual ranges between 5 and 7 cm. The dashed lines represent the individual contributions. The bottom histograms correspond to the pulls of the fits above. Left: MC. Right: data. 144
6.9 $\sigma_{S,L}$ parametric function for data and MC. The band represents the 1σ statistical error. 145
6.10 $\sigma_{S,L}$ parametric function and incoherent $\sigma_{S,L}$ values obtained for MC. 146
6.11 $\sigma_{S,G}$ parametric function for data and MC. The band represents the 1σ statistical error. 147
6.12 $\sigma_{S,G}$ parametric function and incoherent $\sigma_{S,L}$ values obtained for MC. 148
6.13 μ_S parametric function for data and MC. The band represents the 1σ statistical error. 148
6.14 Comparative of data and MC of the residual range slices for the region of discrepancy between both samples. It can be observed how for lower values than 9-11 cm, the difference is more evident. 150
6.15 μ_S parametric function and incoherent μ_S values obtained for MC. . 151
6.16 Likelihood weight with respect to the full likelihood as a function of the RR slice. 152
6.17 $\frac{dE}{dx}$ distribution as a function of the residual range. Top: MC. Bottom: data. The red line represents the MPV, and the black dashed line represents the MPV of the background, both obtained from the Coherent Fit. 153
6.18 Distribution obtained for the μ_S coherent parameters in the stability studies. 155

7.1 Systematic uncertainty propagation of the SCE on the local calibration constants. Top left: error in YZ corrections. Top right: one-dimensional projection of the plot on the left. Bottom: error in X corrections. 165
7.2 Systematic uncertainty propagation of the lifetime correction on the local calibration constants. Top left: error in YZ corrections. Top right: one-dimensional projection of the plot on the left. Bottom: error in X corrections. 166
7.3 dQ/dx distribution along X axis after SCE and lifetime corrections. The non-flat profile is due to the diffusion effect. The red line represents the global MPV value. 167
7.4 Systematic uncertainty propagation of the combined SCE lifetime corrections on the YZ local calibration constants. Top Left: error in YZ corrections for MC simulation. Top right: one-dimensional projection of the plot on the left. Bottom Left: error in YZ corrections for run 5770. Bottom Right: one-dimensional projection of the plot on the left. 168
7.5 Systematic unceratinty propagation of the combined SCE lifetime corrections on the X local calibration constants. Left: MC. Right: Run 5770. 168
7.6 Systematic uncertainty on the $\frac{dQ}{dx}$ calibration procedure. Bins size has been computed so the uncertainty to be applied has only one significant digit below 1%. 169
7.7 Systematic uncertainty of the calorimetric calibration propagated to the selection. The relative error is larger in the regions with lower statistics. 170
7.8 Effect of the calorimetry systematic over the coherent parameters. . . 171
7.9 Recombination systematic uncertainty propagated to the selection. . 173
7.10 SCE systematic uncertainty (at geometric level) propagated to the selection. 174
7.11 Beam particle end position for 6 and 7 GeV sample. The two peaks at 220 and 440 cm correspond to the broken tracks in the region between APAs. This effect is overestimated in MC. 175
7.12 Electron diverters effect on the analysis sample. Top: kaon candidate's Z start position. Bottom: schematic view of this effect. The two kaon tracks correspond to a single kaon, so the one selected as the candidate (the second one) is shorter than what it truly is. . . . 176
7.13 Control sample for breaking efficiency measurement. It is formed by 1 GeV/c μ^+ π^+ from the beam. 177

7.14 Selection of broken tracks. Left: control sample Z end position. Right: cosine between the track and its daughter. Bottom: selection result. 178
7.15 Left: θ_{XZ} angle for the selected sample. Right: θ_{YZ} angle for the selected sample. The difference is due to an error in the beam simulation, which enters the detector with a different orientation than data. 179
7.16 Sample and subsample used to compute the true efficiency of the MC in the analysis sample. 180
7.17 Topologies to be considered when assigning efficiency and inefficiency weights in the broken tracks systematic. From top to bottom: broken track that has to be weighted by the efficiency ratio; non broken track that does not have to be weighted; non broken track that starts naturally in the electron diverters regions and does not have to be weighted; and non broken track that has to be weighted by the inefficiency ratio. 181
7.18 Broken tracks on APAs region systematic propagated to the selection. Left: χ^2_K distribution. Right: Start Z distribution. The region between peaks is merged in a single bin due to the low available statistics. The same is done with the region at the right of the second peak. 182
7.19 Beam particle identification efficiency for different particle species and momenta. Image from [139]. 183
7.20 Beam particle identification efficiency systematic propagated to the selection. 185
7.21 Beam species normalisation systematic propagated to the selection. . 186
7.22 χ^2_K distribution normalized for 6 and 7 GeV/c beam events. Left: MC. Right: data. 187
7.23 Effect of applying different normalisation weights over 7 GeV MC events on the coherent parameters. 188
7.24 Beam momentum systematic propagated to the selection. 189

8.1 All systematic uncertainties propagated to the selection. 193
8.2 Final distributions for the whole sample accounting for statistical and systematic uncertainties. Top left: χ^2_K distribution. Top right: length distribution. Bottom left: Z start position. Bottom right: Z end position. 194
8.3 Top: initial momentum distribution with statistical and systematic error for the signal sample. Mid: length distribution. Bottom: dE/dx distribution. 195

8.4 Top: initial momentum distribution with statistical and systematic error for the daughters of the signal sample. Bottom: dE/dx distribution. 195
8.5 Coherent fit parameters for the signal MPV after the propagation of all systematic uncertainties in 1000 toy experiments. The red line represents the results obtained without systematics, and the pale band represents the associated statistical uncertainty. 197
8.6 K^+ $\frac{dE}{dx}$ MPV comparison for data and MC after systematic uncertainty propagation. 198
8.7 K^+ $\frac{dE}{dx}$ MPV minus MPV(data) for data and MC after systematic uncertainty propagation. 198

A.1 Coherent Fit result for the slice corresponding to residual ranges between 1 and 3 cm. 205
A.2 Coherent Fit result for the slice corresponding to residual ranges between 3 and 5 cm. 206
A.3 Coherent Fit result for the slice corresponding to residual ranges between 5 and 7 cm. 206
A.4 Coherent Fit result for the slice corresponding to residual ranges between 7 and 9 cm. 207
A.5 Coherent Fit result for the slice corresponding to residual ranges between 9 and 11 cm. 207
A.6 Coherent Fit result for the slice corresponding to residual ranges between 11 and 13 cm. 208
A.7 Coherent Fit result for the slice corresponding to residual ranges between 13 and 15 cm. 208
A.8 Coherent Fit result for the slice corresponding to residual ranges between 15 and 17 cm. 209
A.9 Coherent Fit result for the slice corresponding to residual ranges between 17 and 19 cm. 209
A.10 Coherent Fit result for the slice corresponding to residual ranges between 19 and 21 cm. 210
A.11 Coherent Fit result for the slice corresponding to residual ranges between 21 and 23 cm. 210
A.12 Coherent Fit result for the slice corresponding to residual ranges between 23 and 25 cm. 211
A.13 Coherent Fit result for the slice corresponding to residual ranges between 25 and 27 cm. 211

A.14 Coherent Fit result for the slice corresponding to residual ranges between 27 and 29 cm. 212
A.15 Coherent Fit result for the slice corresponding to residual ranges between 29 and 31 cm. 212
A.16 Coherent Fit result for the slice corresponding to residual ranges between 31 and 33 cm. 213
A.17 Coherent Fit result for the slice corresponding to residual ranges between 33 and 35 cm. 213
A.18 Coherent Fit result for the slice corresponding to residual ranges between 35 and 37 cm. 214
A.19 Coherent Fit result for the slice corresponding to residual ranges between 37 and 39 cm. 214
A.20 Coherent Fit result for the slice corresponding to residual ranges between 39 and 41 cm. 215
A.21 Coherent Fit result for the slice corresponding to residual ranges between 41 and 43 cm. 215
A.22 Coherent Fit result for the slice corresponding to residual ranges between 43 and 45 cm. 216
A.23 Coherent Fit result for the slice corresponding to residual ranges between 45 and 47 cm. 216
A.24 Coherent Fit result for the slice corresponding to residual ranges between 47 and 49 cm. 217
A.25 Coherent Fit result for the slice corresponding to residual ranges between 49 and 51 cm. 217
A.26 Coherent Fit result for the slice corresponding to residual ranges between 51 and 53 cm. 218
A.27 Coherent Fit result for the slice corresponding to residual ranges between 53 and 55 cm. 218
A.28 Coherent Fit result for the slice corresponding to residual ranges between 55 and 57 cm. 219
A.29 Coherent Fit result for the slice corresponding to residual ranges between 57 and 59 cm. 219
A.30 Coherent Fit result for the slice corresponding to residual ranges between 59 and 61 cm. 220

List of Tables

1.1 Global fit results of neutrino oscillation parameters for NO and IO. Results from [70] 16

3.1 Beam instrumentation logic to identify particles species. The numeric intervals in the TOF column represent the cut applied in ns. LP and HP refer to low-pressure and high-pressure Cerenkov detectors, respectively; and 1 and 0 represent the presence or absence of signal. A dash is used to indicate that the instrument is not used in the logic. 64

3.2 Beam triggers per beam momentum and particle specie. 64

4.1 SiPMs requirements at operation voltage 83

4.2 HPK SiPMs models and their main characteristics. 85

4.3 FBK SiPMs models and their main characteristics. 85

4.4 Results of the characterization of the HPK 25-batch SiPMs tested at IFIC previous to the LN_2 cycles (PB) and after the cycles. Each value is the average over all SiPMs of each model, and the error corresponds to the standard deviation. 99

4.5 Results of the characterization of the HPK 250-batch SiPMs tested at IFIC after the cycles. Each value is the average over all SiPMs of each model, and the error corresponds to the standard deviation. Measurements of the SiPMs of the same model of the 25-batch are also presented for comparison. 102

4.6 Results of the characterization of the FBK 250-batch SiPMs tested at IFIC after the cycles. Each value is the average over all SiPMs of each model, and the error corresponds to the standard deviation. . . 105

5.1 True information regarding kaons for a subsample of the MC simulation. The percentage shown is with respect to the number above. The particles considered are exclusively the ones belonging to the true beam particle hierarchy. 115

5.2 Reconstructed information regarding kaons for a subsample of the MC simulation. The percentage shown is with respect to the number above. The particles considered are exclusively the ones belonging to the beam particle hierarchy. 115
5.3 Selection summary for data and MC as a function of the cuts applied. 126

6.1 Parameters describing the $\sigma_{S,L}$ coherent function for data and MC. Errors shown are statistical. 146
6.2 Correlation coefficients for data and MC for the $\sigma_{S,L}$ parameters extracted from the Coherent Fit. 146
6.3 Parameters describing the $\sigma_{S,G}$ coherent function for data and MC. Errors shown are statistical. 147
6.4 Correlation coefficients for data and MC for the $\sigma_{S,G}$ parameters extracted from the Coherent Fit. 147
6.5 Parameters describing the μ_S coherent function for data and MC. Errors shown are statistical and have been computed by MINOS. Even though positive and negative errors were slightly different, their first significant digit was equal. 151
6.6 Correlation coefficients for Data and MC for the μ_S parameters extracted from the Coherent Fit. 151

7.1 Summary of systematic uncertainties considered. 159
7.2 Systematic source for the propagation of the calorimetry calibration systematic. 169
7.3 Relative uncertainty of each coherent parameter of the MPV function due to the systematic uncertainty on the calorimetry calibration . . . 170
7.4 Modified Box Model parameters measured in ProtoDUNE-SP. The third row corresponds to the ratio data/MC, and the error is obtained by error propagation from the fitted parameters. 171
7.5 Relative uncertainty of each coherent parameter of the MPV function due to the recombination systematic uncertainty. 172
7.6 Relative uncertainty of each coherent parameter of the MPV function due to the SCE systematic uncertainty. 175
7.7 Broken track efficiency measured with the control sample. The errors shown are statistical. Upper and lower levels of the efficiency are almost symmetric, so the mean value is taken as the error. The error shown for the ratio is computed by error propagation. 178
7.8 Broken track efficiency measured for different subsamples of the control sample. Errors shown are statistical. 179

7.9 Relative uncertainty of each coherent parameter of the MPV function due to the broken tracks systematic. 181
7.10 Ratio data/MC for the beam particle identification efficiency, for different particle species and beam momenta. The true efficiency for the analysis sample is also presented. Errors shown are statistical. Values from [139]. 184
7.11 Relative uncertainty of each coherent parameter of the MPV function due to the beam particle identification efficiency systematic. 184
7.12 Percentage of beam particle species with respect to the total number of beam events as a function of the beam momentum. Errors are computed as Poisson variables and the error on the ratio is computed by error propagation. 185
7.13 Relative uncertainty of each coherent parameter of the MPV function due to the beam particle normalisation systematic. 186
7.14 Total number of beam events for each beam momentum. Errors are statistical. 187
7.15 Relative uncertainty of each coherent parameter of the MPV function due to the beam momentum normalisation systematic. 189

8.1 Summary of the propagation of all the systematic uncertainties individually in the event selection. The last two rows represent the quadratic addition of the individual propagations and the fully correlated study. A hyphen means that a particular systematic has not been considered. 192
8.2 Summary of the propagation of all systematic uncertainties individually over the coherent fit parameters. The last two rows represent the quadratic addition of the individual propagations and the fully correlated study. 196
8.3 Parameters describing the μ_S Coherent function for data and MC. The MC uncertainties shown are first statistical (using MINOS) and second systematic. Data uncertainty is statistical and computed by MINOS. 197

List of Abbreviations and Acronyms

1D . . . . . One-Dimensional

2D . . . . . Two-Dimensional

3D . . . . . Three-Dimensional

ADC . . . . . Analog-to-Digital Converter

AP . . . . . After-Pulse

APA . . . . . Anode Plane Array

APD . . . . . Avalenche Photodiode

BSM . . . . . Beyond Standard Model

CC . . . . . Charged Current

CE . . . . . Cold Electronics

CFD . . . . . Computational Fluid Dynamic

CNN . . . . . Convolutional Neural Network

CP . . . . . Charge-Parity

CRT . . . . . Cosmic Ray Tagger

CS . . . . . Control Sample

CSDA . . . . . Continuous Slowing Down Approximation

CTB . . . . . Central Trigger Board

DAQ . . . . . Data Acquisition

DCR . . . . . Dark Current Rate

DIS . . . . . Deep Inelastic Scattering

DP . . . . . Dual-Phase

DUNE . . . . . Deep Underground Neutrino Experiment

FBK . . . . . Fondazione Bruno Kessler

FC . . . . . Field Cage

FD . . . . . Far Detector

FEMB . . . . . Front-End Motherboard

GUT . . . . . Great Unification Theory

HD . . . . . Horizontal Drift

HPK . . . . . Hamamatsu Photonics Kabushiki-Kaisha

HV . . . . . High Voltage

IFIC . . . . . Instituto de Física Corpuscular

IO . . . . . Inverted Ordering

IV . . . . . Intensity-Voltage

LAPD . . . . . Liquid Argon Purity Demonstrator

LArTPC . . . . . Liquid Argon Time Projection Chamber

LBNF . . . . . Long Baseline Neutrino Facility

LEP . . . . . Large Electron-Position Collider

LHC . . . . . Large Hadron Collider

LNG . . . . . Liquefied Natural Gas

MC . . . . . Montecarlo

MEWP . . . . . Movile Elevating Work Platform

MIP . . . . . Minimum Ionizing Particle

NC . . . . . Neutral Current

ND . . . . . Near Detector

NO . . . . . Normal Ordering

OV . . . . . Over-Voltage

p.e. . . . . Photo-electron

PDE . . . . . Photon Detection Efficiency

pdf . . . . . Probability Density Function

PDS . . . . . Photon Detection System

PID . . . . . Particle Identification

PMNS . . . . . Pontecorvo-Maki-Nakagawa-Sakata

PMT . . . . . Photo-Multiplier

pp . . . . . proton-proton

ppt . . . . . Parts per trillion

PRISM . . . . . Precision Reaction-Independent Spectrum Measurement

PrM . . . . . Purity Monitor

PTP . . . . . p-therphenyl

QE . . . . . Quasy-elastic

R&D . . . . . Research And Development

RCE . . . . . Reconfigurable Cluster Element

RES . . . . . Nuclear Resonance

RR . . . . . Residual Range

SAND . . . . . System for on-Axis Neutrino Detection

SC . . . . . Super-Cell

SCE . . . . . Space Charge Effect

SiPM . . . . . Silicon Photo-multiplier

SK . . . . . Super-Kamiokande

SM . . . . . Standard Model

SNP . . . . . Solar Neutrino Problem

SNR . . . . . Signal-to-Noise Ratio

SP . . . . . Single-Phase

SPS . . . . . Super Proton Synchrotron

SSM . . . . . Standard Solar Model

ST . . . . . Single Trench

SURF . . . . . Sandford Underground Research Facility

TMS . . . . . Temporary Muon Spectrometer

TOF . . . . . Time Of Flight

TPB . . . . . Tetraphenyl-butadiene

TT . . . . . Triple Trench

VD . . . . . Vertical Drift

WIB . . . . . Warm Interface Board

WLS . . . . . Wavelength-Shifting

XBPF . . . . . eXperimental Beam Profile Fibre monitor

XCET . . . . . eXperimental Cerenkov Threshold monitor

XT . . . . . Cross-Talk

1 Neutrino physics and Beyond

So much universe, and so little time.

— Terry Pratchett, *The Last Hero*

Even though neutrinos are the most abundant particles in the Universe after photons, they remain to be the less understood among the so-far discovered particles. This chapter provides an overview of neutrino physics. It starts with an historical introduction in Section 1.1, from the hypothesis of their existence until the discovery of the three flavours. Section 1.2 and 1.3 contain a detailed explanation of why neutrino oscillations were proposed, their discovery and the theoretical framework; and how do they (not) fit within the Standard Model of particle physics. Finally, Section 1.4 provides an overview of neutrino interactions with nucleus, which is the detection mechanism used in most experiments.

1.1 History of Neutrinos

1.1.1 A Desperate Remedy

Neutrinos are, among the so-far known existing particles, probably the most mysterious ones. Indeed, there were no signs of their existence until the middle of the XX century. In the early 1900s three different channels of radioactive decay were observed: the emission of a helium atom from a nucleus (alpha decay), the emission of a photon (gamma decay) and the emission of an electron (beta decay). In 1914, James Chadwick studied the last of these [1], which he believed to happen as follows:

$$ {}^{A}_{Z}N \rightarrow {}^{A}_{Z+1}N' + e^{-} \, . \tag{1.1} $$

Basically, a nucleus N transforms to a daughter nucleus N' with one proton more $(Z+1)$ and same atomic mass A, emitting an electron in the process. In a more actual interpretation:

$$ n \rightarrow p + e^{-} \, . \tag{1.2} $$

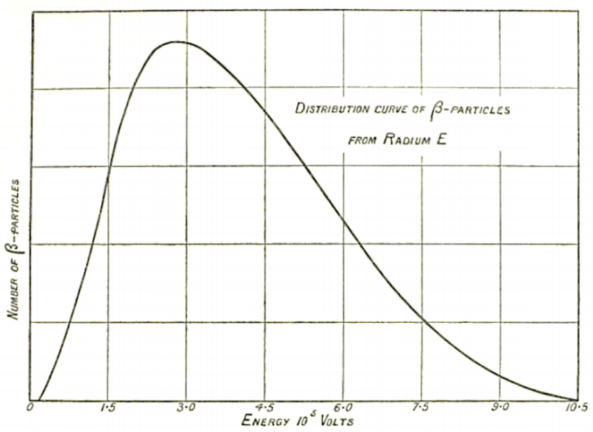

Figure 1.1: Beta decay spectrum of Radium [2].

One way or another, this process was a two-body decay whit very well defined kinematics. Because of that, radioactive decays of Radium nucleus were expected to preserve the laws of angular, charge and, of course, energy conservation. The target of these studies was to measure the energy of the outgoing electron, which was expected to present a discrete spectrum. Plot twist: it didn't. Instead, the measured electrons presented a continuous spectrum (see Figure 1.1) that afterwards was confirmed by Ellis and Wooster [2].

This was a shock to the physics community, and a wide range of theories arised trying to explain the obtained results. It was even proposed that maybe the energy conservation was not an absolute law, but an statistical one (as the second law of thermodynamics), meaning that the energy was only conserved for a sufficiently large ammount of particles, and its conservation did not work in a particle-by-particle basis.

It was Wolfgang Pauli who had to provide a 'desperate remedy' to solve this problem in 1933. He proposed the existence of a new (almost) massless particle with no electric charge and spin $\frac{1}{2}$, which was also a result of the beta decay described above [3]. Thus, the process was no longer a two-body decay but a three-body decay

$$n \to p + e^- + \nu\,, \tag{1.3}$$

and the unexplainable energy spectrum of the beta electrons no longer violated the principle of energy conservation since this new particle would carry the missing energy. However, he solved one problem by presenting another: a ghostly particle that had not been detected until then and that was probably impossi-

ble to detect, or in his own words, 'I have done something very bad today by proposing a particle that cannot be detected; it is something no theorist should ever do' [4].

He suggested to call them neutrons, but after the discovery of what we know as neutron today, it was re-baptized as little neutron —neutrino.

1.1.2 The Discovery

Although Pauli was convinced that it would be impossible to detect neutrinos, Frederick Reines and Clyde Cowan thought otherwise. If they existed, it had to be possible to detect them. It was only required a sufficiently large neutrino flux, a good detection strategy, and patience.

A nuclear plant produces an enourmus flux of neutrinos as a side-product of nuclear fusion, of the order of $\sim 2 \times 10^{20}$ neutrinos per second per GWth of thermal power. In 1956 at Savanna River nuclear powerplant, Reines and Cowan installed a detector full of liquid scintillartor with photo-multipliers (PMT) to look for the neutrino signal, which was expected to be like this: first, neutrino would produce an inverse beta decay reaction (see Equation 1.4), producing an outgoing positron and neutron. The positron would aniquilate with an electron, generating two coincident photons (Equation 1.5). On the other hand, the neutron would be absorved by a cadmium nucleus, emmiting a delayed gamma ray (another photon) afterwards (see Equation 1.6). Thus, the signal of the neutrino was formed by two coincident photons and a delayed gamma ray.

$$\bar{\nu}_e + p \rightarrow n + e^+ \tag{1.4}$$

$$e^+ + e^- \rightarrow \gamma + \gamma \tag{1.5}$$

$$n + {}^{108}Cd \rightarrow {}^{109}Cd* \rightarrow {}^{109}Cd + \gamma \tag{1.6}$$

From time to time experiments work, and this was one of those occasions. The delayed gamma was found and was considered to be an experimental proof of neutrino's existence [5].

1.1.3 1, 2 and... 3?

After Reines and Cowan had demonstrated the existence of electronic neutrinos, a natural question arose: are there other species of neutrinos? The muon had been discovered in 1936 by Anderson and Neddermeyer [6] and was considered

to be the next generation lepton following the electron. Thus, if electrons had an associated neutrino, could muons have associated neutrinos too? And the answer was yes! It was detected for the first time in Brookhaven National Laboratory in 1962 in an experiment led by Lederman, Schwartz and Steinberger [7], in which a beam of protons was made to collide at a Beryllium target, generating π mesons. These π decayed into muons plus neutrinos

$$\pi^{\pm} \rightarrow \mu^{\pm} + \nu_{\mu}/\bar{\nu}_{\mu} \tag{1.7}$$

in a decay volume before hitting a 5 kton steel wall, meant to stop muons and let only neutrinos pass through. Neutrinos would reach a neon-filled spark chamber, producing muons when interacting. The tracks of such muons were considered to be a proof of ν_{μ} existance.

It is in the nature of physicists to keep pushing to find the upper and lower bounds of problems. The lower bound to the question of how many neutrinos existed had been set to two. There was no clear answer to the upper bound yet, so new ways to measure it were suggested. The total number of leptonically active neutrinos could be measured via its coupling with the Z boson. It can decay to any active pair neutrino anti-neutrino

$$Z \rightarrow \nu + \bar{\nu} \tag{1.8}$$

and the width of such process is proportional to the number of neutrino flavours. In the decade of 1990, experiments at LEP (Large Electron-Positron Collider) successfully measured the number of leptonically active neutrinos to be $N_{\nu} = 2.984 \pm 0.008$ [8]. Since only two had been directly observed, and it was known that three existed, there was one left to be found[1]. The discovery of the τ lepton in 1974 in SLAC [9], conforming the third leptonic generation, reinforced the feeling of the existence of a third neutrino associated to this new just discovered particle.

Its finding was done in Fermilab by the DONUT collaboration in 2001 [10], in a similar way as ν_{μ} discovery. A proton beam hitted a tungsten target creating Ds mesons, which decayed into $\tau^{\pm} + \nu_{\tau}/\bar{\nu}_{\tau}$. After filtering the neutrino beam, neutrinos would reach the detector, interact and generate τ leptons (see Equations 1.9 and 1.10), which would leave a ~ 1 mm trace before decaying into a muon and a neutrino.

$$\nu_{\tau} + n \rightarrow \tau^{-} + p \tag{1.9}$$

[1] Or, at least, 0.984 ± 0.008.

$$\bar{\nu_\tau} + p \rightarrow \tau^+ + n \tag{1.10}$$

With this, three neutrino flavours had been discovered, and have remained to be three until today. However, as we just said, physicists like to push upper and lower bounds, and as we will see in the following sections, we keep doing that with the number of neutrinos.

Simply for temporal context, in 2001 I was six years old and I was playing with Spider-man toys in my house. Neutrinos history started one hundred years ago, but it is still ongoing and keeps strongly driving high energy physics. As we are going to see, if detecting them for the first time was complicated, understanding its nature is even more.

1.2 Neutrino oscillations

1.2.1 The Solar Neutrino Problem

Neutrinos had appeared as a mysterious source of questions for the physicist, but their spooky nature and the fact that they only interacted through weak force, made it feel that they could help to answer questions regarding other natural phenomena. Any object in the Universe suffering radioactive decays (as for example, a banana, a human being or a collapsing star) is emitting neutrinos. If these neutrinos can be detected, information from the radioactive decays happening in all of these different things can be obtained.

This was also the case of the Sun. Different thermonuclear reactions are happening continuously in its core. Since neutrinos do not interact electromagnetically, they can easily leave the Sun after being emitted in its core and propagate through the space; differently to what happens to photons, which take millions of years to reach the surface of the star due to scatterings. Thus, neutrinos had became a fantastic candle of information to understand what was happening inside the Sun. The Standard Solar Moder (SSM) states that for a star like the Sun, most of the thermonuclear reactions taking place in its core are orignitad from the so-called proton-proton (pp) chain, where hydrogen transforms directly into helium. This chain has different terminations, in which neutrinos of different energies are emitted (see Figure 1.2).

Since the energies of the pp chains are known, the flux of neutrinos as a function of their energy can be predicted (see Figure 1.3). However, even though the Sun emmits 2×10^{38} neutrinos per second, its ridiculously small cross-section (of the order of 10^{-43}) made the measurement of this flux very challenging. And,

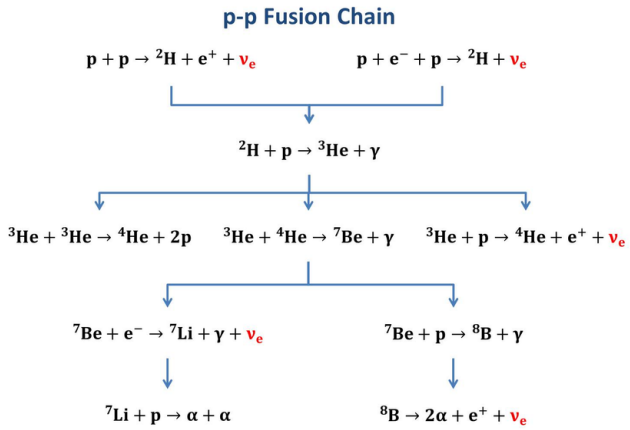

Figure 1.2: Reactions following the pp chain (image from [11]).

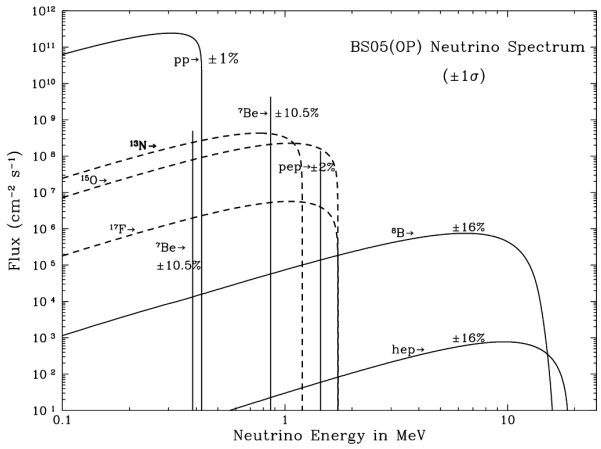

Figure 1.3: Neutrino flux for the different endings of the pp chain (image from [12]).

of course, whenever there is a prediction about something very complicated to measure, there is a physicist willing to give it a try. This was the case of Raymond Davis, who developed an inverse beta decay experiment in a Homestake mine in 1967 for this task. Electron neutrinos were expected to arrive to the detector and interact with the Clorium it was filled with, and produce Argon atoms as a result:

$$\nu_e + {}^{37}Cl \rightarrow {}^{37}Ar + e^- \,. \tag{1.11}$$

Afterwards, the number of neutrino interactions could be known by counting the

argon atoms. It was found that only a third of the expected electron neutrinos were arriving to the detector [13,14]. However, the reaction described in Equation 1.11 requires at least 800 eV to happen. If one looks at Figure 1.3, it can be observed how the biggest part of the neutrino flux is below 1 MeV, and it was argued that the deficit was due to a lack of sensitivity of the Homestake experiment. Then, it was proposed to use Gallium as a target instead

$$\nu_e + {}^{71}Ga \rightarrow {}^{71}Ge + e^- \,, \tag{1.12}$$

which had a 200 eV threshold. The SAGE [15] and GALLEX [16] experiments tried to measure the expected-to-be-correct flux of neutrinos, and they could not help but confirm the deficit observed in Homestake.

This deficit of 2/3 in the ν_e flux was known as the Solar Neutrino Problem (SNP). This, like every time neutrinos do something different to what we expect them to, was a shock for the astrophysicist community. Did this mean that the SSM was wrong? The SSM is based on a series of very precise astrophysical and cosmological observations (basically, the Bing-Bang Model). If the measured flux of neutrinos was so different from what had been predicted, did it mean than our knowledge of nuclear astrophysics (and what it was based on) was wrong?

1.2.2 The Atmospheric Problem

Fortunately for astrophysicists, neutrinos were also misbehaving in other fields. When cosmic rays reach the outer layers of the Earth's atmosphere, they produce pion showers. These particles usually decay to muons and neutrinos

$$\pi \rightarrow \mu + \nu_\mu \,, \tag{1.13}$$

and muons decay to electrons and neutrinos

$$\mu \rightarrow e + \nu_e + \nu_\mu \,. \tag{1.14}$$

Based on this simple reasoning, one would expect that the ratio of atmospheric neutrinos flavours was $\nu_\mu/\nu_e \sim 2$.

Different experiments tried to measure such ratio, as Soudan-2 [17], IMB [18], Kamionkande [19] or Super-Kamiokande (SK) [20], and all of them found approximately half the expected ratio (see Figure 1.4). Once again, neutrinos were providing many questions and few answers.

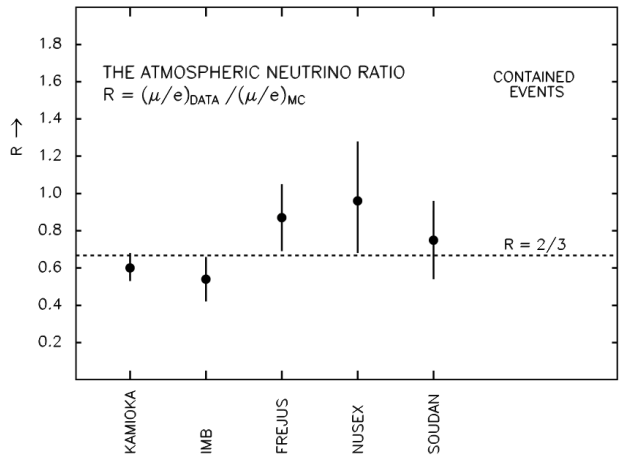

Figure 1.4: Double ratio for atmospheric ν_μ and ν_e for different experiments (image from [21]). The double ratio consists on the ratio between the ν_μ/ν_e ratios for data and MC, in such a way that systematic uncertainties of the different experiments are cancelled and the comparison is easier.

1.2.3 The Discovery of Oscillations

Both of the previously presented anomalies could be explained by the hypothesis of neutrino oscillations, which means that a neutrino can change its flavour state as it propagates through space. This hypothesis was originally presented by Bruno Pontecorvo [22], and was proved by Super-Kamiokante in 1998 and SNO experiment in 2002 [23]. SNO was a 400 tons heavy water Cerenkov detector sensitive to all three neutrino flavours by charged current (CC) (Equation 1.15), neutral current (NC) (Equation 1.16) and elastic scattering (Equation 1.17)

$$\nu_e + d \rightarrow p + p + e^- \tag{1.15}$$

$$\nu_\alpha + d \rightarrow p + n + \nu_\alpha \tag{1.16}$$

$$\nu_\alpha + e^- \rightarrow \nu_\alpha + e^- \tag{1.17}$$

where d stands for deuteron and α refers to three kind of neutrino. Whereas CC channel provides information only about the ν_e, the other two are sensitive to all three neutrino flavours. The ν_e neutrino flux measured by SNO was approximately a third of the predicted by the SSM, in agreement with Homestake, SAGE and GALLEX. However, the total flux of neutrinos was consistent with

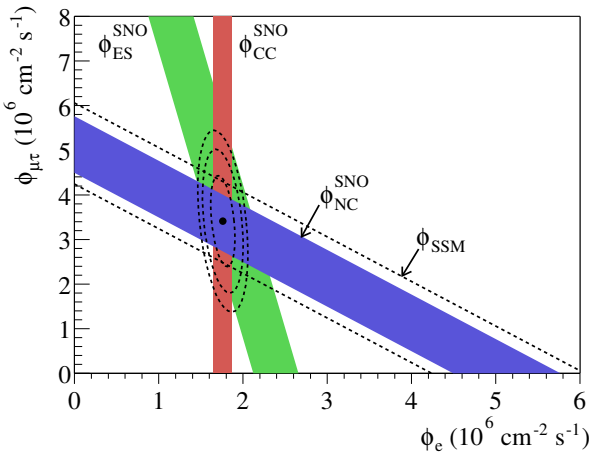

Figure 1.5: Muon an tau solar neutrino flux as a function of electron neutrino flux. The intersection of bands indicates that the combined flux results are consistent with neutrino flavour transformation. Figure from [23].

the SSM prediction (Figure 1.5), solving the neutrino solar problem and proving the neutrino oscillation phenomena at the same time.

On the other hand, the resolution of the neutrino atmospheric problem was solved by Super-Kamiokande, which is an ultra pure water Cerenkov detector. The observed neutrino flux showed a clear dependence with the zenith angle, meaning that neutrinos generated in the atmosphere and reaching the detector after passing through the Earth were more likely to oscillate than the ones arriving directly from the atmosphere [24] (see Figure 1.6).

With this, both neutrino problems were solved and the phenomenon of neutrino oscillations was demonstrated. In the following section, the theory behind the neutrino oscillations and its relevance for high energy physics will be explained, and the most up to date knowledge of the different parameters will be reviewed.

1.2.4 Theoretical Framework

In quantum mechanics [25], neutrino oscillations can be understood as a result of the non-correspondence between the flavour eigenstates and the mass eigenstates. Flavour eigenstates, the ones that suffer electroweak interactions, can be described as a linear combination of mass eigenstates:

$$|\nu_\alpha\rangle = \sum_{k=1}^{3} U^*_{\alpha k} |\nu_k\rangle, \tag{1.18}$$

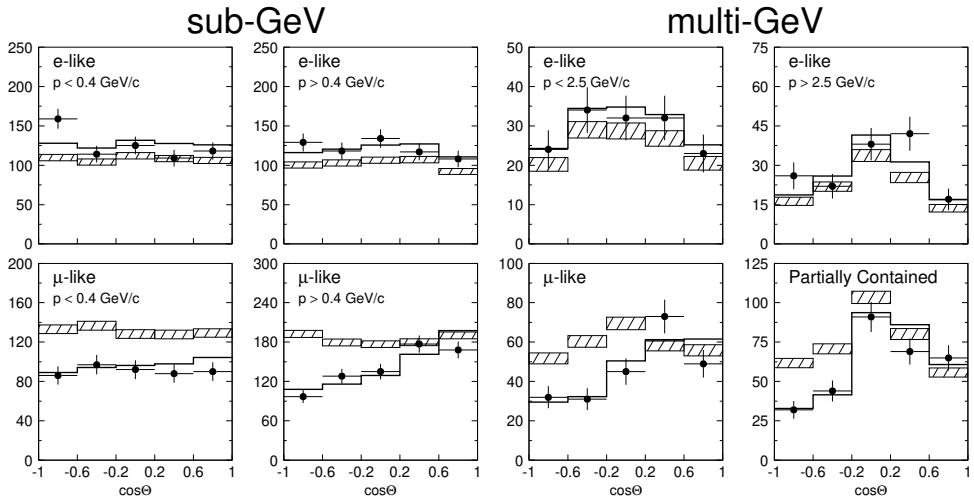

Figure 1.6: Zenith angle distributions of μ-like and e-like events for sub-GeV and multi-GeV data sets. The hatched regions show the MC expectation for no oscillations. The bold line is the best-fit expectation for $\nu_\mu \leftrightarrow \nu_\tau$ oscillations. Figure from [24].

where $\alpha = e, \mu, \tau$; ν_k is each one of the mass eigenstates, and U is a unitarty 3×3 matrix called the Pontecorvo-Maki-Nakagawa-Sakata (PMNS) matrix [26], which can be represented as

$$U = \begin{pmatrix} U_{e1} & U_{\mu 1} & U_{\tau 1} \\ U_{e2} & U_{\mu 2} & U_{\tau 2} \\ U_{e3} & U_{\mu 3} & U_{\tau 3} \end{pmatrix}; \tag{1.19}$$

or in a parametrized[2] way:

$$U = \begin{pmatrix} c_{12}c_{23} & s_{12}c_{13} & s_{13}e^{-i\delta_{CP}} \\ -s_{12}c_{23} - c_{12}s_{23}s_{13}e^{i\delta_{CP}} & c_{12}c_{23} - s_{12}s_{23}s_{13}e^{i\delta_{CP}} & s_{23}c_{13} \\ s_{12}s_{23} - c_{12}c_{23}s_{13}e^{i\delta_{CP}} & -c_{12}s_{23} - s_{12}c_{23}s_{13}e^{i\delta_{CP}} & c_{23}c_{13} \end{pmatrix}, \tag{1.20}$$

where $c_{ij} = cos\theta_{ij}$ and $s_{ij} = sin\theta_{ij}$, θ_{ij} stands for three mixing angles and δ_{CP} is Charge-Parity (CP) symmetry violating complex phase. This is the most general way to parametrize a three-dimensional rotation matrix.

In quantum mechanics the time evolution is only described by mass states. Since they are eigenstates of the hamiltonian

$$H|\nu_k\rangle = E_k|\nu_k\rangle, \tag{1.21}$$

[2]and much more complicated to write

with eigenvalues $E_k = \sqrt{\vec{p}^2 + m_k^2}$, the time evolution is presented through the time-dependent Shrödinger equation

$$i\frac{d}{dt}|\nu_k(t)\rangle = H|\nu_k\rangle. \tag{1.22}$$

Provided that massive neutrino states evolution can be approximated with a plane wave,

$$|\nu_k(t)\rangle = e^{-iE_k t}|\nu_k\rangle, \tag{1.23}$$

the flavour state described in Equation 1.18 can be writen now with a time dependence, in such a way that a flavour state neutrino α created at $t = 0$ is

$$|\nu_\alpha(t)\rangle = \sum_{k=1}^{3} U_{\alpha k}^* e^{-iE_k t}|\nu_k\rangle. \tag{1.24}$$

Since U is unitary, massive states ν_k can be presented as a linear combination of flavour states (in the same way as flavour states are presented as linear combinations of mass states, Equation 1.18). Considering this, the previous equation converts into:

$$\nu_\alpha(t)\rangle = \sum_{\beta=e,\mu,\tau} (\sum_{k=1}^{3} U_{\alpha k}^* e^{-iE_k t}) U_{\beta k}|\nu_\beta\rangle, \tag{1.25}$$

which means that as long as U is not the identity matrix, an originally well-defined flavour eigenstate at $t = 0$ evolves in time to become a linear superposition of flavour eigenstates. With this equation, the oscillation probability from one flavour state to another can be computed as

$$P_{\nu_\alpha \to \nu_\beta}(t) = |\langle \nu_\beta|\nu_\alpha(t)\rangle|^2 = \sum_{k,j} U_{\alpha k}^* U_{\beta k} U_{\alpha j} U_{\beta j}^* e^{-i(E_k - E_j)t}. \tag{1.26}$$

Considering that neutrinos are ultra-relativistic particles we can approximate $E_k - E_j$ by $\frac{\Delta m_{kj}^2}{2E}$, where $\Delta m_{kj}^2 = m_k^2 - m_j^2$. In the same way, in ultra-relativistic limit, $t = L$, where L is the distance travelled by the neutrino. Thus, substituting in Equation 1.26, we have

$$P_{\nu_\alpha \to \nu_\beta}(L, E) = |\langle \nu_\beta|\nu_\alpha(t)\rangle|^2 = \sum_{k,j} U_{\alpha k}^* U_{\beta k} U_{\alpha j} U_{\beta j}^* e^{-i\frac{\Delta m_{kj}^2 L}{2E}}. \tag{1.27}$$

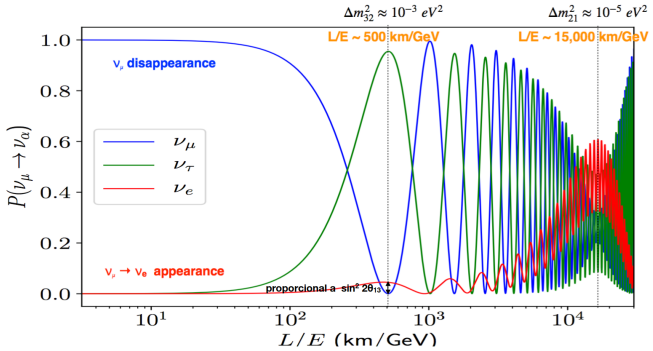

Figure 1.7: ν_μ oscillation probability as a function of the ratio L/E for different neutrino species. After the first maximum, an interference effect can be observed.

The oscillation probability depends on the mixing angles, the CP violating phase, squared mass differences, travelled distance and particle's energy. Separating real and imaginary parts we find

$$P_{\nu_\alpha \rightarrow \nu_\beta}(L,E) = \delta_{\alpha\beta} - 4\sum_{k>j} \mathcal{R}\left[U^*_{\alpha k}U_{\beta k}U_{\alpha j}U^*_{\beta j}\right] \sin^2\left(\frac{\Delta m^2_{kj}L}{4E}\right) + 2\sum_{k>j} \mathcal{I}\left[U^*_{\alpha k}U_{\beta k}U_{\alpha j}U^*_{\beta j}\right] \sin\left(\frac{\Delta m^2_{kj}L}{2E}\right), \quad (1.28)$$

where $\delta_{\alpha,\beta}$ is the Kronecker delta. It is possible to see that neutrino oscillations can not happen unless $\Delta m_{kj} \neq 0$. In other words, the observation of neutrino oscillations implies that neutrinos are massive. Figure 1.7 shows the ν_μ oscillation probability as a function of the ratio L/E.

1.2.5 Neutrino masses

There are some interesting points to highlight from our previous derivation. One of them is that the oscillation probabilities do not depend directly on neutrino masses but on the neutrino mass difference squared. Because of that, neutrino oscillations experiments cannot provide (in principle) a direct measurement of neutrino mass, but a measurement of $|\Delta m^2_{21}|$ and $|\Delta m^2_{31}|$. It is said in principle because there is an additional effect on the oscillations, the so-called matter effects, that can help to reveal the sign of the mass difference. This effect, that will be explained in the following sections, has contributed to measure the sign of $|\Delta m^2_{21}|$, whereas the sign of $|\Delta m^2_{31}|$ remains unknown. Thus there are two possible options for the ordering of the neutrino masses, tipically known as

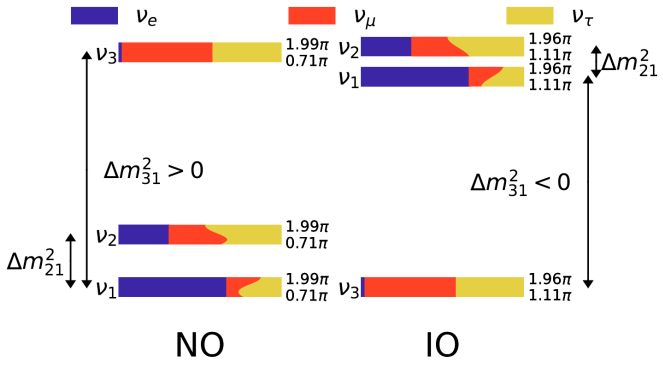

Figure 1.8: Schematic view of normal and inverted mass ordering for neutrinos. The color represents the flavour composition of each mass state. Figure from [28].

'normal ordering' (NO) ($m_1 < m_2 < m_3$) and 'inverted ordering' (IO) ($m_3 < m_1 < m_2$) [27] (see Figure 1.8).

Apart from neutrino oscillations experiments, there are other kind of experiments aiming to provide absolute measurements of neutrino masses, as KATRIN, which have been able to provide only upper limits [29]. However, neutrino-less double beta decay experiments [30] and cosmological bounds [31,32] provide the thightest constrains, whose global fit gives the following limits [33,34]:

$$\sum m_\nu^{NO} \gtrsim 0.06eV\,,$$

$$\sum m_\nu^{IO} \gtrsim 0.01eV\,.$$

1.2.6 CP violation

The other important thing to highlight from the previous derivation is the existence of the δ_{CP} phase. This phase appears naturally since the PMNS matrix is the most general way of writing a unitary rotation matrix in a Hilbert space. However, apart from the mathematical technicality, δ_{CP} has deep physics implications. A value of this phase different from zero would imply that neutrinos and antineutrinos do not oscillate in the same way. This could be related with the baryon asymmetry present in the Universe (or, in other words, the existence of the Universe itself), for which there is no clear answer yet [27]. In section 1.2.8 the current knowledge of this phase will be shown.

1.2.7 Matter effects

Even though a deep understanding of neutrino oscillation is out of the scope of this dissertation, it is interesting to have an insight of its peculiarities for the forthcoming sections. One of them is the effect of matter over neutrino oscillations. The previous theoretical derivation was done considering that neutrinos travel in vacuum, but what happens when they travel through another medium, like the Earth, for example? Whatever medium different from vacuum is formed by matter, i.e. electrons, protons and neutrons. Neutrinos can undergo different interactions with these particles as they travel through the medium. The main difference is that neutrinos can suffer elastic scattering with electrons, whereas antineutrinos cannot, meaning that there is an asymmetry on how the medium affects the neutrino flux whether it is formed by neutrinos or antineutrinos [35,36]. This effect is usually described by adding the following effective potential in the hamiltonian of the neutrinos:

$$V_{CC} = \sqrt{2} G_F N_e, \tag{1.29}$$

where G_F is the Fermi constant and N_e is the electron density of the medium. The most important result of adding this potential is that the final oscillation probability is sensible to the sign of the squared mass differences (for a complete derivation, see [27]). In the case of solar neutrinos, since they have to travel through the Sun itself, this effect was big enough to measure the sign of Δm^2_{21}.

1.2.8 Experiments and Parameters

The confirmation of neutrino oscillations triggered the development of new experiments aiming to exploit every available neutrino source and every energy range. The different approaches and the most updated values of the oscillations parameters are presented here.

The neutrino mixing matrix previously presented in Equation 1.20 can be decomposed in the following way

$$U = \begin{pmatrix} 1 & 0 & 0 \\ 0 & c_{23} & s_{23} \\ 0 & s_{23} & c_{23} \end{pmatrix} \begin{pmatrix} c_{13} & 0 & s_{13} e^{-i\delta_{CP}} \\ 0 & 1 & 0 \\ -s_{13} e^{i\delta_{CP}} & 0 & c_{13} \end{pmatrix} \begin{pmatrix} c_{12} & s_{12} & 0 \\ -s_{12} & c_{12} & 0 \\ 0 & 0 & 1 \end{pmatrix} \tag{1.30}$$

so the different components can be properly highlighted. The first matrix, the one containing θ_{23}, is usually called the atmospheric matrix, the second one is known as reactor matrix, and the third one as solar matrix; since they can be

characterized by studying neutrinos generated in the atmosphere, in nuclear reactors and in the Sun, respectively. Experiments doing this are commonly known as atmospheric neutrino experiments, reactor experiments and solar experiments[3].

These three different types of neutrino experiments have something in common: they characterize the neutrino flux that is naturally produced in different sources. Since each source generates neutrinos with different characteristics, each kind of experiment is optimized to be sensitive to different neutrino flavours and/or energies. For example, reactor neutrinos look for ν_e and $\bar{\nu}_e$ via inverse beta decay, meaning that their target material has to be sensitive to this process. Whilst atmospheric neutrino experiments aim to characterize both electron and muon neutrinos, and since muon neutrinos can only be detected via charged current, they require a very large fiducial mass. Finally, solar neutrino experiments need a low energy threshold and a very good energy resolution because solar neutrinos have, in general, low energy. All of them need, of course, powerful shielding from cosmic rays and other backgrounds, meaning that they are usually located underground. Furthermore, whereas atmospheric and solar neutrino experiments do not have control of the distance travelled by the neutrinos, reactor neutrino experiments are built at a distance from the source that aims to maximize the oscillation probability as a function of the energy distribution of the neutrinos (remember equation 1.28 and the L/E dependence). Examples of solar neutrino experiments have been presented before, as SNO [37], Homestake [38], GALLEX [39] or SAGE [40]. Examples of atmospheric neutrinos are Super-Kamiokande [41] or Icecube Deep-Core [42]. Finally, examples of reactor experiments are Double Chooz [43], RENO [44], Daya Bay [45] or KamLAND [46].

Apart from the three experiment approaches presented above, there is another type which is known as accelerator neutrino experiments, in which neutrinos are produced in an accelerator in a more controlled way. A proton beam with adjustable energy is thrown against a target, and $\pi^{\pm}$ are produced as a result. π^+ or π^- are focused in a decay tunnel, where they produce μ^+ (μ^-) and ν_μ ($\bar{\nu}_\mu$). Muons are stopped by a very thick wall, whereas neutrinos pass through and are sent towards a detector. Among the different accelerator neutrino experiments we find short and long-baseline experiments. In the first case, a detector is located close to the origin of the neutrino beam, and aims to measure the neutrino oscillation at short ranges. In the second case, the detector is located further away from the neutrino beam origin, usually at a L/E value such that the oscillation probability is maximum. Since neutrinos produced in

[3]No surprises here.

Table 1.1: Global fit results of neutrino oscillation parameters for NO and IO. Results from [70]

Parameter	Best Fit $\pm 1\sigma$
$\Delta m^2_{21} : [10^{-5}\text{eV}^2]$	$7.50^{+0.22}_{-0.20}$
$\lvert\Delta m^2_{31}\rvert : [10^{-3}\text{eV}^2]$ (NO)	$2.55^{+0.02}_{-0.03}$
$\lvert\Delta m^2_{31}\rvert : [10^{-3}\text{eV}^2]$ (IO)	$2.45^{+0.02}_{-0.03}$
$\sin^2\theta_{12}/10^{-1}$	3.18 ± 0.16
$\sin^2\theta_{23}/10^{-1}$ (NO)	5.74 ± 0.14
$\sin^2\theta_{23}/10^{-1}$ (IO)	$5.78^{+0.10}_{-0.17}$
$\sin^2\theta_{13}/10^{-1}$ (NO)	$2.200^{+0.069}_{-0.062}$
$\sin^2\theta_{13}/10^{-1}$ (IO)	$2.225^{+0.064}_{-0.070}$
δ_{CP}/π (NO)	$1.08^{+0.13}_{-0.12}$
δ_{CP}/π (IO)	$1.58^{+0.15}_{-0.16}$

accelerators follow a stochastic process, their energy spectrum is wide, so long-baseline neutrino experiments need to characterize the unoscillated neutrino flux before characterizing the oscillated one. Because of that, they use two detectors, one near the origin of the neutrino beam, usually known as Near Detector (ND) and another one at the L/E maximum, known as Far Detector (FD). Examples of short-baseline neutrino experiments are LSND [47] or MiniBooNE [48], and examples of long-baseline neutrino experiments are T2K [49], NOνA [50] or MINOS [51].

All these different experiments have tried to measure the neutrino oscillations parameters they have access to during the last years, usually by combining their results. Results from the solar neutrino experiments presented above [13, 15, 52, 53] are combined with SK [54–56] and KamLAND [57–59] to determine Δm^2_{21} and $\sin^2\theta_{12}$. Results from accelerator experiments have provided precise measurements of $\sin^2\theta_{23}$ and $|\Delta m^2_{23}|$ [60–62]. These two parameters are also measured by atmospheric neutrino experiments [63, 64]. Reactor experiments' main contribution is to $\sin^2\theta_{13}$, although they also contribute to the measurement of $|\Delta m^2_{23}|$ [65–67]. $\sin^2\theta_{13}$ is also accessible for accelerator experiments. Finally, the main contribution to determine δ_{CP} is the one from long-baseline neutrino experiments [68, 69]. Global fits are performed using all available data to provide a general plot of neutrino oscillations. In Table 1.1 the global fit results from [70] are presented.

Although our knowledge of neutrino oscillations parameters has considerably improved in the last decade, there are still some fundamental questions whose answer remains unclear. As previously commented, it is still not known which is the real ordering of the neutrino masses. Even though a preference from one ordering or the other can be obtained from global fits, current experiments cannot provide a direct measurement of it. From the parameters of Table 1.1, it cannot be differentiated whether θ_{23} is above, below or equal to $45°$[4] at a 3σ CL, and the zero value for the δ_{CP} phase has not been excluded either. This two points have deep physics implications, specially the second one, since it could be directly related with the matter-antimatter asymmetry of the Universe. It is already known that even combining the results of all the neutrino experiments of the current generation, the 3σ level for these unknowns is not reachable. Because of that, a new generation of neutrino experiments has been proposed, formed by Hyper-Kamiokande, JUNO and DUNE [71–73]. Particularly interesting is the case of DUNE, a new long-baseline neutrino experiment capable of measuring δ_{CP} and the mass ordering without external constrains, as it will be explained in Chapter 2. DUNE is, somehow, the ultimate goal of this work.

1.3 Neutrinos in the Standard Model

Up to now we have reviewed the story of neutrinos, the discovery of their oscillations and the theory behind this. However, neutrinos are just a piece of the puzzle of particle physics, from which the Standard Model (SM) provides the most comprehensive and precise description. Hence, it is important to understand what part do neutrinos play on it.

The SM is a gauge theory, based on the symmetry group $SU(3)_C \otimes SU(2)_L \otimes U(1)_Y$, which describes strong, weak and electromagnetic interactions respectively, via the exchange of the corresponding gauge bosons: eight massles gluons for strong interaction, one massles photon for electromagnetic interaction, and three massive bosons ($W^{\pm}$ and Z) for the weak interaction [74]. The fermionic matter is formed by three families of leptons and quarks, organized as follows:

$$\begin{bmatrix} \nu_e & u \\ e^- & d' \end{bmatrix}, \begin{bmatrix} \nu_\mu & c \\ \mu^- & s' \end{bmatrix}, \begin{bmatrix} \nu_\tau & t \\ \tau^- & b' \end{bmatrix}, \tag{1.31}$$

[4] In the case of being exactly $45°$, it could be explained either by a new symmetry of leptons or by a fantastic sense of humour of nature.

where

$$\begin{bmatrix} \nu_l & q_u \\ l^- & q_d \end{bmatrix} \equiv \begin{pmatrix} \nu_l \\ l^- \end{pmatrix}, \begin{pmatrix} q_u \\ q_d \end{pmatrix}, l_R^-, q_{uR}, q_{dR}, \tag{1.32}$$

plus the corresponding antiparticles. These three families appear to have identical properties under gauge interaction and only differ in their mass and flavour quantum numbers. It can be seen how the left-handed fields (L) are $SU(2)_L$ doublets, while their right-handed (R) partners transform as $SU(2)_L$ singlets. Notice here that there is no right-handed field associated to neutrinos.

Neutrinos interact excusively through weak interaction, either by charged current (CC), in which its associated charge lepton is needed,

$$\mathcal{L}_{CC} = -\frac{g}{2\sqrt{2}} j_\alpha^{CC} W^\alpha + h.c., \tag{1.33}$$

or neutral current

$$\mathcal{L}_{NC} = -\frac{g}{2\cos\theta_W} j_\alpha^{NC} Z^\alpha + h.c., \tag{1.34}$$

where

$$j_\alpha^{CC} = 2\sum_\beta \overline{\nu_{\beta L}} \gamma_\alpha l_{\beta L} \tag{1.35}$$

represents the leptonic charged current and

$$j_\alpha^{NC} = 2\sum_\beta \overline{\nu_{\beta L}} \gamma_\alpha \nu_{\beta L} \tag{1.36}$$

represents the neutrino neutral current, being W and Z the fields of the $W^\pm$ and Z vector bosons, g the electroweak interaction constant and θ_W the Weinberg angle.

As presented, the SM does not allow mass terms to exist, neither for bosons nor fermions, since they would break the gauge symmetry. This is solved by the so-called Spontaneous Symmetry Breaking mechanism, in which mass is granted to particles by its coupling with the Higgs doublet ϕ

$$\phi(x) = \begin{pmatrix} \phi^{(+)}(x) \\ \phi^{(0)}(x) \end{pmatrix}, \tag{1.37}$$

which obeys a lagrangian of the form

$$\mathcal{L} = (D_\mu \phi)^\dagger D^\mu \phi - \mu^2 \phi^\dagger \phi - h(\phi^\dagger \phi)^2, \tag{1.38}$$

where D_μ represents the covariant derivative of the SM. The lagrangian above is gauge invariant, and for values of $\mu^2 < 0$, the field presents an infinite amount of degenerate states with minimum energy, whose expectation value is $\sqrt{\frac{-\mu^2}{2h}} = \frac{v}{\sqrt{2}}$. The Higgs field can be re-parametrized in a more familiar way

$$\phi(x) = \exp\left(i\frac{\sigma_i}{2}\theta^i(x)\right)\frac{1}{\sqrt{2}}\begin{pmatrix} 0 \\ v + H(x) \end{pmatrix}. \tag{1.39}$$

The covariant derivative couples the Higgs multiplet field with the bosons fields. When the physical (unitary) gauge is taken ($\theta^i(x) = 0$), the vacuum expectation value naturally generates a quadratic mass term for gauge bosons of the form

$$\frac{g^2v^2}{4}W_\mu^\dagger W^\mu \tag{1.40}$$

and

$$\frac{g^2v^2}{8\cos^2\theta_W}Z_\mu Z^\mu. \tag{1.41}$$

On the other hand, fermions require additional yukawa coupling terms of the form

$$\mathcal{L}_Y = -c_d\overline{F_L}\phi f_{d,R} - c_u\overline{F_L}\phi^\dagger f_{u,R} + h.c. \tag{1.42}$$

with $\overline{F_L}$ representing a doublet of left-handed fermions shown in Equation 1.32 and $f_{d,R}$ $f_{u,R}$ representing the doublet's down (up) component right-handed singlet.Under the unitary gauge, they can be expressed as

$$\mathcal{L}_Y = -c_d\frac{v}{\sqrt{2}}\overline{d_L}d_R - c_u\frac{v}{\sqrt{2}}\overline{u_L}u_R + h.c.\,. \tag{1.43}$$

These yukawa couplings are also gauge invariants. Notice here that, since neutrinos do not have such right-handed singlets, they are not coupled to the Higgs field and therefore they are massless in the SM.

The reason for the non-existence of the right-handed singlets of neutrinos is that they had never been observed[5]. The electroweak interaction only couples with left-handed fermions or right-handed antifermions, meaning that it completely violates the Parity symmetry. During the conception of the SM neutrino masses were known to be very small, even compatible with zero, and for that reason they were left as massless.

[5]I could have started by this, but it wouldn't have been as exciting.

However, as we just have seen, neutrino oscillations can only exist if neutrinos have mass. Different approaches are considered to give mass to neutrinos within the SM. On one hand, it is possible to add a mass term for neutrinos similar to the other leptons' (known as Dirac term) by adding the right-handed singlets ν_R, non-existent until now, with the only condition of being sterile: they are singlets of the full SM gauge group, meaning that they do not interact via strong or electroweak interaction. In this way neutrinos can couple with the Higgs as the other leptons do

$$\mathcal{L}_Y = -c_\nu \frac{v}{\sqrt{2}}(\overline{\nu_L}\nu_R + \overline{\nu_R}\nu_L), \tag{1.44}$$

at the expense of introducing new sterile neutrinos. However, this would leave open other questions: why are neutrino masses so small compared to the ones of the other fermions? and, more importantly, what are these sterile neutrinos? Do they exist exclusively to provide mass to the neutrinos?[6]

On the other hand, it is possible to give mass to neutrinos considering that they are Majorana particles, meaning that the right-handed state of the neutrino is the antiparticle of the left-handed state [75]. In this way, the mass term would be

$$\mathcal{L}_Y = -c_\nu \frac{v}{\sqrt{2}}(\overline{\nu_L}\nu_L^C + \overline{\nu_L^C}\nu_L), \tag{1.45}$$

where $\overline{\nu_L^C}$ is the right-handed component $C\nu_L^T$, with C indicating the charge conjugation operation. If this option happens to be true, it has to be produced by some new physics with a larger energy scale and not by the SM, since it would violate lepton number conservation (it allows neutrinos to become antineutrinos and vice-versa). This is not valid for charged fermions because it would violate the charge conservation.

As we have just seen, neutrinos do not completely fit yet on the SM, since they are considered to be massless, while it is known they are not. Indeed, neutrino oscillations are a very strong proof of physics beyond the SM. We are in a similar situation to the one in which the physics community was in the 1930', in which the beta decay spectrum sought for an explanation, and the proposed answer (the existence of neutrinos) brought even more complicated questions. Now, neutrino masses also seek for an explanation, and any of the possible answers are bringing even more complicated questions.

[6] And, what's even more important, how much do we have to push the upper bound of the number of neutrinos so that we can find an appropriate explanation for their masses?

1.3.1 Great Unification Theories and Proton Decay

Apart from the neutrino masses, the SM has also difficulties explaining other aspects of the Universe as its matter-antimatter asymmetry or the existence of the Dark Matter. Like it usually happens, it tends to be considered that the current model we have (the SM) explains a lower energy regime of a higher energy scale of physics, thus it is nothing but a low energy approximation of a more complete theory. The different approaches for this theory usually predict the unification of electromagnetic, weak and strong interactions at very large energies, in the same way as electromagnetic and weak interactions are unified; and also the unification of quarks and leptons. This is why they are called Great Unification Theories (GUTs) [27].

GUTs have a wide range of predictions at different ranges of energies. At sufficiently high energies, they involve the existence of too-many-new-particles-to-be-counted[7] which we cannot aim to search in the near future. However, they also have some predictions at lower energies that can be tested, as the generation of on-shell particles in the LHC (Large Hadron Collider) or nucleon decays [76].

Nucleon decays are provided by the quark-lepton unification previously mentioned: if leptons and quarks are the same, then lepton and baryon number are no longer a conserved quantity, and consequently the proton can undergo decay processes. Several experiments have been looking for such phenomenon, as Super-Kamiokande, since its observation would be a direct proof of GUTs and this new high energy regime of physics. Among the two big groups of GUTs theories, we find the supersymmetric and the non-supersymmetric ones, which differ in the dominant decay mode of the proton. Supersymmetric GUTs generally predict that the main channel for the proton decay is $p \to K^+\bar{\nu}$, whereas non-supersymmetric GUTs prefer $p \to e^+\pi^0$ [77]. Although no evidence for proton decay has been found, limits to the lifetime of such processes provide constraints to the different GUT models, dismissing some of them. Due to its large sensitive mass and exposure, SK has been able to set the strongest upper limits for several channels. For example, in the case of channels with a pion in the final state, SK has a limit at 90% CL of 7.7×10^{33} years for $p \to \pi^0 + \mu^+$, and 1.6×10^{34} yearsfor $p \to \pi^0 + e^+$ [78]. SK has also reported limits on $p \to K^+\bar{\nu}$ [79], but not as strong as the previous ones. This is because the K^+ momentum (339 MeV/c^2) is below the Cerenkov threshold, so it can only detected via the decay products of the kaon. On the contrary, experiments using different detector approaches, as the emerging Liquid Argon Time Projection Chamber (LArTPC), are partic-

[7] I am honestly afraid of where the upper bound for the number of neutrinos is set in these theories.

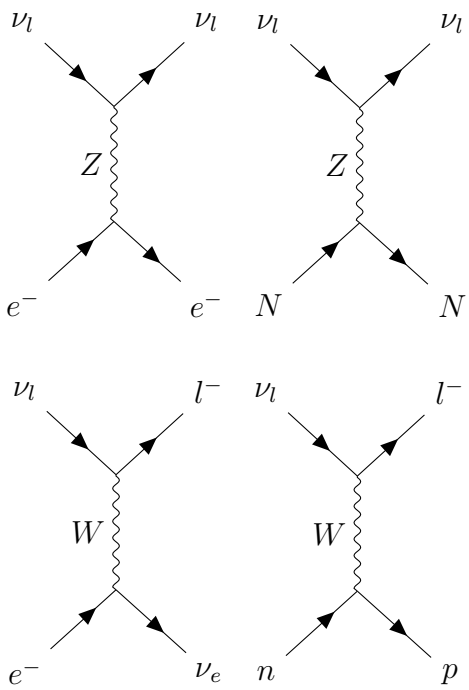

Figure 1.9: Feynman diagrams of the four interactions neutrinos can undergo with the target. Top: Neutral currents. Bottom: Charged currents.

ularly interesting to study decay channels with charged kaons, since they can reconstruct the full decay chain of the process.

The new generation of neutrino experiments aforementioned also include in their physics programme the search of this strange process. The case of DUNE, which uses the LArTPC technology, will be thoroughly explained in Chapter 2.

1.4 Neutrino Interactions

Up to now we have spoken a lot about the nature of neutrinos, the different experiments aiming to study them and the most up-to-date measurements, but we have not spoken yet about how they are detected. As we said before, neutrinos can only undergo neutral and charged current interactions (weak interactions) with other fermions: protons, neutrons and electrons. In the first case, which is mediated by the Z boson, an outgoing neutrino of the same flavour as the incoming neutrino is generated. In the second case, which is mediated by the $W^{\pm}$ boson, the incoming neutrino generates an outgoing charged lepton of the same flavour. All the possible interactions are summarized in Figure 1.9.

Neutrinos have no electric charge, so they cannot be 'seen' by the detector, meaning that in order to 'see' them, we have to look for their reaction products. Therefore, CC interactions are the most important type of interactions to identify neutrinos. The outgoing products not only provide an energy reconstruction of the incoming neutrino, but also its flavour as long as the flavour of the outgoing lepton is identified. This is of particular importance for neutrino oscillations experiments. Of course, the appropriate characterization of the neutrino depends on the proper characterization of the outgoing particles.

In general, real interactions are not as clean as displayed in Figure 1.9, particularly when nucleons are involved (almost always). For neutrinos in the range of $\sim$GeV, the CC interactions can be classified depending on whether the nucleon breaks up. If the nucleon does not break, the interaction is called quasi-elastic (QE) scattering. If the nucleon results in an excited state before decaying into hadrons and mesons, it is called nuclear resonance (RES). Finally, if the nucleon directly breaks up during the interaction in different hadrons and mesons, it is called deep inelastic scattering (DIS). The probability of each process to happen depends on the energy and the flavour of the neutrinos, and on whether it is a neutrino or an antineutrino. Figure 1.10 shows this dependence for ν_μ and $\bar{\nu}_\mu$. It can be seen how in the range of energies of neutrino oscillations experiments, all three processes are relevant. As a consequence, this kind of experiments require a deep understanding of neutrino cross-sections and the behaviour of the outgoing particles, so neutrino interactions can be properly reconstructed and characterized.

With this, the first chapter of this dissertation finishes. We have reviewed the nature of neutrinos and the most up to date knowledge of them at experimental and theoretical level. We have learnt that the current generation of neutrino experiments is not enough to understand properly neutrinos, so a new generation of experiments is in preparation for the next decade. DUNE is one of these experiments, and the incoming chapter will explain its main features.

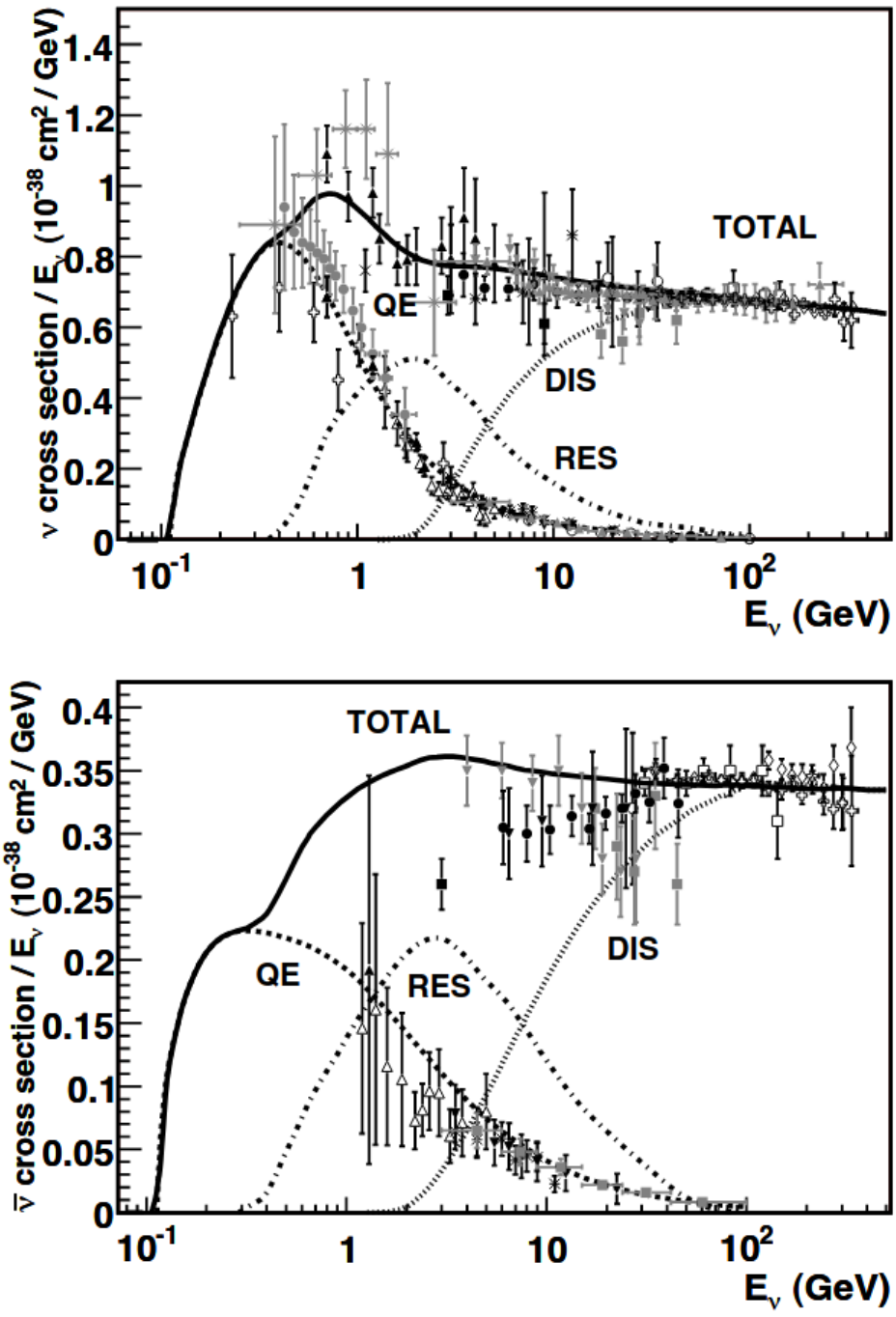

Figure 1.10: Predictions and measurements for neutrino nucleon cross-sections [80]. The three channels, QE, RES and DIS are shown, and the total cross-section as well. Top: ν_μ. Bottom: $\bar{\nu}_\mu$.

2 The DUNE Experiment

'I like that explanation,' said Ridcully. 'It is elegant, Mister Stibbons.'

'It's only a guess, sir.'

'Good enough for physics,' said Ridcully.

— Terry Pratchett, *The Science Of Discworld*

DUNE [73], which stands for Deep Underground Neutrino Experiment[1], is a next generation neutrino experiment aiming to answer the questions previously introduced, and to which this chapter is dedicated. It is organized as follows: starting off by a general overview in Section 2.1, where we highlight the main objectives and features of DUNE; continuing with a review of its physics programme in Section 2.2; then, a brief presentation of DUNE's Near Detector in Section 2.3, followed by a thorough description of DUNE's Far Detector in section 2.4; and an introduction to the ProtoDUNE programme in Section 2.5.

2.1 Overview

DUNE is a long-baseline neutrino experiment, as T2K [49] or NOVA [50], in which two different detectors are used to characterize a neutrino flux generated in an accelerator. The neutrino beam will be produced in the accelerator complex of Fermilab (Illinois), in what we call the Long Baseline Neutrino Facility (LBNF) [81]. It will deliver between 1.0 to 1.2 MW of proton beam power in on-axis configuration, expected to be upgraded later on up to 2.4 MW. Protons with an energy between 60 and 120 GeV will collide with a high-power production target, from where the most intense neutrino beam ever will emerge. The first one of the two detectors, known as Near Detector (ND), is located besides the neutrino beam, so the flux can be characterized at its starting point. The second one,

[1] It is also the name of a famous science-fiction saga. This coincidence could have been exploited to provide more DUNE related names for other concepts, as LArrakis. (Un)fortunately, it wasn't done.

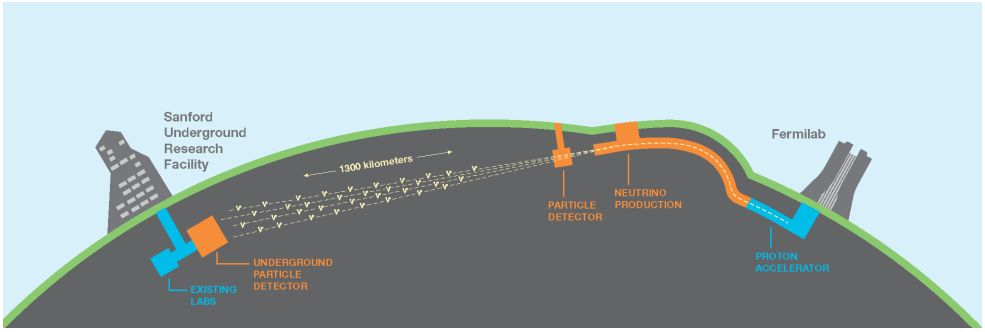

Figure 2.1: Schematic view of DUNE experiment and its locations.

known as Far Detector (FD), is located at a distance L such that the value L/E provides a maximum oscillation probability (remember Equation 1.28). In the case of DUNE, the ND will be located at Fermilab, and the FD will be located in the Sandford Underground Research Facility (SURF) in South Dakota, 1300 km away from the origin of the beam and 1.5 km underground. A schematic view of DUNE and the locations can be seen in Figure 2.1.

DUNE's ND follows a multi-detector approach which will have the possibility of being moved off-axis of the neutrino beam [82]. In this way, the ND will be responsible of the characterization and monitoring of the neutrino flux, its energy and composition, and provide an expected flux in the FD. It will also provide valuable data to study neutrino cross-sections, which are one of the main systematic uncertainty sources when doing oscillations analysis. On the other hand, DUNE's FD [83], the one measuring the oscillated neutrino flux, will be formed by four modules containing Liquid Argon Time Projection Chambers (LArTPC), each one of them with a fiducial mass of 10 kt. The LArTPC technology has proven to have excellent calorimetric and reconstruction capabilities, providing three-dimensional images of events happening inside the detector [84–87]. Its configuration and detectors' approach will allow DUNE to perform comprehensive neutrino oscillations analysis no other experiment can do by its own [88]. Apart from this, due to its large sensitive mass, detector capabilities and low background levels, DUNE will also be able to perform baryon number violation searches, to study neutrinos originated in supernovas, and a wide range of Beyond Standard Model (BSM) physics.

The preparation of DUNE is organized in two phases. In the first one, expected for the beginning of next decade, the data taking will start with 2 out of 4 of the FD's modules, a neutrino beam with 1.2 MW of power, and a baseline ND capable of characterizing the neutrino beam. This will allow to start the physics studies and the accumulation of neutrino statistics. The second phase is

expected to start six years later, in which the FD and the ND will be completed, and the neutrino beam upgraded to reach 2.4 MW of power, so that DUNE can exploit its full physics potential.

2.2 DUNE Physics

As presented in the previous chapter, neutrinos have been studied during the last hundred years and have aroused more complicated questions every time. The discovery of neutrino oscillations has proved doubtlessly that neutrinos are massive particles, in contrast with the SM description [27]. Different expansions of the SM, as GUTs, have tried to give mass to neutrinos but none of them has been confirmed experimentally. DUNE aims to study in-depth neutrinos, to search for different nucleon decay channels, to characterize the neutrino flux of dying stars and to exploit the detector capabilities for beyond SM searches and low energy physics [88].

2.2.1 Neutrino Oscillations Physics

During the last years, the three neutrino oscillation paradigm has been well established, and the six parameters ruling it (three mixing angles, θ_{12}, θ_{23}, θ_{13}, two mass squared differences, Δm^2_{21} and Δm^2_{31}, and a complex phase, δ_{CP}) have been measured, but not precisely enough, as remarked in Chapter 1. DUNE is a long-baseline neutrino experiment conceived to provide a precise study of these parameters.

DUNE's neutrino beam can be tuned to be mainly formed either by ν_μ or $\bar{\nu}_\mu$, providing the opportunity to measure the oscillation probability $P(\nu_\mu \to \nu_e)$ and $P(\bar{\nu}_\mu \to \bar{\nu}_e)$ [89]. Differences in the oscillation of neutrinos and antineutrinos are associated to the value of δ_{CP}, as seen in Figure 2.2.

As earlier commented, the matter effects generate an asymmetry in the oscillation probability depending on whether the beam is formed by neutrinos or antineutrinos, since the first ones are sensitive to the presence of electrons on Earth and the second ones are not. This asymmetry can be used to determine the sign of the mass squared differences, as it was done with solar neutrinos. This effect becomes more noticeable the greater the amount of matter the neutrinos go through. Particularly, for a baseline of 1300 km, this asymmetry is approximately $\pm 40\%$ in the region of the peak flux, meaning that DUNE will be able to unambiguously determine the neutrino mass ordering *and* measure the value of δ_{CP} [88] for a range of δ_{CP} values. Sensitivity studies have shown (see Figure 2.3) that 50% of δ_{CP} values can be determined at 5σ CL, and 75% can

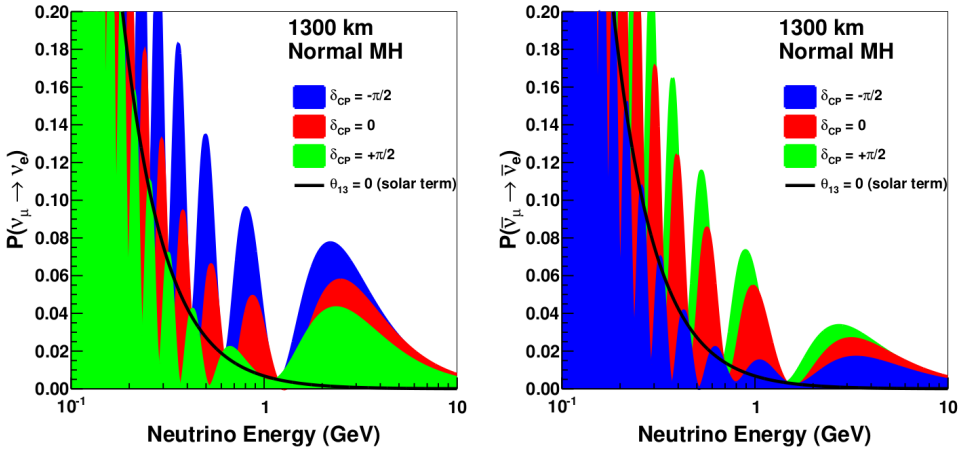

Figure 2.2: Probability of oscillation from muon flavour to electron flavour for neutrinos (left) and antineutrinos (right), assuming different values of δ_{CP} and normal mass ordering. Image from [88].

be determined with 3σ CL. Neutrino mass hierarchy can be determined above 5σ for all values of δ_{CP} [88].

Apart from mass hierarchy and the CP phase, DUNE seeks to give a very accurate measurements of θ_{23} and determine if it is above or below 45°, and after some years of operation, an independent measurement of θ_{13} using ν_e and $\bar{\nu}_e$ appearance channels with a precision competitive with reactor experiments [89]. In summary, DUNE will be able to do a full analysis of all the parameters of the accelerator sector without external constraints.

2.2.2 Proton Decay Searches

DUNE FD will be located 1.5 km underground, which will provide a powerful shielding against cosmic rays. This, along with its large fiducial mass ($\sim$ 40 kt) and outstanding detector capabilities of the LArTPC technology, make DUNE sensitive to different baryon number violating processes [88]. These are neutron-antineutron oscillations and different proton decay channels [91]. Because of the scope of this dissertation, only the second ones will be detailed here.

The proton decay is an hypothetical phenomena predicted by GUT theories. As commented in the previous chapter, the channels with kaons in the final state are particularly interesting for DUNE, since the LArTPC can provide a full reconstruction of the decay chain [92]. The most likely decay channels for charged kaons are $K^+ \to \mu^+\nu_\mu$ (64% BR) and $K^+ \to \pi^+\pi^0$ (21% BR) [27].

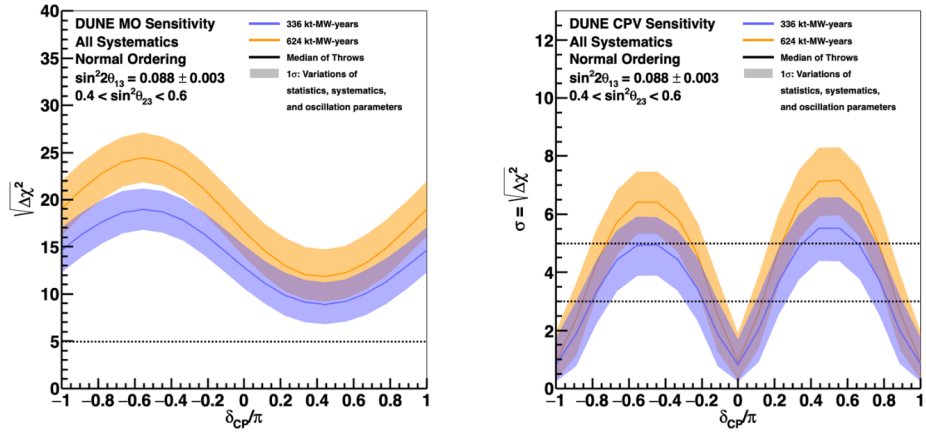

Figure 2.3: Sensitivity to the neutrino mass ordering (left) and CP violation (right) as a function of the true value of δ_{CP} for several exposures. The solid lines shows the median sensitivity while the width of the band represents 1σ of variations of statistics, systematics and oscillations parameters. Figure from [90].

For the first of them, the signal of the proton decay would be the one of a low energy kaon ($p \sim 340$ MeV/c) in the middle of the TPC followed by a low energy muon ($p \sim 237$ MeV/c). The dominant background for this process is generated by neutrino charged current quasi-elastic scattering, $\nu_\mu n \rightarrow p\mu^-$. If the muon has a momentum similar to the 237 MeV/c expected from the K^+ decay, the identification of the proton decay process depends on the proper differentiation between kaons and protons. In Figure 2.4 the simulation of a signal and a background event are displayed. Sensitivity studies have shown that, provided a good detector performance, DUNE can achieve a 90% CL lower limit on the proton lifetime in the $p \rightarrow K^+\bar{\nu}$ channel [88].

In view of this, it is fundamental to understand kaon behaviour at low energies, so it can be properly identified and separated from the background. From Chapter 5 to 8 of this dissertation, a detailed selection and study of low energy kaons in LAr is presented by using ProtoDUNE-SP data, in which the capabilities of the LArTPC technology to tag kaons will be presented. Apart from the TPC, the Photon Detection System (PDS) plays an essential role in proton decay, since, as we will see, it is in charge of establishing the trigger for non-beam events. Without this trigger it would not be possible to position the event inside the detector and to apply the corresponding energy corrections. Furthermore, PDS can improve the discrimination between signal and background by identify-

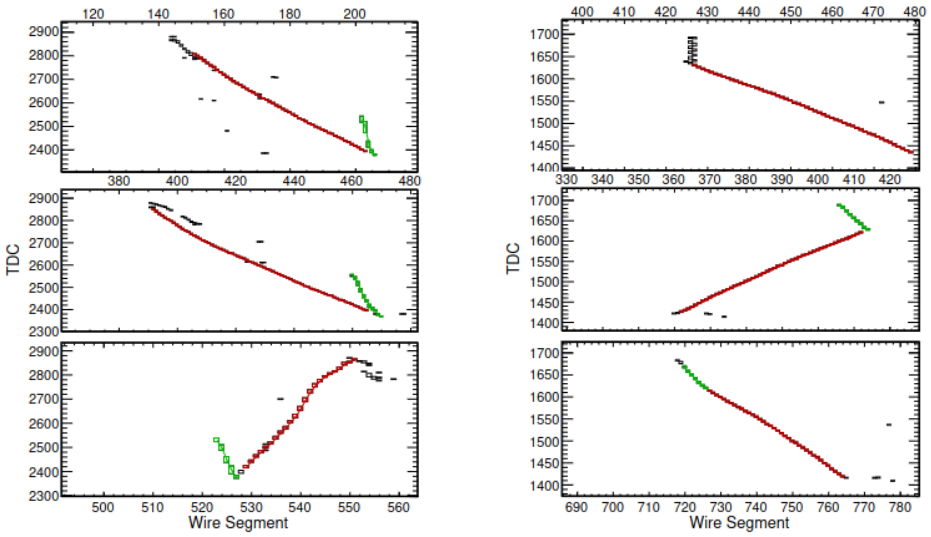

Figure 2.4: Left: Simulated event with a proton decay with a kaon (green) and the muon resulting from its decay (red). Right: Simulated CCQE background event with an outgoing proton (green) and a muon (red). The topology of both events is the same. The x-axis corresponds to the wire number whereas the y-axis corresponds to the readout time. Figure from [92].

ing the michel electron resulting of the μ^+ decay. In Chapter 4, R&D activities regarding the PDS will be presented.

2.2.3 Supernova Searches

As in the previous case, the low background and the outstanding capabilities of the LArTPC technologies, makes of DUNE a powerful experiment to study neutrinos generated in a core-collapse supernova [88], which happens at the end of a massive star's life. This was already done with the only supernova humankind has observed, SN1987A, by water cerenkov detectors [93, 94], which allowed for a qualitative understanding of this process.

After the continuous nuclear burning throughout the star's life, its nucleus develops an onion structure with the most stable and heavy element in the core (Fe) and more lighter elements in the outside. Since Fe cannot be longer burnt, at a certain point the equilibrium between radiation pressure and gravity no longer holds, producing the collapse of the star. During the very few instants after the collapse (10^{-2} s), a nuclear continuous medium with densities of order 10^{12}-10^{14} g/cm^3 is formed, which is opaque even for neutrinos. Eventually, this medium will break and the gravitational binding energy of the collapsing core is

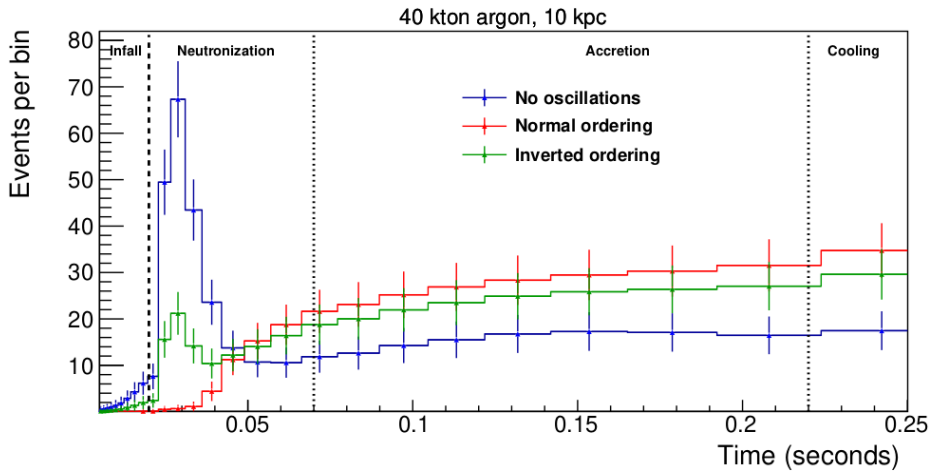

Figure 2.5: Neutrino spectrum of a supernova as a function of time for different cases: no oscillations (blue), oscillations with matter effects and normal ordering (red), oscillations with matter effects and inverted ordering (green). Figure from [88].

emitted in a 99% as neutrinos and antineutrinos of every flavour.

Detecting such neutrinos can provide truly valuable information not only from neutrinos but also from the intrinsic nature of the supernova. Apart from finding its most probable location, the neutrino flux is different depending on the phases of the collapse and its final result. For example, a black whole formation would cause a sharp cut-off in the flux, and shock wave or turbulence effects can imply flavour dependence with time. With respect to neutrinos themselves, the measured flux of the different flavours depends on the mass hierarchy, as presented in Figure 2.5 [88].

2.2.4 BSM and Low Engery Physics

In addition to the topics presented above, having a large fiducial mass, a capable near detector, an intense neutrino beam and low backgrounds allows DUNE to study a wide range of topics of low energy physics and BSM. Some of these include searches for solar neutrinos in the FD, sterile neutrinos in the ND and FD, searches for Lorentz invariance violations, searches for neutrino tridents or light and boosted dark matter [88].

The expected ratio of solar neutrino events per 40 ktons of LAr ∼100 per day. This high rate compensates the intrinsic high energy detection threshold

of the LArTPC, allowing to make studies of the Sun dynamics and the solar oscillation parameters.

The tension between some experimental results and the three-neutrino flavour paradigm could be explained by means of the mixing with sterile neutrinos. DUNE long baseline allows to search for this effect look for the disappearance of CC and NC interactions, in both the ND and the FD, over a broad range of potential sterile neutrino mass splittings, improving the sensitivity of previous experiments.

The high precision expected for the measurement of the oscillation parameters can be used to look for small deviations of the current paradigm. A deviation from the unitarity of the PMNS matrix could imply the existence of more massive neutrino state. In the same way, differences in the oscillation parameters for neutrinos and antineutrinos could be related to a possible violation of the CPT symmetry, a cornerstone of the SM of particle physics. Furthermore, the large sensitivity to matter effects can be used to look for non standard interactions of the neutrinos with the matter of the Earth.

Finally, the high intensity of the neutrino beam predicts an annual rate of over 100 dimuon neutrino trident interactions at the ND. These processes are very suppressed by the SM. However, this high rate will allow to test possible deviations that could be explained by the presence of new gauge symmetries beyond the SM. The beam is also expected to cover a complementary parameters space regarding the search for light-mass dark matter that cannot be search by direct detection or collider experiments.

2.3 Near Detector

Although it is outside of the scope of this dissertation, it is interesting to present a short overview of DUNE's Near Detector, so its relevance can be well understood. The ND will be located also at Fermilab, 0.575 km away from the neutrino beam. It follows a multi-detector approach with the possibility of measuring the neutrino flux on and off-axis. It will have a modular liquid argon time projection chamber (NDLAr), a muon spectrometer (TMS) and an on-axis beam monitor called SAND (System for on-Axis Neutrino Detection) [90]. The first two of these will be movable off-axis of the beam, characterizing the neutrino beam at different angles (and energies) (see Figure 2.6). The system in charge of the off-axis movement is known as PRISM (Precision Reaction-Independent Spectrum Measurement) [82].

The main goal of the ND is to serve as experiment's control, characterizing

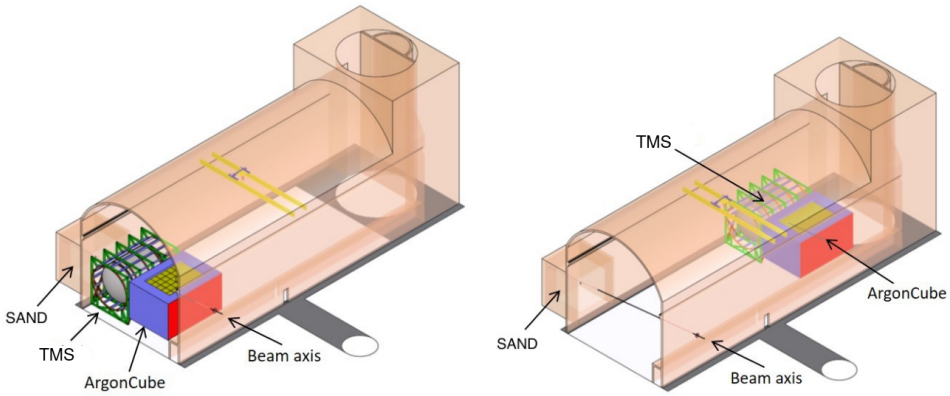

Figure 2.6: Schematic view of DUNE's ND. Three consecutive detectors, NDLAr, TMS, and SAND, are exposed to the neutrino beam. The first two can be moved off axis with the PRISM system. Figure from [73].

the unoscillated neutrino spectrum so an oscillated one can be predicted for the FD. This depends on a complicated product of flux, cross sections, and detector response, all of which have large *a priori* uncertainties. ND will be used to constrain all these three components. Furthermore, the ND is an experiment on its own, and its data will be used to study neutrino-nucleus interactions and more non-standard physics, like sterile neutrinos or other exotic particles [73].

NDLAr, also known as ArgonCube [95], is a LArTPC with enough active volume to provide high statistics of neutrino interactions and for hadron containment, which allows for a better characterization of neutrino energy. It uses a pixelated readout and optical segmentation to deal with the high rate of events in the near location. In addition, having the same target in both ND and FD (liquid argon) and, to some extent, technology, is the only way to constrain the three systematic sources commented above. However, ArgonCube is not large enough to contain ongoing muons result of neutrino interactions, so another detector is needed for a proper characterization of their momentum [82]. That is the main goal of the TMS (Temporary Muon Spectrometer). It is a wavelength-shifting scintillator based detector, which is embedded between two layers of magnetic coils. The resulting magnetic field will deviate muons, allowing for their charge and momentum measurement [90]. Finally, these two detectors will be movable sideways up to 33 m to take data in positions off the beam axis, using the PRISM system [82]. Measuring the neutrino flux at different angles will help to disentangle degenerate effects due to systematic biases of the energy reconstruction.

The last component of the ND is the beam monitor, SAND, which is a three-dimensional scintillator tracker meant to be always on-axis monitoring the neutrino spectrum, so intentional or accidental changes on the flux can be detected [82].

At the time of this writing, the ND detector is expected be built in two phases, being the first one capable of characterizing the initial neutrino beam with a reduced cost, and a second one with upgraded components, aiming to develop its full potential. In this second phase, the TMS will be exchanged by a more complex detector with more physics capabilities: a gaseous argon detector (NDGAr) [90].

2.4 Far Detector

The FD will be located at SURF, 1300 km away from the neutrino beam and 1.5 km underground. It will characterize the oscillated neutrino flux by measuring the different neutrino interactions with argon nuclei. It will be formed by four liquid argon time projection chambers (LArTPC) detector modules, each of them with 10 kt of fiducial mass and hosted by a cryostat of 15.1 m (w) $\times$ 14.0 m (h) $\times$ 62.0 m (l) with a total LAr mass of about 17.5 kt. Apart from the modular LArTPC, each cryostat will also contain the complementary photon detection system and the cryogenic system, which is the one in charge of ensuring the adequate conditions of the liquid argon during the different stages of the experiment. Knowing the constant improvement of the LArTPC technology, the modular approach for the FD was followed because of its flexibility: whereas the first and second modules have an already closed design, the last two are not yet decided and can include improvements or variations of the technologies [73].

In this section, the LArTPC technology and the Photon Detection System of DUNE's FD are presented. Even though each module is expected to follow slightly different approaches for these two systems, since this dissertation is based in the ProtoDUNE-SP experiment, we will describe particularly the one of the first FD module, originally known as Single-Phase (SP) module [83], and currently known as Horizontal-Drift (HD).

2.4.1 Liquid Argon Time Projection Chamber Technology

A LArTPC is a time projection chamber whose active medium is liquid argon. TPCs are an evolution of multi wire proportional chambers and drift chambers

[96], in which a large electric potential is applied between an anode and a cathode (both separated by the active medium), in such a way that a strong electric field is generated in the medium region the field lines of which go from the anode to the cathode. When a charged particle crosses this medium, nuclei are ionized and freed electrons are affected by the electric field, drifting towards the anode. There, they are collected, providing a two-dimensional reconstruction in the plane perpendicular to the drift direction. If the time in which the particle has crossed the detector, a.k.a. the t_0, is known, the drift time of electrons can be used to compute the third coordinate and hence the final three-dimensional reconstruction. In this way, a TPC generates an image-like reconstruction of particles crossing the detector (tracking), and a calorimetric measurement as well [96].

LAr has been chosen as active medium for DUNE for different reasons. First, because it is a noble element, so its electronegativity is reduced. In this way, freed electrons are less likely to be captured again by other argon nuclei and the charge loss during the drift in minimum. Second, because it is a relatively heavy nucleus, which means that neutrino interactions are more likely to happen. Third, because it is a fantastic scintillator [97]. When a charged particle interacts with argon nuclei, 24000 scintillation photons per MeV are produced, and they take ns to reach de detector wall, whereas electron drift towards the anode takes ms. Thus, the appropriate detection of scintillation light can provide a t_0 for the three-dimensional reconstruction. Lastly because compared with other noble elements, as xenon, it is cheap[2].

The description of the TPC detection technology above is quite general, and there are several ways of implementing it. Originally, DUNE was planned to use two different approaches: single-phase (SP) and dual-phase (DP). In a SP TPC, electrons' drift occurs completely in the liquid phase. In a DP TPC, the charge collection planes are located outside the liquid argon, in the gas phase, in such a way that the last part of electrons' drift happens outside the liquid. When they are crossing from one phase to another, a charge amplification is produced, which provides an improvement on energy resolution with respect to the SP technology. Since the charge collection planes are outside the liquid, it is clear than electrons have to drift in the vertical axis, meaning that the cathode has to be 'on the floor' and the anode has to be 'on the ceiling'. On the contrary, in the SP technology, the disposition of the TPC is arbitrary: anode and cathode planes can be put

[2]Unfortunately, after the war of Ukraine started, it generated a energy crisis in Europe with an unstoppable increase of electricity prices. This has significantly augmented the cost of LAr production, complicating its supplying.

horizontally or vertically[3]. This generates two variants of the SP technology, the Horizontal-Drift (HD) and the Vertical-Drift (VD). The first FD modules was planned to be SP, whereas the second one was planned to be DP. However, due to the experience gained in the ProtoDUNE programme (described in the last section of this chapter), the DP technology was dismissed because of the technical difficulties found when trying to reach its peak performance. Due to this, the two first FD modules will be SP, one HD and the other VD.

As mentioned above, in the LArTPC HD technology a large LAr volume is subdued to a strong electric field, due to a potential difference between the (vertical) cathode and anode planes. Electrons result of charged particles ionization drift horizontally towards the anode, where they are collected. This detector technology has been validated by different experiments as MicroBooNE [98], ICARUS [86], ArgoNeuT [99] and LArIAT [100]. The anode is formed by three layers of active wires at different angles forming a grid, and they are commonly known as Anode Plane Array (APA). The first two layers of wires are known as induction planes and are transparent to charge, whereas the third one, known as collection plane, is the one meant to collect the electrons (as its name suggests). Having three layers at different angles allows the two-dimensional reconstruction of the events[4]. As outlined above, if the t_0 is known, the coordinate on the drift direction can also be deduced [83] (see Figure 2.7).

The wire planes are known as U, V and X, respectively. The first two lie at an angle of $\pm 35.7°$ relative to the vertical axis, while the third one runs parallel to it. U and V are what we just called induction planes, and they provide induction signals when charge approximates, passes through and moves away. Thus, induction signals are bipolar. On the other hand, X wires (collection wires) provide unipolar signals when collecting the charge. The size of the signal is proportional to the deposited energy of the particles, allowing a $\frac{dE}{dx}$ measurement. Finally, signals undergo digitization via an analog-to-digital converter (ADC) that works at cryogenic temperature [83]. There is an additional grid plane known as G plane behind these three layers which acts as grounding, protecting the detector from electrostatic discharges (see Figure 2.8). Most experiments using this technology have a distance between wires of 5 mm, however DUNE and its prototypes use a spacing of 4.67 mm between induction wires and 4.79 mm between collection wires.

The electric field is generated by applying a negative electric potential in the

[3]There are much more orientations for the anode and cathode planes, as long as they are in parallel and inside the liquid phase. However, they are not recommended.

[4]Technically it would be enough with two, but three provides redundancy. This is not a humoristic footnote.

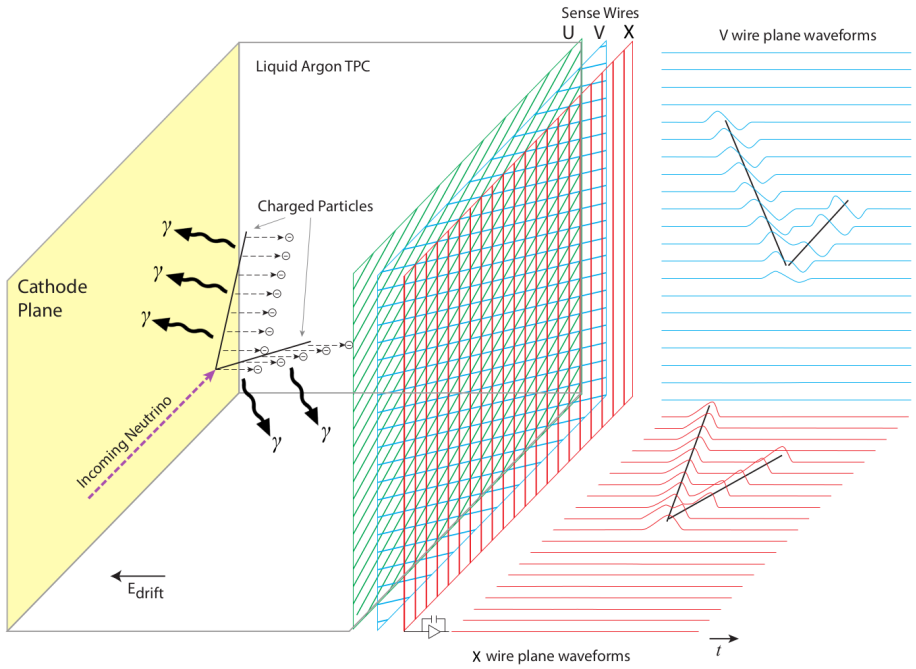

Figure 2.7: Schematic view of the principle of operation of a LArTPC. Ionization electrons drift towards the anode plane, where they generate signals in the three layers of wires. This information is used for the two-dimensional reconstruction of the event, which is ultimately completed with the t_0 information provided by the beam trigger or the detected photons. Figure from [83].

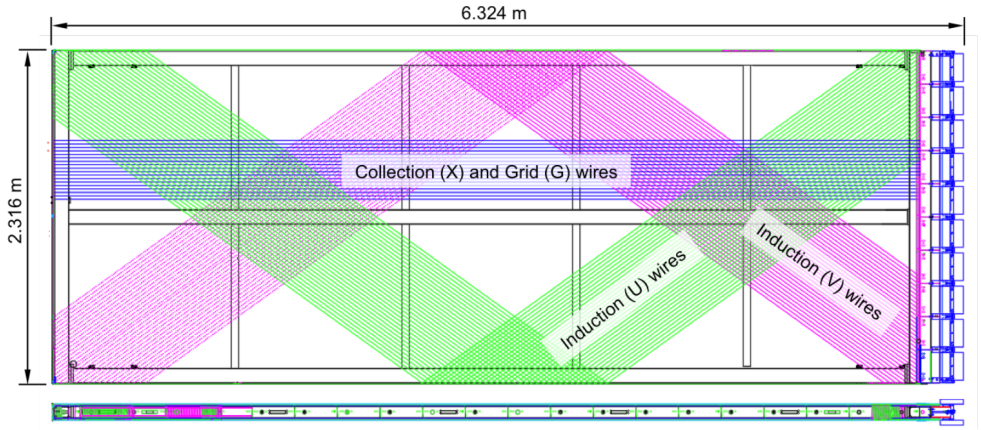

Figure 2.8: Rotated view of an APA and its different wire planes. U and V are the induction planes, and are rotated with respect to the vertical axis. X is the collection plane and runs parallel to the vertical axis. Figure from [83].

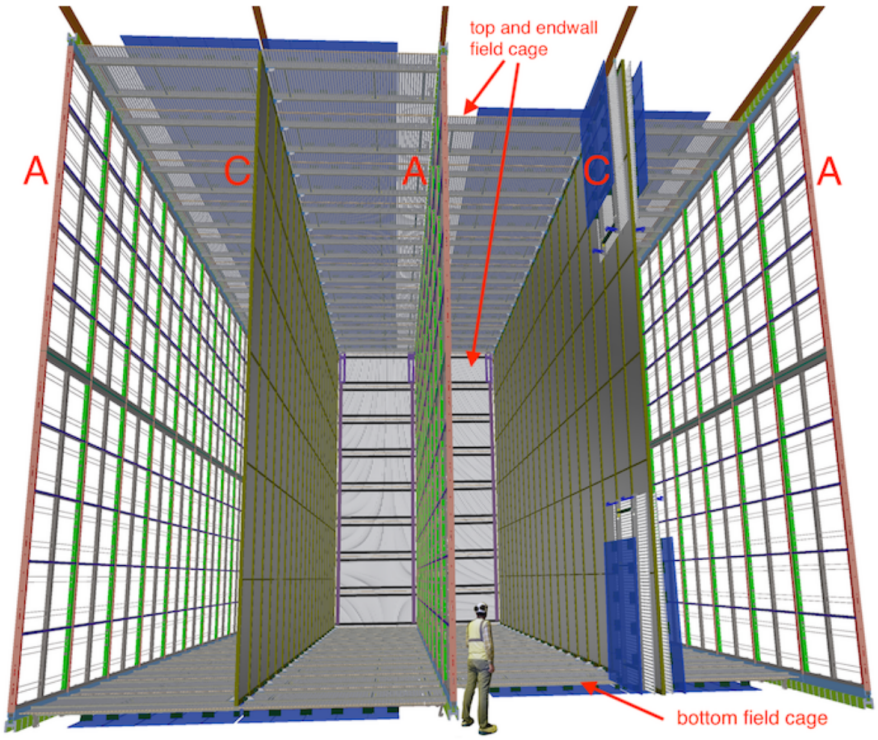

Figure 2.9: Cross section view of the FD1 module. The dimensions of the APA and CPA structures are 58.2 m long into the page and 12.0 m high. Each drift volume is approximately 3.6 m wide.

cathode plane assembly (CPA), formed by various individual panels of FR4. In the case of FD1, the active volume will be divided in three active volumes of 3.5 m drift length, with a cathode-anode sequence of A-C-A-C-A (see Figure 2.9). CPAs will be set at -180 kV, generating an electric field of 500 V/cm, and granting electrons a drift velocity of approximately 1.6 mm/µs [83]. A field cage (FC) formed by aluminium bars surrounds the remaining open sides of the TPC, granting homogeneity to the electric field inside the active volume of up to 1% [83].

So that the LArTPC provides a good performance, it is fundamental to ensure the purity of the liquid argon. Even though argon is a noble gas and it has a very low electronegativity, impurities such as oxygen, nitrogen or water can be attached to the argon nuclei and trap the ionization electrons that should be collected in the anode plane. This generates a charge loss that, in the worst case scenario, could turn blind the TPC. Not only that, but it can also reduce the detectable scintillation light, further aggravating the situation. DUNE's ob-

jective is to have a purity better than 100 ppm (parts per million). In order to accomplish this, the cryogenic system is in charge of recirculating and constantly purifying the liquid argon; and the cryogenic instrumentation constantly monitors its characteristics, so any unexpected problem can be detected and solved on time, minimizing the impact on the physics measurements [83].

2.4.1.1 Particle Identification

The physics goals DUNE aims to achieve require a large baseline (1300 km) and a relatively large neutrino energy ($\mathcal{O}$(1-10 GeV)) [88]. At this range of energy, any neutrino interaction can happen: quasi-inelastic scattering, nuclear resonance or deep inelastic scattering [80]. Thus, different particles with complicated topologies are expected as final states of neutrino interactions: hadrons, mesons, muons, electrons, etc. The LArTPC tracking capabilities are used to disentangle these hierarchies of particles. Since magnetic fields are not used inside the TPC to curve particles' trajectories, the particle identification relies on the proper characterization of their energy loss. Its mean value is well described by the Bethe-Bloch formula [27, 96]

$$\langle -\frac{dE}{dx} \rangle = Kz^2 \frac{Z}{A} \frac{1}{\beta^2} \left[\ln \left(\frac{2m_e c^2 \beta^2 \gamma^2 W_{max}}{I^2} \right) - \beta^2 - \frac{\delta(\beta\gamma)}{2} \right], \tag{2.1}$$

with $K = 4\pi N_A r_e^2 m_e c^2$, where N_A is the Avogadro's Number, r_e is the classical radius of the electron; z is the charge number of the incident particle; Z and A are the atomic and mass numbers of the medium the particle is passing through, respectively; I is the mean excitation potential; $\delta(\beta\gamma)$ accounts for density effects; and W_{max} is the maximum transferable energy to an atomic electron in a single collision, which for a particle of mass M is given by

$$W_{max} = \frac{2m_e c^2 \beta^2 \gamma^2}{1 + 2\gamma m_e/M + (m_e/M)^2}. \tag{2.2}$$

As it can be seen in Equation 2.1, the energy loss of a particle in a medium depends on two different things: the charge and the velocity of the particle. The velocity dependence ($1/\beta^2$) allows for discrimination between particles of the same charge and energy, since more massive particles will have a slower velocity than lighter particles, hence depositing more energy in the medium.

Since the momentum cannot be measured by a LArTPC, there is no information about the velocity of the particles passing through. What is typically done in these experiments is to represent the deposited energy as a function of the residual range [101]. It is defined as the distance of a given point of the track to its end (see Figure 2.10). In Figure 2.11, one can see the different dE/dx

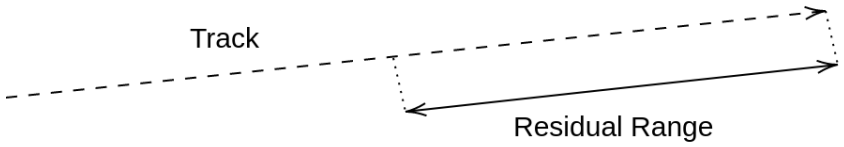

Figure 2.10: Diagram showing the residual range concept.

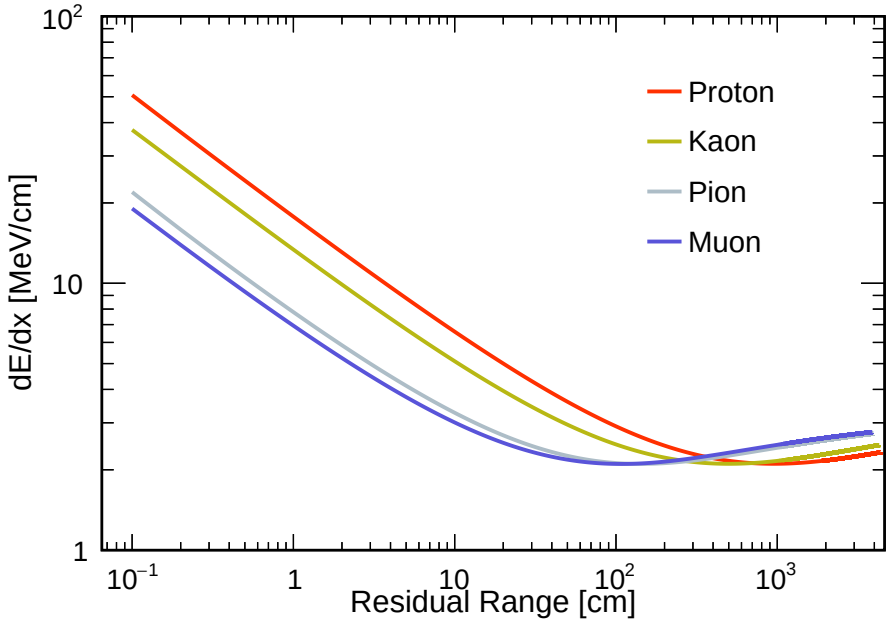

Figure 2.11: Theoretical dE/dx profile for different particle species as a function of the residual range.

profiles for a different particle species. A stepped distribution can be observed depending on the mass of the particle, with the heavier ones loosing more energy for the same residual range than the lighter ones.

2.4.2 Photon Detection System

Apart from the LArTPC, DUNE's FD has a complementary light detection system (the Photon Detection System, PDS), whose objective is twofold: first, to measure the t_0 for non-beam events by detecting LAr scintillation light (see Fig-

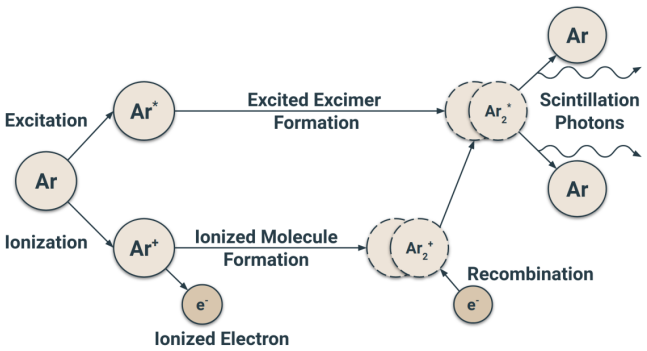

Figure 2.12: Scheme of scintillation light production in argon. Figure from [83].

ure 2.12); and second, to provide a complementary energy reconstruction based on this light collection [102].

As indicated earlier, the t_0 permits the three-dimensional reconstruction of the events. When doing neutrino beam physics, the t_0 is given by the beam trigger, which means that the PDS is not needed for oscillation physics. However, when doing non-beam physics, only LAr scintillation light (which takes nanoseconds to reach the detector walls) can be used to measure the t_0. This is fundamental since many of the non-beam physics (as proton decay searches) rely on a proper fiducialization of the detector volume, vertex identification and charge attenuation corrections (which depends on the drift coordinate). In addition, PDS can improve the reconstruction, sensitivity and resolution of the experiment, since its independent energy measurement provides a redundancy that can be used to fine-tune TPC performance. Furthermore, PDS can be used to develop advanced trigger techniques that can improve background rejection for low energy physics, as solar neutrinos or BSM searches [83]. In other words, in order to make DUNE a multi-purpose experiment, a proper PDS is needed.

Developing one for DUNE's FD was particularly challenging for different reasons. First, the available space. Almost all the LAr inside the cryostat is enclosed by the TPC, meaning that there is not much space left out of the TPC. Furthermore, the TPC and the field cage are set at a very large potential. In the case of a single-phase TPC, the anode planes are the only region with no electric potential. Second, LAr scintillation light is peaked at 127 nm [103], what is considered to be deep ultraviolet. There are very few light detection systems that can perform properly at that wavelength, but they are too expensive to achieve the necessary optical coverage for DUNE's physics. Third, the multiplicity of the

optical readout. Obtaining the needed optical coverage could not imply having an arbitrarily large amount of optical channels, since the data rate would be gigantic.

Thus, the PDS for DUNE's FD (at, least for the HD module) had to be located inside the APAs, and to find an agreement between photon detection efficiency (PDE) for LAr scintillation light, price, optical coverage and number of readout channels. All of this, with a background level that should not dominate over radiogenic backgrounds [104]. Different options were explored in ProtoDUNE-SP [105], among which the X-ARAPUCA was selected [106].

Arapuca is a native Brazilian word that means 'bird trap', which refers to the idea of this device: trapping photons. The X stands for 'extended', since the X-ARAPUCA is an evolution of the S (standard) ARAPUCA. For simplicity, only the current version (the X-ARAPUCA) will be described here. In Figure 2.13 an schematic view of this device and its working principle is shown. It consists of a wavelength-shifting (WLS) plate, on top of which a dichroic filter is placed (with a separation of few mm, such that LAr can flow within). There is an evaporation of p-therphenyl (PTP) in the outer face of the filter. In the other face of the wavelength shifting plate a reflective foil is located. Finally, several visible-light silicon photomultipliers (SiPM) are attached to the WLS plate. When LAr scintillation light reaches the PTP, it is absorbed and re-emitted at 350 nm. Dichroic filters are transparent to this wavelength, so photons can reach the plate. There, they are absorbed and re-emitted at about 430 nm. Because of the refractive index of LAr and the WLS, generally photons are trapped by internal reflection and bounce until they either are detected by the attached SiPMs, absorbed by the material, or escape the plate. If photons escape, they reach the dichroic filter (which has a sharp cut-off at 400 nm, meaning it is reflective above that wavelength) or the reflective foil, bouncing back again to the plate. Finally, all SiPMs are polarized and read all together, meaning that each X-ARAPUCA consists of a single electronic channel. In this way, LAr scintillation light is shifted two consecutive times reaching 430 nm, which is the working range of the attached SiPMs, and it is trapped by internal reflection until it is detected [83].

The X-ARAPUCA concept fulfils all the previous requirements: its geometry allows it to be located inside the APAs, it provides a sufficient optical coverage with an affordable cost, and the number of optical channels is relatively small.

The design just explained is quite general, and its geometry can be tailored for different needs. The particular design of the HD module will be described now (see Figure 2.14). The minimal unit of the HD PDS is known as X-ARAPUCA Super-Cell (SC). It is formed by a WLS plate of 487 mm $\times$ 93 mm $\times$ 3.5 mm,

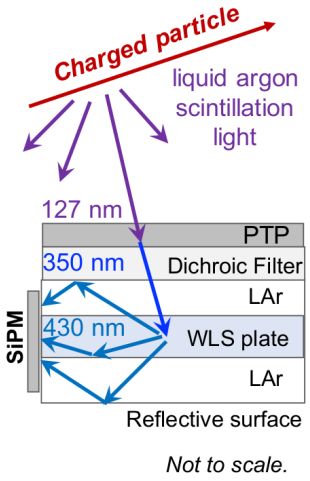

Figure 2.13: Schematic representation of a single sided X-ARAPUCA operating principle, assuming a 400 nm sharp cut-off in the dichroic filter. Figure from [83].

with six PTP-evaporated dichroic filters of 78 mm × 93 mm covering the side facing the active volume of the detector, and 48 SiPMs whose signals are added to a single electronic channel. This addition is done by passively ganging the sensors in groups of six, and then ganging actively the eight groups of six. Apart from that, the SC has different FR4 pieces and frames to provide mechanical stability and rigidity to the system. DUNE requires the PDS to achieve at least a PDE of 2.6%. Ongoing studies have demonstrated that the X-ARAPUCA SC has an efficiency above 3.5% [83, 107].

If the SC has dichroic filters with a PTP evaporation on each side, it is called double-sided SC, meaning that it can detect photons emitted from both sides of the optical device. These will be used for the APA plane shared between TPCs in the FD1 module (remember Figure 2.9). If the SC has only one face covered by dichroic filters and the other with reflective foils, it is called single-sided and can only detect photons coming from one side of the device. These will be used in the outermost APA planes of the FD1.

Four SC are assembled mechanically together in what is called a photon detection module (see Figure 2.15). The dimensions of this structure are 2092 mm × 118 mm × 23 mm, and the electronic board in charge of the ganging is located in its center. Each PD module is inserted inside an APA, between the wires planes and the grid planes of both APAs' faces. All these planes are transparent to light, so LAr scintillation light can easily reach the optical

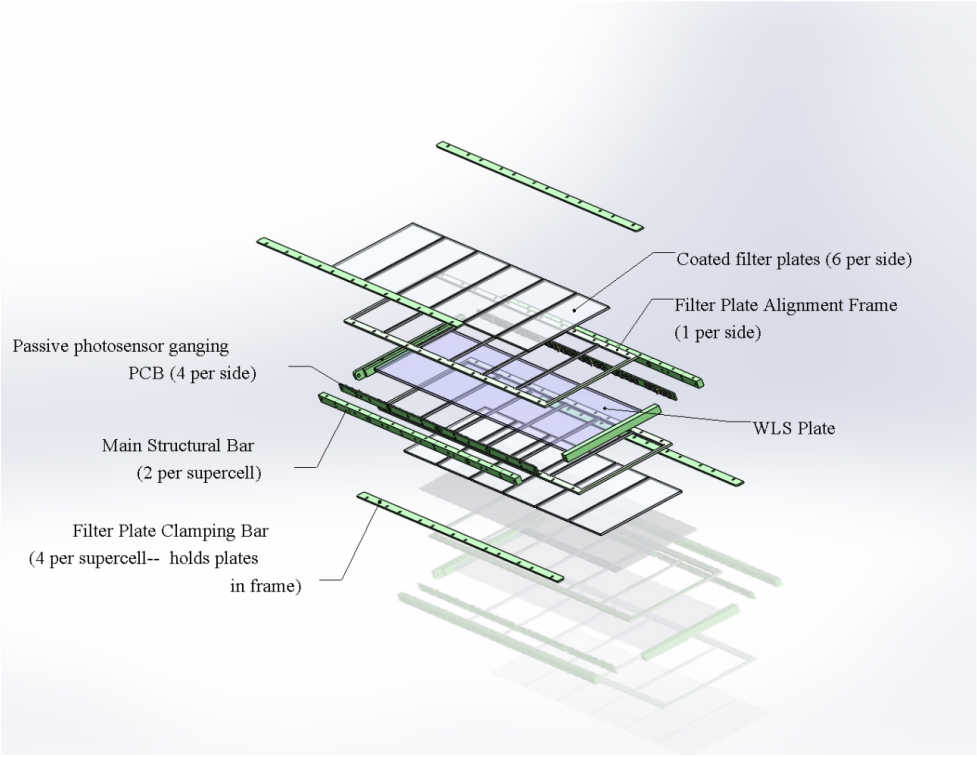

Figure 2.14: Detailed exploded view of X-ARAPUCA supercell. Figure from [83].

modules. Photoelectron signals are transmitted from the modules to the readout system by a cold cable that runs through the APA frame.

As commented above, the X-ARAPUCA design was selected as baseline for the PDS based on ProtoDUNE-SP performance studies. After this choice was made, different lines of R&D were developed to study the most efficient geometry, the electronic readout, the dichroic filters or the SiPMs. These were carried out in different institutions in a joint effort to optimize the X-ARAPUCA technology. In Chapter 4, a detailed study of different SiPMs models used in the optical modules is presented. This was the so-called down-selection procedure, in which different photosensors were tested in cryogenic conditions to find the one that best fulfilled DUNE's specifications. In addition to this, the IFIC group has been involved in the studies of the dichroic filters for the FD2, the results of which could be fed back into FD1.

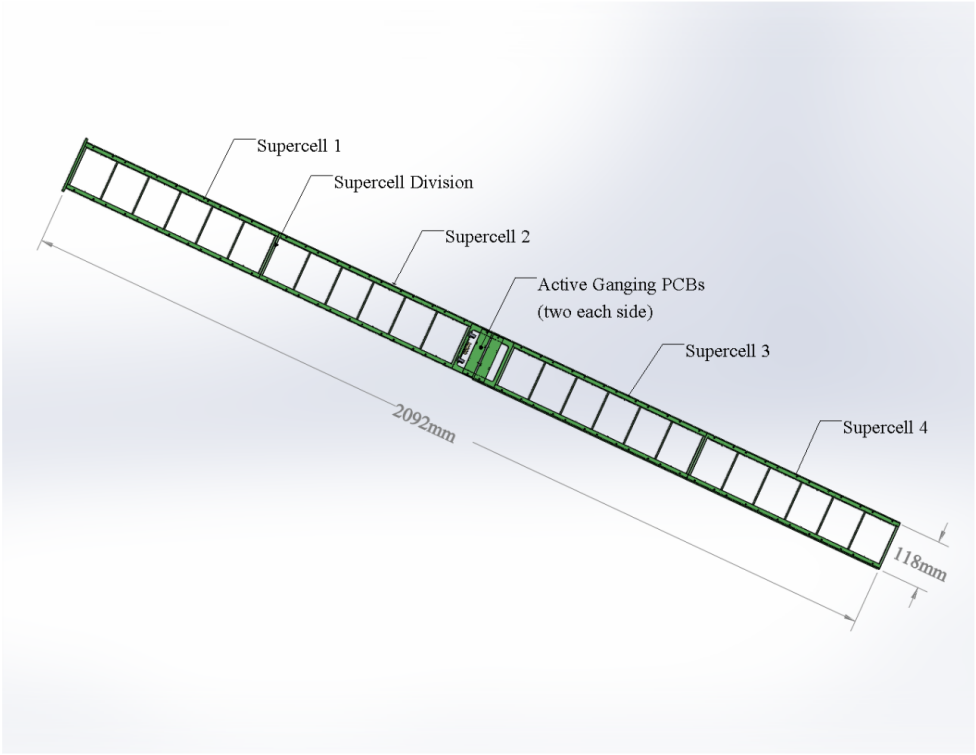

Figure 2.15: Full optical module that is inserted inside an APA. It is a mechanical structure combining four different SC. Figure from [83].

2.5 The ProtoDUNE Programme

Even though the LArTPC technology has been previously used in other particle physics experiments, it has never been used in a scale as big as DUNE's. Because of that, a strong prototyping programme has been developed to validate the different DUNE technologies, the installation and commissioning procedures, and the detector performance. This programme is commonly known as ProtoDUNE, and has been hosted at the CERN Neutrino Platform [108]. The Neutrino Platform is an extension of the CERN North Area with two dedicated beamlines, whose objective is to provide the infrastructure for the different neutrino experiments at CERN. Its construction started in 2016, and in 2017 the installation of the first two DUNE prototypes started. They were ProtoDUNE-SP [105] and ProtoDUNE-DP [109], demonstrators of the LAr single-phase and dual-phase technology, respectively. ProtoDUNE-SP, to which the next chapter is dedicated, was successfully installed, commissioned and exposed to a charged beam during 2018, and was operated until Summer 2020 [106, 110]. ProtoDUNE-DP was installed and operated from 2019 to 2021 [109].

These two experiments are currently known as ProtoDUNE phase I, and their results have guided the configurations of DUNE's FD modules. The first of them, as previously stated, is going to be SP. This follows the original plan, which was reinforced by the outstanding performance of ProtoDUNE-SP. However, the second one, originally meant to be DP, won't be it anymore. The reason for this are the difficulties found to properly operate such a big DP LArTPC. Even though the DP technology is supposed to bring a better performance than the SP, the technological effort needed for it to properly operate is not worth it.

After a phase I, there is usually a phase II, and this is also the case of the ProtoDUNE programme. Phase II will consist of two more ProtoDUNEs hosted in the same cryostats as phase I. The first of them, ProtoDUNE-HD (Horizontal Drift), is a new SP LArTPC meant to be a 'module 0' of DUNE's FD1: its different components will be used afterwards in the first module in South Dakota. Additionally, the detector's disposition inside the cryostat is slightly different from ProtoDUNE-SP, being now more similar to the detector disposition in DUNE's FD1. The second one, ProtoDUNE-VD, is a variation of the SP technology aimed to substitute the DP technology. VD stands for Vertical Drift, meaning that the electron drift happens in the vertical direction. The VD FD module is expected to have two drift volumes separated by an inner central cathode, and two charge collection planes formed by perforated PCBs [111]. The installation of ProtoDUNE-HD started in Spring of 2022, where I was directly involved, and to which the last section of the Chapter 4 is dedicated. The installation of ProtoDUNE-VD is happening at the time of writing.

3 The ProtoDUNE-SP Detector at CERN

It's still magic even if you know how it's done.

— Terry Pratchett, *A Hat Full of Sky*

This chapter describes the ProtoDUNE-SP detector in-depth. Section 3.1 presents its motivation and main goals; Section 3.2 describes the different detector components; Section 3.3 provides a brief description of the cryostat, the cryogenic system and some highlights of the cryogenic instrumentation; the beam line delivering the charged particle beam to the detector is reviewed in Section 3.4; the data acquisition process, the reconstruction and the simulation of ProtoDUNE-SP data is detailed in Sections 3.5, 3.6 and 3.7, respectively; the procedure to calibrate the detector is presented in Section 3.8; and finally, the most important results obtained are commented in Section 3.9.

3.1 Overview and goals

ProtoDUNE-SP was one of the two first DUNE's demonstrators of the ProtoDUNE programme [105]. Located at CERN's Neutrino Platform (see Figure 3.1), it was a Single-Phase LArTPC which prototyped DUNE's FD1 technology at a technological scale of 1:1 and a LAr scale of 1:20. It constituted the largest monolithic LArTPC ever built and operated, with a total LAr mass of 0.77 kt. It was hosted by a cryostat with outer dimensions of 11.4 m × 11.4 m × 10.8 m (W×L×H) that kept the LAr at 87 K. The main objectives of the ProtoDUNE-SP detector were the following:

- Prototype and validate the production, delivery and installation procedures of the detector components.
- Validate the detector performance of the SP technology.
- Accumulate sufficiently large test-beam data samples to understand and calibrate the response of the detector to different particle species and to perform physics analysis.

Figure 3.1: View of the Neutrino Platform. In the front of the picture the cryostat of ProtoDUNE-SP can be observed. In the left back part, the cryostat of ProtoDUNE-DP is present too. Image from [112].

- Ensure the long-term operational stability of the detector.

ProtoDUNE-SP installation was completed in Summer 2018, and it was commissioned and exposed to a test-beam from September to November 2018. Afterwards, it operated taking cosmic rays data until Summer 2020, when its decommissioning started so that the work with the ongoing ProtoDUNE-HD detector could start. The analysis carried out with ProtoDUNE-SP's data have shown that it exceeded DUNE's requirements for the FD1 technology [106,110], demonstrating the viability of the SP LArTPC at this scale and reinforcing the choice of building a SP Horizontal Drift module.

3.2 The Detector

ProtoDUNE-SP comprehended two back-to-back LArTPCs that shared a common cathode plane, in such a way that the electron drift direction was opposite in each drift volume. They were hanging from the structure of the cryostat hosting them [113]. The APAs, previously described in Section 2.4.1, were enclosing different photon-collection modules (as the ARAPUCA presented in the previous chapter), and a cosmic ray tagger system was located outside the cryostat to accurately identify cosmogenic muons, useful for calibration purposes [105].

3.2.1 The LArTPC

The TPC had active dimensions of 7.2 m × 6.0 m × 6.9 m (see Figure 3.2), separated in two different volumes by a cathode plane located at $x = 0$. The coordinate system used to describe the detector is the following: the x axis runs parallel to the drift direction, and its zero is located in the cathode plane (meaning that one drift volume has negative x coordinates and the other has positive); the y axis runs parallel to the vertical axis and its zero is located at the bottom of the APAs; and finally the z axis runs downstream the face of the detector with the beam plug, with its zero coinciding with the beginning of the TPC.

Each drift volume had a drift length of 3.6 m and was exposed to a electric field of 500 V/cm, generated by a -180 kV bias applied to the shared cathode plane. This was formed by 18 CPAs of 1.16 m wide and 2 m high positioned forming a grid of 6 columns and 3 rows. In order to protect the TPC from electric discharges, they were made of a fire-retardant fibreglass-epoxy composite material and were laminated on both sides with Kapton, which are both heavily resistive. In addition to the CPAs, a field cage made of aluminium bar profiles covering the open-sides of the TPC was responsible of bringing the necessary electrostatic conditions inside the active volume. The bars were connected by means of resistive divider chains that provided the required voltage gradient. A high voltage (HV) feedthrough was attached to the CPA connecting it and the FC with the HV power supply. Ground planes covering the upper and bottom faces of the FC were used to avoid electric discharges to the argon gas phase and the cryogenic system deployed in the floor of the cryostat, respectively [105].

Each anode plane was formed by three APAs, composed by a stainless-steel frame 6.1 m high, 2.3 m wide and 76 mm thick. Four bronze wire planes were bonded directly over the frame, the first two of which were formed by induction wires (U and V), the third one by collection wires (X), and the last one by protective wires (G). As described in the previous chapter, U wires were set at 35.7° with respect to the vertical axis, V wires at -35.7°, and X and G wires parallel to it. This made induction wires cross only once a given collection wire on each face of the detector, avoiding reconstruction ambiguities. The voltage of each wire plane is different ($V_U = -370$V, $V_V = 0$V, $V_X = 820$ V and $V_G = -665$ V) so that electrons can flow through the induction wires towards the collection ones. On top of that, electron diverters were installed between APAs to reduce the amount of charge reaching this inert region. These were formed by two electrode strips mounted on an insulating board, which after being biased by an external voltage, modified the local drift field in such a way that

electrons were redirected towards the active regions of the APAs and away from the gaps [105]. Unfortunately, during the operation of the detector, the electron diverters presented short-cuts producing high currents in the active volume, so they were left unpowered. This generated problems during the reconstruction of events, in which a big percentage of tracks crossing from one APA to the next one were miss-recognized as two consecutive tracks instead of a single one [106, 110].

The read-out electronics were installed on top of the APAs inside the liquid argon, and were known as cold electronics (CE) [114]. Front-End Motherboards (FEMBs) were in charge of reading, amplifying, shaping and digitizing the signal of the 2560 channels of each APA. FEMBs were connected through the CE feedthrough to the Warm Interface Boards (WIBs), which distributed the information to the data acquisition system (DAQ) [105].

Finally, in order to minimize the energy loss of particles from the test-beam crossing the cryostat, a beam plug was installed in the face of the detector in front of the beam. It consisted of a cylindrical pressure vessel filled with nitrogen gas that penetrated inside the TPC (up to five centimetres inside the FC), so that the interaction of beam particles and inactive material was minimized. In Figure 3.2, a model of the ProtoDUNE-SP detector just described is presented. It can be seen how the disposition of the beam plug made beam particles cross only one detector volume, making this the 'beam side' while the other was the 'non beam side' [105].

3.2.2 The Photon Detection System

As commented in the previous chapter, several photon-collector approaches for the PDS of DUNE's FD were tested in ProtoDUNE-SP. They were bar-shaped optical modules of 8.6 cm high, 2.2 m long and 0.6 cm thick, embedded in the APAs, between the wire planes. All of them worked under the principle of photon trapping. Each APA had 10 support structures, so 60 optical modules were installed in total. Two of the available slots were used by a primitive version of the ARAPUCA concept presented in Chapter 2. The others 58 were split equally between two other options, known as Dip-coated and Double-Shift WLS Light Guides [105].

The first approach used a light-guide dipped in a solution of tetraphenyl-butadiene (TPB) and other solvents to produce a wavelength-shifting layer on the outer face of the light-bar. LAr scintillation light would reach this layer, shifting to blue light (425 nm) that would be trapped by total internal reflexion in the light-guide until being detected by the attached SiPMs [115]. The second approach used two rounds of shifting (similarly to the X-ARAPUCA), the first

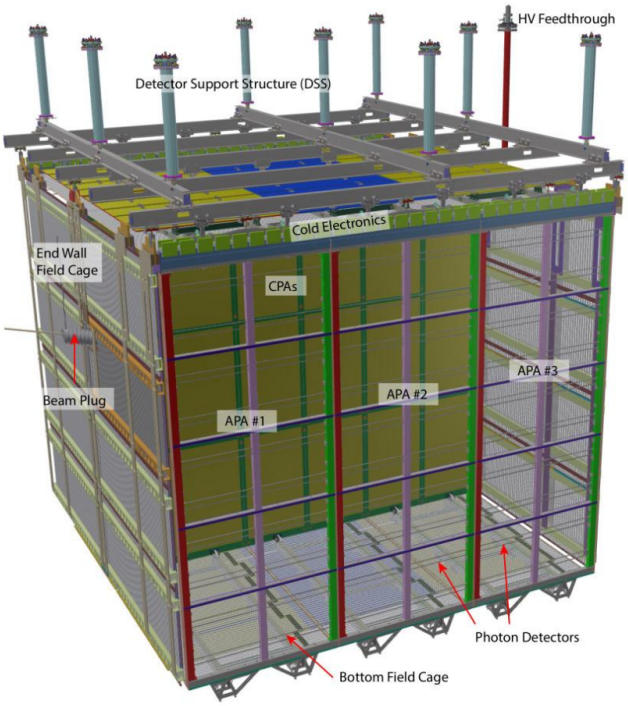

Figure 3.2: Schematic view of ProtoDUNE-SP TPC detector components. Image from [105].

one produced by a TPB-coated radiator plate and the second one by a WLS light-guide, generating a final wavelength of 490 nm [116, 117]. The first one had a larger optical acceptance due to a single shift of light, whereas the second one had a larger photon detection efficiency thanks to the largest wavelength achieved, for which the SiPMs had a better PDE. The ARAPUCA concept mixed both ideas [118]. Further details are given in Section 2.4.2.

3.2.3 Cosmic Ray Tagger

The Cosmic Ray Tagger (CRT) was a group of scintillator detectors positioned as XY planes in the upstream and downstream (with respect to the z direction) faces of the cryostat used to provide triggers from cosmic rays running parallel to the anode planes [105]. They were recycled from the outer veto of the Double Chooz experiment [119], formed by four 6.8 m high and 3.65 m wide assemblies with scintillation strips in two perpendicular directions. This allowed to coarsely measure the x and y position of cosmic rays passing through in both sides of the detector. This two hits could be associated with the TPC reconstruction,

granting a t_0 for the cosmic ray that triggered the CRT.

Being ProtoDUNE-SP a surface experiment, it was exposed to a 20 kHz rate of cosmic rays, adding up to 60 cosmic tracks in each 3 ms TPC acquisition window. These were particularly interesting for calibration reasons [106, 110].

3.3 Cryogenic System and Instrumentation

The ProtoDUNE-SP detector was hosted by the largest LAr cryostat ever constructed, with inner dimensions of 8.5 m × 8.5 m × 7.9 m (W×L×H). It was formed by an outer free-standing stainless steel structure (from which the TPC was hanging), layers of insulation and an inner corrugated membrane [113], with several openings (mainly on the top) to allow the installation of the detector components and the different electrical/signal feedthroughs. It was based on the technology used for liquefied natural gas (LNG) storage and transport. A detailed description of its design, construction and validation can be found in [106].

Being such a large detector, ensuring LAr purity was essential to guarantee charge and light collection. Argon received from the supplier had water, oxygen and nitrogen impurities at the level of parts per million, a contamination substantially above DUNE requirements (100 ppt oxygen equivalent) [83]. The cryogenic system was responsible of purging, cooling down, and filling the cryostat, maintaining the LAr in the cryostat at the desired temperature, pressure and level, and more importantly, of purifying the argon and maintaining the required purity levels [106, 120].

A schematic view of the purifying system is presented in Figure 3.3. It was based on the experience gained from Fermilab with the Liquid Argon Purity Demonstrator (LAPD), the 35t prototype [121], and MicroBooNE [98]; from the ICARUS detector [86]; and from the WA105 prototype [122]. It consisted of three purifying loops: one for the liquid phase, in which argon was pumped through a series of filters before being reintroduced again by four pipes at the bottom of the cryostat; another for the argon purged from the cryostat penetrations, which was filtered as gas, liquefied and merged with the liquid flow on the first loop; and the last one which directly retrieved and re-condensed argon gas from the boil-off before mixing it with the liquid loop. All the LAr volume was recirculated through the purification system in about 4.5 days [106].

Aside from the cryogenic system, a wide range of different devices meant to monitor the quality and stability of the overall detector environment, to ensure that the LAr quality was adequate for the operation of the detector, and to help diagnose the source of any changes in detector operations, was installed inside

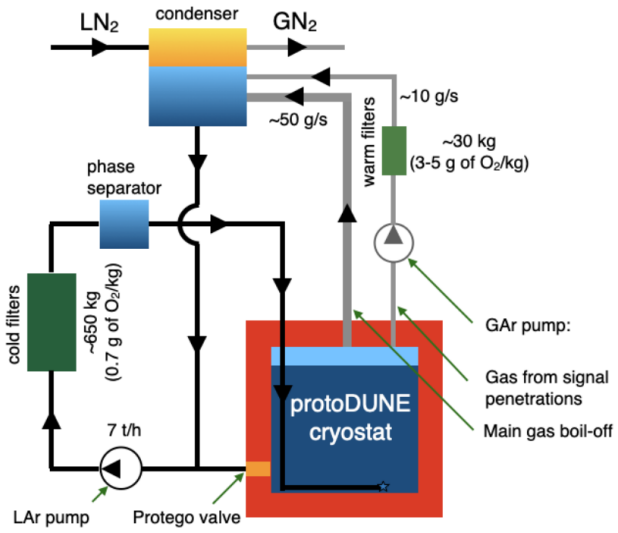

Figure 3.3: Schematic view of ProtoDUNE-SP recirculating and purifying system. Image from [110].

the cryostat [105]. Some of them are purity monitors, temperature monitors, cameras, level meters and gas analysers. In Figure 3.4, an schematic view of the ProtoDUNE-SP cryostat with the location of many of these devices is presented. A detailed description and motivation of the purity and temperature monitors is presented next, and some comments on the performance of the rest can be found in [123].

3.3.1 Purity Monitors

The probability of charge survival from the ionization point to the collection point is inversely proportional to the concentration of impurities in LAr. Electron loss due to these impurities can be parametrized as

$$Q(t) = Q_0 e^{-t/\tau}, \tag{3.1}$$

where Q_0 is the charge generated by ionization and not recombined with argon ions, $Q(t)$ is the charge after a given time t, and τ is the so-called electron lifetime. Having ProtoDUNE-SP a drift distance of 3.6 m and an electron drift velocity of 1.5 mm/µs (as DUNE FD1 is going to have, [83]), the expected drift time from cathode to anode is around 2.3 ms. DUNE's requirements for the FD1 is to have at least 3 ms electron lifetime (equivalent to 100 ppt of oxygen) [83], which would imply a charge loss of more than 50% from cathode to anode. As it

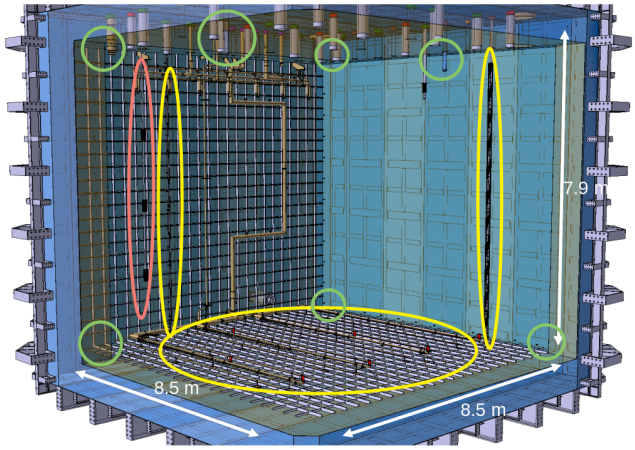

Figure 3.4: Diagram of ProtoDUNE-SP inner cryostat and some cryogenic instrumentation. In green, the location of the cameras is highlighted; In yellow, temperature sensors; in red, purity monitors.

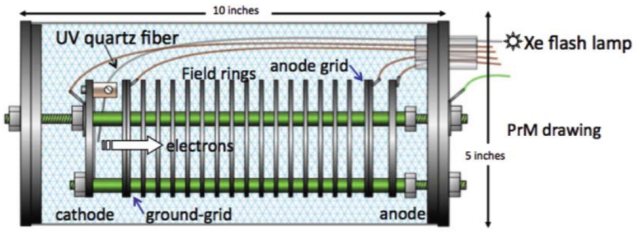

Figure 3.5: Representation of a purity monitor. Image from [86].

can be noticed, this effect is dramatic, and an inappropriate purification of LAr can blind the TPC.

Purity monitors (PrM) were designed to frequently measure the electron lifetime of the LAr inside the cryostat, independently of the TPC. They are, indeed, small TPCs, as it can be seen in Figure 3.5. Their design was based on the ones used in the ICARUS T600's detector [86]. A Xenon lamp flashes a photo-cathode generating ionization electrons that travel towards the anode. The electric field is homogenized by the field rings, which act as a field cage. By measuring the ratio of charge in the cathode and the anode $R_Q = Q_A/Q_C$, the value of the electron lifetime can be deduced:

$$Q_A = Q_C e^{-t/\tau} \rightarrow R_Q = e^{-t/\tau}. \tag{3.2}$$

A vertical array of three PrMs was installed in ProtoDUNE, behind the APA

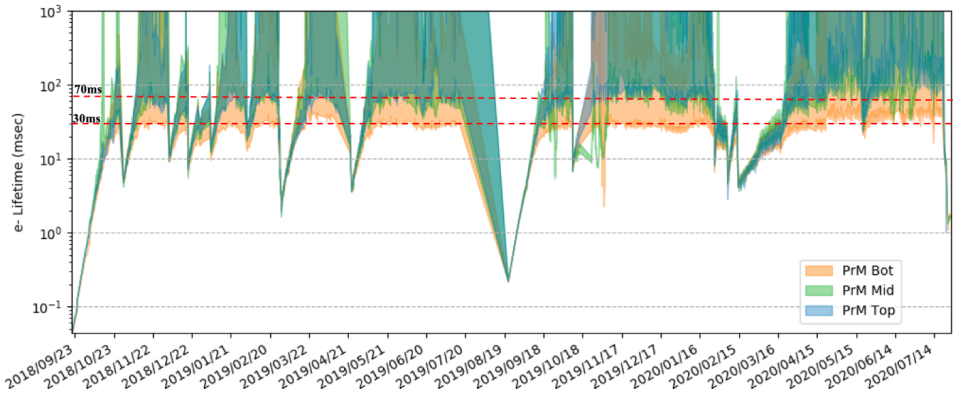

Figure 3.6: Electron lifetime measured by the three PrMs as a function of time from September 18 until February 2020. At the beginning, the purity was low because recirculation had not started yet. Later dips represent recirculation studies and pump stoppages. The bands represent the uncertainty of the measurements. Image from [110].

plane of the non-beam side. They were located at 1.8 m, 3.7 m and 5.6 m from the bottom of the cryostat [105]. They measured the electron lifetime through all stages of the experiment (see Figure 3.6) and, even though the results obtained were below the 100 ppt oxygen equivalent requirement (particularly, for the last day of beam data taking, since it was 3.4 ± 0.7 ppt), a purity stratification was observed: purity decreased towards the bottom of the cryostat. This effect, although innocuous to the physics results due to the exceptional high purity achieved, is currently being investigated.

3.3.2 Temperature Monitoring System

Purity monitors could provide a direct measurement of electron lifetime and the ppt oxygen equivalent outside the TPC active volume. Because of the detector geometry, the liquid argon flow and the position of the PrMs, extrapolating this value to the inner bulk of the TPC is not straightforward. Computational Fluid Dynamic (CFD) simulations aim to accomplish this. The two main outputs of these calculations are 3D maps of temperatures and impurities. From the first simulations that were done before the installation of ProtoDUNE-SP and the experience gained in the 35 t prototype [121], it was soon realized that the relative vertical temperature gradient of the liquid argon was strongly correlated with the concentration of impurities. Particularly, it was observed that temperature

Figure 3.7: Static T-Gradient Monitor installed inside ProtoDUNE-SP cryostat.

gradients larger than 30 mK along the more than 7 m high LAr were likely to produce a stratification of the purity. Because of that, simulations pointed out that injecting LAr at the cryostat's bottom at a temperature 400 mK above the average would improve convection movements of LAr, hence reducing the stratification effect [105]. However, no experimental proof of this was available for cryostats as large as DUNE's (nor ProtoDUNE's).

In order to constrain and validate CFD simulations, a broad set of high precision temperature sensors were disposed in different locations of the cryostat. Particularly, 12 were located over the pipes injecting the LAr inside the cryostat, 8 over the top ground planes of the detector, 24 forming a vertical array close to the PrMs, and 48 forming another vertical array behind the FC in the downstream face of the detector; adding up to a total of 92. The first array mentioned was commonly known as Dynamic T-Gradient Monitor, since its sensors could be moved up and down thanks to a stepper motor in such a way that each sensor would reach the position of the sensor above, allowing for an *in situ* calibration (under the assumption of negligible temperature change during the operation) [124]. The second vertical array mentioned was known as Static T-Gradient Monitor, since as its name suggests, was not movable [105]. In Figure 3.7 two pictures of this device installed in the cryostat are presented.

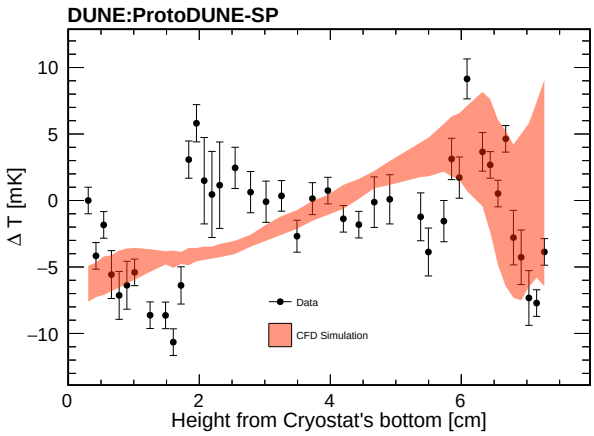

Figure 3.8: Comparison between the vertical temperature gradient measured in ProtoDUNE-SP by the Static T-Gradient Monitor and the CFD's prediction. The red band represents the CFD uncertainty, the data error point account for statistical and systematic uncertainties. Discrepancies are evident.

Specifically, Lake Shore TP102 platinum sensor with 100 Ω resistance were used (see 3.7, right). All of them were relatively calibrated in the laboratory before the installation. The calibration procedure was an iterative process that improved little by little, and which reached its best performance when calibrating the 48 sensors of the Static T-Gradient. The estimated average relative precision of the calibration was 2.6 mK. This is explained in detail in [125].

A comparison between the measurements provided by the Static T-Gradient Monitor and the output of the CFD simulations is presented in Figure 3.8. As it can be observed, there are evident discrepancies. During the operation and commissioning of the detector different tests were done to ensure the measurements were not biased, as exchanging the readout electronics, the cables, or recalibrating the different current sources. Moreover, after the decommissioning of ProtoDUNE-SP, the sensors were recalibrated again in the laboratory with a new set-up and approach, finding the same result. Consequently, it was clear that CFD simulations were roughly predicting correctly the vertical temperature gradient, but it was not reproducing the local features observed by the temperature monitors.

In addition to this, comparisons were also made in a plane located 40 cm above the cryostat floor using the sensors installed over the pipes. Whereas the simulation predicted a temperature gradient of about 3 mK between the sensors located below the cathode plane and the sensors further away from the injection of argon, experimental measurements showed a gradient of about 20 mK (see

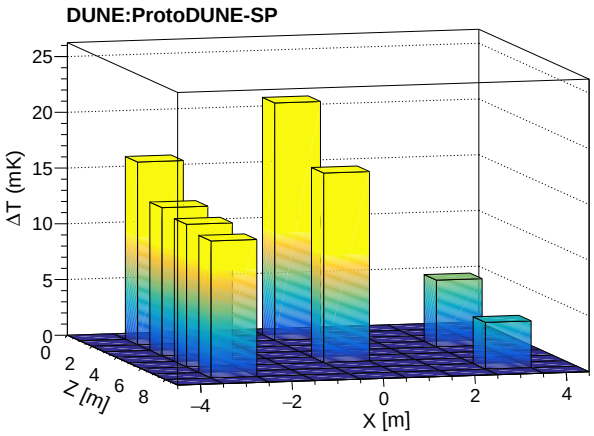

Figure 3.9: Relative temperature distribution measured at $y = 40$ cm plane with respect to the bottom sensor of the Static T-Gradient. The four sensors on the left ($x \approx -3$ m) were the ones on top of the pipes outlet, below the beam side APAs; the ones in the middle ($x \approx 0$ m) were the ones below the CPAs plane; and the ones on the right ($x \approx 3$ m) the ones below the non-beam side APAs plane, where the extraction pump was located. A gradient of ~ 20 mK was measured between the sensors below the cathode and the sensors closer to the pump. The colors are used so that temperatures and differences are understood easily.

Figure 3.9), making it evident that more studies were needed to fully understand liquid argon dynamics inside the cryostat. These studies are currently ongoing and are expected to be validated in the second phase of ProtoDUNE.

Apart from working as a test-bench for the CFD simulations, temperature sensors were extremely useful during all stages of the ProtoDUNE-SP experiment. During the filling and emptying process, they were used to measure the level of LAr inside the cryostat, and also to ensure the detector structural stability. During the filling (emptying), detector components were exposed to very large differences of temperature, large enough to break from thermal stress. In Figure 3.10 this effect can be observed: when the filling started, the temperature gradient was larger than 100 K in the APA region (red curve), being this a potential threat to their structure. Due to this observation, LAr was sprayed from the top of the cryostat so that temperature gradient in the region was reduced (blue curve).

They were also used to ensure the long-term operational stability of the detector by measuring the vertical temperature gradient during the two years of operation. This was found to be about 18 mK, stable within approximately

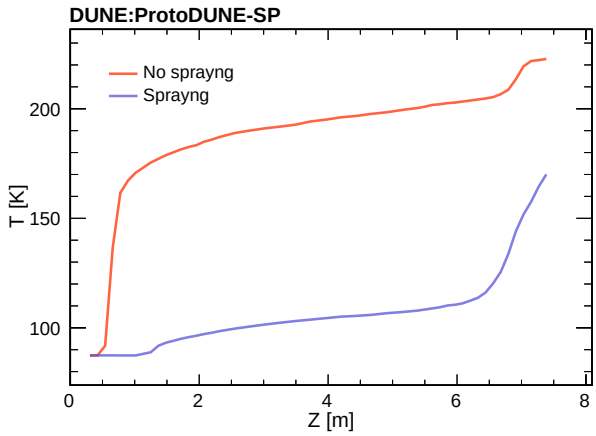

Figure 3.10: Vertical temperature gradient measured by the Static T-Gradient Monitor during the filling process of ProtoDUNE-SP. In red, the measurement before LAr was sprayed from the top of the cryostat; in blue, the measurement after the spraying started.

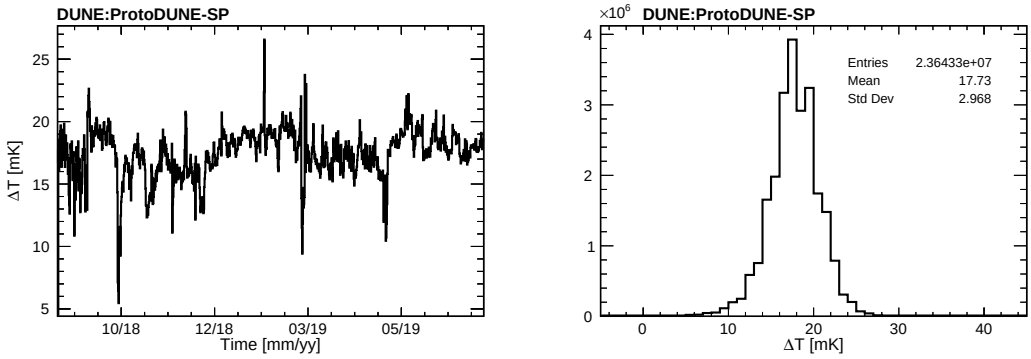

Figure 3.11: Left: maximum temperature gradient measured by the Static T-Gradient Monitor during almost a year. The spikes were caused by recirculation stoppages. Right: projection of the plot in the left. Each entry corresponds to a data readout done each few seconds.

3 mK, confirming that the recirculation system performed stably during all the operation of ProtoDUNE-SP and validating the CFD hypothesis. This can be observed in Figure 3.11.

Moreover, it was found that they could be used as trigger under accidental stoppages of the purifying system. At the end of October 2018, due to a coding error on the cryogenic system, the recirculation and purification processes were stopped during hours. This was not noticed until the next day, in which a purity measurement was done with the PrMs. This was a dramatic accident in which

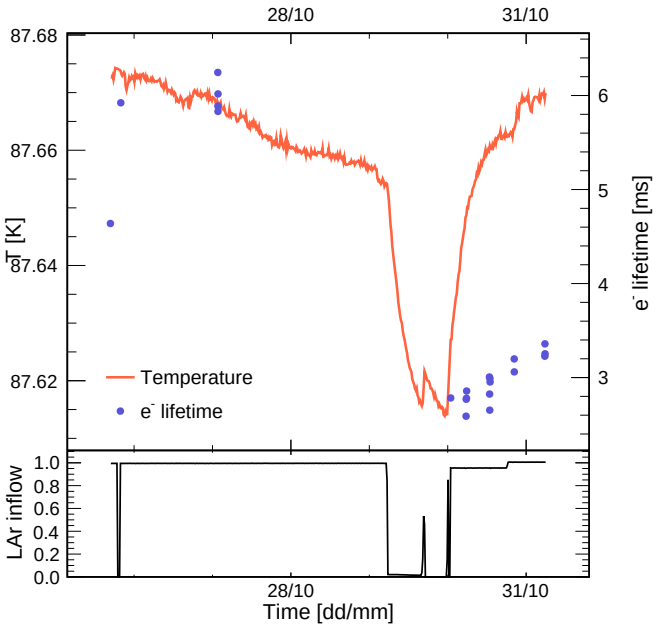

Figure 3.12: Overview of the accidental stoppage of the recirculating and purifying system of ProtoDUNE-SP at the end of October 2018. In the top plot, temperature (red) and electron lifetime (blue) are displayed. In the bottom plot, the normalized argon flow is represented. All three magnitudes are presented as a function of time. It can be observed how, after the LAr inflow was stopped on 29/10, there was an instantaneous drop of temperatures. This stoppage lasted for a day, when a new lifetime measurement was done and the problem was identified. A proper monitoring of temperature profiles would have helped to recognize this issue much earlier, avoiding loosing half of the electron lifetime.

the electron lifetime of 6 ms that had taken more than one month to achieve was halved only in a few hours. Afterwards it was understood that this effect could have been recognized almost immediately if temperature trends would have been thoroughly monitored, since they were very sensitive to the absence of incoming warmer LAr through the bottom pipes in the cryostat (see Figure 3.12). Consequently, it was concluded that trigger strategies could be developed to alert in case of sudden drops in temperature.

Due to the utility of temperature sensors, the not yet completely understood liquid argon dynamics inside the cryostat, and the importance of properly determining the electron lifetime inside the active volume of the TPC with sufficient precision to ensure that the physics results are not compromised, it was decided to further increase the presence of temperature sensors in FD1. Apart from the

sensors that will be placed in specific cryogenic locations, like the ones close to the liquid argon extraction pump, the cryostat walls or the pipes, it was also decided to place temperature sensors inside the APA frames, behind the wire planes. In this way the temperature profile measured is closer to the inner active volume of the detector and will allow a better comparison with CFD simulations.

3.4 Beam Line

ProtoDUNE-SP was located in the CERN North Area, just downstream of the H4 beam line. The proton beam extracted from the SPS (Super Proton Synchrotron) is collided against a beryllium target generating a mixed hadron beam of about 80 GeV/c of momentum. This secondary beam is collided once more against another target (made of copper or tungsten), providing a tertiary beam with momentum ranging from 0.3 up to 7 GeV/c.

The H4 beam line was the one bringing the tertiary beam from the last target to the detector. It was instrumented with an array of monitors and magnets that allow to tune the desired beam characteristics and to identify the different beam particles [126, 127]. These are schematically presented in Figure 3.13, top. Eight profile monitors (XBPF) allow for beam tracking on a particle-by-particle basis [128] and to reconstruct particles' momentum (see Figure 3.13, bottom), with a resolution of 2.5 %. The last XBPFs are the ones that extrapolate the position and the direction of the particles inside the TPC. Three trigger counters (XBPF) are used as the beam trigger system and as a time of flight (TOF) monitor. One is located upstream, another one in the middle of the beam line, and the last one downstream. A coincident signal in the middle and downstream ones is used to trigger the TPC read-out during beam data-taking. The upstream and downstream trigger counters are separated 28.575 m, and the time between signals is used to compute the TOF (see Figure 3.14), which can be used for particle identification (PID). In addition, two Cerenkov (XCET) counters are used to improve this PID. They are $\sim$2 m long tubes filled with CO_2 at different pressures, allowing to discriminate between heavier and lighter particles depending on their momenta [129]. In Table 3.2 the logic applied to identify particle species is presented. Note that for large momentum, particle identification relies exclusively on Cerenkov counters, since TOF is the same for all particle species.

3.4.1 Test Beam of ProtoDUNE-SP

As earlier commented, ProtoDUNE-SP was exposed to a charged beam during the Fall of 2018, before the long shutdown of the SPS. Different particle species at

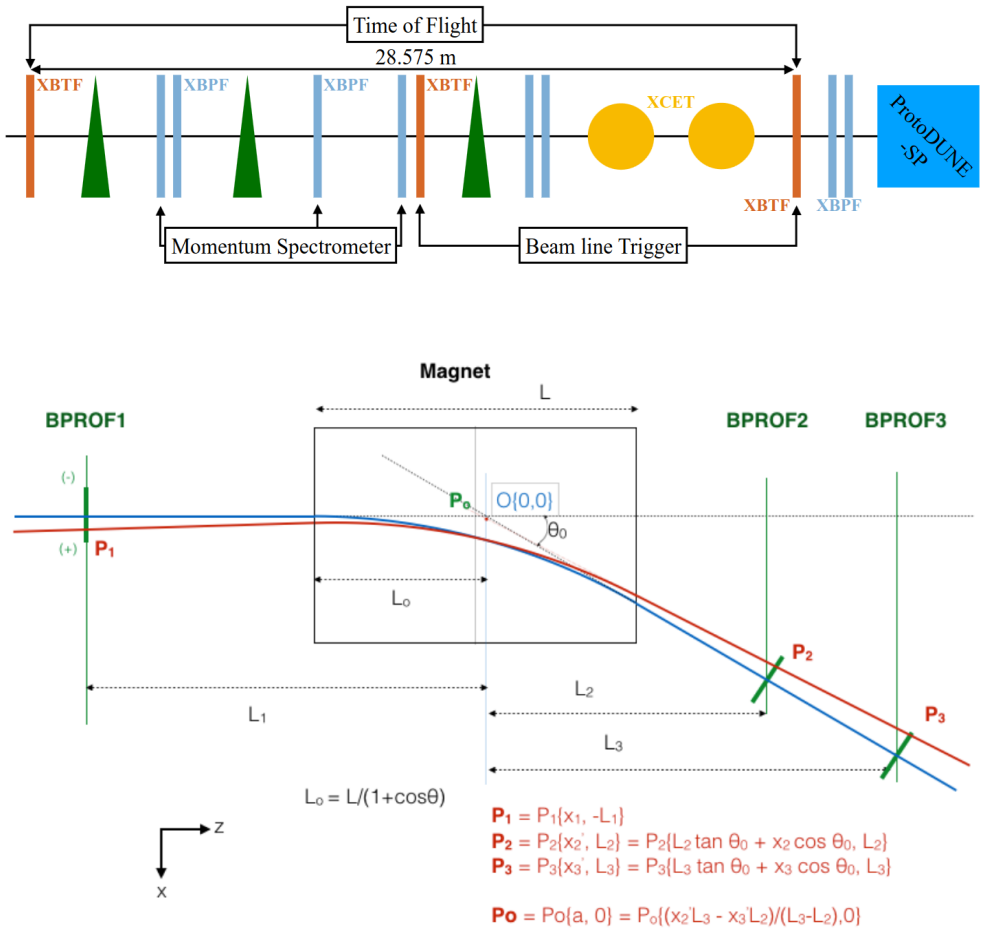

Figure 3.13: Top: schematic view of the H4 beam line, its monitors and magnets. Bottom: diagram of how XBPF can be used to compute particle momentum. Images from [110].

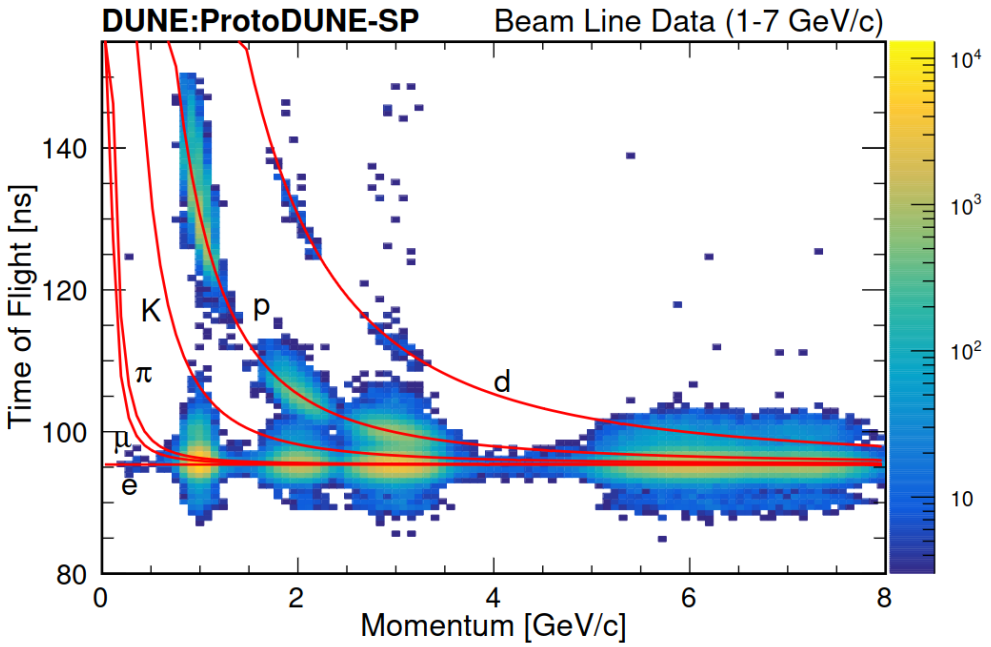

Figure 3.14: Particles' time of flight against reconstructed momentum for several ProtoDUNE-SP beam runs. Red curves represent predictions for the different particles species. Image from [110].

different momenta were thrown to the detector, so that it could be calibrated and its performance studied in-depth. In Table 3.1 a summary of the beam triggers per particle specie and momentum are presented. Although the original plan for the test beam was to include both beam polarities and more momentum values, the data taken have allowed to develop important physics analysis for DUNE. It is also important to remark that, from the two available targets supposed to generate the tertiary beam –copper and tungsten, as presented above– tungsten is preferred to increase the hadron content of the beam at low momentum (below 4 GeV/c). However, the copper target was unintentionally used for the 2 GeV/c runs, substantially decreasing their hadron abundance.

3.5 Data Acquisition, Timing and Trigger

Data coming from the three detector subsystems described earlier (the TPC, the PDS and the CRT) were collected, filtered and stored by the data acquisition system (DAQ). Two different read-out solutions were tested in ProtoDUNE-SP's

Table 3.1: Beam instrumentation logic to identify particles species. The numeric intervals in the TOF column represent the cut applied in ns. LP and HP refer to low-pressure and high-pressure Cerenkov detectors, respectively; and 1 and 0 represent the presence or absence of signal. A dash is used to indicate that the instrument is not used in the logic.

Particle	Momentum (GeV/c)	TOF (ns)	LP XCET	HP XCET
e	1	0-105	1	-
	2	0-105	1	-
	3	-	1	1
	6-7	-	1	1
μ/π	1	0-110	0	-
	2	0-103	0	-
	3	-	0	1
	6-7	-	1	1
K	1	-	-	-
	2	-	-	-
	3	-	0	0
	6-7	-	0	1
p	1	110-160	0	-
	2	103-160	0	-
	3	-	0	0
	6-7	-	0	0

Table 3.2: Beam triggers per beam momentum and particle specie.

Momentum (GeV/c)	Triggers (k)			
	Pion-like	Proton-like	Electron-like	Kaon-like
0.3	0	0	242.5	0
0.5	1.5	1.5	296.3	0
1	381.8	420.8	262.7	0
2	333.0	128.1	173.5	5.4
3	284.1	107.5	113.2	15.6
6	394.5	70.1	197.0	27.9
7	299	58.4	112.9	28.2

TPC with the aim of selecting the best one for DUNE's FD: Reconfigurable Cluster Elements (RCEs) [130] and FELIX [131]. The first one was used in the three APAs of the beam side, and two out of three of the non beam side. FELIX, originally designed for the ATLAS experiment, was used in the remaining APA. Both received the data from the cold electronics and sent it to the DAQ system [106], controlled by the artDAQ software [132, 133].

The timing system was responsible of synchronizing all detector components by grating a 50 MHz clock, sending triggers from the central trigger board (CTB), and also interfacing with the SPS. The CTB was a hardware triggering system that formed high-level trigger signals from the low-level ones from the different subsystems (PDS, SPS, CRT, beam instrumentation). Simultaneous trigger conditions could be checked (for example, checking that all detector components were active) and hence sending a trigger signal to the timing system which ultimately decided what to do depending on whether a previous trigger signal was ongoing [106].

If a trigger was accepted, a read-out window (an *event*) started: 6000 ADC samples from each TPC wire were digitalised during 3 ms (which represented 2 MHz sampling frequency). Each sample, known as *tick*, lasted 500 ns. Events usually started with data acquisition 250 µs before the trigger time, so that charge deposited before the trigger could also be collected. Coinciding data from the PDS, the CRT and the beam line was also stored and matched. The CTB could discriminate between beam-on and beam-off triggers, allowing a straightforward identification of events with a beam particle entering the detector [106, 110].

3.6 Event Reconstruction

After a trigger signal had been sent and an event recorded, the reconstruction could start. It is in charge of providing high-level analysis objects from the low-level waveforms generated by each subsystem, which gets particularly complicated when there are several processes happening inside the TPC at the same time [134]. Since the analysis presented in this dissertation only uses information from the TPC, this section is dedicated to describe exclusively the TPC reconstruction process.

Before any reconstruction could be done, the TPC response had to be properly characterized. The pedestal and the gain of each ADC channel was measured in specific calibration runs. Readout, correlated noise and tail-removal issues were also treated before the final characterization step, which provides the amount of charge collected by the collection wires or induced in the induction

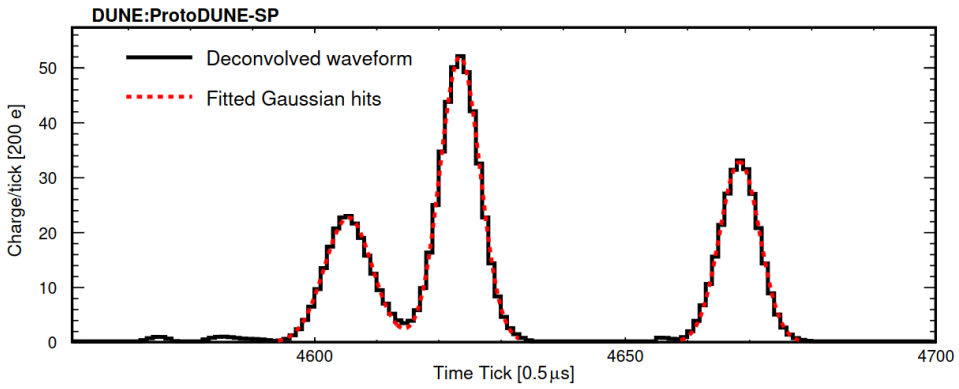

Figure 3.15: Example of a reconstructed waveform on a single wire fitted to three Gauss functions. Image from [110].

wires. After this, signals could be processed appropriately [110].

The signal processing consists in separating the real charge-vs-time waveforms from the detector effects [134]. For example, the signal in the induction wires is also sensitive to charge moving away from the wire itself. Because of that, a two-dimensional deconvolution involving time and wire dimensions is needed, producing unipolar signals as output simplifying the hit-finding procedure. Finally, a search for regions of interest within the waveform are done so that the resolution is increased. A detailed description of this process can be found in [135, 136].

After the waveforms are processed, the reconstruction followed two steps: first, hit-finding, and second, pattern recognition. In the LArTPC experiment jargon, a hit corresponds to a two-dimensional object representing a cluster of electric charge being deposited (or passing by) a wire at a given time, forming a Gaussian-shaped distribution. Hit-finding algorithms aim to search in the region of interest and fit these distributions. The area of the curve corresponds to the total measured charge (in ADC counts$\times$ticks) whilst the mean value corresponds to the time in which the charge reached the wire [110]. An example of three hits fitted to Gaussian functions is presented in Figure 3.15.

Since induction wires were wrapped around the APA, a disambiguation is needed to know where the charge was coming from. Moreover, multiple induction wires can be matched to a given collection wire. In order to identify the appropriate matching and the side, the algorithm compares the measured charge in each wire and matches the most similar ones. Simulations have shown an efficiency larger than 99% for this procedure. Finally, there could be situations in

which hits are not represented by a simple Gaussian, for example in the case of a track parallel to the x axis, in which hits would pile-up in the same wire. Under this situation, the pulse is divided in an evenly-spaced number of hits [110].

Once the hits have been identified and characterized, the pattern recognition is ready to start. In the case of ProtoDUNE-SP, it was performed by Pandora [137], a specific software toolkit extensively used in different LArTPC neutrino experiments as MicroBooNE [138]. Being a software dedicated to neutrino experiments, particular developments were needed so that Pandora could work with two different drift volumes and with the beam particle [139]. The approach followed by Pandora consists of three steps: firstly forming hit clusters, secondly reconstructing tracks under the hypothesis of cosmic rays, and lastly removing all cosmic rays and reconstructing what is left as particles whose origin is the beam. The result of this process is a hierarchy of particles, in which daughters and parents are associated.

During the first step, a two-dimensional map of each wire plane, in which hits are organized in clusters, is created. Then, the clusters across the different maps are associated, using the excess of information granted by the three planes to prevent errors. When an appropriate match has been found between the three planes, a three-dimensional hit (a.k.a. space-point) is created. After all space-points have been formed, hierarchies can be built.

Pandora attempts to first reconstruct the clusters as cosmic rays. Some are easily identified either by the fact of being through-going tracks (they cross the detector from the top face to the bottom face); by having a different t_0 than the one given by the beam trigger; or by not having an associated t_0 and consequently having hits 'outside' the TPC volume when reconstructed using the beam t_0. Due to the high rate of cosmic rays crossing the detector, using the PDS to provide a t_0 was complicated.However, if cosmic rays crossed the APAs plane or the CPA a t_0 could be assigned.

The clusters whose origin has been identified as cosmic are removed. Then, Pandora divides the detector volume in 3D regions containing all hits produced by a given interaction. These regions could contain unidentified cosmic rays and particles originated from the beam as well. Because of that, two reconstruction algorithms are run in parallel (under cosmic hypothesis and under beam hypothesis) and a boosted-decision tree is used to determine which interaction regions have been produced by the beam and which have not, based on the topology of the interaction. The algorithm used to reconstruct beam interactions aims to solve complicated hierarchies with different hadrons or decays in the final states, so that the final output is the one commented above: a 'flow' of object particles with links between parents and daughters, thus the full chain of processes

originated from the beam are easily accessible for later analysis. These object particles can be either showers or tracks [110, 139].

Thanks to the development of a convolutional neural network (CNN), further information from the hits was obtained. This algorithm was trained to associate a score from 0 to 1 to each hit depending on how likely it was to have been created by a track, a shower object or a Michel electron [140, 141]. This has been broadly used in the different ProtoDUNE-SP analysis, since it helped to identify events depending on their topology or to identify miss-reconstructions, like for example Michel electrons that were reconstructed as part of muon tracks.

3.7 Event Simulation

The Montecarlo (MC) simulation of ProtoDUNE-SP is done with LArSoft [142], a set of software tools developed to simulate, reconstruct an analyse events in liquid argon experiments. It is based on Art [143], an event framework created at Fermilab, that is used by many LAr experiments. They all share the same software core whilst each of them builds up experiment-dedicated code on top of it.

In LArSoft, simulation is divided in three steps: i) particle generation, ii) propagation and iii) detector response simulation. In the first step, the initial particles with defined specie, momentum and direction are generated. For ProtoDUNE-SP, they involve beam particles, beam halo particles and cosmic rays. The first two are simulated by the G4Beamline event generator [144], FLUKA [145, 146] and MAD-X [147], whereas the latest are simulated by CORSIKA [148]. Moreover, LArSoft has a dedicated generator for radionuclei decays [105], as ^{39}Ar.

In the second step, all these particles are passed to GEANT4 [149], which propagates them through the full geometry of the experiment, simulating their interactions. This propagation is done in steps of 300 µm, far beyond the resolution of the detector, in which the energy deposited by each particle is computed. This is GEANT4's main output.

A minimum ionizing particle deposits approximately 2.12 MeV/cm in liquid argon, which has an ionization potential of 23.6 eV and a excitation (scintillation) threshold of 19.5 eV. Thus, thousands of electrons and photons are generated by each particle each cm they travel. Simulating all these resulting particles and propagating them up to the wires or the PDS is unfeasible [105]. LArSoft has tools to reduce the computational time using parametric models and approximative techniques that provide accurate signal predictions in an affordable time.

Furthermore, these tools can also simulate other effects as electron drift, recombination, charge attenuation, diffusion or space charge effects (described in the next section).

In the last step, the charge and the light reaching the TPC wires and the PDS modules at a given time is calculated, and the true signals are convoluted with the full electronics response (including noise). The resulting objects are simulated waveforms which can be fed into the reconstruction chain described above. Differently to what happens with real data, here the truth information is available: it is possible to know which particle species were generated, their location and their exact four-momentum, the relationship between all the other particles and the processes they underwent, and what kind of signals produced in the detector.

3.8 Detector Calibration

The LArTPC technology was proposed for neutrino experiments due to its excellent calorimetric capabilities. The appropriate characterization of final-state particles $\frac{dE}{dx}$ constitutes the main source of information to identify particle species and to reconstruct the energy of the interacting neutrinos. This was one of the main objectives of ProtoDUNE-SP, and in order to accomplish it, a proper understanding of the relationship between the deposited energy and the response of the detector was needed.

Once electrons conforming hits are collected by the X wires, the total charge associated to each hit (dQ) corresponds to the area under the Gaussian curve that best fits the hit signal, as shown in Figure 3.15. At this point, charge is in ADC×ticks units, and it can be converted to an absolute number of electrons using the ADC calibration constant. To compute the amount of charge per unit length, $\frac{dQ}{dx}$, the dx value (a.k.a. the *pitch*) is needed. It is obtained by projecting the direction of the track over the wire axis [110] (in the case of a collection wire, the vertical axis), as displayed in Figure 3.16.

Afterwards, the number of electrons can be transformed into calorimetric information ($\frac{dE}{dx}$). The relationship between the number of ionization electrons and the deposited energy is not linear due to the recombination effect, in which freed electrons are trapped by ions [150–154]. This effect can be described via the modified box model developed by ArgoNeuT [155], which in an ideal detector

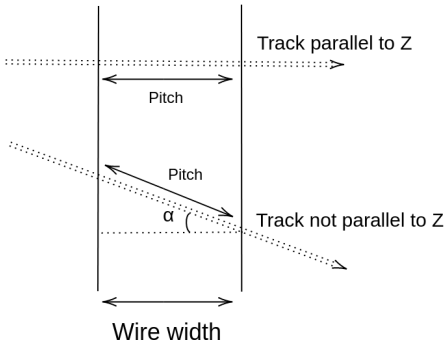

Figure 3.16: Diagram showing how the pitch of a hit is estimated.

would be

$$\frac{dE}{dx} = \frac{\rho\mathcal{E}}{\beta'}\left[\exp\left(\frac{\beta' W_{ion}\frac{dQ}{dx}}{\rho\mathcal{E}C_{cal}}\right) - \alpha\right], \tag{3.3}$$

where ρ is the density of liquid argon, $\mathcal{E}$ is the electric field, W_{ion} is the argon ionization potential, C_{cal} is the ADC calibration constant and α and β' are the modified box parameters measured by ArgoNeuT [155] (0.93 and 0.212 (kV/cm)(g/cm^2)/MeV, respectively). This model is also used to simulate recombination in the MC.

However, different effects were observed in the detector's response as the space charge effect, the charge attenuation, and the detector non-uniformities; modifying the measured $\frac{dQ}{dx}$ and the electric field inside the active volume, making it necessary to calibrate them [110]. These are reviewed next.

3.8.1 Space Charge Effect

As mentioned above, ProtoDUNE-SP was located at the surface and thus it that was exposed to a high rate of cosmic rays, which continuously crossed the detector ionizing argon atoms. The ionization electrons drift towards the anode at a velocity of ∼1.6 mm/µs, whereas the more massive Ar^{1+} ions drift to the cathode at a much smaller velocity (∼5 mm/s) [134]. This asymmetry generated a quick build-up of positive charge in the active volume, which modified persistently the electric field lines inside the TPC. This is the so-called Space Charge Effect (SCE), which had a significant effect on ProtoDUNE-SP spatial and calorimetric reconstruction due to the large dimensions of the detector [110].

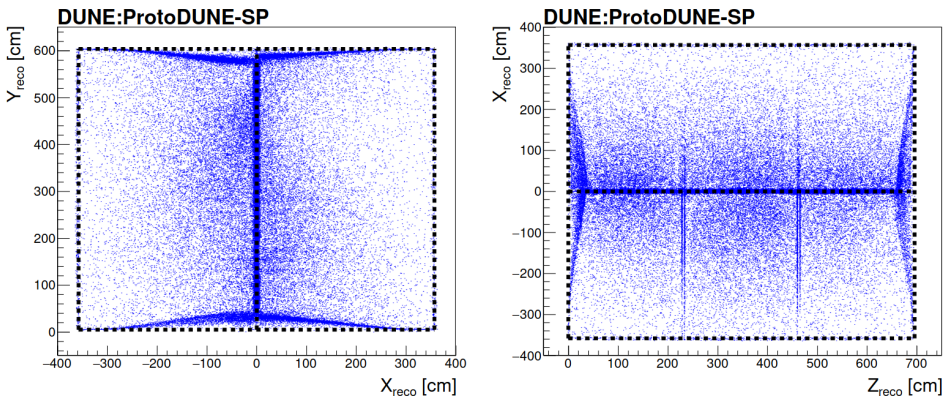

Figure 3.17: Projections of the end position of reconstructed t_0-tagged cosmic rays in the xy plane (left) and zx plane (right). In absence of SCE, projections should lay over TPC boundaries, represented as black dashed lines in the plots. Image from [110].

Even though DUNE will not suffer this effect thanks to its underground location, extrapolating ProtoDUNE-SP results to DUNE required an adequate calibration.

The modification of field lines inside the TPC distorts the electrons drift path towards the anode. Particularly, they are bent towards the bulk of the active volumes, since ions tend to accumulate close to the CPA. As a consequence, trajectories and lengths differ from the original ones. Aside from tracking, SCE also affects the calorimetry measurements: the relative variation of hits' position generates a change on the track local direction, which affects the computation of hits' pitch and hence $\frac{dQ}{dx}$. On top of this, electron-ion recombination depends on the magnitude of the local electric field, further affecting the final $\frac{dE}{dx}$ measurement. In other words, the SCE makes the tracking and the calorimetry depend on the position inside the detector [110].

The magnitude of the SCE distortion can be qualitatively understood in Figure 3.17. There, the end-position projections of t_0-tagged cosmic rays is represented in the XY and XZ planes. Through-going cosmic rays should end at the TPC faces, however their end position is displaced up to tens of centimetres away from the faces of the TPC due to the SCE.

Although this effect has been simulated in the MC samples by generating 3D positional and electric field displacement maps, significant differences were found between the positional offsets in data and simulation. Figures 3.18 and 3.19 show these offsets in the end point of the tracks in the direction perpendicular

to each face of the detector for data and MC, respectively. These discrepancies were probably due to the unknown value of ion drift velocity and to the effect of liquid argon flow, which has a similar magnitude to the ions velocity. In order to overcome these discrepancies, a data-driven approach partially based on MicroBooNE [156] was followed:

1. The top and bottom (y axis), and downstream and upstream (z axis) faces of the detector were divided in voxels (or cells) of $\sim$20$\times$20 cm^2 in data and MC. The average positional offset in the direction perpendicular to each face was measured for the $t0$-tagged cosmic rays ending in each of them, thus allowing to compute a ratio data/MC for each voxel. This ratio was used as a scale factor for each MC cell.

2. The two drift volumes were completely divided in 3D voxels of $\sim$20$\times$20$\times$20 cm^3. For each voxel, a scale factor was computed in each direction by means of of linear interpolation algorithms. The scale factor in the y axis for each cell was computed by linearly interpolating the ratios obtained in the voxels in the top and bottom faces of the detector. In the case of the scale factor in the z axis, it was computed by linearly interpolating the scale factors measured in the upstream and downstream faces of the detector. Finally, the scale factor in the x axis for each voxel was determined as the mean of the scale factors in the y and z directions. With this, a 3D map of scale factors in each axis was obtained.

3. The simulated displacement map on each axis was corrected being multiplied by the 3D map of scale factors on each axis, generating the final data-driven SCE spatial distortion maps.

4. The gradient of the spatial distortion along the local drift direction could be determined by inverting the spatial distortion maps. This, along with the known electron drift velocity as a function of the electric field, was used to obtain the electric field distortion maps [110].

Once the data-driven positional and electric field distortion maps were obtained, they were inverted and used to correct the data samples and to simulate more accurately the SCE effect on the MC simulation.

It is also interesting to note here that SCE presents a clear asymmetry in both detector volumes, probably due to the fact that LAr injecting pipes were situated below the beam side of the TPC. This further reinforces the necessity of developing more accurate CFD simulations, so that this effects can be properly understood, simulated and calibrated.

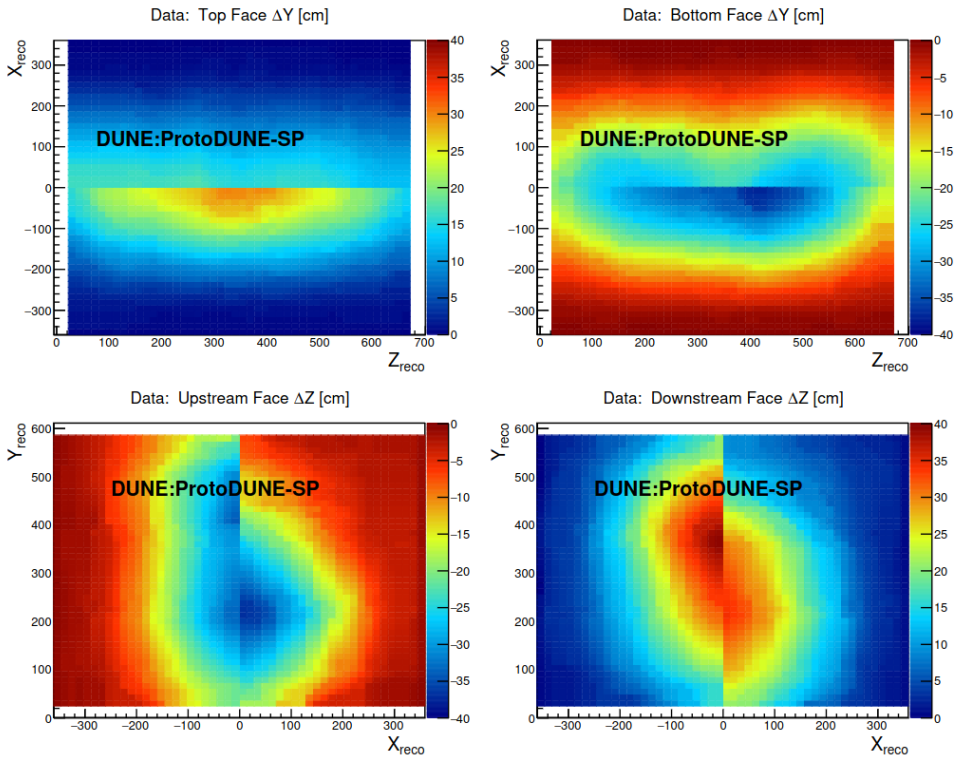

Figure 3.18: Data distortions normal to the top detector face (upper left), bottom detector face (upper right), upstream detector face (bottom left) and downstream detector face (bottom right) for data. Colour scale represents the distortion in cm. Image from [110].

3.8.2 Charge Attenuation

As previously commented in Section 3.3, electronegative impurities such as O_2, H_2O or N_2 can be attached to argon atoms and reduce the amount of electrons reaching the collection plane, which generates an attenuation of the collected charge. This effect, produced by a finite lifetime of drifting electrons in the TPC, has a larger impact the further away from the collection plane a track crosses the detector (because it takes more time for electrons to reach the anode and hence they are more likely to be trapped by impurities). Thus, hits' $\frac{dQ}{dx}$ has to be corrected by this effect. Although alternative methods using cathode-crossing cosmic muons were developed, the electron lifetime used to correct it was the one provided by the top PrM, which had an uncertainty of 1.8% when measuring the anode-cathode charge ratio [106, 110].

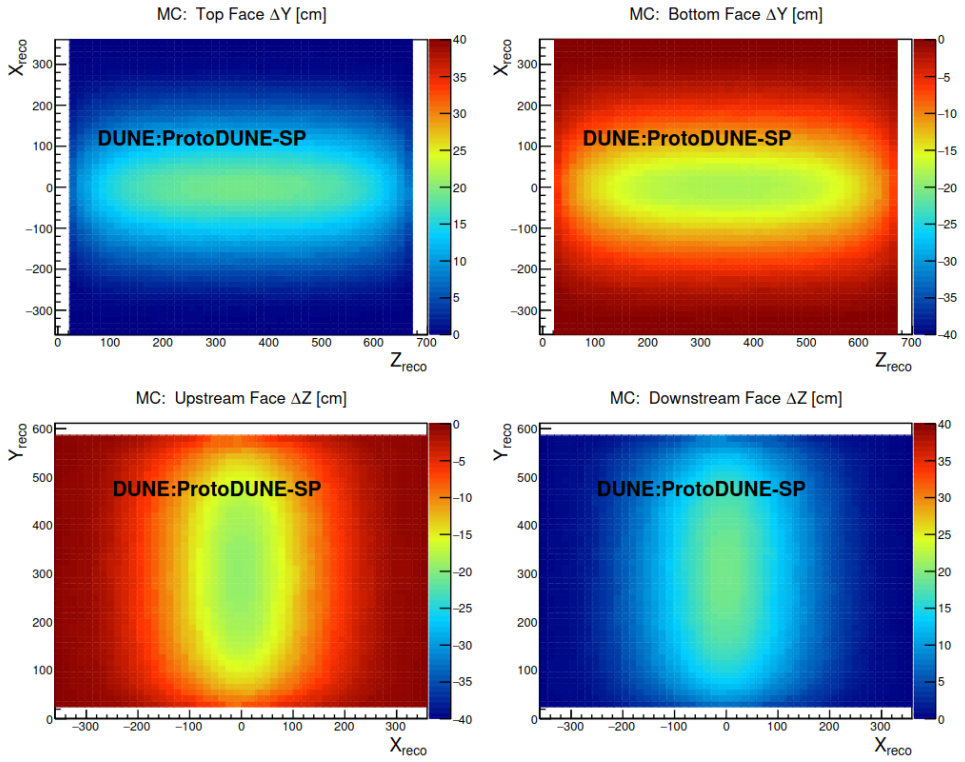

Figure 3.19: MC spatial distortions normal to the top detector face (upper left), bottom detector face (upper right), upstream detector face (bottom left) and downstream detector face (bottom right). Colour scale represents the distortion in cm. Image from [110].

3.8.3 Detector Non-Uniformities

The SCE and lifetime corrections described above are not perfect. The SCE affecting the detector is not truly known, in the same way as the distribution of the electron lifetime in the detector is not known and it is assumed to be the one measured by the top purity monitor. This may generate small local inefficiencies after these corrections are applied. Apart from this, there are other kind of circumstances that could affect the detector's response that have not been considered yet, like non-uniform wire response from nearby dead channels, the presence of electron diverters, or transversal and longitudinal diffusion. These effects can be corrected by homogenizing the detector response to a nominal value in a run by run basis using t_0-tagged cosmic rays, as it was done in MicroBooNE [157].

The homogenization process is done separately in the YZ plane and the x

axis since the aforementioned effects depend either on hits' y and z coordinates (dead wires, electron diverters and transversal diffusion) or x coordinate (longitudinal diffusion). Firstly, each TPC volume is divided in 5×5 cm^2 voxels in the YZ plane (which adds up to 16560 voxels per volume) and the measured $\frac{dQ}{dx}$ distribution on each voxel is compared to the measured distribution in its corresponding detector volume. This way, correction factors can be computed for each voxel

$$C_{YZ}(y,z) = \frac{MPV(dQ/dx)_{DV}}{MPV(dQ/dx)_{YZ}}, \tag{3.4}$$

where MPV means most probable value and DV refers to a given detector volume (beam side or non-beam side), in such a way that the $\frac{dQ}{dx}$ distribution is normalized in the YZ plane. Being this a relative correction, it is indifferent to use the MPV, the Median, the Mean or the average of the distribution. Secondly, the whole detector volume is divided in 5 cm wide slices in the X axis (adding up to 144 slices) and the charge distribution on each slice is compared to the charge distribution in the whole TPC (considering the just computed C_{YZ} calibration constants and the diffusion effects):

$$C_X(x) = \frac{MPV(dQ/dx)_{Run}}{MPV(dQ/dx)_X}, \tag{3.5}$$

where $MPV(dQ/dx)_{Run}$ refers to the MPV value of the charge deposition distribution after the YZ and diffusion corrections over the whole detector volume during a data taking run. In this manner, the detector response in the X axis has been normalized too. Finally, this response is normalized in a run-by-run basis, by rescaling every run to a nominal value

$$C_{Norm} = \frac{MPV(dQ/dx)_{Nominal}}{MPV(dQ/dx)_{Run}}. \tag{3.6}$$

With this, the detector response to the $\frac{dQ}{dx}$ has been completely standardized along the detector volume and the different runs [110].

3.8.4 Energy Calibration

The equation describing the modified box model presented above can be written now as

$$\frac{dE}{dx} = \frac{\rho\mathcal{E}(x,y,z)}{\beta'}\left[\exp\left(\frac{\beta' W_{ion}\frac{dQ}{dx}_{Calibrated}}{\rho\mathcal{E}(x,y,z)C_{cal}}\right) - \alpha\right], \tag{3.7}$$

in which the electric field position dependence has been taken into account, and where

$$\frac{dQ}{dx}_{Calibrated} = \frac{dQ}{dx}_{SCE+\tau} C_{YZ} C_X C_{Norm} \tag{3.8}$$

represents the calibrated $\frac{dQ}{dx}$ of the hits accounting for SCE, electron lifetime and detector non-uniformities. The absolute energy scale is then given by the ADC calibration constant, C_{cal}, which is computed by fitting the obtained $\frac{dE}{dx}$ distribution to the theoretical $\frac{dE}{dx}$ distribution predicted by the Landau-Vavilov theory [27] for a sample of stopping cosmic muons in the minimum ionising region. Since MC simulation considers the same effects presented here, MC samples are corrected following the same procedure. With this, the detector response has been fully calibrated and the calorimetry information can be used for the different analysis.

3.9 ProtoDUNE-SP Performance Summary

ProtoDUNE-SP was successfully installed, commissioned and exposed to a charged particle beam during 2018. Subsequently, it operated taking cosmic rays data until 2020, when its decommissioning started. During these years, different analysis have validated the single-phase LArTPC capabilities and the detector performance, whose most important conclusions can be found in [106,110]. Here, a brief summary is presented.

From the operational point of view, the HV system provided an electric field in the TPC active volume of 500 V/cm during more than 99.5% of the data taking periods with beam and cosmic rays. The cryogenic system and the instrumentation granted a detailed monitoring of the LAr conditions, especially the electron lifetime. The 3 ms DUNE's requirement was achieved some weeks after the purification process started. Concretely, during the last day of beam data-taking, the electron lifetime was measured to be 89 ± 22 ms. This value can be transformed to ppt oxygen equivalent, 3.4 ± 0.7, a much lower value than DUNE's requirement of 100 ppt O_2 equivalent.

Regarding the TPC and the CE, only 0.2% of the channels were unusable, five times less than the required value for DUNE's FD; and an outstanding signal-to-noise ratio of 40.3 was obtained for the collection wires. This allowed to demonstrate the PID capabilities of the SP LArTPC technology with muons, protons, pions and electrons, with a similar resolution that the one used in DUNE's sensitivity studies. In Chapter 5, this will be also demonstrated for kaons.

With respect to the PDS, the ARAPUCA concept presented the best performance among the three proposed technologies, with a good linearity within the number of detected photons and the momentum of the incoming particles, and a light-yield four times larger than what is requested by DUNE. Thus, it was selected as baseline for DUNE's PDS, as mentioned in the previous chapter.

This outstanding performance presented by the SP LArTPC reinforced the original DUNE's plan for the first FD module to be SP.

Finally, the beam data taken is currently being used to develop several analysis of interest for DUNE's physics programme. These include argon-hadron cross-sections, which are necessary to reduce the systematic uncertainty of models predicting final states particles; recombination, diffusion and lifetime characterizations; or particle identification strategies, among others.

4 SiPM Characterization for DUNE's Far Detector

Light thinks it travels faster than anything but it is wrong. No matter how fast light travels it finds the darkness has always got there first, and is waiting for it.

— Terry Pratchett, *Reaper Man*

From the different photon detection technologies tested at ProtoDUNE-SP, the X-ARAPUCA was the best performing one [106,110], and hence the one selected to be used in DUNE's far detector [73]. X-ARAPUCA modules are designed to shift the deep UV light resultant of LAr scintillation into visible light that can be detected by SiPMs. After this decision was made, different R&D lines started to explore the optimization of this technology before the starting of the FD installation. Different studies were done (and are currently being done) regarding the geometry of the modules, the wavelength-shifting material, the dichroic filters, or the SiPM model. Particularly interesting were the last ones, in which I was involved, and to which this chapter is partially dedicated.

After all these studies were relatively concluded, a standardized X-ARAPUCA module was defined to be used in FD1 [83]. However, before their final installation in South Dakota, these modules must be tested in ProtoDUNE-HD, the second phase of ProtoDUNE-SP, meant to be a 'module 0' of FD1. ProtoDUNE-HD installation took from April to December of 2022. I spent that time at CERN participating and coordinating the installation of the X-ARAPUCA modules.

This chapter is organized as follows: a detailed explanation of SiPMs is presented in Section 4.1; the down-selection procedure developed by DUNE to select the best performing SiPM model is described is Section 4.2; the experimental set-up and the different measurements carried out at IFIC are reviewed in Sections 4.3 and 4.4 respectively; the results obtained at IFIC during the down-selection are detailed in Section 4.5; finally, the activities carried out during the ProtoDUNE-HD installation at CERN are briefly commented is Section 4.6.

4.1 Silicon Photomultipliers

SiPMs are photon-counting devices [158, 159], based on semiconductor materials with a p-n junction [96]. They have been developed to achieve a high gain and photon detection efficiency, similar to PMTs, but with a much reduced size and insensitivity to magnetic fields, as Avalanche Photodiodes (APD). They are indeed formed by multiple APDs operating in the so-called Geiger mode.

When an inverse voltage is applied to a p-n junction, a depletion area is formed (see Figure 4.1, left). Photons with higher energy than the band gap are absorbed in this region and generate charge carriers. There are two types of avalanche processes that the carriers can generate, depending mostly on the intensity of the electric field result of the applied voltage. For low electric fields, avalanche processes are created almost entirely by electrons and are one directional, which implies that they are self-quenched and limited by the thickness of the depletion area. On the other hand, when the electric field is high, both type of carriers participate in the avalanche processes making it to grow exponentially. The value of the voltage separating these two regimes is known as breakdown voltage. Below the breakdown voltage, the photodiodes behave linearly: the number of electrons released is directly proportional to the energy of the incident particle. On the contrary, if the breakdown voltage is exceeded, the APD starts to work in Geiger mode: the amount of charge carriers released (and hence the charge) in independent of the energy of the incident photon. Furthermore, even if two or more photons arrive to an APD simultaneously, it provides a single photoelectron signal.

As mentioned above, a SiPM is an array of several APDs connected in parallel to the same anode and cathode (see Figure 4.1, right). When all APDs work in Geiger mode, the SiPM becames a photon-counting device, whose signal is proportional to the number of fired APDs, and hence proportional to the number of incident photons. To ensure a Geiger mode operation, the photomultipliers contain a quenching mechanism which limits the current drawn by the diode and lowers the reverse voltage. This is obtained by connecting a quenching resistance in series with the APD, forming what is known as microcell or pixel. Each APD is formed by a layer of substrate, which is Silicon, and a window material, usually made of epoxy resin transparent to visible light.

Unlike other light detection systems, SiPMs have an amplification factor that depends exclusively on the p-n junction characteristics and the quenching structure. This provides the opportunity to study the configuration that best fits the experiment's requirements, ensuring that the response provided by the sensors is the one that best fits the expected photon flux.

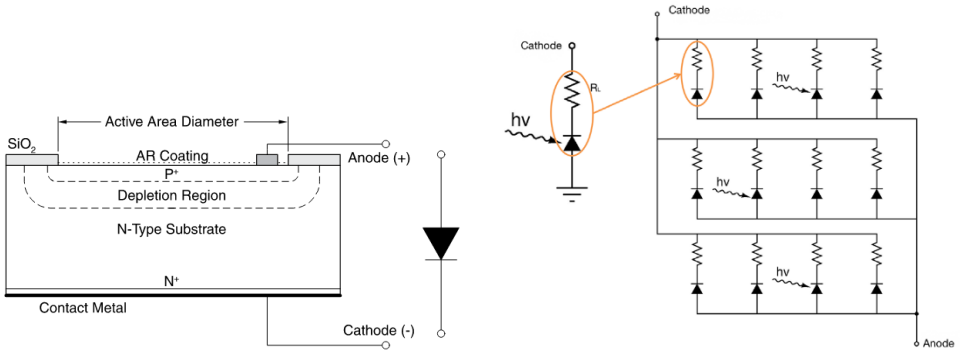

Figure 4.1: Left: schematic cross-section view of an APD. When there is incident photon in the photodiodes active area, with energy greater than the band gap energy, valence electrons are excited. They are accelerated in the depletion area towards the N-layer, generating a current flow. Image from [160]. Right: schematic view of the pixels forming an SiPM. Each of them has a quenching resistor. All of them share the same cathode and anode, thus the signal of the SiPM is the sum of the signals of every cell. Image from [161].

4.1.1 SiPMs Characteristics

The pulse shape of the detected signal gives information about the SiPM. The rise time is directly proportional to the total area of the device, whereas the recovery or fall time is given by the product of the quenching resistance of the microcells involved in the detection and its effective capacitance.

The sensitivity of the sensor, known as photon detection efficiency (PDE), is defined as the ratio between the number of detected photons and the number of incident photons. It is calculated as the product of the quantum efficiency, that is the probability that carriers are generated by light incident on a pixel; the fill factor, which is the ratio of active to inactive area of the SiPM; and the avalanche probability, that is the probability that carriers cause avalanche multiplication. Mathematically,

$$\text{PDE} = Q_{eff} \cdot F_{fill} \cdot P_{avalanche}\,. \tag{4.1}$$

However, the main characteristic of a photodiode is the gain, defined as the amount of electrons released when a photon is detected. This output charge is determined as the product of the photodiodes junction capacitance and the applied voltage, $Q = CV$. The boundaries of the depletion region act as plates of a capacitor and therefore we obtain a capacitance proportional to the active

area and inversely proportional to the width of the depletion area, $C = \frac{\epsilon_0 S}{d}$. Usually, a larger gain value provides a better signal-to-noise ratio (SNR).

The range of detected photons for which the photodetector provides a linear response defines its dynamic range. For SiPMs this range goes from a single photon up to incident photons on all of its microcells simultaneously. It is a magnitude that depends on the number of microcells and their recovery time.

In the photodiode, pulses are produced not only by photon-generated carriers but also by those that are thermally produced. This happens in semiconductors because there is a small band gap and valence electrons can gain sufficient energy when they are thermally excited to go to the conduction band. This is commonly known as a dark pulse. In Geiger mode, this dark pulses can generate avalanches, and thus signals indistinguishable from the ones produced by photons. This effect occurs randomly and it is usually defined as the ratio of pulses surpassing the half photoelectron level in absence of light. This is know as dark current rate (DCR).

In addition to this source of uncorrelated noise, there are two sources of correlated noise that need to be presented: cross-talk and after-pulses. The (optical) cross-talk (XT) phenomenon happens when a bremsstrahlung photon emitted during an avalanche of an APD is detected by a neighbouring cell, creating another avalanche. It happens instantaneously and consequently a single photon generates pulses of 2 or more photons. It is a phenomenon that has almost no dependence on temperature, however it does increase as the bias voltage is increased, and it also depends on the distance between microcells and its size. The after-pulse (AP) may happen during the avalanche multiplication process: the generated carriers can be trapped by lattice imperfections. When they are released they are multiplied and we observe them as a secondary pulse following the first one. It also depends on the applied voltage and the size of the cells. These two kinds of fake signals cannot happen on their own, they need the existence of a primary real pulse to happen, this is why they are called correlated noise [158, 159].

As it can be noticed, the different SiPMs parameters are somehow interdependent. Larger cell pitches guarantee larger gains and PDE, but lower dynamic ranges and more probability of correlated noise. On the contrary, smaller pitches provide a larger dynamic range and lower probability of correlated noise, whereas the gain is lower. Because of that, a compromise needs to be found so that the characteristics of the SiPM are the ones that best fit each experiment.

Table 4.1: SiPMs requirements at operation voltage

Parameter	Value
PDE	$> 35\%$
Gain	2-8·10^6
DCR	< 200 mHz/mm^2
XT	$< 35\%$
AP	$< 5\%$
T(V_B)	< 200 mV

4.2 Down-selection

The down-selection of the appropriate SiPM model is based on a set of high level physics requirements, that translate on requirements for the photosensors. Those are listed below:

- The SiPM quantum efficiency –or photon detection efficiency, PDE– in the photon energy range emitted by compatible wavelength-shifters (peak wavelength 430 nm) should be at least as good as commercial devices (35% at 430 nm).
- The SiPM characteristics (along with the associated front-end electronics) should allow single photon identification. This also applies to the full optical channels (X-ARAPUCA or any of its variants).
- For a given threshold, the dark count rate of the SiPM at LAr temperature should not dominate that from radiological decays in the noble liquid.
- SiPMs must perform adequately during long time (years) in cryogenic conditions.
- SiPMs must have mechanical compliance with the X-ARAPUCA model.

These translate into specific low level requirements listed in Table 4.1. Additional specifications that are not relevant for the discussion in this chapter include the dynamic range (since this is evaluated as a feature of the X-ARAPUCA module and not of the single SiPM), the size of the sensors (6×6 mm^2), the packaging and the cell pitch.

In order to find the sensor that better fulfilled these requirements, the DUNE's photosensor working group contacted two different manufacturers, Hamamatsu

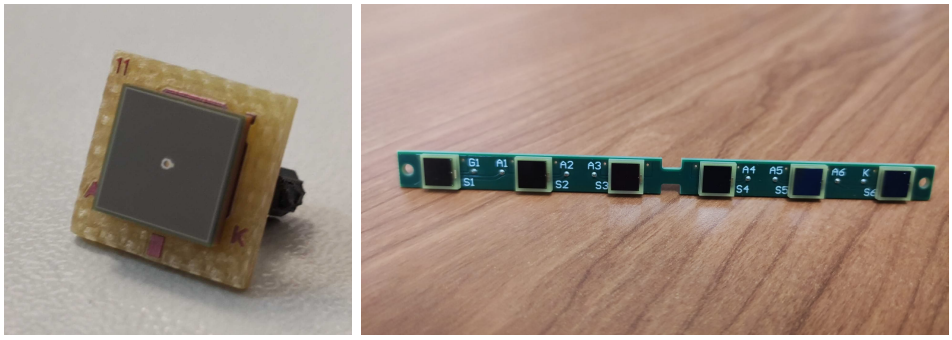

Figure 4.2: Left: individual SiPM. Right: six-SiPM board.

Photonics (HPK) and Fondazione Bruno Kessler (FBK), which produced custom SiPM models. These were thoroughly tested in different institutions of the collaboration during the down-selection procedure.

First, vendors provided small samples of 25 SiPMs per model (the 25-batch), and after a preliminary round of measurements, they provided samples of 250 SiPMs for a massive characterization (the 250-batch). In the first case, sensors were delivered to the institutions individually (see Figure 4.2, left), while in the second case sensors were grouped in arrays of six (see Figure 4.2, right), disposition in which they are installed in the X-ARAPUCA Supercells. In the following sections, a detailed analysis of the SiPM characterization done at IFIC is presented.

4.2.1 SiPM Models

Four different models were developed by HPK, whose characteristics are summarized in Table 4.2. Two main features were modified: cell pitch and quenching resistance. Larger cell pitch provides larger PDE, gain and signal-to-noise ratio (SNR), at the expense of larger correlated noise. Larger quenching resistance provides longer pulses and it is expected to reduce dark current and correlated-noise, but at the same time it should provide lower values of SNR because the time window to measure the charge of the pulse is longer too. Initially, 16 units of the 25-batch were received At IFIC: 4 units of LQR50µm, 6 units of LQR75µm and 6 units of HQR50µm. An average of their first photoelectron signal is presented in Figure 4.3. As it can be seen, the shape of the signal strongly depends on the SiPM model. Later, 20 6-SiPM arrays (120 sensors in total) of the LQR50µm model were received.

In the case of FBK, two different models were prepared (see Table 4.3). The first of them had a cell pitch of 30 µm and the trench separating the pixels was

Table 4.2: HPK SiPMs models and their main characteristics.

Model	Cell Pitch (µm)	R_Q (kΩ) at LN_2
HPK S13360-9932 50µm-LQR	50	280
HPK S13360-9933 50µm-HQR	50	660
HPK S13360-9934 75µm-LQR	75	280
HPK S13360-9935 75µm-HQR	75	660

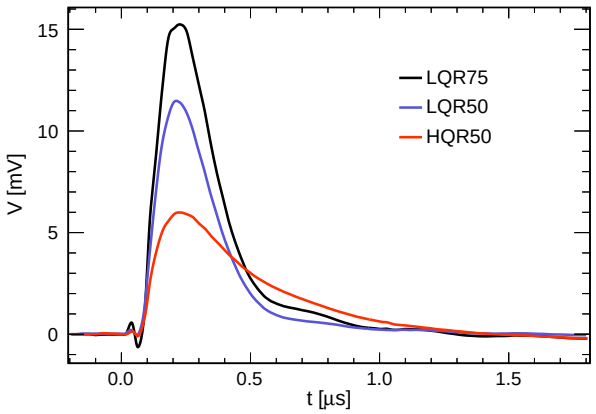

Figure 4.3: Average single photoelectron signal for each SiPM model tested at IFIC at 50% PDE.

Table 4.3: FBK SiPMs models and their main characteristics.

Model	Cell Pitch (µm)	R_Q (kΩ) at LN_2
Single Trench	30	70
Triple Trench	50	230

the commercial one, and was named as 'Standard Trench' or 'Single Trench' (ST) model. The second one had a larger pitch, of 50 µm, and the trench was thicker to decrease the cross-talk probability. This model was known as 'Triple Trench' (TT). 16 6-SiPM arrays of the ST model and 12 arrays of the TT model were tested at IFIC.

4.2.2 Validation procedure

In order to ensure that the different models fulfilled DUNE specifications, the following procedure was followed:

1. Measurement at room temperature of the breakdown voltage and the quenching resistance and validation with vendor data.
2. Measurement in LN_2 of the breakdown voltage and the quenching resistance.
3. Gain and SNR measurement in LN_2.
4. Correlated noise measurement (DCR, XT and AP) in LN_2.
5. Exposure to thermal cycles.
6. Measurement in LN_2 of the breakdown voltage and the quenching resistance.
7. Gain and SNR measurement in LN_2.
8. Correlated noise measurement (DCR, XT and AP) in LN_2.
9. Measurement at room temperature of the breakdown voltage and the quenching resistance.

A model is considered to be valid if its different parameters are within DUNE specifications and it does not show any significant difference after the thermal cycles. This process was strictly followed for the first batch of SiPMs, and since no discrepancies were found after the thermal cycles, steps 3 and 4 were skipped for the second batch in order to speed up the process. Gain and correlated noise were characterized at three different over-voltages (OV), corresponding to 40%, 45% and 50% PDE. The dependence OV-PDE was provided by the vendor. The OV is known as the voltage above the breakdown voltage at which a SiPM is biased. In the case of HPK, for the 50 µm cell pitch models these PDE values correspond to +3, +4 and +5 OV, whereas for the 75 µm cell pitch models they are +2, +2.5 and +3 OV. In the case of FBK, the ST model had to be characterized at +4, +5 and +6 OV, and the TT model at +3.5, +4.5 and +7 OV.

4.3 Experimental set-up

The experimental set-up had to fulfil some specifications so the measurements described above could be performed in adequate conditions. First, the system had to perform properly in cryogenic conditions (LN_2 temperature). Second, the

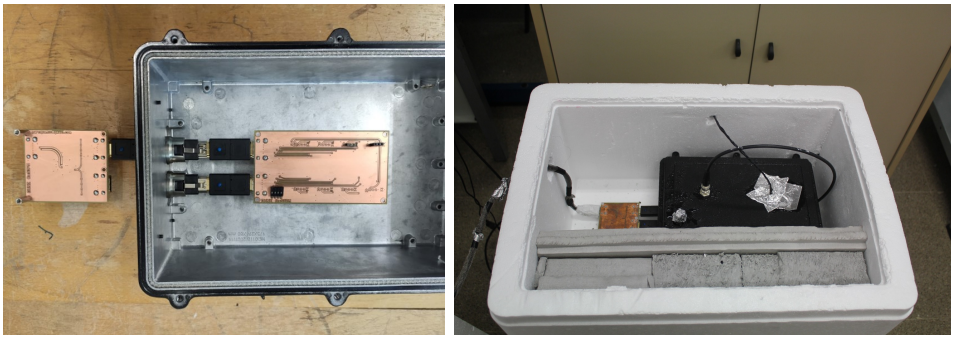

Figure 4.4: Left: black box hosting the electronic boards. Originally both boards should have been placed inside the box, but a problem with the feed-throughs made it necessary to locate the amplifier outside the box. Right: black box inside the cork box, filled with LN_2 and ready to take measurements. An optical fibre was inserted through the cork box and the black box to illuminate the SiPMs when necessary.

electronic noise level had to be low enough to enable the single p.e. characterization and the correlated noise measurements. Third, it had to be light tight, so that the DCR measurement was not biased. Last, due to the tight schedule for the down-selection, the set-up had to be easily manageable to speed up the cool down and warm up processes.

From the mechanical point of view, the system consisted of a stainless steel box (black box) of $12\times16\times29$ cm^3 with two HDMI feed-throughs inside which the SiPMs and the necessary electronic boards were placed (see Figure 4.4, left). It provided light-tightness and electronic shielding, acting as a Faraday cage. The black box was placed inside a larger polystyrene box, which played the role of a dewar (see Figure 4.4, right). Although it did not provide the thermal insulation of a real dewar, it was much more versatile and practical to perform fast thermal cycles. The electronics components of the system were: a power supply (Rhode & Schwarz HPM4040) was used to bias the electronic boards, a picoammeter Keithley 6487 was used to bias the SiPMs and measure their current when necessary, a pulse generator Agilent 33250A was used to fire an LED whose light was inserted through an optical fibre inside the black box, and a source current and a RTD monitored the temperature. Finally, an oscilloscope Tektronix MSO44 was used to digitalize the output signals of the sensors, which would be analysed offline afterwards.

The electronics evolved from one batch to another. For the first batch, single SiPMs were received and conditioned to be tested at IFIC. Two custom electronic boards were designed too. One of them, whose schematic can be seen in Figure

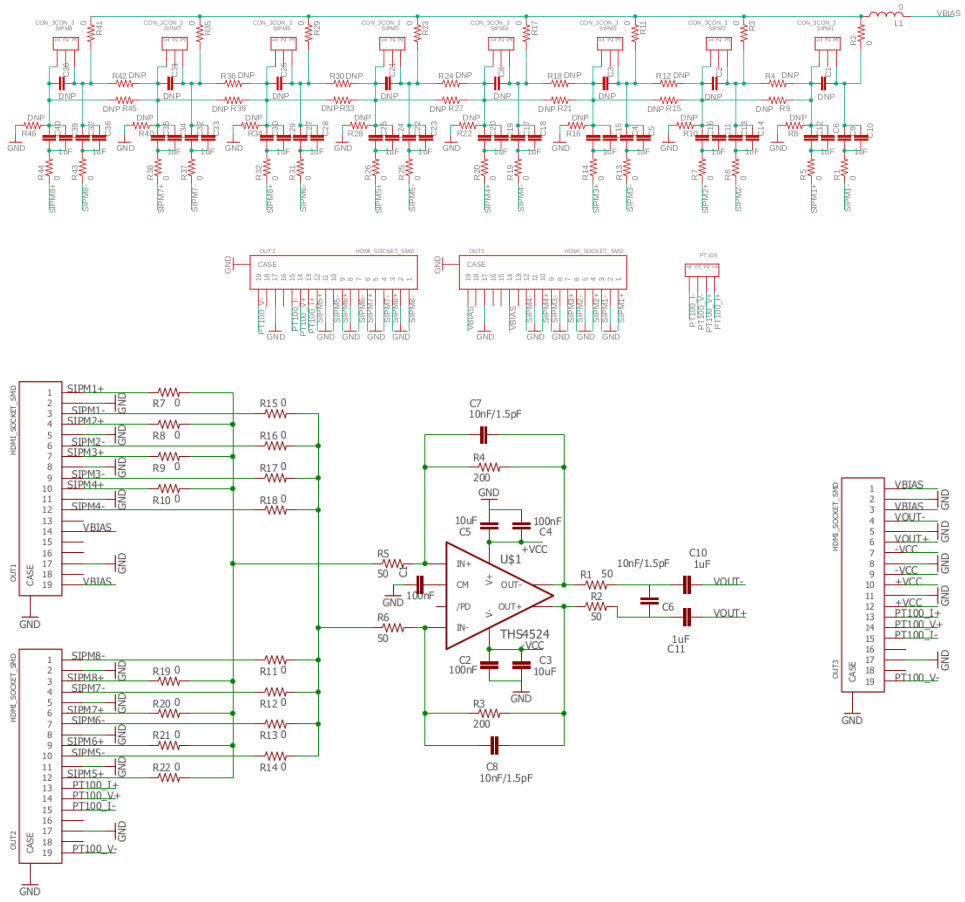

Figure 4.5: Top: SiPM hosting board used during the 25-batch tests. Although it could fit up to eight SiPMs, only one channel was used during the down-selection. Bottom: differential amplifier to which the first board was connected.

4.5-top, could hold up to eight SiPMs and an RTD to measure temperature. It was designed to perform ganging tests, as it could be possible to add resistances and capacitors between SiPMs and ground to simulate active and passive ganging. The other one, whose schematic can be seen in Figure 4.5-bottom, consisted of a trans-impedance differential amplifier that could enlarge the signal from the eight SiPMs of the first board. Even though the amplifier could work inside and outside LN_2, it was always immersed. The voltage bias for the boards and the SiPMs was provided through the amplification board.

For the second batch, SiPMs were received in arrays of six, format in which they are installed in the X-ARAPUCAS. In this case, the electronics used were the same among all laboratories, and it consisted of a first cold stage hosting

six single-ended amplifiers [162], one per SiPM, and a second warm differential amplification stage.

4.4 Measurements

4.4.1 Breakdown Voltage and Quenching Resistance

Breakdown voltage and quenching resistance are obtained from the so-called Intensity-Voltage (IV) curves. For the breakdown voltage measurement, the SiPM is connected in reverse bias mode and the outcoming current is measured as a function of the applied bias voltage. This was done using the Keithley and a dedicated LabView programme that sequentially measured the current while varying the voltages in steps of 1 mV. The breakdown voltage is defined as the point in which the sensor stops working in linear mode and starts working in Geiger mode, and it is computed as the maximum of the variation rate of the current, defined as

$$\frac{1}{I}\frac{dI}{dV}. \tag{4.2}$$

An example of this measurement can be seen in Figure 4.6.

The quenching resistance is measured by connecting the sensor in forward mode, thus the diode resistance is negligible compared with the one in series of the quenching resistor. The output current is measured with the Keithley as a function of the bias voltage, as it was done before. The slope of the curve (see Figure 4.7) is the inverse of the resistance. Considering the number of cells of the SiPM (which are connected in parallel) one can compute the quenching resistance of a single cell. In order to compare the measured quenching resistance with the information provided by the vendor, the fit has to be done in the range 5.2-6-0 mA.

4.4.2 Gain

The gain is defined as the number of electrons a cell releases each time it is activated by a photon. In Geiger mode, it is independent of the energy and the trajectory of the photon, and the number of electrons depends exclusively on the applied bias voltage. In a controlled set-up with a light source, it can be easily measured by recording the waveforms generated by the sensor each time light is emitted by the source (see Figure 4.8 for an example). The waveforms (that generally represent voltage vs time) can be integrated to obtain their associated

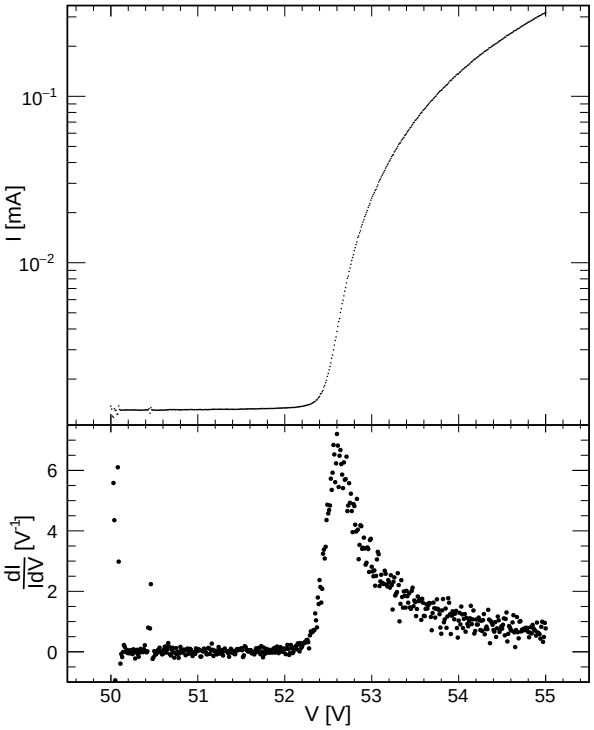

Figure 4.6: IV curve with reverse bias. Bottom plot shows variation rate of the current.

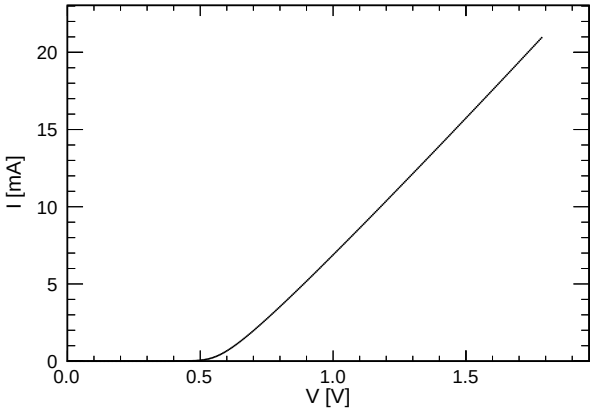

Figure 4.7: IV curve with forward bias at room temperature of a LQR75 SiPM.

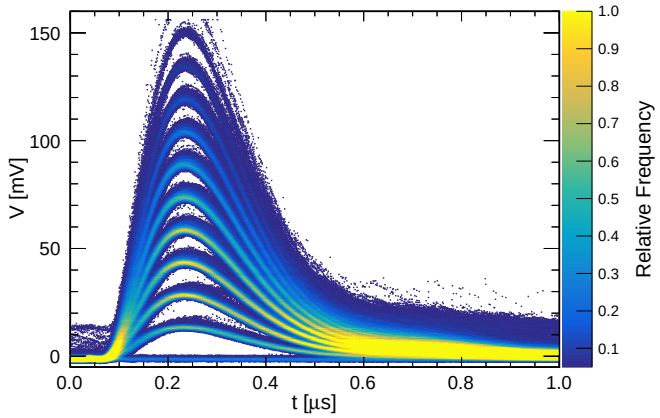

Figure 4.8: Recorded waveforms with the light source activated. It can be seen the nice performance offered by the electronic boards developed at IFIC, with very clean and fast signals with single photoelectron sensitivity and almost no underflow.

total charge. In order to reduce the fluctuations from waveform to waveform, a simple offline analysis can be done. First, the time region preceding the pulse –the baseline– is set to zero, so that the integration does not change from positive to negative regions. Second, the integration is done up to the point in which the baseline is recovered, or alternatively up to a predefined time value. This value was set to 1.5 µs for the 25-batch and 5 µs for the 250-batch. 20000 waveforms were recorded per measurement. If the charge is represented in a histogram (see Figure 4.9), a distribution with several peaks can be observed (provided that the SNR of the system is sufficiently large). The first peak corresponds to the pedestal, which is the integral of the baseline of the system, obtained by integrating waveforms with no optical pulse. The successive peaks correspond to one photoelectron (p.e.) signal, two p.e. signal, and so on.

This distribution can be fitted to a sum of Gaussian distributions:

$$C(Q) = \sum_{i=0}^{N} A_i G(Q; \mu_i, \sigma_i)\,, \tag{4.3}$$

and the distance between any two consecutive peaks is considered to be the gain. Ideally, the gain should be independent of the number of detected p.e., meaning that the distance between any two consecutive peaks should be the same. However, this also depends on the front end electronics, the amplifier, etc. and usually the gain linearity is lost for a large number of detected p.e.'s.

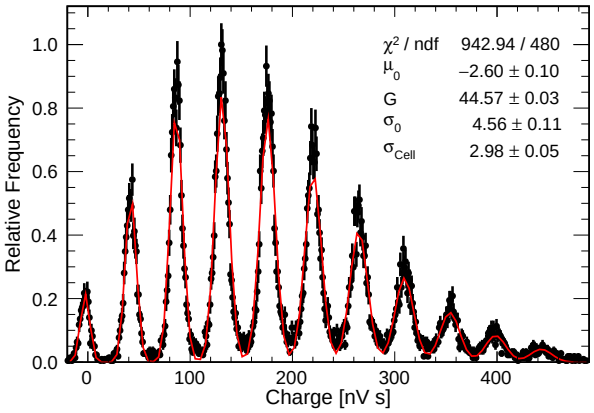

Figure 4.9: Charge histogram from a LQR 75 µm SiPM at 50% PDE. The first peak corresponds to the pedestal (the width of the baseline in the absence of signals), and the subsequent peaks to a single photoelectron, two photoelectrons, and so on. The red line represents a fit to the model described by the equations 4.5 and 4.5.

The SNR is computed from the same measurement, and it is defined as the ratio between the gain, G and the width of the pedestal, σ_0:

$$SNR = \frac{G}{\sigma_0}\,. \tag{4.4}$$

The sum of Gaussian peaks can be re-parametrized to reduce the number of free parameters in the following way: first, the mean value of the i-th p.e. peak can be expressed as the mean value of the pedestal plus i times the gain,

$$\mu_i = \mu_0 + iG; \tag{4.5}$$

second, the width of each peak can be expressed as

$$\sigma_i = \sqrt{\sigma_0^2 + i\sigma_{cell}^2}\,, \tag{4.6}$$

where σ_0 is the width of the pedestal and σ_{cell} is the spread of the gain associated to the random fluctuations between cells when fired. In this way, the free parameters of the fit are reduced to μ_0, G, σ_0, σ_{cell} and the different normalization constants A_i. An example of the fit result can be seen in Figure 4.9. Two more definitions of SNR can be derived from this parametrization, which are

$$SNR_c = \frac{G}{\sigma_{cell}} \tag{4.7}$$

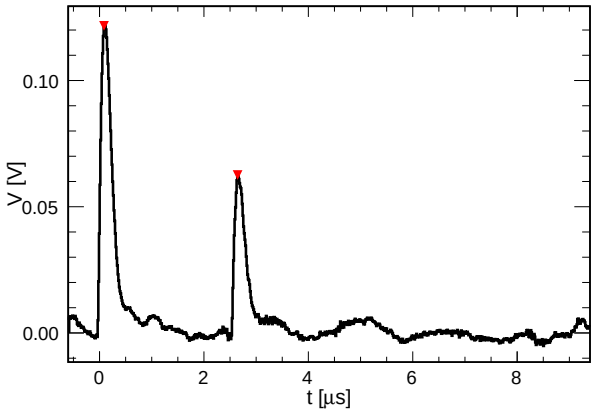

Figure 4.10: AP candidate. The identification of the peaks was done with the ROOT library TSpectrum.

and

$$SNR_F = \frac{G}{\sqrt{\sigma_0^2 + \sigma_{cell}^2}}\,. \tag{4.8}$$

4.4.3 Uncorrelated and Correlated Noise

The characterization of the DCR, XT and AP probabilities can be done in a single measurement. In absence of light, waveforms surpassing the threshold level of half p.e. are recorded. The total number of recorded waveforms divided by the time of the measurement is considered to be the DCR. At the same time, if the DCR is sufficiently low, it can be assumed that any signal coming from the SiPM corresponding to more than a single p.e. has been generated by optical cross-talk, so it can be estimated as the ratio of events above one and a half p.e. divided by the total number of events. Finally, under the same assumption, if two events happen very close in time ($\sim$ µs), it can be considered that the second event is an after-pulse of the first one; thus, the AP probability can be estimated as the number of events whose delay time with respect to the previous event is below a given temporal threshold divided by the total number of events. This temporal threshold can be chosen arbitrarily depending on the needs of the experiment, and for the scope of DUNE it was decided to be set to 5 µs. An example of an AP event can be seen in Figure 4.10.

The above definitions are summarized in Equations 4.9,4.10,4.11.

$$DCR = \frac{\#Events}{T}\,, \tag{4.9}$$

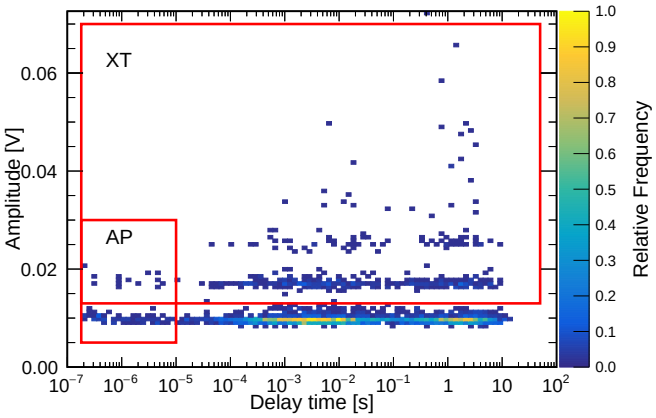

Figure 4.11: Correlated plot distribution. The AP events are the ones on the left box, the XT candidates the ones in the big box, and all of them contribute to the DCR.

$$XT = \frac{\#Events(> 1.5pe)}{\#Events}\,, \tag{4.10}$$

$$AP = \frac{\#Events(\Delta t < 5\mu s)}{\#Events}\,. \tag{4.11}$$

As in the case of the gain, waveforms are recorded and analysed offline. In this way, the waveforms triggered by electronic noise can be removed. The identification of the peaks was done using the ROOT library TSpectrum. In Figure 4.11 the result of one of these measurements is shown. The amplitude of each peak is represented against the delay time with respect to the previous one. The events with a very short delay time (the ones in the left rectangle) are the ones contributing to AP. The ones above the one and a half photoelectron level (the ones in the big rectangle) are the ones contributing to the XT probability. All of them contribute to the DCR. In order to have significant results and to avoid statistical fluctuations, waveforms were recorded during 40 minutes or up to 4000 waveforms.

One of the very first thing noticed when performing these measurements was that, instead of following a clear correlation with the bias voltage, DCR apparently followed no trend, no matter the SiPM model (see Figure 4.12-left). A closer look at the delay time between events (see Figure 4.12-right) revealed that DCR had two different components: one corresponding to the standard DCR (right peak of the distribution) and another one corresponding to the so-called 'burst' phenomena (left peak of the distribution). Bursts were observed to

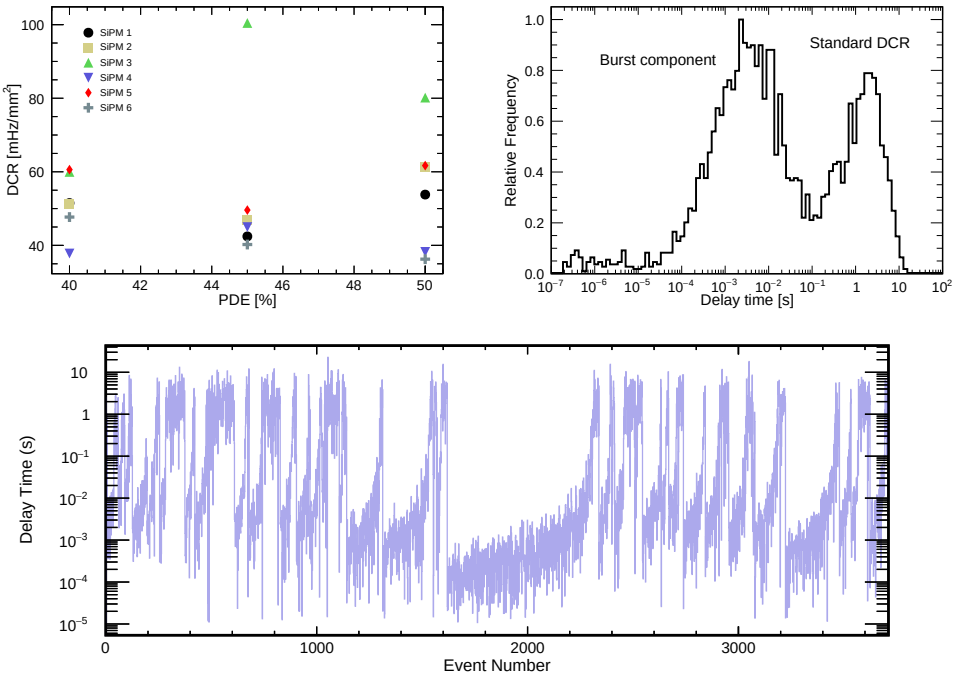

Figure 4.12: Top-left: DCR measured for the six LQR 75µm SiPMs. No clear trend with the PDE was observed for any of them. Top-right: Delay time distribution for a correlated noise measurement. Bottom: delay time of each event with respect to the previous event. Valleys are associated to the so-called burst phenomena.

be very large optical pulses, of the order of hundreds of p.e.'s, that were followed by trains of single p.e. pulses separated by ms. This can be appreciated in Figure 4.12-bottom, in which the delay time of each event is presented in a logarithmic scale. We can distinguish 'mountains' (consecutive uncorrelated dark events with a time separation of the order of seconds) and 'valleys' (trains of events with a separation of ms, or 'bursts').

This phenomenon was finally attributed to cosmic rays. Since this effect will be highly suppressed in DUNE's FD, only the standard DCR contribution needed to be characterized. Therefore, a fit was needed, either in the delay time plot, or its inverse (which is directly the rate) (see Figure 4.13). In the case of the fit to the rate distribution, a Landau function with a constant was used to identified the most probable value of the rate.

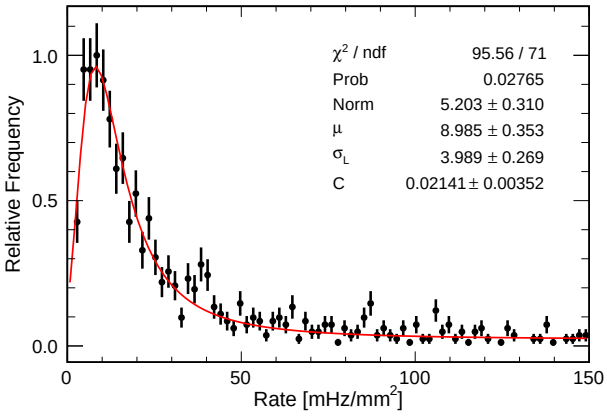

Figure 4.13: Rate distribution (inverse of the delay time) fitted to a Landau distribution plus a constant. The peak corresponding to the burst contribution does not appear because of the axis range.

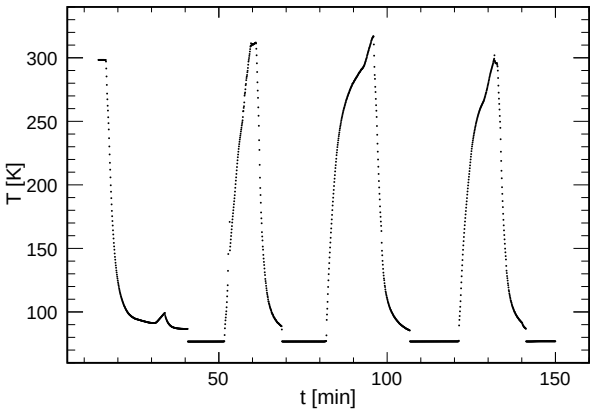

Figure 4.14: Temperature profile during some cryogenic cycles.

4.4.4 Cryogenic Cycles

The resistance to cryogenic conditions was tested by exposing the SiPMs to several controlled cryogenic cycles. The sensors were slowly cooled down from room temperature to LN_2, first by being exposed to nitrogen gas, and when temperature was close to LN_2 temperature, being completely immersed. After a period of ten minutes, sensors were brought back to room temperature by extracting them from the liquid phase and warming up slowly in the gas phase. This cycle had to be repeated 20 times. In Figure 4.14 the temperature profile during few cycles can be observed.

4.5 Results

In this section the results of the characterization done at IFIC are presented. For the 25-batch SiPMs from HPK, only gain, SNR, and correlated and uncorrelated noise will be reviewed, since it is interesting to see the measurements before and after the thermal cycles for different models. The results of the IV curves will be presented only for the SiPMs of the 250-batch, since the available statistics were much larger.

4.5.1 25-batch HPK

Figure 4.15 shows the results of the characterization of the HPK single SiPMs after the LN_2 thermal cycles. In Table 4.4 these results along with the measurements performed before the cycles are shown. In general, all models fulfilled DUNE's specifications. All of them had a DCR much smaller than 200 mHz/mm^2 (even considering bursts), a XT below 35% and an AP below 5% for all OVs. Moreover, none of the SiPMs showed a particular deviation after the thermal cycles.

Particularizing, it can be observed in the plots how the larger pitch model, LQR75µm, presents a much higher gain and SNR for the same PDE than the other models, without a significant increase of DCR or correlated noise. For the 50 µm models, the LQR50µm presented a slightly larger SNR value due to the shorter waveforms. On the other hand, the HQR model presented a relative smaller XT probability. With this information, and considering DUNE's requirements, it is clear that the larger pitch model is preferable due to their significantly larger gain and SNR.

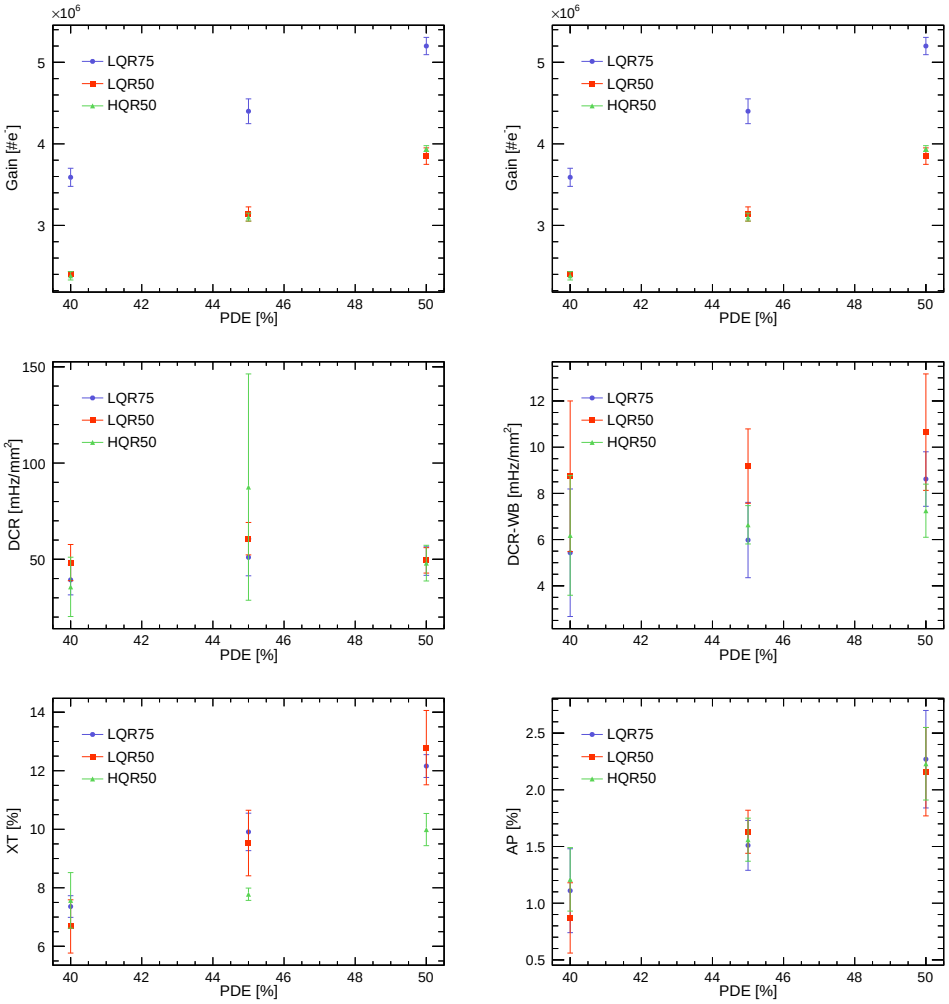

Figure 4.15: HPK characterization after the thermal cycles. Each point corresponds to the average of all SiPMs of each model, and the error corresponds to the standard deviation. Top left: gain. Top right: SNR_F. Mid left: total DCR. Mid right: DCR subtracting burst component. Bottom left: XT probability. Bottom right: AP probability.

Table 4.4: Results of the characterization of the HPK 25-batch SiPMs tested at IFIC previous to the LN_2 cycles (PB) and after the cycles. Each value is the average over all SiPMs of each model, and the error corresponds to the standard deviation.

Feature	PDE (%)	LQR75µm		LQR50µm		HQR50µm	
		PB	AB	PB	AB	PB	AB
Gain ($\#e^-$) $\times 10^6$	40	3.62 ± 0.06	3.59 ± 0.11	2.20 ± 0.03	2.40 ± 0.02	2.41 ± 0.06	3.38 ± 0.05
	45	4.40 ± 0.09	4.40 ± 0.15	3.15 ± 0.07	3.14 ± 0.09	3.14 ± 0.08	3.14 ± 0.05
	50	5.22 ± 0.11	5.20 ± 0.11	3.87 ± 0.08	3.85 ± 0.10	3.94 ± 0.09	3.94 ± 0.04
SNR	40	8.8 ± 0.7	7 ± 2	5.1 ± 0.8	4.9 ± 0.4	3.4 ± 0.8	4.3 ± 0.3
	45	10.4 ± 1.5	9 ± 2	6.6 ± 1.3	5.8 ± 0.6	5.0 ± 0.5	5.4 ± 0.4
	50	12.4 ± 0.4	11 ± 2	7.6 ± 1.3	6.9 ± 0.4	5.7 ± 0.6	6.5 ± 0.6
DCR (mmHz/mm^2)	40	50 ± 9	40 ± 8	56 ± 19	48 ± 9	70 ± 30	36 ± 15
	45	47 ± 5	51 ± 10	92 ± 14	61 ± 8	69 ± 17	90 ± 60
	50	52 ± 13	49 ± 7	70 ± 8	49 ± 7	46 ± 5	48 ± 9
DCR-WB (mmHz/mm^2)	40	6.2 ± 1.5	5 ± 3	7.6 ± 0.8	9 ± 3	6 ± 2	6 ± 3
	45	7.6 ± 1.6	6.0 ± 1.6	7.9 ± 1.7	9.2 ± 1.6	6.7 ± 0.3	6.6 ± 0.8
	50	10.0 ± 1.4	8.6 ± 1.1	8.0 ± 1.0	11 ± 3	9.0 ± 0.6	7.3 ± 1.1
XT (%)	40	8.0 ± 0.6	7.4 ± 0.4	6.5 ± 1.0	6.7 ± 0.9	6.8 ± 1.5	7.6 ± 1.0
	45	10.1 ± 0.5	9.9 ± 0.6	9.6 ± 1.1	9.5 ± 1.1	8.0 ± 1.3	7.8 ± 0.2
	50	12.5 ± 0.7	12.2 ± 0.4	12 ± 2	12.8 ± 1.3	10.4 ± 1.6	10.0 ± 0.6
AP (%)	40	1.0 ± 0.4	1.1 ± 0.4	0.84 ± 0.02	0.9 ± 0.3	1.3 ± 0.5	1.2 ± 0.3
	45	2.0 ± 0.4	1.5 ± 0.2	2.0 ± 0.8	1.6 ± 0.2	1.5 ± 0.2	1.6 ± 0.2
	50	2.3 ± 0.4	2.3 ± 0.4	2.0 ± 0.4	2.2 ± 0.4	2.1 ± 0.2	2.2 ± 0.3

4.5.2 250-batch HPK

As previously mentioned, from the 250-batch provided by HPK, the IFIC received 20 boards of six SiPMs. The breakdown voltage and the quenching resistance of these SiPMs were measured at room temperature—and in LN_2, before and after being exposed to 20 cryogenic cycles. In Figure 4.16-top, the comparison between the measurements done at room temperature and the information of the vendor is shown. As it can be observed, the breakdown voltage distributions are very similar in shape but they present a small shift. This is due to the different method used to compute the breakdown voltage: while in this work the maximum of the variation rate of the intensity vs voltage curve is used, HPK estimates the breakdown voltage from the gain vs voltage curve, extrapolating the voltage to the point of zero gain. On the other hand, in the quenching resistance comparison it can be seen how the distribution measured in Valencia is consistent with the single measurement given by the vendor. These compatible measurements were taken as a validation of the experimental set-ups of the different laboratories involved in the down-selection procedure.

Figure 4.16-bottom, shows the impact ot thermal cycles on the breakdown voltage and the quenching resistance. As it can be seen, for the breakdown voltage the differences are below 0.5%, while for the quenching resistance they are around 2% and homogeneously distributed among zero, which indicates that sensors were not changing their behaviour after the thermal cycles.

A subsample of 12 SiPMs was fully characterized after the cryogenic cycles, and in Table 4.5 the resulting measurements are shown. The results obtained for the 25-bath LQR50µm model after the thermal cycles are also presented so they can both be compared. It can be observed an increase of the measured gain, probably due to an improper calibration of one of the two set-ups. However, this is not relevant since all laboratories used the same electronic set-up for the 250-batch tests, not affecting the down-selection procedure. It can also be observed an increase in the SNR, which was expected since the set-up used to characterize the 250-batch SiPMs had two amplification stages[1]. What is more interesting to note is the systematic increase in the measurements of DCR without bursts and XT, and also in their respective associated errors. This effect, observed for all SiPM models and in all laboratories, is not yet understood.

[1] and SiPMs were plugged-in the cold amplifiers

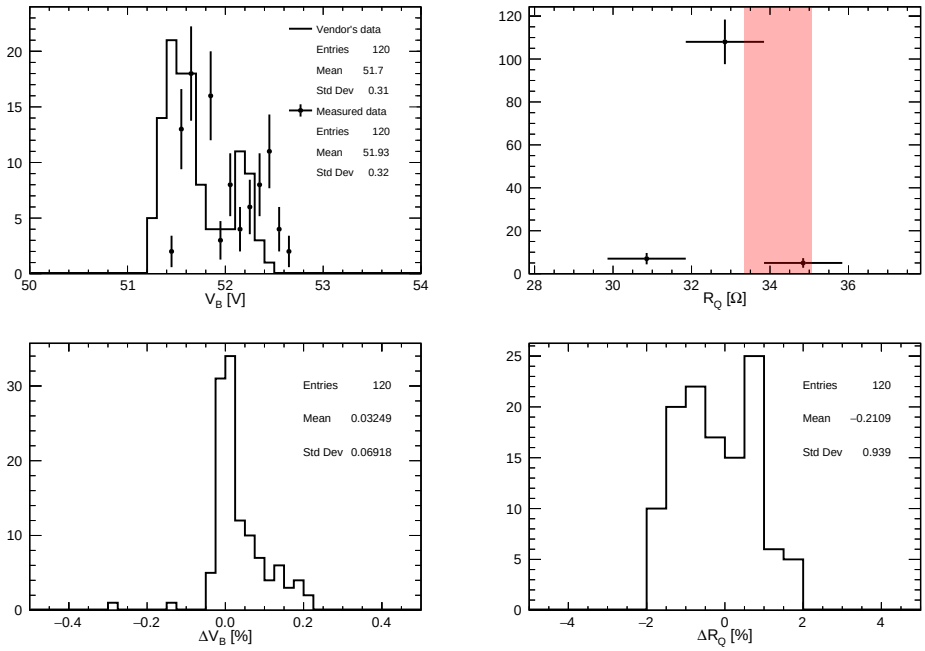

Figure 4.16: IV characterization for the 120 LQR50µm tested at IFIC. Top left: breakdown voltage at room temperature and comparison with vendor's information. Top right: quenching resistance at room temperature. The red band represents the measurement provided by the vendor with the associated uncertainty. Bottom left: variation of the breakdown voltage at LN_2 temperature before and after thermal cycles. Bottom right: variation for the quenching resistance at room temperature before and after thermal cycles. Bin width has been chosen to represent set-up sensitivity.

4.5.3 250-batch FBK

16 and 12 six-SiPMs boards were received at IFIC from the ST and TT models respectively. The IV measurement was done for all of them before and after the thermal cycles, and none of the sensors presented degradation, as shown in Figure 4.17. Data from the vendor was not available for a comparison.

After that, 6 SiPMs of each model were fully characterized, and their results are presented in Figure 4.18 and Table 4.6. The results of the LQR50µm are also represented in these plots for reference. A substantially larger gain and SNR for the TT model can be observed with respect to the ST model, thanks to its larger pitch. DCR and XT are similar for both models, while AP is clearly lower for the ST model. XT is particularly high for both of them, being close to the upper limit set for DUNE of 35% correlated noise probability. Then, it is clear

Table 4.5: Results of the characterization of the HPK 250-batch SiPMs tested at IFIC after the cycles. Each value is the average over all SiPMs of each model, and the error corresponds to the standard deviation. Measurements of the SiPMs of the same model of the 25-batch are also presented for comparison.

Feature	PDE (%)	LQR50µm 250-batch	LQR50µm 25-batch
Gain ($\#e^-$) $\times 10^6$	40	2.55 ± 0.05	2.40 ± 0.02
	45	3.28 ± 0.04	3.14 ± 0.09
	50	4.01 ± 0.06	3.85 ± 0.10
SNR	40	9.2 ± 1.7	4.9 ± 0.4
	45	10 ± 3	5.8 ± 0.6
	50	12 ± 3	6.9 ± 0.4
DCR (mmHz/mm^2)	40	51 ± 9	48 ± 9
	45	48 ± 5	61 ± 8
	50	58 ± 13	49 ± 7
DCR-WB (mmHz/mm^2)	40	17 ± 7	9 ± 3
	45	16 ± 6	9.2 ± 1.6
	50	18 ± 7	11 ± 3
XT (%)	40	10 ± 3	6.7 ± 0.9
	45	11 ± 3	9.5 ± 1.1
	50	13.7 ± 1.8	12.8 ± 1.3
AP (%)	40	1.1 ± 0.5	0.9 ± 0.3
	45	1.5 ± 0.3	1.6 ± 0.2
	50	2.0 ± 0.6	2.2 ± 0.4

that the TT presented the better performance for gain and SNR, but it did not show the reduction of correlated noise that was expected. It is also worth noting that despite having a larger gain than the HPK model, the TT does not present a significantly larger SNR, probably due to its larger capacitance.

4.5.4 Down-selection Result

The results presented above were used along the ones obtained in other institutes to decide what model would perform better in DUNE. A detailed explanation of these procedures can be found in [163, 164]. The tests carried out with the individual SiPMs demonstrated that all models fulfilled DUNE's requirements, including the thermal resistance. Then the 250-batch was requested, in which 250 sensors of each model were delivered and mounted in the 6-SiPMs boards

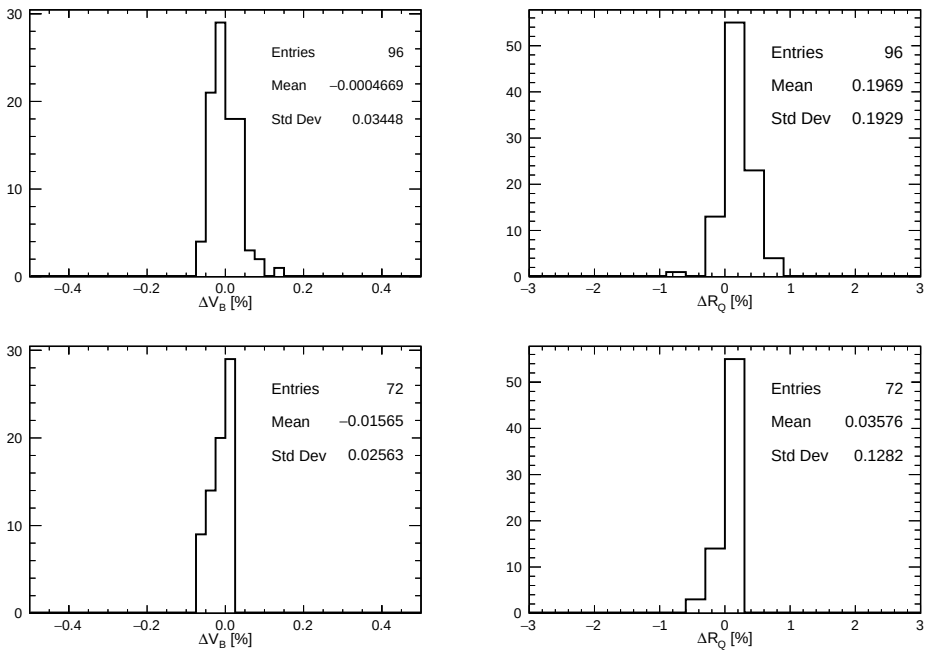

Figure 4.17: IV difference before and after thermal cycles for the FBK sensors tested at IFIC. Top left: breakdown voltage difference for ST sensors. Top right: quenching resistance difference for ST sensors. Bottom left: breakdown voltage difference for TT sensors. Top right: quenching resistance difference for TT sensors.

used in the X-ARAPUCA design. All of them passed the thermal tests. However, although the second batch of sensors was tested using the same electronic set-up in all laboratories, systematic differences were found between the results of the first and second batches. These differences were mainly observed in DCR and XT, being larger in the second batch than in the first, and more spread within each sensor model, no matter the laboratory or model. Despite this, all sensors were still fitting DUNE's specifications.

Regarding the HPK models, it was observed than the 75µm cell-pitch SiPMs presented a significant increase in the gain and the SNR for the same PDE than 50µm models, with no significant increase in dark current and correlated noise. Indeed, it was observed that the high quenching resistance models presented an overall correlated noise (XT+AP) smaller than the LQR ones, demonstrating with this the initial intention of the vendor. In view of these two results, the selected model from HPK was the HQR75µm [163]. This was also validated later by testing X-ARAPUCA Supercells formed by SiPMs of different models, and it was found that the ones using the selected model were the ones that performed

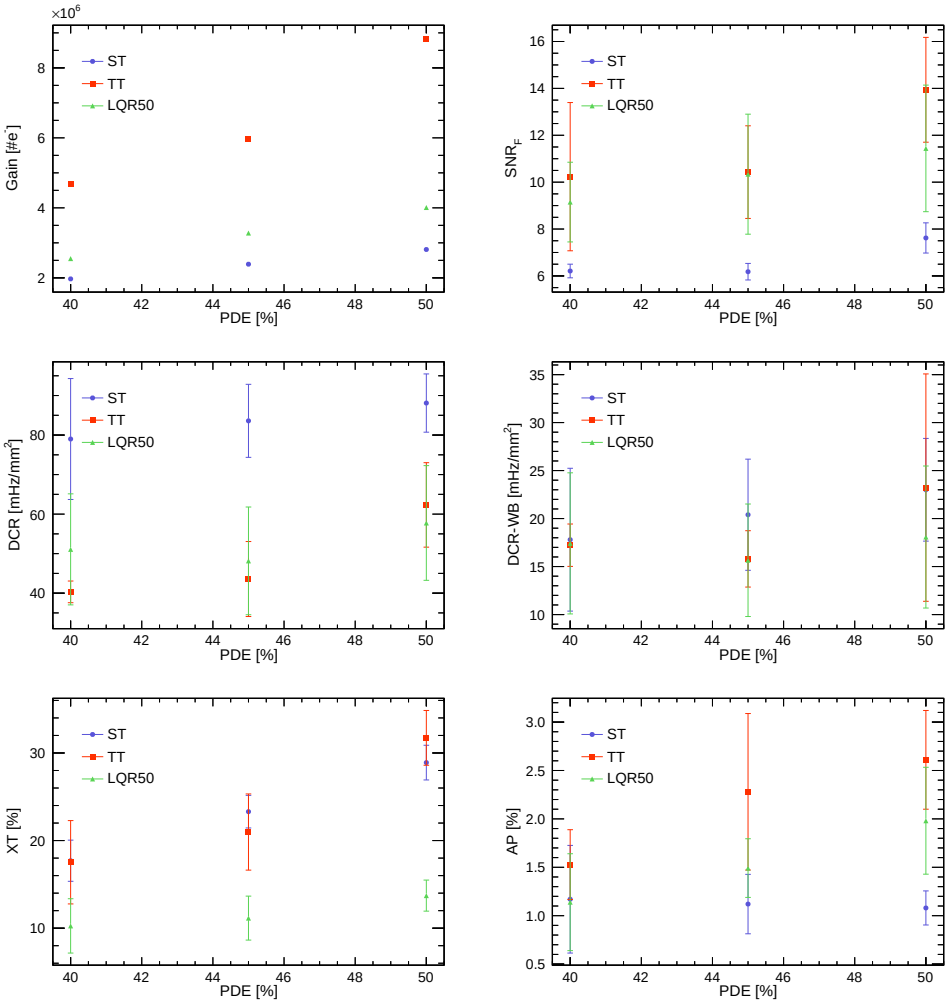

Figure 4.18: FBK characterization after the thermal cycles. LQR50µm results are also presented for reference. Each point corresponds to the average of all SiPMs of each model, and the error corresponds to the standard deviation. Top left: gain. Top right: SNR_F. Mid left: total DCR. Mid right: DCR subtracting burst component. Bottom left: XT probability. Bottom right: AP probability.

Table 4.6: Results of the characterization of the FBK 250-batch SiPMs tested at IFIC after the cycles. Each value is the average over all SiPMs of each model, and the error corresponds to the standard deviation.

Feature	PDE (%)	ST	TT
Gain ($\#e^-$) $\times 10^6$	40	1.97 ± 0.03	4.69 ± 0.03
	45	2.39 ± 0.02	5.96 ± 0.02
	50	2.81 ± 0.02	3.85 ± 0.06
SNR	40	6.2 ± 0.3	10 ± 3
	45	6.2 ± 0.4	10 ± 2
	50	7.6 ± 0.6	14 ± 2
DCR (mmHz/mm^2)	40	79 ± 15	40 ± 3
	45	84 ± 9	44 ± 9
	50	88 ± 7	62 ± 10
DCR-WB (mmHz/mm^2)	40	18 ± 7	17 ± 2
	45	20 ± 6	16 ± 3
	50	23 ± 5	23 ± 12
XT (%)	40	18 ± 2	16 ± 5
	45	23.3 ± 1.9	21 ± 4
	50	29 ± 2	32 ± 3
AP (%)	40	1.2 ± 0.6	1.5 ± 0.4
	45	1.1 ± 0.3	2.2 ± 0.8
	50	1.1 ± 0.2	2.6 ± 0.5

best [163].

On the other hand, regarding FBK models, it was also observed that the triple-trench design presented a much larger gain and SNR than the single trench due to its larger cell pitch. However, the TT was expected to have a lower XT probability than the ST, but this was not clearly observed. The TT model was the one selected from FBK [164].

Comparing the models provided by the two vendors, it is clear that HPK's models performed better overall than the FBK's. Even though the TT model had a larger gain than the HQR75µm, it presents a significantly larger XT probability, being close to the upper limit of 35% for 50% PDE; and a slightly larger AP probability. This is probably due to the fact that the FBK models need a much larger bias voltage to reach the same PDE than HPK SiPMs.

Regardless of this, the approach decided by the photosensors working group was to select the best model of each vendor, being one the 'primary' choice

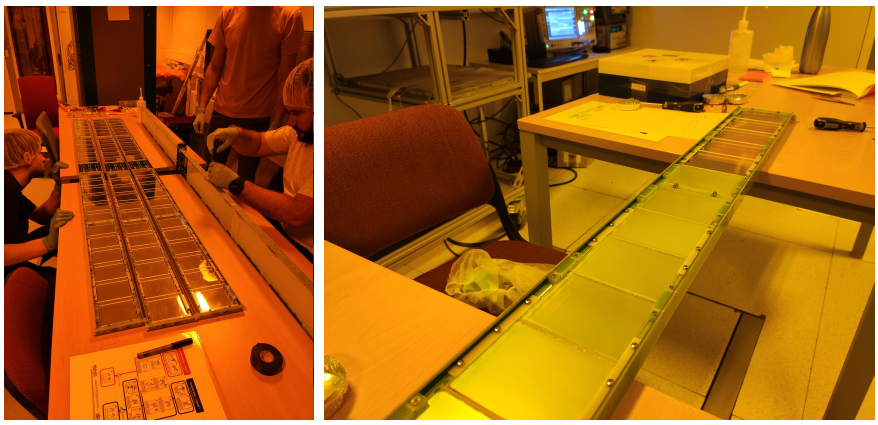

Figure 4.19: Left: working group assembling the optical modules. Right: installation of the dichroic filters with the PTP evaporation.

(the HQR75µm HPK model) and the other the 'secondary' choice (the TT FBK model), and split the DUNE SiPM production between both models (in a 60-40 proportion). In this way, if any of the vendors had problems during the production of the devices, the other would still have time to provide the remaining sensors.

4.6 Installation in ProtoDUNE-HD

As previously explained at the beginning of the chapter, the installation of the next iteration of ProtoDUNE-SP detector, ProtoDUNE-HD, started in Spring of 2022, including the PDS. After the down-selection of the SiPM models, a mass-test process was developed to validate all the sensors to be installed, and to prepare the optical modules. The X-ARAPUCA supercells were produced and tested by different laboratories and delivered to CERN, where they had to be mechanically and electronically assembled in groups of four to form the final optical modules. It was a tough and long process that had to be done carefully. First the mechanic structure had to be prepared, then all the pins of the SiPMs had to be routed to the electronic leading board, and finally the four supercells had to be connected to the electronic mother board (Figure 4.19, left). This board had four cold amplifiers, one per supercell. Four different SC were prepared, mixing the two SiPMs models down-selected and two wavelength-shifting plate technologies. These are Glass To Power and Eljen.

After the assembly, each module was tested in a black box to ensure the electronic routing had been done appropriately. Then, the dichroic filters had to

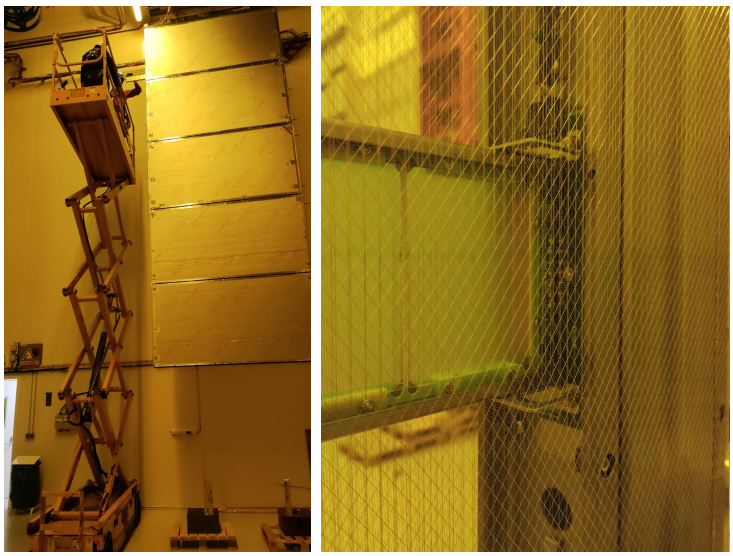

Figure 4.20: Left, insertion of the modules in an APA. Right, module inside the APA frame, behind the wire planes.

be installed in the outer surface of the modules so they were completed. Each optical module had 24 filters. The PTP evaporation on the filters surface was really sensitive, so this process required a high level of precision (Figure 4.19, right).

Once filtered, the modules were ready for the installation in the APAs frames. In total, 40 optical modules were successfully prepared for the installation, 10 per APA. The installation inside the APAs was a delicate operation that required the use of a mobile elevating work platform (MEWP) (see Figure 4.20). From the 40 inserted modules with 160 channels in total, only one of them belonging to APA2 had no electrical continuity after the insertion. The cause of this problem was found to be that one of the wires of the channel had no continuity between the optical module and the inner APA cabling. Although irreparable, understanding the source of the problem has helped to improve the QA procedures needed for DUNE.

Each APA, after being completely instrumented, had to be tested in the cold box, which is a large stainless steel structure capable of keeping an APA at argon gas temperature. This was the last step before the final installation in the cryostat. The PDS had to be connected to the readout system and continuously tested during the cool down and warm up processes. When in cold, optical channels' performance was studied. Mainly, the gain what was studied in a similar way to the one described in section 4.4.2. After the whole process of testing the four APAs, the following incidences were found:

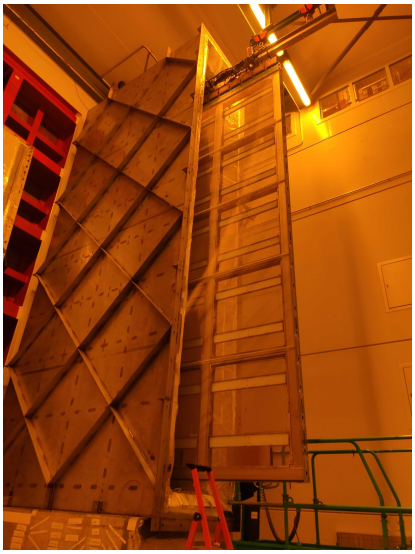

Figure 4.21: APA completely instrumented about to be tested in the cold box.

- a channel from APA1 presented deformed signals at cold temperature, probably caused by a malfunctioning wire.
- the channel without electronic continuity in APA2 presented some deformed signals at cold temperature. This reinforced the hypothesis of a wire not properly soldered, which made a better contact after thermal contractions of the different materials.
- a channel from APA4 had no electronic continuity after the warm up process.

From a total of 160 optical channels, only three (2%) presented problems after the cold box testing. This ratio of failure is compatible with the DUNE requirements for the far detector installation. Moreover, no outliers were found when studying channels' response.

Following cold-box tests, APAs had to be installed inside the cryostat, two on each drift volume, which was a complicated operation. This included connecting the cold cables, bundling them with the cold electronics cables (Figure 4.22, top, left), installing the cable trail (Figure 4.22, top, right), lifting the cables out of the cryostat through the corresponding chimney, connecting cables to the flange and testing continuity (Figure 4.22, bottom).

In summary, the installation of the PDS of ProtoDUNE-HD was successful. It was done in time with a failure rate compatible with DUNE specifications. What is most important, the sources of these failures were identified and understood,

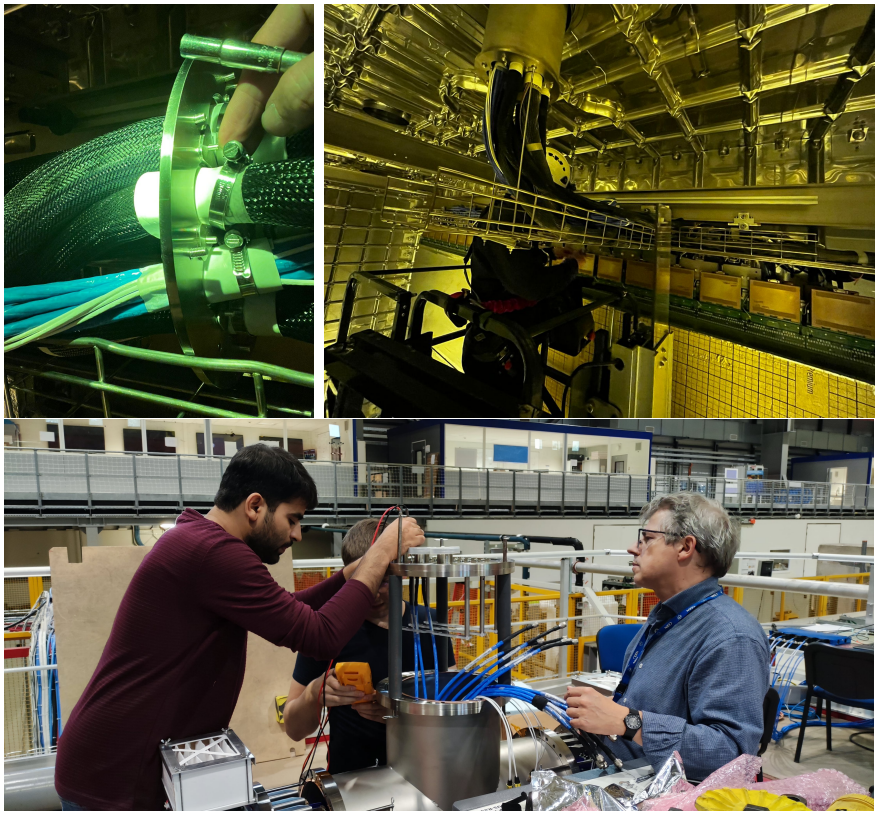

Figure 4.22: Installation of the APAs inside the cryostat. Top left: cold cables installation. Top right: cable trail installation. Bottom: flange installation.

and the QC/QA procedures have been improved. Currently ProtoDUNE-HD is completely assembled in the Neutrino Platform (Figure 4.23) waiting for LAr, so its operation can start.

Figure 4.23: ProtoDUNE-HD beam drift volume completely instrumented.

5 Secondary K^+ selection in ProtoDUNE-SP

I have no use for people who have learned the limits of the possible.

— Terry Pratchett, *The Last Hero*

This Chapter presents an overview of the secondary kaon selection developed in ProtoDUNE-SP, and it is organized as follows: Firstly, Section 5.1 motivates the necessity of this analysis; secondly, Section 5.2 explains why stopping kaons could not be generated as primary particles in the beam and had to be searched as secondary products in hadronic reactions; thirdly, Section 5.3 presents the event selection with a detailed explanation of each cut applied to the sample; and finally, Section 5.4 presents the kaon PID capabilities of the detector.

5.1 Motivation

As discussed in section 2.2.2, several channels have been presented for the proton decay hypothetical phenomenon [77], amongst which the so-called golden channel $p \to K^+\bar{\nu}$ has the largest branching ratio [91] (in general, even though it depends on the theoretical framework). Since the neutrino escapes the detector without interacting, the only signal of the process is the kaon, whose momentum is around 340 MeV/c. For the case of water Cerenkov detectors, the momentum is below the Cerenkov threshold [71], so this channel can only be detected by the decay products of the K^+ at rest or de-excitation photons of the nucleus that suffered the proton decay. One way or another, it is a complicated search for water Cerenkov detectors. On the other hand, this particular channel is optimum for LArTPC detectors, which can provide a full reconstruction and identification not only of the kaon but also its decay products.

The main decay channel of the kaon is $K^+ \to \mu^+\nu_\mu$ (64%), so the expected signal of this process in DUNE is a low-momentum track compatible with a kaon originated within the fiducial volume of the detector, followed by a low-momentum muon. The dominant background is generated by neutrino charged current (CC) quasi-elastic (QE) scattering, $\nu_\mu n \to p\mu^-$. When the muon happens to have a momentum similar to the 237 MeV/c expected for the K^+ decay at

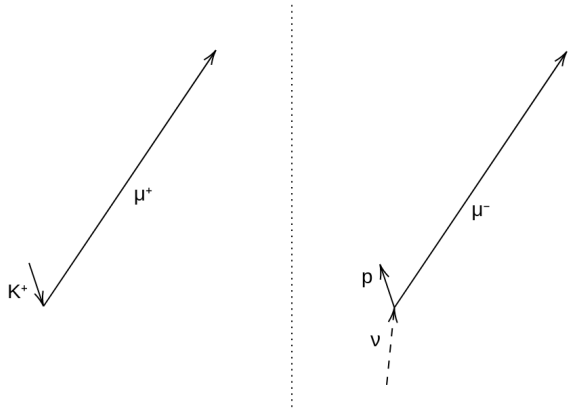

Figure 5.1: Diagram of proton decay signal (left), and the main source of background, (right).

rest and does not capture, it is indistinguishable from the one resulting from $p \to K^+\bar{\nu}$ followed by $K^+ \to \mu^+\nu_\mu$. So the discrimination between signal and background relies on two factors: first, the capability to differentiate kaons and protons, and second, the direction of the hadronic track. In Figure 5.1, a drawing of the different topologies for signal and background is displayed.

It is usually argued that, if the reconstruction cannot differentiate between kaons and protons, the direction of the hadronic track should be sufficient to discriminate between signal and background events [88]. For an atmospheric neutrino, the proton and muon are originated from the same neutrino interaction point, so for both tracks the Bragg peak is in the farthest end with respect to the vertex. For the kaon decay, the Bragg peak of the kaon happens to be in the vertex.

However, this backward-forward differentiation of the tracks could be compromised in events where final-state interactions are significant, because additional energy deposition may happen at the vertex point. We are not expecting to have many proton decays in general, thus it is fundamental to ensure the LArTPC capabilities to identify kaons and distinguish them from all other particles species, particularly from protons.

In this chapter, a selection of low-energy (stopping) kaons is presented, thanks to which the kaon PID capabilities of ProtoDUNE-SP –and, by extension, of DUNE– will be demonstrated. Afterwards, in Chapter 6, a detailed study of their energy loss will be discussed. Chapter 7 will study the effect of the systematic uncertainties of the ProtoDUNE-SP detector over this selection. The final results will be presented in Chapter 8.

5.2 Stopping K^+ in ProtoDUNE-SP

The ideal situation to study stopping particles is to generate them in the beam with a momentum such that they can arrive to the detector and, at the same time, not interact with argon nucleus, thus depositing all their energy within the active volume. Additionally, as the beam instrumentation is capable of tagging different species of particles, the selection of these stopping particles should be straightforward. As explained previously in Chapter 3, during the beam time of ProtoDUNE-SP several particle species with different momenta were thrown to the detector, and the ideal situation described above was found for positrons, protons, pions and muons. Naturally, this was not the case for kaons.[1]. The beam target more likely to produce hadrons at 2 GeV/c was unintentionally not used, significantly reducing the hadron proportion at that energy. For this reason, almost no low energy kaons were produced during the beam runs. This is why the first analysis carried out with the ProtoDUNE-SP beam data presented the Particle Identification for muons, positrons and protons [110], but not for kaons.

Beam kaons were residually produced at 2 GeV/c, and more significantly produced at 3, 6 and 7 GeV/c momenta. From 3 GeV/c, almost all of them interact inelastically when reaching the detector. Furthermore, at 2 and 3 GeV/c they are indistinguishable from protons for the beam instrumentation. All things considered, studying stopping kaons from the beam was very unlikely.

It was considered then the idea of looking for secondary kaons on hadronic reactions of higher energy. For protons at 7 GeV/c, approximately 1% are expected to generate charged kaons [165].

Assuming similar multiplicities for primary pions and kaons, and taking into account the number of triggers of each specie at 6 and 7 GeV/c, it was decided to study the feasibility of finding stopping kaons among all the secondary particles generated on reactions from primary particles of the beam.

5.3 Event Selection

The event selection is based on the kaon's main decay channel, which is $K^+ \rightarrow \mu^+\nu_\mu$. Neutrinos are not interacting inside the detector, so from the reconstruction point of view the wanted signature is the one of a track with a single daughter, which is compatible with an stopping muon (which is indeed the same signature that will be used in DUNE for proton decay searches). Here it is intro-

[1] Thankfully! this chapter would have not existed otherwise

duced the definition of 'candidate' for the event selection. **Any descendant of the beam particle with a single reconstructed daughter is considered to be a candidate**. Thus, even though this selection has been presented as 'secondary kaon selection', we are not only trying to select secondary kaons but any kaon generated inside the TPC by the beam particle, no matter its position in the genealogical tree. It is important to notice that, for a given beam event, the beam particle —or any of its descendants— can generate more than one particle compatible with the definition above, therefore having more than one possible candidate per event. In other words, the event selection which is going to be explained does not work on an event-by-event basis but on a candidates-by-event basis —more than one candidate in a single event can pass the selection.

It is interesting to highlight here some information obtained from the simulation before developing the event selection (see Tables 5.1 and 5.2). 12% of the beam events generate at least one kaon inside the detector, and their reconstruction efficiency is around 45%. Approximately 1% of the reconstructed particles originated by a beam event correspond to a kaon, and only 5% of these reconstructed kaons are properly reconstructed along the associated muon consequence of their decay. Overall, an identifiable kaon is produced per 203 beam events at 6 GeV/c and per 212 beam events at 7 GeV/c. Considering that these ratios are the same for data, and considering all available statistics (463043 and 252598 beam events identified within the TPC at 6 and 7 GeV/c, respectively), approximately 3500 selectable kaons are expected. The size of the final selected sample will depend on the selection efficiency. So, as it can be seen, selecting a sufficiently large sample of stopping kaons among all the particles inside the detectors is a challenging task.

In the following subsections the different cuts applied will be explained and justified. Their values have been estimated by maximizing the product $Efficiency \times Purity$.

5.3.1 Beam Particle cuts

As commented in Chapter 3, a beam line with different instrumentation was responsible of throwing charged particles to ProtoDUNE-SP. This instrumentation was used to characterize the particle of the beam, commonly known as beam particle, and provide a measurement of its momentum, expected position and direction in the TPC volume, and a PDG hypothesis using the TOF and the Cerenkov counters.

However, regarding our analysis, only one cut can be done. As previously explained, secondary kaons are produced in hadronic reactions. At 6 GeV/c

Table 5.1: True information regarding kaons for a subsample of the MC simulation. The percentage shown is with respect to the number above. The particles considered are exclusively the ones belonging to the true beam particle hierarchy.

Beam Momentum (GeV/c)	6	7
# Events	47906	49854
# Events with at least one true K^+	5435 (11.3%)	6462 (13.2%)
# True Kaons	9191	11064
# True $K^+ \to \mu^+ \bar{\nu}_\mu$	2532 (27.6%)	2965 (26.8%)

Table 5.2: Reconstructed information regarding kaons for a subsample of the MC simulation. The percentage shown is with respect to the number above. The particles considered are exclusively the ones belonging to the beam particle hierarchy.

Beam Momentum (GeV/c)	6	7
# Events	47906	49854
# Events with at least one reco K^+	4226 (8.8%)	3582 (7.2%)
# Total particles	379994	413789
# Reco kaons	4226 (1.1%)	5017 (1.2%)
# Reco K^+ truly decaying to μ^+	944 (22.3%)	1002 (20.0%)
# Reco K^+ and μ^+	236 (25%)	235 (23.5%)

of momentum, the beam instrumentation can distinguish between kaons and protons, but not between muons, pions and electrons [110]. Looking at Figure 5.2, one can see how the most abundant particles in the beam are pions, thus, if we want to have a sufficiently large sample of kaons, no hadron filtering can be done using the beam instrumentation PID. Because of that, the only cut that can be done with respect to the beam instrumentation is to request that the event has a reconstructed beam particle.

- **Beam particle existance**: the event must have a reconstructed particle inside the TPC considered to be the beam particle.

It has been usual in other ProtoDUNE-SP analysis focused on the particle generated by the beam to consider extra geometric cuts on its characteristics [166–168] for several reasons. First, to ensure that the particle selected as beam particle by Pandora was truly a particle coming from the beam and not a miss-identified cosmic. Second, to reject events in which the beam particle interacts with the cryostat wall and generates particles of different species and different

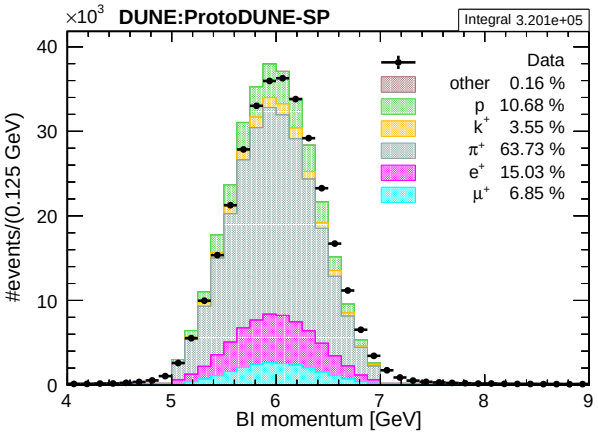

Figure 5.2: Beam particle momentum measured by the beam instrumentation for 6 GeV/c runs and MC. The plotted category correspond to the true beam particle.

trajectories. Third, to reduce residual differences between the beam simulation and the real beam. However, since the scope of this analysis is not the primary particle but its reaction products, this kind of cuts are not necessary.

5.3.2 Candidate existance

Once events with a primary particle have been selected, they are requested to have at least one candidate, which is any descendant of the beam particle with a single reconstructed daughter.

- **Candidate existance**: the event must contain at least one candidate.

It can be observed in the distribution of candidates per event (Figure 5.3) a difference between data and MC, which apparently indicates that more candidates per event are generated in MC than in data. This is due to a known issue in the MC simulation. When the first analysis of ProtoDUNE-SP started, it was noticed that tracks passing from one APA to another were usually broken at reconstruction level due to the not-powered electron diverters. Thus, instead of reconstructing a single track, two tracks were reconstructed and one assigned as daughter of the other (which matches the definition of candidate presented above). This effect was reproduced in MC, but the amount of broken tracks was overestimated. As a consequence, the proportion of candidates is larger in MC than in data.

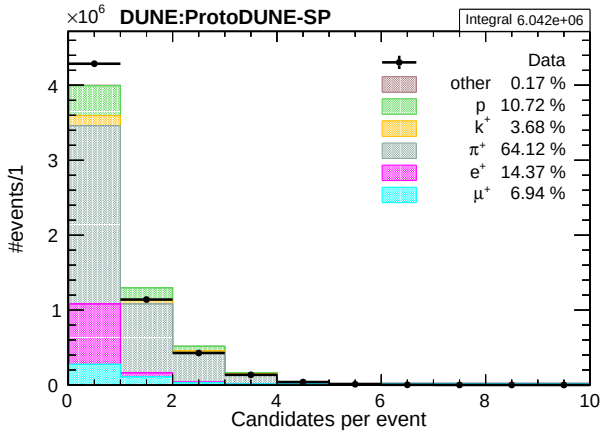

Figure 5.3: Number of candidates per event. The category plotted represents the particle specie of the true beam particle.

For coding comfortability, a maximum number of 10 candidates per event is considered for the event selection.

5.3.3 Candidate's daughter cuts

As explained above, the daughter of the candidate should be compatible with a stopping μ^+ with a very well defined momentum centred in 237 MeV/c. Several cuts can be obtained from this. First, from the reconstruction point of view, Pandora can differentiate between tracks and showers inside the TPC and, consequently, it provides an object code of 1 for showers, 2 for tracks and 0 for unknowns (see Figure 5.4). Muons are more likely to behave as tracks rather than showers.

- **Track-like**: The daughter must be a track-like object, meaning that its reconstructed object code must be equal to 2.

Secondly, from the calorimetric point of view, stopping muons should be easily distinguishable from heavier particles. The particle identification based on calorimetry is done by comparing the deposited energy per unit length ($\frac{dE}{dx}$) as a function of the residual range with the MC expectation for a given particle specie. Remember that the residual range is defined as the distance from a given point of a track to its end point. This comparison allows to define a χ^2 value for

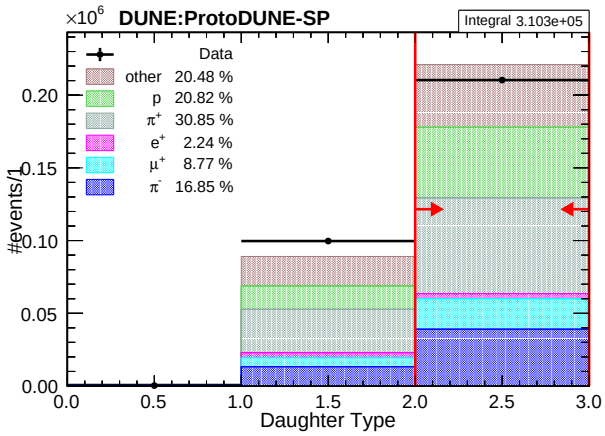

Figure 5.4: Daughter object type. Zero corresponds to unknown, 1 to shower, 2 to track. The category plotted represents the particle specie of the true particle associated to the daughter of the candidate. The discrepancy in the relative proportion between tracks and showers is due to the broken tracks between APAs overestimation in the MC simulation.

each track as:

$$\chi^2_{Part} = \frac{1}{N_{hits}} \sum_{i}^{N_{hits}} \frac{(\frac{dE}{dx}\big|_i^{\text{Data}} - \frac{dE}{dx}\big|_i^{\text{MCPart}})^2}{\sqrt{[\sigma(\frac{dE}{dx}\big|_i^{\text{Data}})]^2 + [\sigma(\frac{dE}{dx}\big|_i^{\text{MCPart}})]^2}}, \tag{5.1}$$

where i runs over all the hits of the track within its last 26 cm, $\sigma(\frac{dE}{dx}_i)$ is the associated error of the $\frac{dE}{dx}$ for the i-th hit, and MC Particle refers to the expectation based on the simulation for a given particle specie, so that a different χ^2 value can be defined for each of them. For our purpose, we can use the χ^2_μ, and select the tracks with low value of this parameter (see Figure 5.5):

- χ^2 **PID**: The daughter χ^2_μ should be compatible with the one of a muon, daughter $\chi^2_\mu < 6$.

Finally, from the kinetic point of view, the momentum by range of the daughter should be compatible with the one of a muon of 237 MeV/c (Figure 5.6). The momentum by range is computed by assuming a particle specie (and hence an $\frac{dE}{dx}$ profile) and applying the continuous slowing down approximation (CSDA) [169].

- **Momentum by range**: The daughter must have a momentum by range under muon hypoteshis compatible with 237 MeV/c, 0.221 < daughter p_{Range} [MeV/c]< 0.245.

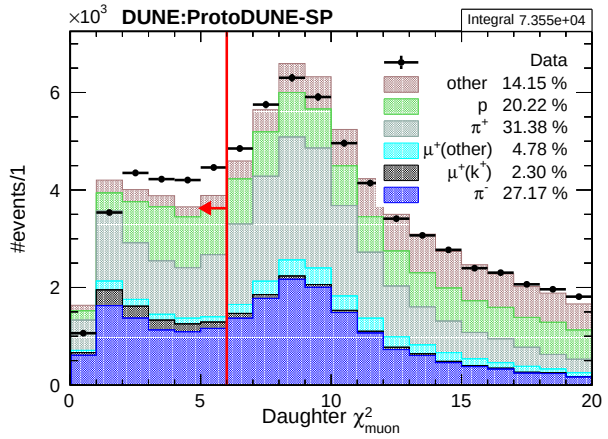

Figure 5.5: χ^2 distribution under muon hypothesis for candidates' daughters.

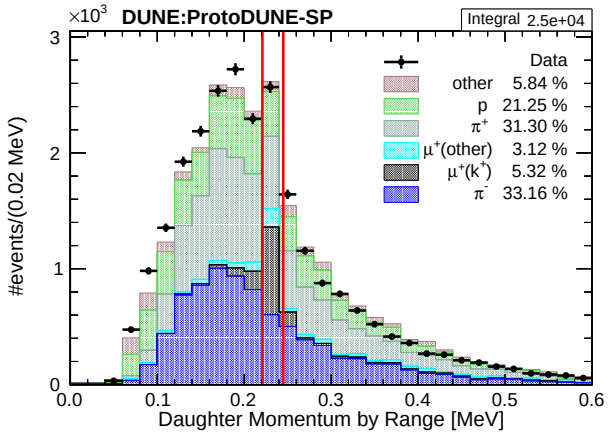

Figure 5.6: Momentum by range under muon hypothesis for candidates' daughters.

5.3.4 Candidate cuts

Although the sample has been already cleaned substantially, some more cuts are needed to further isolate stopping kaons and differentiate them from background, which is mainly formed by pions. First, as the K^+ decay happens at rest (and has zero spin), the muon direction with respect to the kaon end direction is isotropic. This is not the case for the pions, the distribution of which is more forward than backward (see Figure 5.7). Thus, rejecting the forward distribution is a good way of reducing the background even more. This approach is similar to what was done in MINERνA, where they also looked for kinks in order to identify kaons [170].

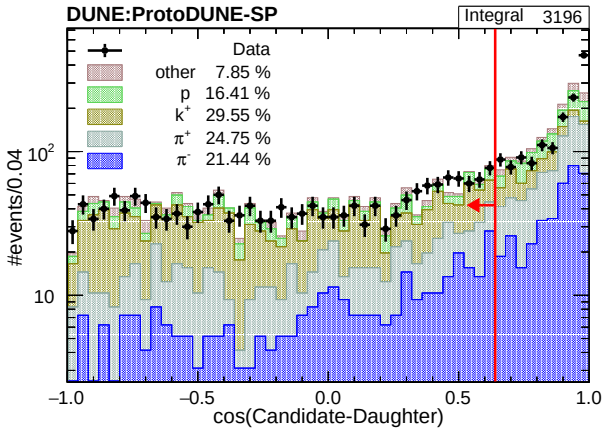

Figure 5.7: Daughter angular distribution with respect to candidate end direction.

- **Candidate-daughter angle**: Daughter should not go forward with respect to candidate's end direction, cos(candidate-daughter) < 0.64.

Part of the remaining background is formed by miss-reconstructed inelastic interactions. In some interactions with two outgoing daughters, frequently one of the daughters and the incoming particle are reconstructed as a single track, having as a result a track with a single daughter compatible with the candidate definition (Figure 5.8, top). However, in these cases, the starting point of the daughter tracks is far away from the end point of the mother track. One can make use of this distance to remove this kind of events.

- **Candidate-daughter distance**: The distance between the end point of the candidate and the beginning point of its daughter must be small, $0.0 <$ distance candidate-daughter [cm] < 10.

After applying all cuts mentioned above the resulting sample has, approximately, a 50% purity, and it can be seen how kaon population (signal) and pion population (main source of background) are clearly distinguishable in the χ^2_K (under kaon hypothesis) distribution (Figure 5.9). Furthermore, they can also be distinguished in the two-dimensional distribution of $\frac{dE}{dx}$ vs residual range, which, as it will be explained in the following Chapter, is where this analysis is focused on (see Figure 5.10).

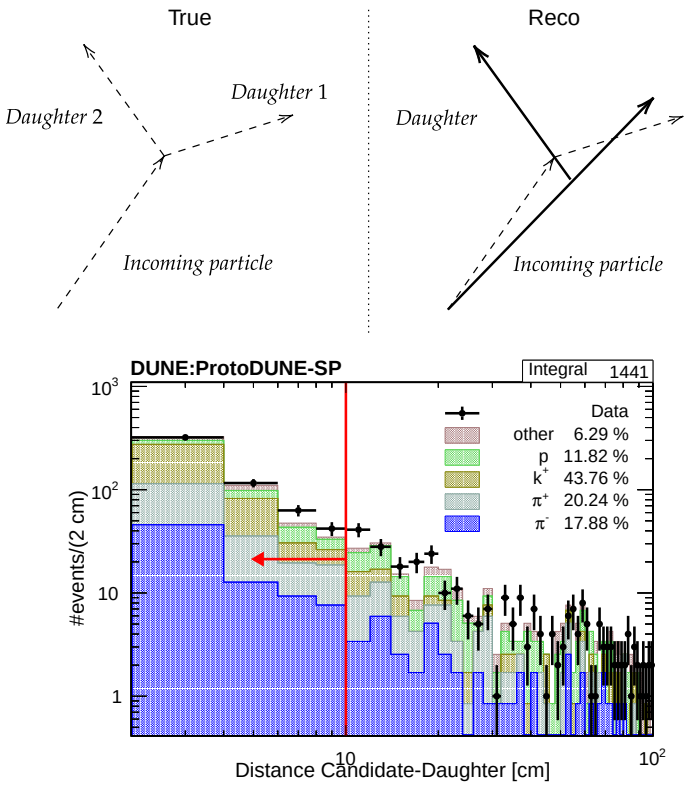

Figure 5.8: Top: Diagram showing background formed by miss-reconstructed inelastic interactions. Bottom: Distance between daughter and candidate.

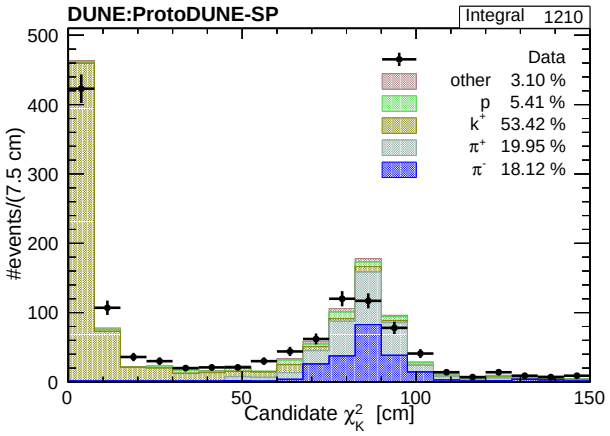

Figure 5.9: Top: Kaon candidates χ^2 distribution under kaon hypothesis. Two peaks are clearly distinguishable, the one in the left corresponding to the stopping kaons (signal), and the one in the right corresponding to the background.

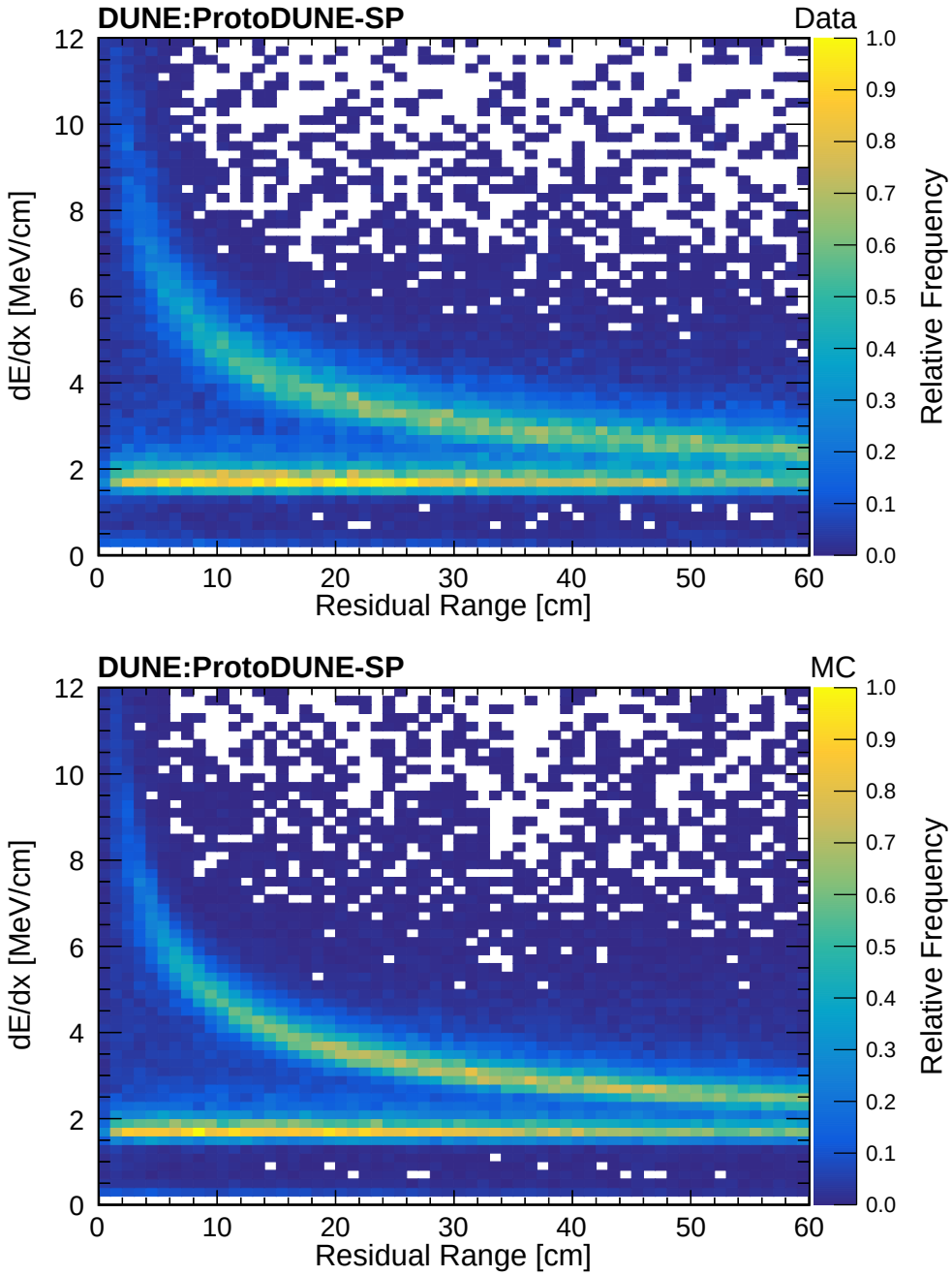

Figure 5.10: $\frac{dE}{dx}$ distribution as a function of the residual range. Top: Data. Bottom: MC. The up-going population corresponds to the selected stopping kaons, whereas the flat distribution corresponds to the background.

5.3.5 Selection Result

After the event selection described above, a sample of about 600 kaons with a purity of 50% has been obtained (the total selected population is 1200 candidates). The sample is sufficiently large and the separation with background is large enough to perform a detailed study of K^+ energy loss in liquid argon, which will be presented in Chapter 6. It is interesting to notice here that this complicated selection has been achieved making use only of the TPC information. The information of the photon detection system has not been used, so this is a different approach from scintillation experiments. This highlights the capabilities of the LArTPC as a particle detector, which will be considerably increased when combined with the photon detection system in DUNE's far detector.

Since the kaons we have selected are stopping, we can estimate their initial momentum from the calorimetric measurement done by the TPC. The total energy deposited by the particle is

$$E_d = \sum_i^{N_{hits}} \left.\frac{dE}{dx}\right|_i dx_i \tag{5.2}$$

were dx_i is the pitch of each hit. Using energy conservation, we have

$$\sqrt{p_i^2 + m_K^2} = m_K + E_d \rightarrow p_i = \sqrt{E_d^2 + 2E_d m_K} \tag{5.3}$$

where p_i is the initial momentum of the kaon and m_K is the kaon mass. The initial momentum distribution for the sample of stopping kaons is presented in Figure 5.11-left. A cut has been applied in the χ^2_K distribution (see Figure 5.9, $\chi^2_K < 50$) so that only kaons are represented. It can be observed how the initial momentum of these particles is very low, slightly above the expected momentum of a K^+ result of a proton decay (red vertical line in the plot, 340 MeV/c [88]). Even though the real momentum of a kaon result of a proton decay would be lower due to nuclear effects, it it really encouraging to see the capabilities of ProtoDUNE-SP to properly tag and characterize these low momentum particles.

Figure 5.11-right shows exactly the same figure but the category plotted represents the particle specie of the MC beam particle that generated the beam event. As we will see later, the proportion of pion-like, proton-like and kaon-like beam events is approximately 85%, 10% and 5%. however, it can be observed that kaon-like beam events generate about 15% of the selected kaons, being the particle more efficient producing selectable secondary kaons. This is due to the strangeness conservation: it is easier to produce a secondary kaon when there was a already a primary kaon.

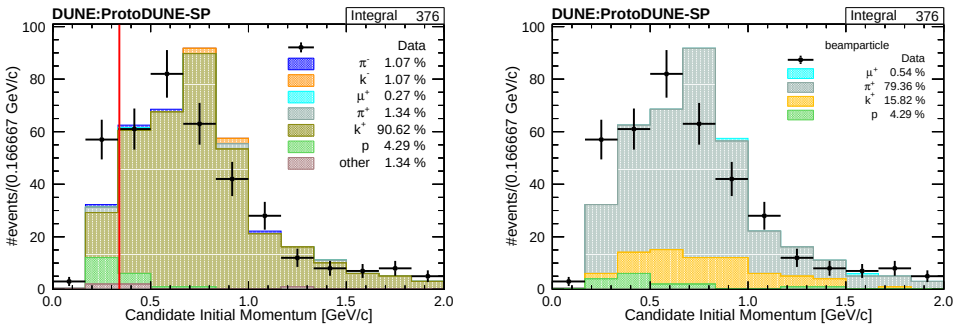

Figure 5.11: Left: initial momentum of the stopping kaons sample computed using calorimetry information. The red line represents the initial momentum of a kaon resulting of a proton decay. Right: same distribution, but the category plotted represents the particle specie of the primary MC beam particle.

It is important no notice here that we have not studied yet the effect of systematic uncertainties on the selection. This will be done in Chapter 7

5.3.6 Efficiency and Purity

In Figure 5.12 the evolution of the efficiency and the purity is presented. As it has been seen during this chapter, the purity of the sample has gone from less than 1% up to 50%, using exclusively the TPC information. For the same reason, the truly low efficiency achieved (0.5%, approximately) is not a surprise. The efficiency for each cut is computed from the true information, as the amounts of true kaons that pass the cut divided by the initial amounts of true kaons. Note that for a true kaon to pass any cut, it has to be associated to a reconstructed object (which are the ones that are being analysed in the event selection). This is why there is such a big drop from the second step to the third, in which we are indeed requesting the reconstructed candidate to exist.

There is no variation in the first cut because of how the analysis n-tuple is generated: it does not fill any entry of the output tree unless there is a particle tagged as beam particle.

5.3.7 Summary of the selection

Table 5.3 presents a summary of the different cuts of the selection, and the evolution of candidates (not events) in data and MC, along the efficiency and the purity of the selection.

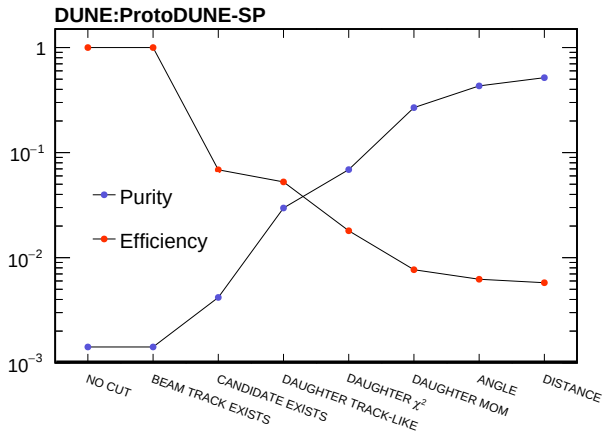

Figure 5.12: Evolution of purity and efficiency as a function of the applied cuts during the event selection.

Table 5.3: Selection summary for data and MC as a function of the cuts applied.

Cut	Data Candidates	MC Candidates	Efficiency (%)	Purity (%)
No cut	715641	613520	100	0.14
Beam Particle Existence	715641	613520	100	0.14
Candidate Existence	207598	207192	6.86	0.42
Daughter Track-Like	210367	223257	5.26	2.97
Daughter χ^2_μ	32926	31716	1.80	6.89
Daughter Mom by Range	3607	3447	0.77	26.81
Candidate-Daughter Angle	1759	1738	0.62	43.15
Candidate-Daughter Distance	1311	1345	0.58	51.67

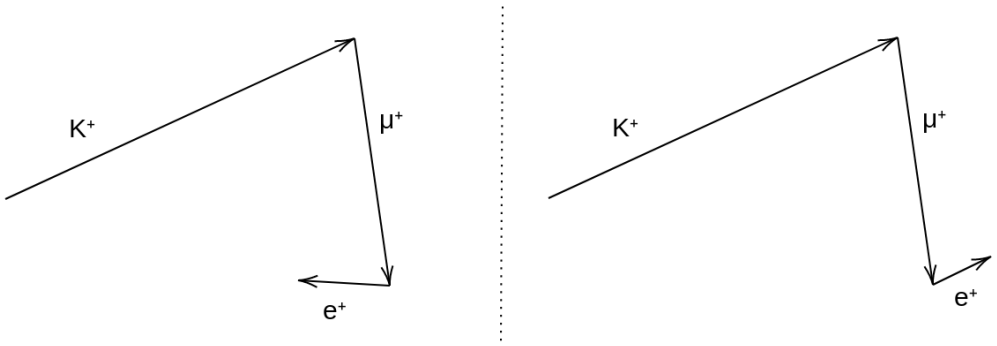

Figure 5.13: Diagram of the two different topologies of the signal events.

5.3.8 Event Displays

Here a selection of data events passing the selection are presented in Figures 5.14, 5.15, 5.16, 5.17 and 5.18. They can be recognized for the kinks formed by the kaon and the muon, and the muon and the Michel electron, forming a 'hook' (see Figure 5.13). It can be appreciated the truly complicated topologies that have been reconstructed thanks to the good tracking capabilities of the LArTPC technology.

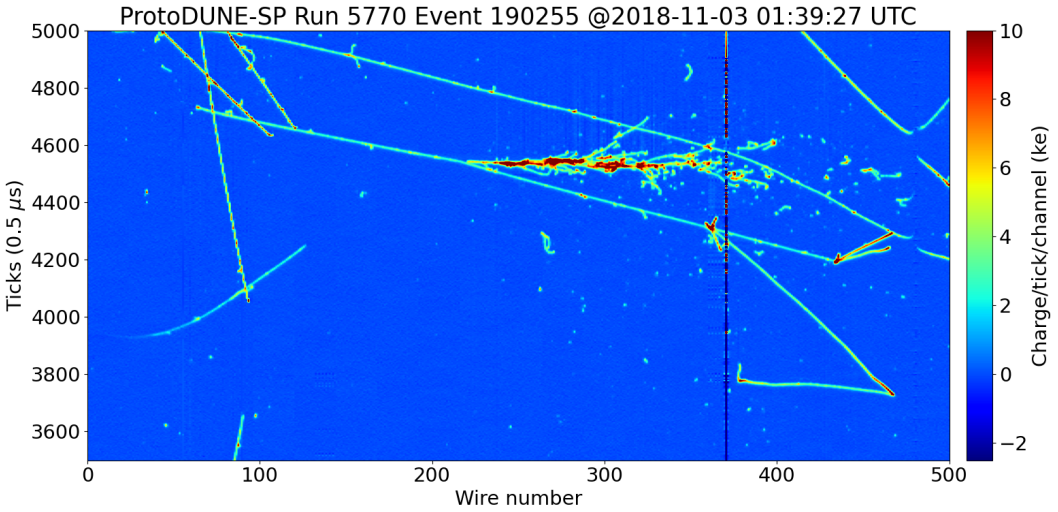

Figure 5.14: Kaon candidate event display. The candidate is in the bottom right of the image.

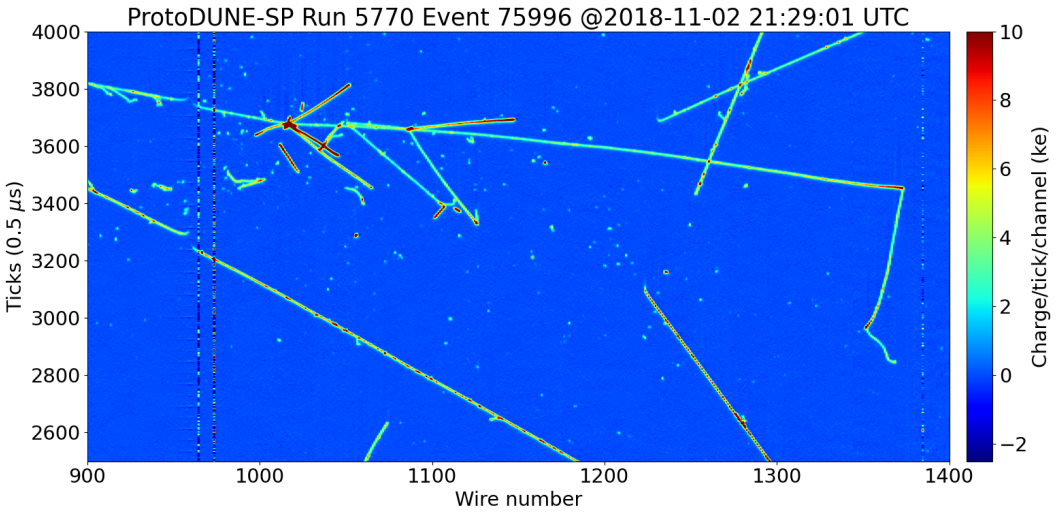

Figure 5.15: Kaon candidate event display. The candidate is a long track crossing the detector and ending in the right side of the image.

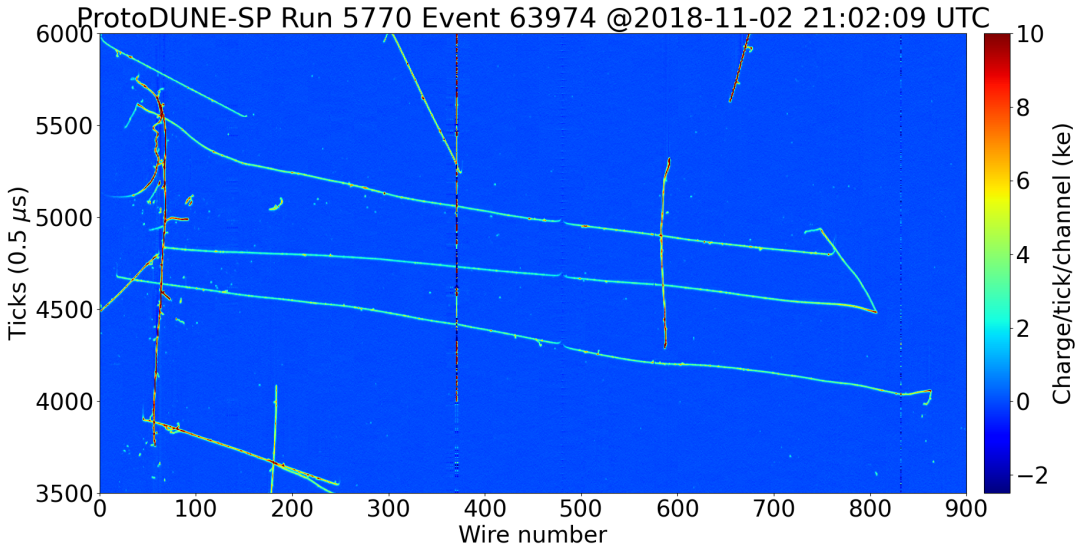

Figure 5.16: Kaon candidate event display. The candidate is the middle large track going from left to right. It can also be observed the effect of the electron diverters, splitting the tree long tracks.

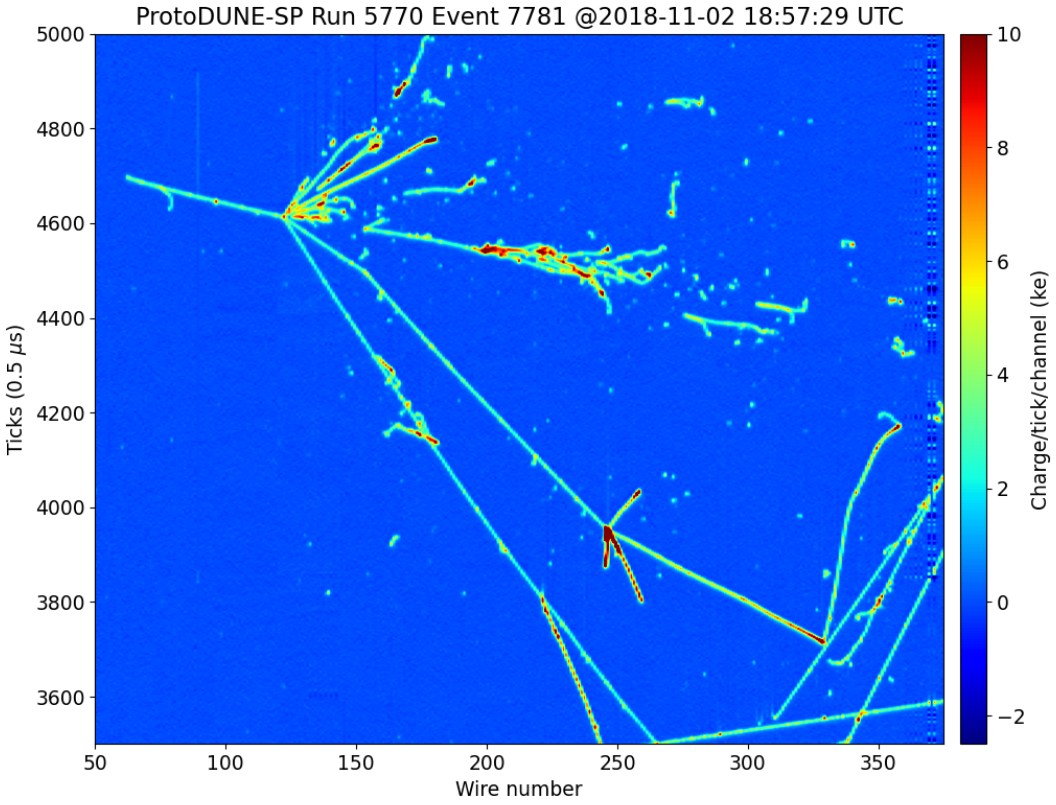

Figure 5.17: Kaon candidate event display. At the wire $\sim$ 250, there is a vertex with four outgoing particles. The longest one is the candidate, forming the hook described above.

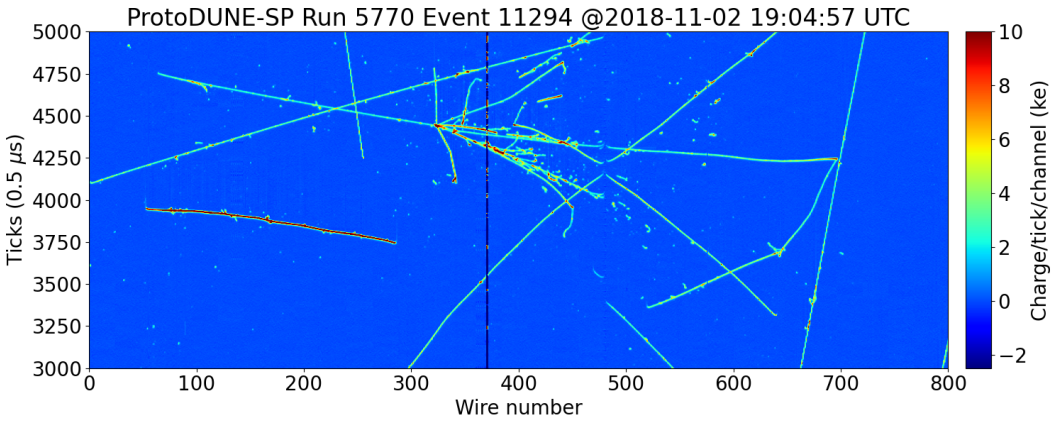

Figure 5.18: Kaon candidate event display. The candidate tracks starts approximately at the wire 400 and ends in the 700.

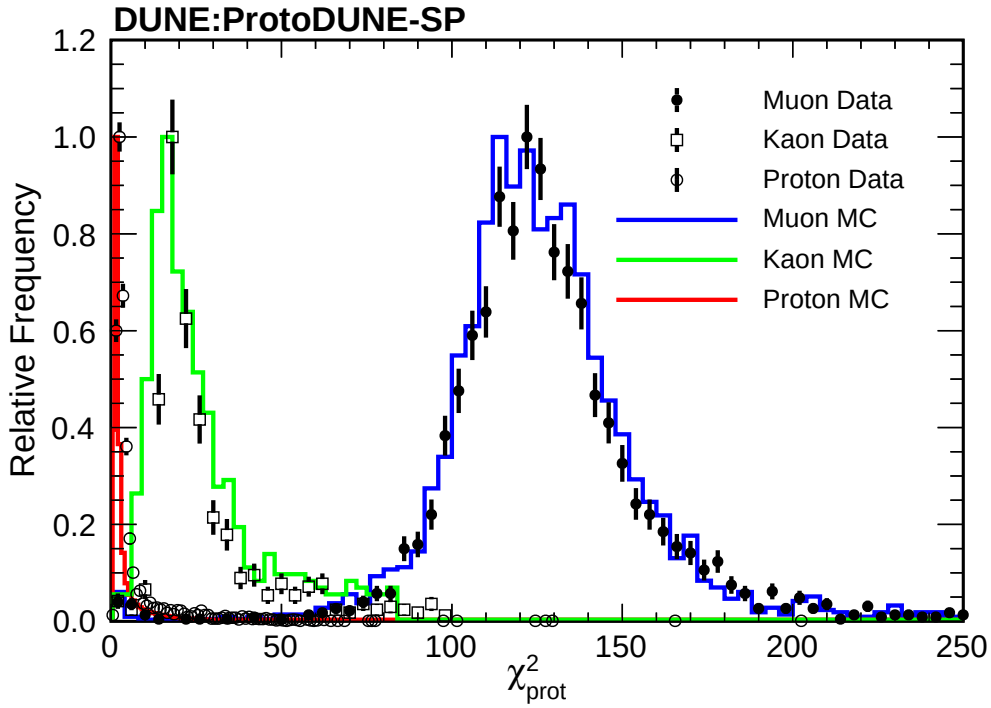

Figure 5.19: χ^2_{prot} for stopping protons, kaons and muons.

5.4 ProtoDUNE-SP Kaon PID Capabilities

Figure 5.19 presents the χ^2_{prot} distribution for stopping protons, kaons and muons. The kaons are the ones obtained from this analysis. It can be observed how clearly the LArTPC technology differentiates heavier and lighter particles, and also how kaons and protons are well distinguished too. This is a key point for proton decay searches, since it should be possible to differentiate background and signal events only by studying the hadronic track $\frac{dE}{dx}$ profile, as assumed in the sensitivity studies of DUNE's FD.

6 Detailed study of K^+ energy loss

THAT'S MORTALS FOR YOU, Death continued. THEY'VE ONLY GOT A FEW YEARS IN THIS WORLD AND THEY SPEND THEM ALL IN MAKING THINGS COMPLICATED FOR THEMSELVES. FASCINATING.

— Terry Pratchett, *Mort*

As previously explained in Chapter 5, a proper identification of low energy K^+ is fundamental for proton decay searches in DUNE's Far Detector. In the case of a LArTPC, the identification is done through calorimetric information: the energy deposited in the detector by a charged particle depends on its velocity, hence, the distribution of the $\frac{dE}{dx}$ as a function of the momentum allows to distinguish between particle species [96].

However, neither ProtoDUNE-SP nor DUNE can directly measure particles momenta inside the TPC. What is typically done for stopping particles is to exchange the momentum by the residual range (RR from now on) [101]. The RR of a hit is defined as the distance from the hit to the end of the track, as previously seen in Section 2.4.1.1.

In the previous Chapter, a selection of stopping kaons was developed without using their calorimetric characteristics, meaning that this information has not been biased by the selection. Consequently, it is possible to do now an in-depth study of the $\frac{dE}{dx}$ versus RR profile, such that the MC prediction and the sensitivity studies carried out for the Far Detector searches can be validated. In the case of finding discrepancies, these can be used to fine-tune the simulation and to propagate systematic uncertainties in other analysis considering kaons.

This chapter is organized as follows: first, the approach to differentiate signal and background contributions is presented in Section 6.1; second, Section 6.2 describes the fitting algorithm developed to characterize the $\frac{dE}{dx}$; Section 6.3 presents the results from the fit; finally, the fit stability is evaluated in Section 6.4.

6.1 Residual Range slices

In order to properly characterize signal and background contributions, one can divide the 2D plot presented at the end of the previous Chapter in residual range slices, forming 1D $\frac{dE}{dx}$ histograms as the ones presented in Figure 6.1, in which both contributions can be differentiated: the left one corresponding to the background, and the right one corresponding to the signal. This way, the energy loss per unit length can be fitted in order to properly consider both samples.

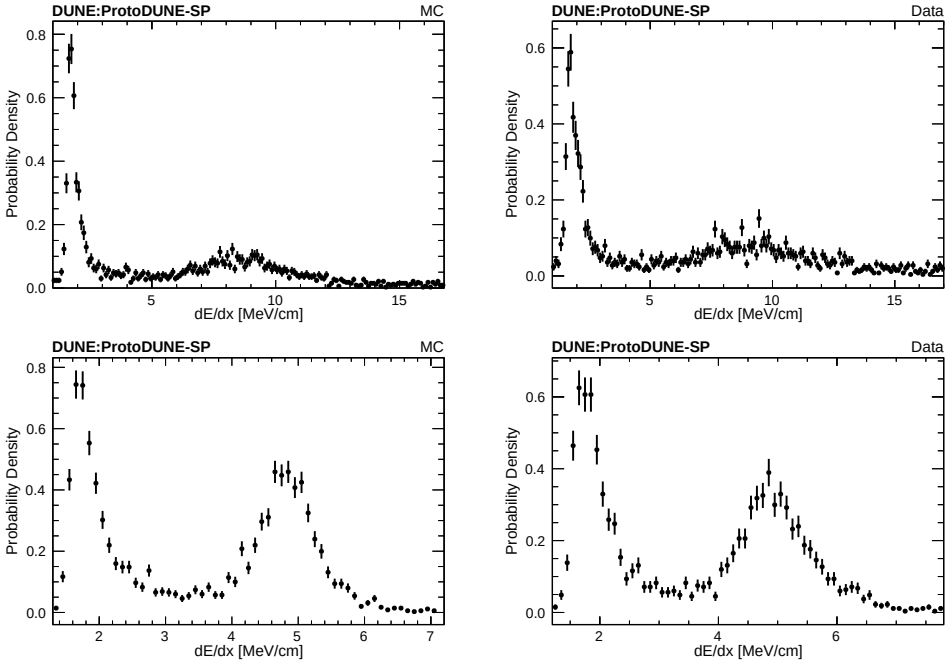

Figure 6.1: $\frac{dE}{dx}$ distribution for different residual ranges. The top two plots correspond to the RR slice between 1 and 3 cm; the bottom two plots to the slice between 9 and 11 cm. The right peak corresponds to the stopping kaon population, and the left one to the background. The histogram has been normalized in such a way that the sum of all of the entries is 1. The RR slice width of 2 cm has been chosen so that a compromise is found between statistics and resolution.

Concretely, each contribution can be described as a convolution between a Gaussian and a Landau distribution, so the total distribution is the sum of two Landau-Gaus distributions. This is done because the Landau distribution is the one describing the energy loss and the Gaussian is used to account for detector resolution and smearing produced by the RR binning. The resultant distribution has 4 independent parameters: the most probable value of the Landau (μ), the

Landau width (σ_L), the Gaussian width (σ_G) and a normalization factor. The Gaussian is centred in the Landau's μ. In Figure 6.2, an example of this fit can be observed for data and MC.

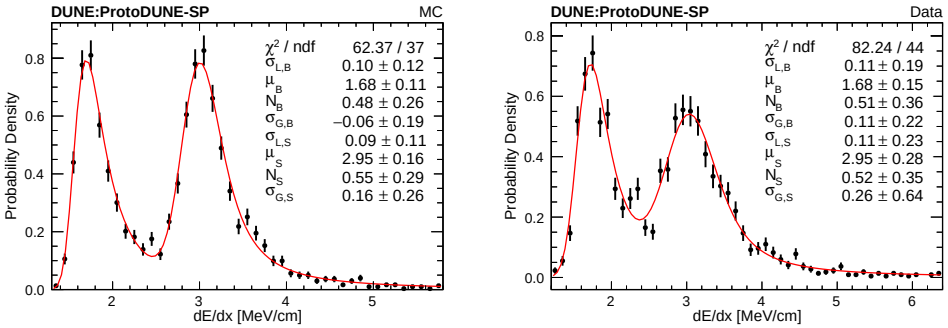

Figure 6.2: $\frac{dE}{dx}$ distribution for residual range between 31 and 33 cm fitted to a sum of two Landau-Gaus distributions. Left: MC. Right: Data

It could be possible to apply this approach to every RR slice and make an estimation of the most probable value (μ) of the energy loss per unit length of the signal for each slice. However, it is clear that this way the information is not being shared between slices since they are being treated independently. In addition, the available statistics –which are sufficient but not excessive– have more impact with this approach. In order to maximize the information available and the correlation between consecutive slices, and additionally reduce the effect of the low statistics, the Coherent Fit approach is used.

6.2 Coherent Fit

The so-called Coherent Fit strategy aims to characterize the $\frac{dE}{dx}$ considering the correlations between RR slices. It is based on the approach developed to study the PID capabilities of the ALICE TPC [171]. It relies on the following observation: **the parameters describing each contribution along the RR slices should vary smoothly from one slice to another**.

Let's consider the most probable value of the signal distribution (μ_S). It is clear than for the first RR slice (the one closest to the end of the track), μ_S should be larger than for the second slice. In the same way, μ_S in the second slice should be larger than in the third slice, and so on. Provided infinite statistics, one could make differential RR slices and study μ_S for each one of them, and it would be seen how μ_S varies continoulsy from one slice to another. This variation could be described as an smooth function of RR, namely $\mu_S = f(RR, \vec{a})$, with $\vec{a}$ a vector

of parameters. Coming back to our real-life problem, and given an appropriate function $f(RR, \vec{a})$, the goal changes from finding the μ_S that best describes each RR slice individually, to find the best estimation for the parameters $\vec{a}$ that describe μ_S across all the slices simultaneously. The same applies to the other parameters of the different contributions.

If this is done, all dependencies lie down exclusively on the RR and only a single minimization procedure for all histograms is needed. This way, the information across slices is used *coherently* (contrarily to what was done in the previous section, in which the information was not shared and then used *incoherently*).

From now on, the MC information will be used to find the functions that better describe every family of parameters across the slices.

6.2.1 Parametric Functions

Using the MC information, one can study separately the signal contribution (the one formed by kaons) and the background, and look for appropriate models describing each family of parameters.

As it will be explained later, the minimization procedure uses the Migrad algorithm [172], which uses first and second —numerical— derivatives to reach the minimum, hopefully in a finite amount of time. In order for Migrad to find a proper minimum with a well-defined error matrix, one needs to make sure that the function to be minimized and its derivatives are well-behaved (namely, that a small variation in one of the parameters generates a small variation on the function).

The parametric functions that are going to be presented next have been selected to fulfil two requirements: first, to properly describe the $\frac{dE}{dx}$ distributions; and second, to ensure a good convergence of the Migrad minimization algorithm.

6.2.1.1 Signal Parametrization

In Figure 6.3 different signal slices (formed exclusively by reconstructed objects associated to true kaons) are presented. Two different contributions can be observed. The one in the right, which is the 'pure' signal that needs to be characterized, and the one in the left, formed by reconstruction errors or miss-associations of cosmic rays' hits. The one in the left, as it will be seen afterwards, is partially absorbed by the background contribution, so in this section we are only trying to parametrize the pure signal.

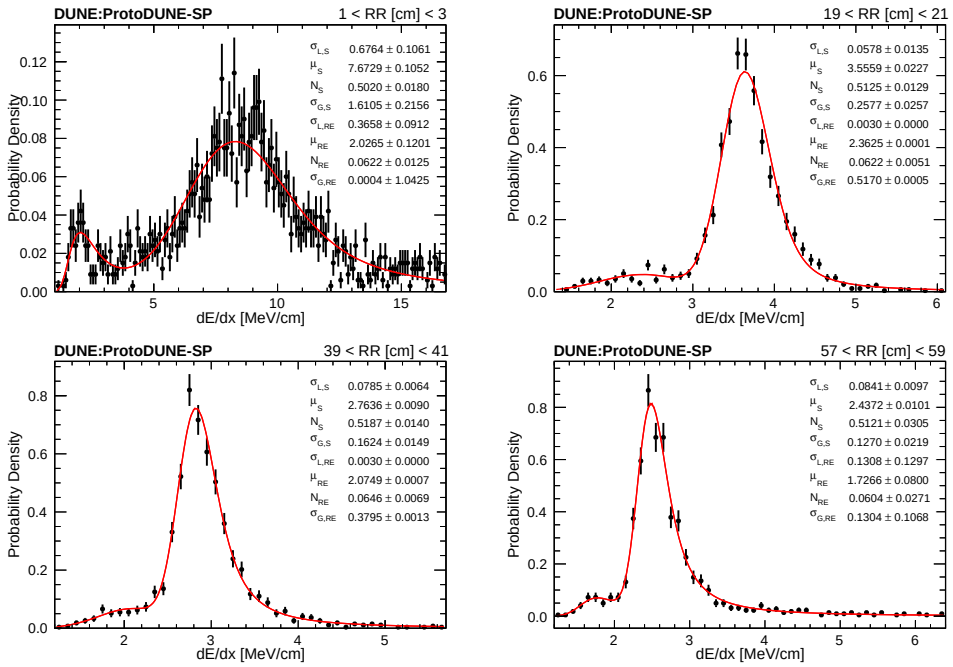

Figure 6.3: Signal distribution for different residual range slices. The big peak corresponds to the real contributions, whereas the left distribution of points are caused by reconstructed errors and miss-associated cosmic rays' hits. The red line corresponds to a double Landau-Gauss fit.

Each residual range slice can be fitted independently to a sum of two Landau-Gauss distributions, as can be seen in Figure 6.3. The four parameters describing the Landau-Gauss of the pure signal can be represented as a function of the RR (see Figure 6.4). The red line present in some of the plots corresponds to the parametric function describing the behaviour across slices, and they are given by equations 6.1, 6.2 and 6.3. In these equations, x represents the residual range in cm, and the parameters used to describe each one of them are different from one another (in other words, α in equation 6.1 is different from α in equation 6.2 or 6.3). Normalization is left constant across the slices.

$$\sigma_{S,L}(x) = (\frac{\alpha}{x} - 1)/x + \beta \tag{6.1}$$

$$\mu_S(x) = \alpha \left[\frac{\beta x - 1}{\beta x + 1} + \gamma\right] \tag{6.2}$$

$$\sigma_{S,G}(x) = \frac{\alpha}{x + 1} + \beta \tag{6.3}$$

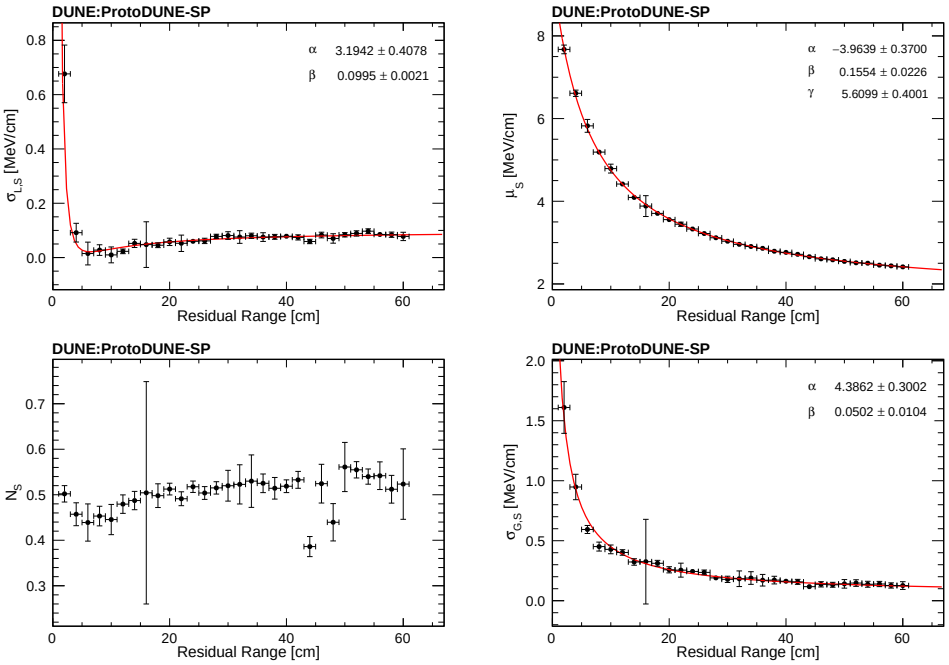

Figure 6.4: Dependence of the Landau-Gauss parameters with the residual range. The error bar is given by the fit result. The red line represents the chosen parametrization, given by the equations 6.1, 6.2 and 6.3.

6.2.1.2 Background Parametrization

In Figure 6.5 different background slices (formed by reconstructed objects that have no true kaon associated) are presented. In general, the background contribution is quite homogeneous along slices, and they can be fitted to a Landau-Gauss function too.

In Figure 6.6 the evolution of the different parameters with the residual range slice is presented. All of them are almost constant along slices, and are left as a constant during the Coherent Fit. Only the most probable value is assumed to have a linear variation with the RR:

$$\mu_B(x) = \alpha + \beta x \tag{6.4}$$

6.2.1.3 What-Is-Left Parametrization

As previously presented, signal and background contributions are easily described as Landau-Gauss distributions. However, there are some leftover regions which have no easy description (see the left group of points present in each plot

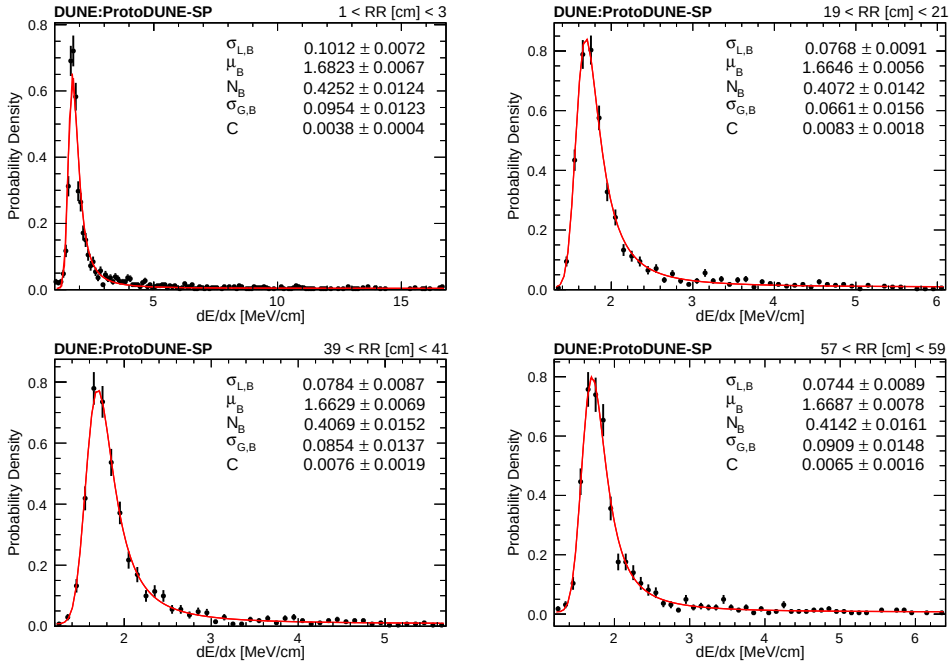

Figure 6.5: Background distribution for different residual range slices. The red line corresponds to a Landau-Gauss (plus constant) fit. The constant is added to take into account the homogeneous layer of counts covering all the X-axis, which would have strongly driven the fit otherwise.

of Figure 6.3, or the ones visible just at the right of the main peak in Figure 6.5-top-left, or the layer of points covering all the X axis homogeneously in each slice of Figure 6.5). Furthermore, these regions of points overlap with each other when the whole sample is represented. In other words, describing appropriately this region between both peaks is not easy. However, it is necessary, because the fit procedure (which will be explained in the next section) is a maximum likelihood fit, thus heavily driven by low statistics. In order to find an appropriate description, the following approach was developed: once the signal and background descriptions were known, the whole sample was fitted to the fixed signal and background distributions with and additional contribution, meant to consider this non-yet-fitted regions.

Several options for this extra contributions were tried. The first one was, of course, a Gaussian function, provided that, in general, any distribution with sufficiently high or sufficiently low statistics can be fitted to a Gaussian. It worked well when signal and background contributions were fixed, but it did not work when everything was left free in the last stage of the fitting algorithm.

Next option was, for the sake of coherence, another Landau-Gauss distribu-

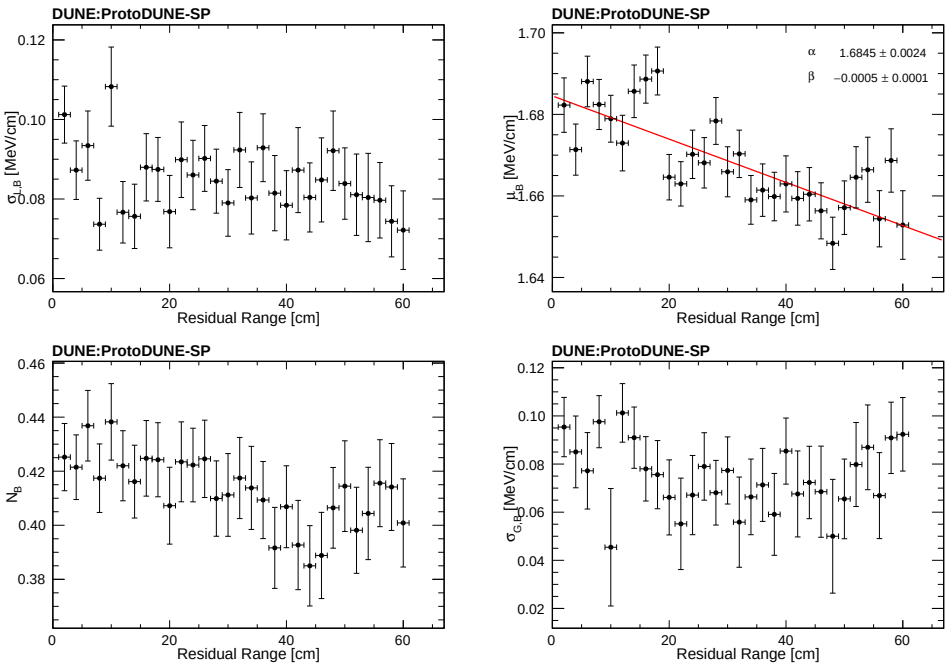

Figure 6.6: (Almost non) dependence of the Landau-Gauss parameters with the residual range. The error bar is given by the fit result.

tion, which worked well in this stage and also in the last stage of the fitting procedure. Each residual range slice was fitted then to the (fixed) signal plus background distribution plus an additional Landau-Gauss function with no constraints to its parameters. Then, the dependence of each family of parameters with the residual range was studied. Only a clear dependency was found for σ_L (shown in Figure 6.7):

$$\sigma_{W,L}(x) = \frac{\alpha}{x+1} + \beta, \tag{6.5}$$

whilst the other three parameters, μ_W, N_W and $\sigma_{W,G}$ were left as constants across slices.

6.2.2 Minimization Procedure

Now that every family of parameters has been parametrized as a function of RR, we can proceed to explain the fitting procedure. Since the 1D $\frac{dE}{dx}$ histograms represent counts, the fit is based in a maximum likelihood estimation method

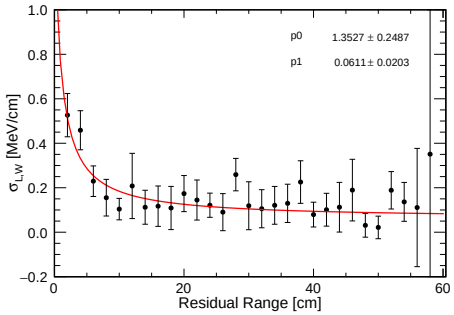

Figure 6.7: σ_L dependence for the what-is-left contribution.

[173] in which the function l is maximized

$$l = \sum_i \sum_j P\left[f\left(RR_i, \frac{dE}{dx}_j\right); M\left(RR_i, \frac{dE}{dx}_j\right)\right], \tag{6.6}$$

where i runs over RR slices and j runs over $\frac{dE}{dx}$ bins. f is the measured distribution and it is normalized at every RR such that

$$\sum_j f\left(RR_i, \frac{dE}{dx}_j\right) = 1; \tag{6.7}$$

M is the proposed model, and is given by

$$M\left(RR_i, \frac{dE}{dx}_j\right) = \sum_{k=B,W,S}\left[N_{i,k}\mathcal{LG}(\frac{dE}{dx}_j; \mu_{i,k}, \sigma_{i,k;L}, \sigma_{i,k;G})\right], \tag{6.8}$$

where subscripts B, W and S refer to background, what-is-left and signal contributions, respectively. $\mathcal{LG}$ represents the Landau-Gauss distribution. Implicit RR dependence is assumed for each parameter μ_k, $\sigma_{k,L}$, and $\sigma_{k,G}$, following the parametric functions described in the previous sections. The model is normalized at each slice so that

$$N_{i,B} + N_{i,W} + N_{i,S} = 1. \tag{6.9}$$

Finally, P represents the Poisson probability density function (p.d.f)

$$P(n, m) = \frac{m^n e^m}{n!}. \tag{6.10}$$

In other words, we look for the set of parameters described in the previous sections that make the distribution M more likely to have generated the measured distribution f slice by slice and bin by bin.

The minimization procedure is done with the program TMinuit of the ROOT software [174], concretely using the MIGRAD algorithm [172]. It is a variable-metric method with inexact line search, a stable metric updating scheme, and checks for positive-definiteness. The main weakness, as previously stated, is that it depends heavily on the knowledge of the first derivatives, and it is very likely to fail if they are very inaccurate or sensitive.

6.2.3 Fit Algorithm

Although the Coherent Fit allows to substantially reduce the number of parameters used to characterize the K^+ energy loss and consider correlations, it is needed to develop a proper algorithm that guarantees the convergence of the fit in MC and data. Such algorithm proceeds as follows:

1. MC is separated in signal and background distributions. Signal is fitted incoherently at each RR slice (as shown in Section 6.1). From the obtained results, a first approximation of the coherent parameters can be done. Repeat for background.

2. MC signal is fitted coherently across all RR slices using as a seed for the fit the results obtained in 1. Repeat for background.

3. MC signal and background are left constant to the values obtained in 2 to estimate the best description for the so far non-considered part of the distribution (a.k.a what-is-left).

4. The whole MC sample is fitted coherently using as a seed the results obtained in 2 and 3.

5. Data sample is fitted coherently using as a seed the results obtained in 4.

In this way, the estimation of the parameters is guided from what is known (MC true information) to what is unknown (data samples).

6.3 Fit Results

The Coherent Fit approach provides a good convergence for MC and data as well, with a well-defined positive error matrix. In Figure 6.8 an example of the fits is presented. All histograms with their corresponding fits can be found in Appendix A. We can make here some general appreciations:

- The pulls show in general a good behaviour, being distributed between ± 1.

- The statistical fluctuations are more evident in data than in MC. Even though data and MC have similar statistics, having MC thinner distributions makes them smoother.

- The model has problems to describe the far right end of some of the histograms, since the Landau-Gauss functions tend to zero whereas the homogeneous layer of entries covering the X axis does not. This happens for histograms where the X axis extends further away from the peaks' region, as in Figures A.13, A.14 or A.24. It was considered the option to add a constant to take care of that effect, but then normalizing the model would have been more complicated. Nevertheless, this effect is small on the overall result of the fit, as seen in the pulls, mainly because these regions are indeed far away from the peaks we are trying to describe.

- The region between peaks is better described in data than in MC. This is due to the resolution of the peaks being worse in data than in MC, and it happens that the main two peaks are covering almost completely that region.

- The what-is-left contribution behaves differently in data than in MC. This a consequence of what was explained in the last point: this contribution was added to account for the region between peaks. Since this region is not well defined in data and can be covered by the two main contributions, the third one is somehow hidden below the main background peak and has a small effect. On the other hand, in MC, this third contribution is placed between peaks because this region is more clear and needs to be considered. An agreement had to be found to describe equally data and MC, and this option was the one working properly in both samples.

- Particularly, the model has problems to describe the last slice in MC (see Figure A.30).

Despite these previous comments, it is important to notice here that just using 17 parameters (8 for signal, 5 for background, and 4 for what-is-left) it has been possible to fit 30 residual range slices to a sum of three Landau-Gauss distributions each, which would have used 360 parameters if they had been fitted incoherently. Also, it is also important to remind that the displayed fits are not the result of individual fits, but the result of a single global fit of the coherent

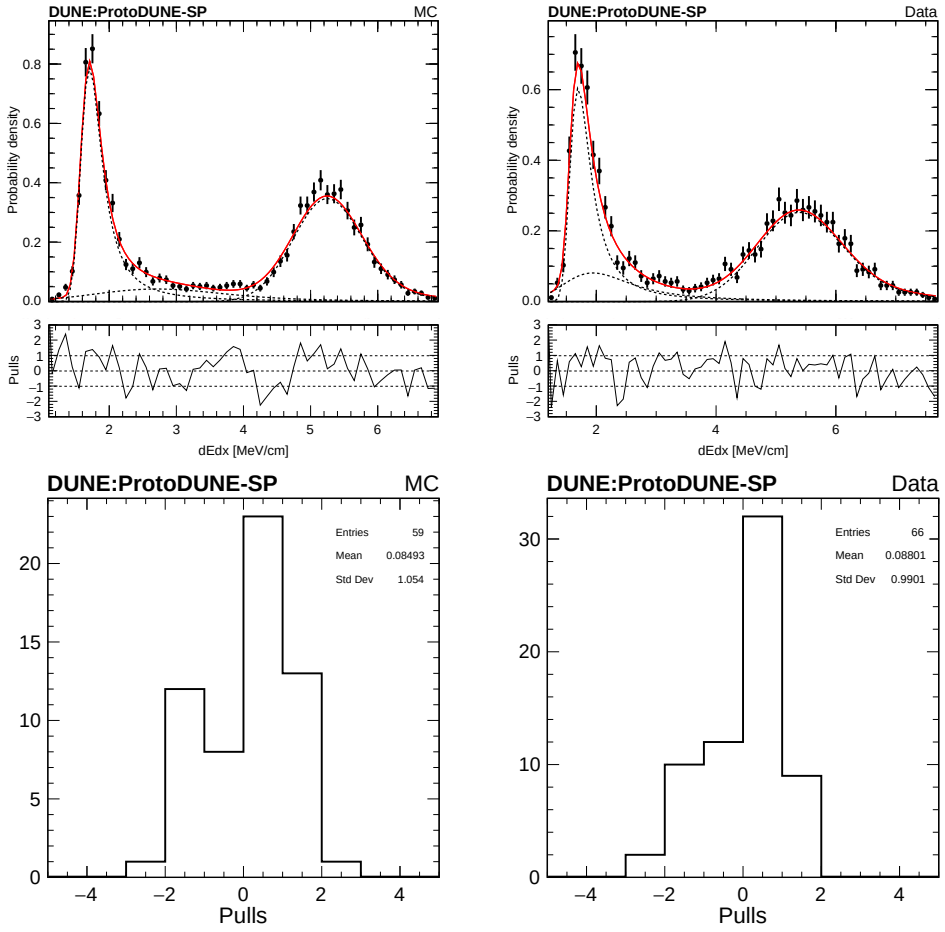

Figure 6.8: Coherent Fit result for the slice corresponding to residual ranges between 5 and 7 cm. The dashed lines represent the individual contributions. The bottom histograms correspond to the pulls of the fits above. Left: MC. Right: data.

parameters: this ensures that all information has been used, and that all the slices have an effect on others.

In the following subsections, the different parametric functions of the signal distribution will be discussed.

6.3.1 $\sigma_{S,L}$ Coherent Fuction

In Figure 6.9 the $\sigma_{S,L}$ is presented for data and MC. The fact that data presents a larger width than MC is not a surprise, since this could be seen directly from the one-dimensional histograms. In the Table 6.1 the values obtained for the coherent parameters for data and MC are presented (remember that $\sigma_{S,L}$ is described by Equation 6.1), and in Table 6.2 the correlation coefficients obtained from the Coherent Fit. The error of the graph is propagated by throwing random Gaussian numbers for each parameter following the correlation coefficient.

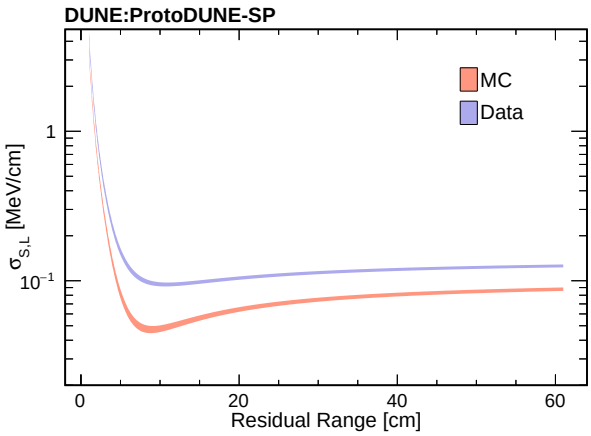

Figure 6.9: $\sigma_{S,L}$ parametric function for data and MC. The band represents the 1σ statistical error.

Figure 6.10 shows a comparison between the MC $\sigma_{S,L}$ coherent function and the $\sigma_{S,L}$ result of fitting the true signal histograms incoherently. It can be observed a similar shape, it both cases, but the coherent function presents in general a larger value of the Landau's width.

6.3.2 $\sigma_{S,G}$ Coherent Fuction

In Figure 6.11 the $\sigma_{S,G}$ is presented for data and MC. As in the previous case, data presents a larger width than MC. In the Table 6.3 the values obtained for the coherent parameters for data and MC are presented (see Equation 6.1), and

Table 6.1: Parameters describing the $\sigma_{S,L}$ coherent function for data and MC. Errors shown are statistical.

	α (MeV cm)	β (MeV/cm)
MC	4.48 ± 0.14	0.103 ± 0.002
Data	5.4 ± 0.2	0.141 ± 0.003

Table 6.2: Correlation coefficients for data and MC for the $\sigma_{S,L}$ parameters extracted from the Coherent Fit.

	MC		Data	
	α	β	α	β
α	1	-0.242	1	-0.364
β	-0.242	1	-0.364	1

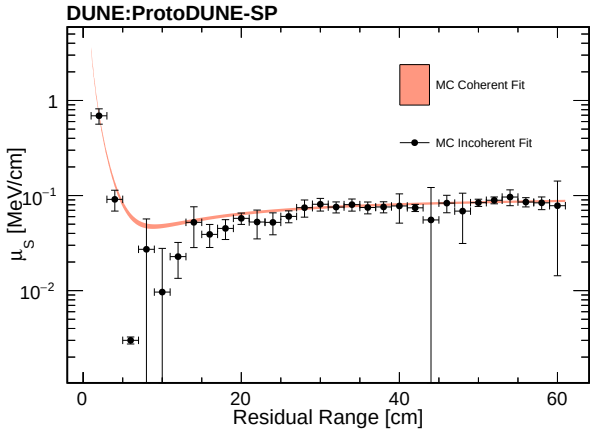

Figure 6.10: $\sigma_{S,L}$ parametric function and incoherent $\sigma_{S,L}$ values obtained for MC.

in Tables 6.4 the correlation coefficients obtained from the Coherent Fit. As before, the error of the graph is propagated numerically.

Figure 6.12 shows a comparison between the MC $\sigma_{S,G}$ coherent function and the $\sigma_{S,G}$ result of fitting the true signal histograms incoherently. In this case, the coherent function is below the result of the incoherent fits, compensating the behaviour observed for the $\sigma_{S,L}$. This points that the global fit favours more the Landau behaviour than the Gaussian behaviour.

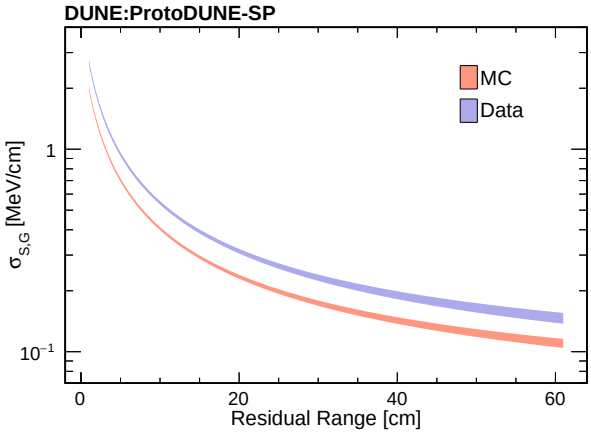

Figure 6.11: $\sigma_{S,G}$ parametric function for data and MC. The band represents the 1σ statistical error.

Table 6.3: Parameters describing the $\sigma_{S,G}$ coherent function for data and MC. Errors shown are statistical.

	α (MeV)	β (MeV/cm)
MC	3.95 ± 0.09	0.046 ± 0.005
Data	5.31 ± 1.4	0.061 ± 0.008

Table 6.4: Correlation coefficients for data and MC for the $\sigma_{S,G}$ parameters extracted from the Coherent Fit.

	MC		Data	
	α	β	α	β
α	1	-0.717	1	-0.762
β	-0.717	1	-0.762	1

6.3.3 μ_S Coherent Fuction

It is not accidental that, having presented during all this dissertation the Landau-Gauss parameters in the order of σ_L, μ and σ_G, μ_S is presented now the last. It is, of course, the most important result of this work, thus deserving the maximum expectation possible. But, at the same time, it is presented the last one because there is an unexpected result. In Figure 6.13 the signal MPV obtained for data and MC is presented, in Table 6.5 the fit results and in Table 6.6 the correlation coefficients. As it can be seen, there is good agreement between both for larger residual rangers, however there is a clear difference when the residual range goes to zero: data presents larger values of $\frac{dE}{dx}$ than MC.

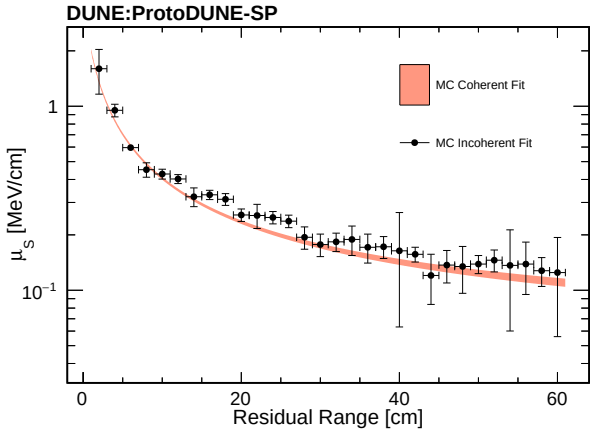

Figure 6.12: $\sigma_{S,G}$ parametric function and incoherent $\sigma_{S,L}$ values obtained for MC.

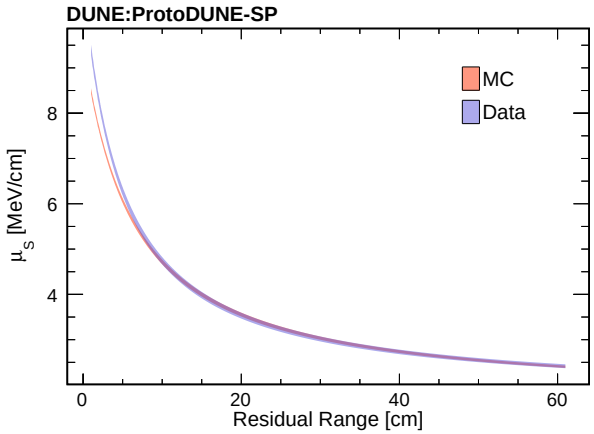

Figure 6.13: μ_S parametric function for data and MC. The band represents the 1σ statistical error.

In Table 6.5 the results obtained for each parameter and its error are presented. Differently to what was done for the previous coherent parameters, in this case a more comprehensive study of the errors has been done. Once Minuit finalizes the minimization procedure, it provides what is known to be a parabolic approximation of the error. This means that it computes the error of the parameters assuming that the function that has just been minimized (either a χ^2 or a likelihood) behaves as a parabola. These are the errors that have been presented previously. However, if the found minimum is robust and has a well defined error matrix, one can call the MINOS algorithm [175, 176] for a comprehensive analysis of the errors. MINOS does not assume any shape of the likelihood function, instead it just follows its shape until it crosses the value $(min + n\sigma)$, where min is the minimum of the minimized function and n the number of statistical significances desired. In the case of a χ^2 minimization process, σ corresponds to 1; for a maximum likelihood minimization, σ corresponds to 0.5. When there are more than one free parameters, the MINOS error of a parameter is defined in the following way: the change in the value of the parameter which causes min' to increase $n\sigma$, being min' the minimum of the minimized function with respect to all of the other free parameters. In this way, MINOS is considering not only the shape of the function, but also non-linearities and correlations between parameters. Usually, the errors provided by MINOS are asymmetric. This computation is very time consuming, so it was only performed for the μ_S parameters. As it can be seen, in MC, the α, β and γ parameters have a 1σ relative statistical uncertainty of 1%, 2% and 0.2% respectively, whereas in data they have a 2%, 3% and 0.4%. The difference is probably due to the wider distributions of data, for which statistical fluctuations become more evident.

In Figure 6.14 the residual range slices corresponding to the region with a different behaviour of the MPV in data and MC are presented. As it can be seen, there is a clear discrepancy between both samples for low residual ranges, but when residual range is close to 10 cm this discrepancy starts to disappear. This means that the observed difference in μ_S is not a whim of the fitting procedure but a real effect that the Coherent Fit is highlighting.

Finally, Figure 6.15 shows a comparison between the MC μ_S coherent function and the μ_S result of fitting the true signal histograms incoherently. A good agreement is observed, remarking what was said before: the observed difference between data and MC is a real effect and it is not generated by the fitting algorithm.

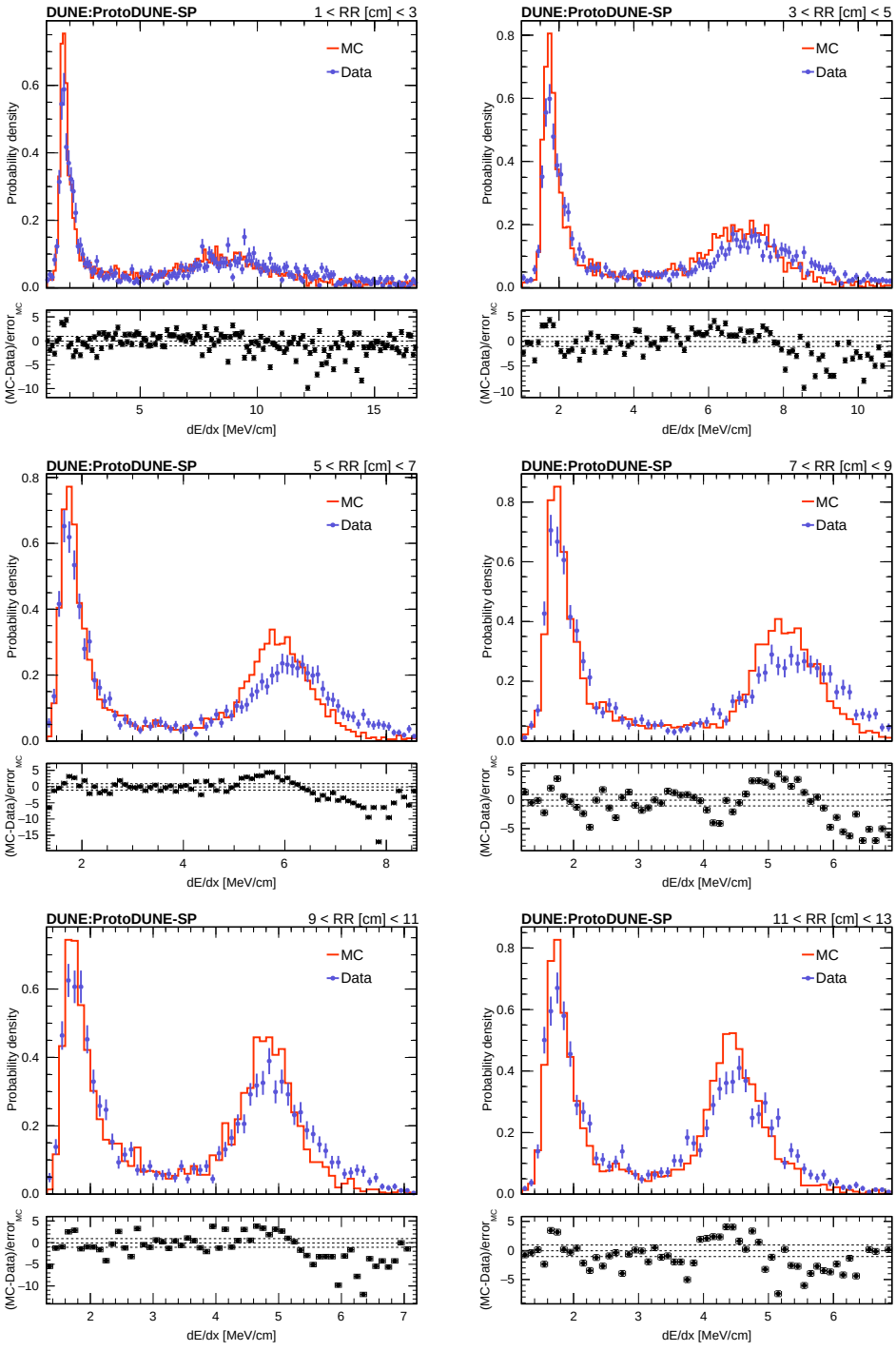

Figure 6.14: Comparative of data and MC of the residual range slices for the region of discrepancy between both samples. It can be observed how for lower values than 9-11 cm, the difference is more evident.

Table 6.5: Parameters describing the μ_S coherent function for data and MC. Errors shown are statistical and have been computed by MINOS. Even though positive and negative errors were slightly different, their first significant digit was equal.

	α (MeV/cm)	β	γ
MC	-3.96 ± 0.04	0.160 ± 0.003	-1.420 ± 0.003
Data	-4.63 ± 0.08	0.208 ± 0.006	-1.375 ± 0.005

Table 6.6: Correlation coefficients for Data and MC for the μ_S parameters extracted from the Coherent Fit.

	MC			Data		
	α	β	γ	α	β	γ
α	1	-0.881	-0.816	1	-0.966	-0.893
β	-0.881	1	0.466	-0.966	1	0.754
γ	-0.816	0.466	1	-0.893	0.754	1

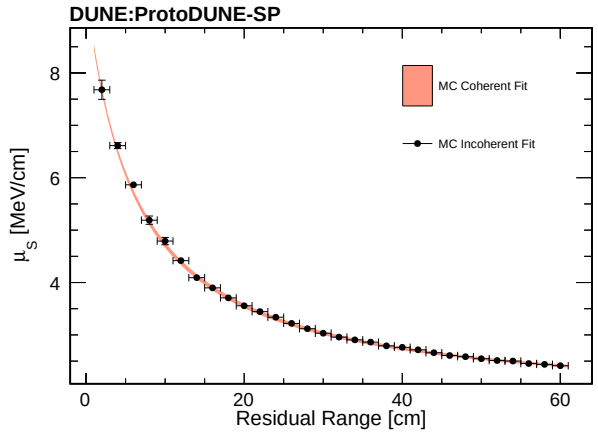

Figure 6.15: μ_S parametric function and incoherent μ_S values obtained for MC.

6.3.4 Likelihood Weight

Looking at Figure 6.13 it may feel strange the obtained error band. Seeing the different slices, it is clear than the signal distribution is much widther for lower residual ranges than for larger. One would have expected to find the opposise behaviour: larger errors for lower residual ranges than for larger. However, some considerations need to be done. First, the available statistics for the first slices are larger than for the last slices. This is because all tracks have and end, meaning that all selected tracks contribute to the first slices, but not all of them contribute to the last ones. Because of that, the statistical weight during the minimization procedure is larger for lower residual ranges than for larger, as it can be seen in Figure 6.16. Second, even though the signal peak is wider for the first slices, it is clearly more separated from the background peak than for the last slices. Considering this two things one can understand why the statistical error shown presents such shape.

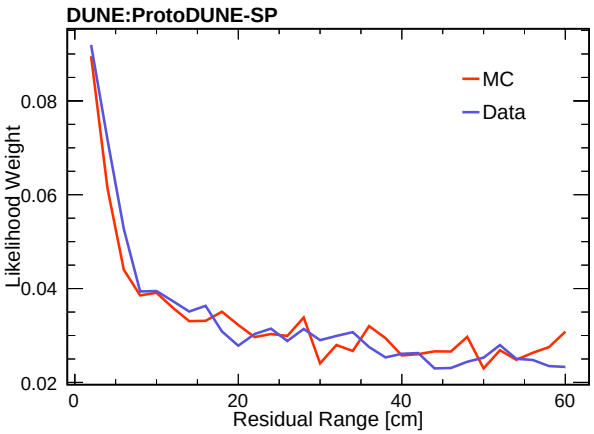

Figure 6.16: Likelihood weight with respect to the full likelihood as a function of the RR slice.

6.3.5 Signal and Background: combined result

Even though we are still missing the evaluation of systematic unceratinties, it is worth now to have a look at the two-dimensional distribution of the $\frac{dE}{dx}$ against the residual range, in which the result of the Coherent Fit has been superimposed (see Figure 6.17). As it can be appreciated, the agreement between the fitted model and signal and background contributions is quite good, for both data and MC.

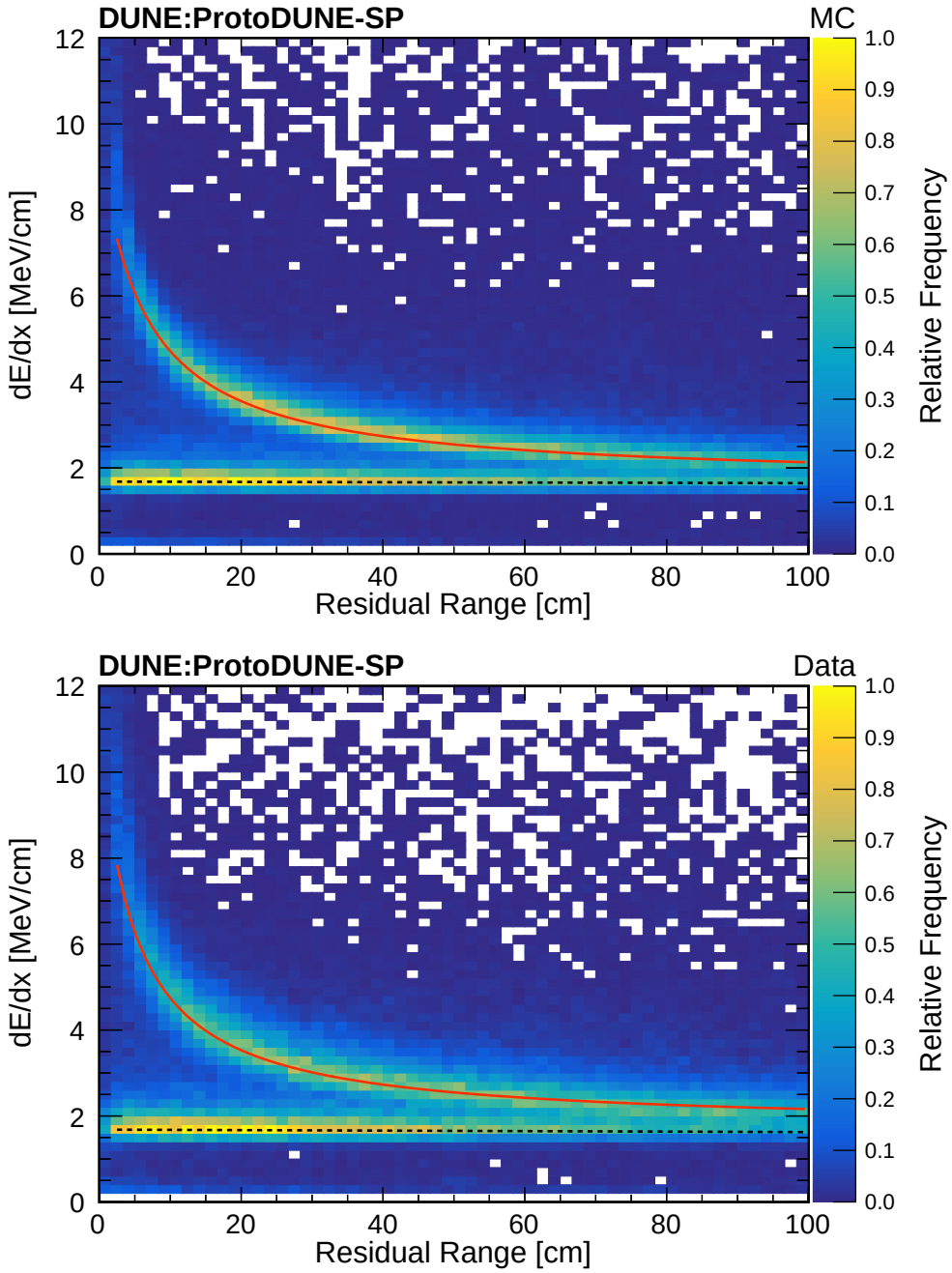

Figure 6.17: $\frac{dE}{dx}$ distribution as a function of the residual range. Top: MC. Bottom: data. The red line represents the MPV, and the black dashed line represents the MPV of the background, both obtained from the Coherent Fit.

6.4 Fit Stability

The fit algorithm explained above consists in a set of sequential steps that allows us to go from what is known (MC true information) to what is unknown (data). Before applying the coherent fit to the whole MC sample, we estimate the seeds for the parameters to be used during these steps: first, incoherent fits are applied to the residual range slices of signal and background, then both samples are fitted coherently on its own, and lastly the last contribution (what-is-left) is estimated. With this, the seeds to be used to fit the whole MC sample are computed. However, that estimation has an associated uncertainties (of the order of few percent), so one could wonder how much stable is the algorithm with respect to these uncertainties. Or, in other words, what is the systematic error associated to the fitting procedure.

In order to ensure that the fit algorithm provides a good convergence within the range of these initial estimation, or in case it doesn't, to estimate the confidence in the results we are obtaining, we repeat the last stage of the fitting algorithm (the fit to the whole MC sample) in multiple toy experiments, in which each seed of each parameter has been randomly varied within their estimation error, independently of one another. After 100 toys, the maximum spread on the three μ_S coherent parameters is fit results is below 0.05, 0.07 and 0.01% for α, β and γ (see Figure 6.18). The maximum spread is defined as the maximum variation obtained for any two toy experiments, divided by the mean value obtained for all of them. This means that the systematic error associated to the fit algorithm is negligible. Furthermore, this means that the developed procedure is robust, and that the likelihood function is stable, producing almost identical results from one toy to another.

The results presented in this Chapter were not considering yet the effect of the detector systematic uncertainties. They will be evaluated in the following chapter, and the final results of the $\frac{dE}{dx}$ measurement will be shown in Chapter 8.

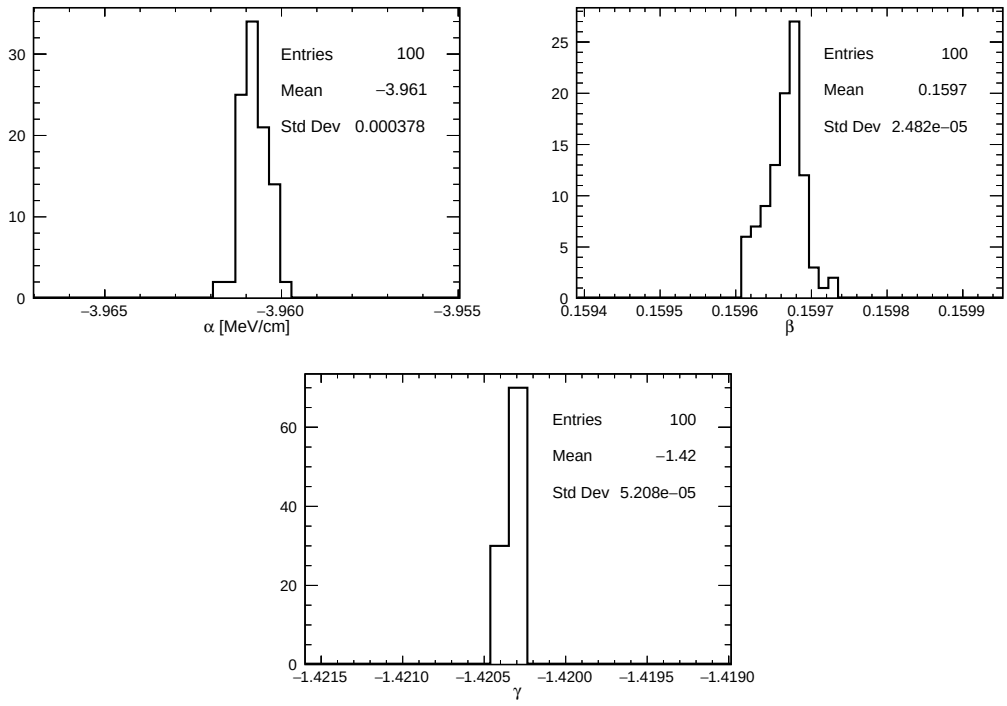

Figure 6.18: Distribution obtained for the μ_S coherent parameters in the stability studies.

7 Evaluation of Systematic Uncertainties

The presence of those seeking the truth is infinitely to be preferred to the presence of those who think they've found it.

— Terry Pratchett, *Monstrous Regiment*

The results presented so far were considering only statistical uncertainties. The effect of systematic uncertainties will be discussed in this Chapter, which is organised as follows: Section 7.1 describes how systematic uncertainties can affect our analysis; the different methods to propagate these uncertainties are presented in Section 7.2; finally, the different systematic sources are evaluated from Section 7.3 to 7.9. The final results of this dissertation accounting for the systematic unceratinties studied here will be presented in Chapter 8.

7.1 Effect of Systematic Uncertainties

Systematic uncertainties include –forgive the repetition– systematic differences between data and MC after the entire simulation process (usually at reconstruction level), MC imperfections, and inaccuracies associated to some magnitudes that are used during the analysis. Propagating them consists in studying their effect on the final number of selected events and on the $\frac{dE}{dx}$ fitting procedure described in the last chapter. Ideally, one should study the effect of varying basic parameters in the MC (like the electron lifetime or the recombination effect) so that their effect can be propagated to the entire simulation and reconstruction chain, finally affecting all physics quantities used in the event selection and the $\frac{dE}{dx}$ study. In this way, all correlations between the different effects would be taken into account. However, this requires a deep knowledge of all the underlying physics processes involved, in both data and MC, and large computational and time resources to generate all possible outcomes, which is impractical. Consequently, what is done in practice is to characterize some derived parameters used during the event selection for data and MC (as the calorimetric calibration constants) so that the differences in these parameters can be propagated.

As an example of this method the simulation of the beam plug of Proto-DUNE-SP could be mentioned. It could be possible that the MC simulation does not reproduce exactly the pressure of the nitrogen inside the plug, which is exposed to variations due to atmospheric conditions, leading to different interaction probabilities of the beam particles in MC with respect to data. This, at the same time, could generate differences when Pandora tries to identify the beam particle, resulting in asymmetries between data and MC for the different particle species and momenta. For example, it could be possible that MC has a better efficiency than data identifying pions in comparison to kaons and protons, producing as a result a larger proportion of pion beam events selected in MC than in data. In view of this situation, one could try to properly characterize the nitrogen pressure accounting for the multiple effects in it, and re-run the MC production so that it could better reproduce the data; or simply compare the beam particle selection efficiency for data and MC and propagate the possible differences.

Data-MC dissimilarities can be observed in the mean and in the resolution of the reconstruction observables, as in the case of the calorimetric calibration constants mentioned above. These constants depend on the SCE and lifetime corrections, which are not exactly reproduced in MC. Consequently, it may be possible that the accuracy determining them is different in data and MC. Ultimately, these differences alter the number of events passing the cuts using the calorimetric information.

When quantifying these differences, associated uncertainties are obtained. Thus the propagation of systematics has two steps: first, to correct the simulation so that it reproduces better the observed data (if needed); and second, to apply variations that account for the uncertainty in the corrections. Consequently, they are propagated by multiple random throws (a.k.a. toy experiments). This second step is the one accounting for the effect of the systematic uncertainties, since it is taking into account all possible outcomes of the experiment. In general, any systematic uncertainty can be propagated as a weight or as a variation.

Weight systematics are used for general event properties (normalisations) or reconstruction efficiencies. After the event selection, a weight different than 1 is assigned to each event such that its contribution when represented in an histogram is different than the original one. The weight is variated from toy to toy to consider the associated uncertainty. For the Coherent Fit procedure previously explained, this implies that the same event will contribute differently to the $\frac{dE}{dx}$ histograms from one toy to another, thus a different set of 1D histograms is obtained for each throw.

Variation systematics account for uncertainties in continuous magnitudes

Table 7.1: Summary of systematic uncertainties considered.

Systematic error source	Propagation model	Correction
Calorimetry Calibration	Variation	No
SCE (geometric level)	Variation	No
Recombination	Variation	Yes
Broken tracks in APAs borders	Efficiency-like	Yes
Beam PID Efficiency	Efficiency-like	Yes
Beam species composition	Normalisation	Yes
Beam momenta composition	Normalisation	Yes

and/or reconstructed observables. These magnitudes (and their derived quantities) are varied for each toy experiment previous to the event selection. This means that a given event may or may not pass the selection in different pseudo-experiments, and it will have a different value for each of them when represented in a histogram. Thus, migration of events from bin to bin may happen. As in the previous case, a different set of histograms is obtained for each throw.

As a result of the propagation of the different systematic uncertainties, we obtain a different number of events passing the selection from one toy to another, and this variation of events is the effect of the systematic over the selection. We also obtain a different set of $\frac{dE}{dx}$ histograms for each toy. The Coherent Fit procedure is then applied to each set and a different result is obtained for each pseudo-experiment. When all results corresponding to, for example, the MPV parameters, are represented in a histogram, the width of the distribution is a direct measurement of the effect of a given systematic uncertainty over these parameters (and hence also over the MPV).

In both weight and variation systematics, a Probability Density Function (pdf) needs to be assumed. In all cases treated here a Gaussian pdf will be used. In Table 7.1, a summary of the systematic uncertainties considered for this analysis is presented. They will be described in the following subsections, after the different propagation methods are explained.

7.2 Propagation Models

7.2.1 Efficiency-like systematics

Efficiency-like systematics are computed by comparing well-understood control samples (CS) in data and MC, so that differences in tracking/reconstruc-

tion/identification between data and MC can be measured. However, the analysis samples do not satisfy (in general) the same conditions as the control samples, so a model is needed to extrapolate the data-MC differences from the control sample to the analysis sample. Provided that a good control sample is available, the simplest approach is to assume that the ratio of efficiencies in the control sample is the same that in the analysis sample:

$$\frac{\epsilon_{data}}{\epsilon_{MC}} = \frac{\epsilon^{CS}_{data}}{\epsilon^{CS}_{MC}} \rightarrow \epsilon_{data} = r_{CS}\epsilon_{MC}\,, \tag{7.1}$$

where ϵ_{data} and ϵ_{MC} are the data and MC efficiencies in the analysis sample, and ϵ^{CS}_{data} and ϵ^{CS}_{MC} are the data and MC efficiencies in the control sample, respectively. It is also deduced that r_{CS} is the data/MC efficiency ratio in the control sample. When a MC object has been properly (or efficiently) reconstructed/matched/identified, it has to be weighted by the efficiency ratio in such a way that the corrected efficiency is the one of the real data:

$$W_{eff} = r_{CS}\,. \tag{7.2}$$

On the contrary, when a MC object has not been treated efficiently, it contributes to the inefficiency and has to be weighted by the ratio of inefficiencies:

$$W_{ineff} = \frac{1-\epsilon_{data}}{1-\epsilon_{MC}} = \frac{1-r_{CS}\epsilon_{MC}}{1-\epsilon_{MC}}\,. \tag{7.3}$$

Notice here that the efficiency weight depends only on the control sample whereas the inefficiency weight depends on the MC efficiency of the analysis sample.

In order to propagate a systematic instead of doing a simple correction, a variation has to be done from toy to toy, as commented above. This variation has the form of

$$W'_{eff} = r'_{CS} = r_{CS} + \delta \cdot \sigma_{r_{CS}}, \tag{7.4}$$

where δ is the variation in number of standard deviations and can assume positive and negative values, and $\sigma_{r_{CS}}$ is the uncertainty associated to the efficiency ratio computed using the control samples. This variation is also applied to the inefficiencies,

$$W'_{ineff} = \frac{1-r'_{CS}\epsilon_{MC}}{1-\epsilon_{MC}}. \tag{7.5}$$

In the case that more than one MC object contributes to the efficiency (or inefficiency) of an event, the weight of the event is computed as the product of efficiencies (or inefficiencies) of the different MC objects. Overall, a single weight is computed for each event, so the selection does not need to be redone.

7.2.2 Normalisation systematics

This method is applied when the systematic uncertainty accounts for a general property of the event that is different for data and MC. Each MC event is weighted following the variation suggested by the systematic error studies:

$$W = W_0(1 + \delta \cdot \sigma_W), \tag{7.6}$$

where W is the weight to be applied to the MC event, W_0 is the value of the correction weight (1 when no correction is needed; different from 1 if a correction is needed), σ_W is the associated uncertainty of the correction and δ is the number of variations in number of standard deviations. As in the previous case, there is one weight per event, meaning that the selection does not need to be redone.

7.2.3 Reconstructed observable variation

This method is used to consider differences between data and MC in the mean or resolution of continuous variables that affect the event selection. In general, the magnitude variation is applied as follows:

$$x' = x + \Delta x + \delta \cdot \sigma_{\Delta x}, \tag{7.7}$$

where x is the nominal value of the MC variable, Δx is the correction that should be applied such that the mean of the MC matches the one of the data, $\sigma_{\Delta x}$ is uncertainty associated to the correction, and δ is the variation in number of standard deviations. In the case that the mean of data and MC coincide but the resolution is different, Δx would be 0 and $\sigma_{\Delta x}$ would be the quadratic difference between data and MC.

Since the variables change from one toy to another, the selection has to be redone for each toy experiment so that the events passing or discarded during the selection are properly considered.

7.3 Calorimetric calibration

As previously explained in Section 3.8, the TPC's response is affected by physics processes that may deteriorate the detector performance, so it has to be calibrated. From the raw $\frac{dQ}{dx}$, the $\frac{dE}{dx}$ is obtained as

$$\frac{dE}{dx} = \frac{\rho\mathcal{E}(x,y,z)}{\beta'}\left[\exp\left(\frac{\beta' W_{ion}\frac{dQ}{dx}_{Calibrated}}{\rho\mathcal{E}(x,y,z)C_{cal}}\right) - \alpha\right], \tag{7.8}$$

with

$$\frac{dQ}{dx}_{Calibrated} = \frac{dQ}{dx}_{SCE+\tau} C_{YZ} C_X C_{Norm}, \tag{7.9}$$

meaning that several steps are applied to the $\frac{dQ}{dx}$ before it is fully calibrated. These steps are:

- SCE correction. It modifies the position of each hit and therefore their pitch. Thus, $\frac{dQ}{dx}$ value is affected since dx is related to the pitch. The correction depends exclusively on the position of each hit.
- Lifetime correction. Change attenuation from the production point to the APAs depends on the electron lifetime. A change on this quantity affects the magnitude of the correction for the $\frac{dQ}{dx}$. It depends on the X position of each hit.
- Local corrections. After the two steps above, local corrections are computed to erase any remaining fluctuations of the TPC response and accounts for other local effects. Corrections are computed first for YZ voxels and then for X voxels. They depend on the hits' position and the hits' $\frac{dQ}{dx}$. They are computed for each data run.
- Run normalisation. All runs are normalized to a reference value taken arbitrarily for the detector.
- ADC calibration. It converts ADC counts into number of electrons based on the absolute energy scale.

In order to study the systematic uncertainties associated to the entire calibration procedure, one can study the uncertainty on the computation of the calibration constants, and from that point, only consider the error associated to such constants. This simplifies the process since the $\frac{dQ}{dx}$ is multiplied by these constants and, once their error is known, the propagation is trivial. This approach is the one typically followed in the literature [101, 157], usually focusing on the systematic uncertainty of the local corrections. This is because these local corrections are supposed to absorb the inaccuracies on the SCE and lifetime calibrations.

These local corrections are computed using t_0-tagged muons that do not stop in the active volume, so that it can be assumed to be Minimum Ionizing Particles (MIPs). They are tagged because they cross either the cathode plane, the anode plane or the cosmic ray tagger. Each TPC volume is divided in voxels, and the

mean (or median or MPV) of the $\frac{dQ}{dx}$ distribution in each voxel is scaled to match the one of the whole volume. Fractional corrections are computed for each voxel and, in this way, the TPC response is completely homogenized along the entire volume. This procedure is performed in two steps: first in the YZ plane (each detector volume is divided into 16800 $5 \times 5 \times 360$ cm^3 voxels)

$$C_{YZ} = \frac{MPV[dQ/dx]_{run}}{MPV[dQ/dx]_{YZ,run}}\,; \tag{7.10}$$

and second in the X axis (the whole volume is divided into 144 slices of 5 cm) (see equations 7.10 and 7.11)

$$C_X = \frac{MPV[dQ/dx]_{run}}{MPV[dQ/dx]_{X,run}}\,. \tag{7.11}$$

To assign a systematic uncertainty to these constants, the following procedure was followed in MicroBooNE [157]: first, the constants are computed using all available tracks; second, the constants are computed again but now using subsamples of the tracks utilized in the first step, binning in the angle of the track with respect to the wires; and finally, the difference between the constants obtained in the two steps is taken as the systematic uncertainty. The result obtained was an increasing uncertainty with the binning angle. The cause of this is the alignment of the tracks with the wires: the more parallel the tracks are to them, the larger their pitch and their sensitivity to corrections.

This approach was reproduced in ProtoDUNE-SP [167]. Due to the limited available statistics, only two angular subsamples could be compared, and the average uncertainty on the $\frac{dQ}{dx}$ calibration was estimated to be 1% in the MC and 1.8% in the data. As a conservative choice, the uncertainty in the final $\frac{dE}{dx}$ has been 3% so far.

Alternatively to this method, one can directly propagate the uncertainty on the SCE and the lifetime corrections to the local calibration constants, providing a direct measurement of the uncertainty of these constants. This approach will be explained and followed in this analysis using information from the MC and the data run 5770.

7.3.1 Space Charge Effect on calibration constants

The SCE effect, as previously explained in Section 3.8.1, is generated by the constant high rate of cosmic rays crossing the detector. The argon nuclei are continuously being ionized, and the ions' drift velocity is lower than that of the electrons. This generates a total electric charge present inside the active volume

of the detector that is not zero, thus modifying the electric field within. This variation affects the drift of the electrons towards the APAs when a track crosses the detector, biasing its reconstruction [110]. As explained in Chapter 3, a 3D correction map was obtained with a data-driven method, which provides spatial and electric field calibrations using interpolation algorithms.

Variations on the SCE corrections can affect the computation of local constants in two different ways: first by changing the voxel to which a hit is contributing; second, by modifying the $\frac{dQ}{dx}$ of the hit (because of its pitch and the diffusion). In order to quantify this effect, the local calibration procedure is repeated in several toy experiments in which the SCE correction map is varied from one to another. The variations are done by Gaussian random throws with a 5% σ, since this is the estimated error of the SCE calibration [110]. One calibration constant per voxel is obtained for each throw. When all the values obtained for the different toys for a given voxel are represented in a histogram, the width of the distribution is a direct measurement of the effect of the SCE uncertainty on that calibration constant.

When this process is done for all voxels, two different uncertainty maps are obtained, one for YZ coordinates (corresponding to YZ local corrections, Figure 7.1 top left) and another one for X (corresponding for X local corrections, Figure 7.1 bottom). This computation is very time and memory consuming, so it was restricted to the beam side of the detector (where the majority of the analysis takes place).

As it can be observed, the effect of the SCE correction uncertainty is of the order of 0.5% for both XY and X calibration constants. This is due to the fact that SCE is smoothly parametrized and corrected, and the voxels used for the SCE evaluation are much larger than the voxels used for the corrections.

7.3.2 Electron lifetime effect on calibration constants

The electron lifetime correction accounts for the attenuation effect during electrons drifting towards the anode. The electron lifetime used is the one measured by the top purity monitor closest to the data taking period. The error associated to the charge ratio is 1.9% [106] (remember Equation 3.2). As for the SCE, this uncertainty can be propagated to the computation of the calibration constants using toy experiments. For each one of them, the charge ratio is varied by random Gaussian throws with a σ of 1.9%, and then the electron lifetime used to correct the charge attenuation is different from one toy to another. Note that the relationship between the charge ratio and the electron lifetime is not lineal, so the electron lifetimes used during the toy experiments will not form a symmetric

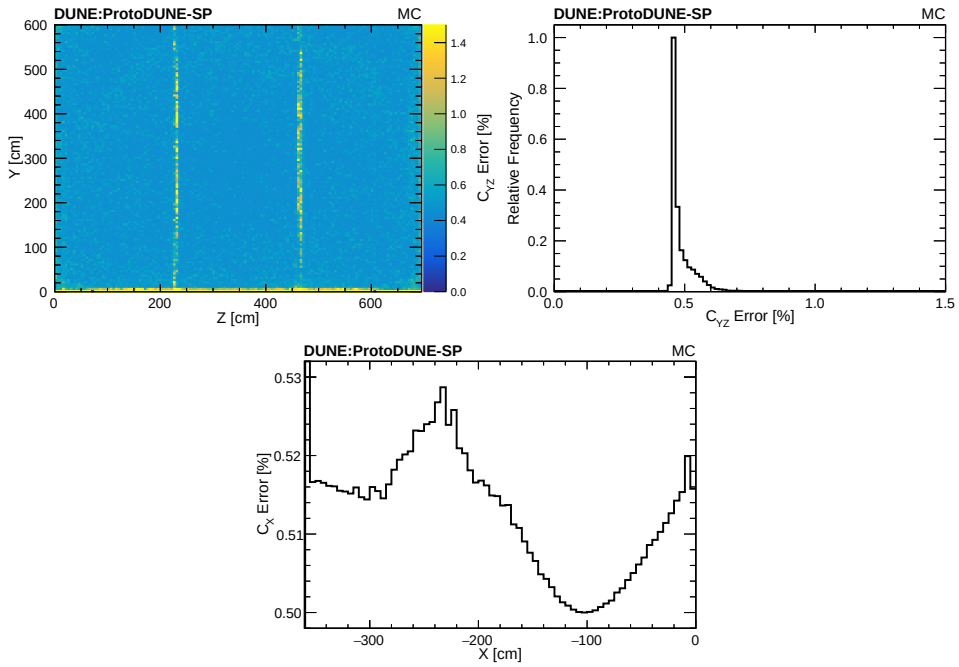

Figure 7.1: Systematic uncertainty propagation of the SCE on the local calibration constants. Top left: error in YZ corrections. Top right: one-dimensional projection of the plot on the left. Bottom: error in X corrections.

distribution.

During the 6 GeV data taking period, the average R_Q measured was 0.891 (that corresponds to $\tau \approx 20$ ms). During the 7 GeV runs, R_Q was found to be 0.720 ($\tau \approx 7$ ms). The MC simulation is done with a nominal τ of 35 ms, which corresponds to $R_Q \approx 0.936$. The effect of the R_Q uncertainty has been studied for these three different values in the MC sample, finding no significant differences. In Figure 7.2, the error maps are displayed for MC with $\tau = 35$ ms. It can be observed a similar effect than the generated by the SCE for the YZ corrections, whereas for the X corrections it is not only is larger in average, but also has a very well defined profile.

This profile may feel strange, considering that the charge attenuation increases the further away from the APAs (located at -360 cm in the X plot). Intuitively, one would have expected that the error on the correction of the attenuation effect generated a larger uncertainty in the corrections closer to the cathode (located at 0 cm in the X plot), and that this error would decrease towards the APAs. Ideally, after applying SCE and lifetime corrections, the $\frac{dQ}{dx}$ distribution versus the X coordinate should be flat and, under these circumstances, an error on the electron lifetime correction would generate this behaviour. How-

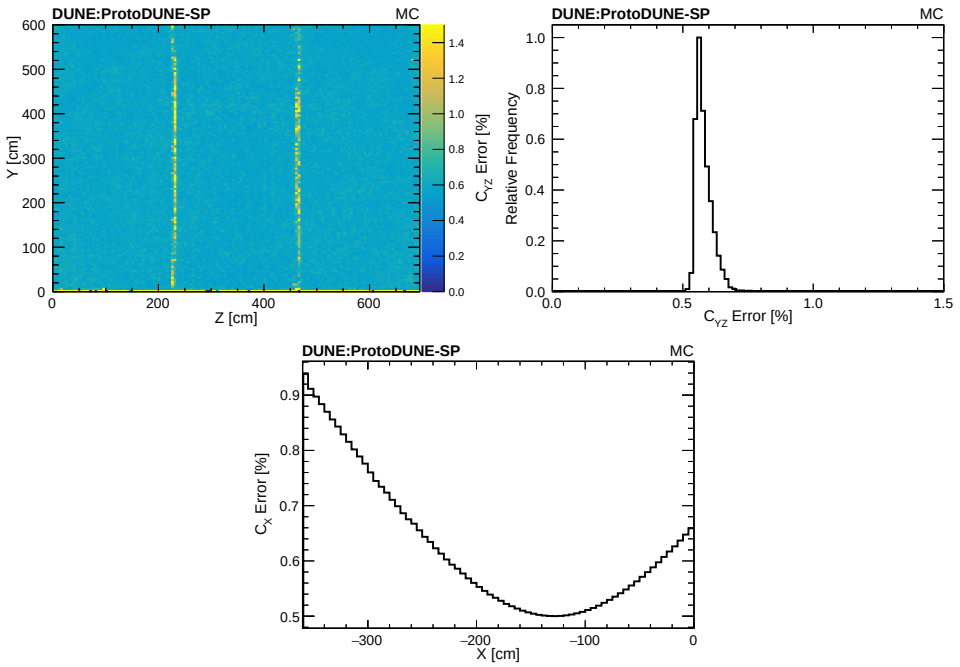

Figure 7.2: Systematic uncertainty propagation of the lifetime correction on the local calibration constants. Top left: error in YZ corrections. Top right: one-dimensional projection of the plot on the left. Bottom: error in X corrections.

ever, in our detector, after applying the SCE, lifetime and YZ calibrations, the diffusion effect is still present, which makes the $\frac{dQ}{dx}$ profile on the X axis non-flat (see Figure 7.3). The local corrections are relative corrections, meaning that they refer each voxel to the average value of the whole volume, which happens to be located around -110 cm. Variations of the electron lifetime are generating larger absolute variations of the $\frac{dQ}{dx}$ further away from the APAs, but the relative variation with respect to the average $\frac{dQ}{dx}$ is smaller, thus generating a smaller uncertainty on the X calibration constants and this unusual profile.

7.3.3 SCE and Electron Lifetime combined effect

The two effects described above can be propagated simultaneously to account for correlations or anti-correlations. In Figure 7.4 the effect on the YZ corrections are presented for data (concretely, run 5770) and MC. Two things can be highlighted here: first, that the combination of both effects in the MC generates a lower effect than the one presented by the electron lifetime uncertainty alone, meaning that they are slightly anti-correlated; second, that data and MC show a similar behaviour, although data shows a larger mean error (as expected, since the true

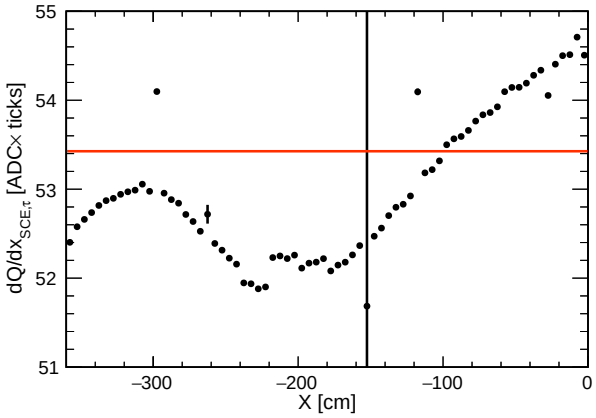

Figure 7.3: dQ/dx distribution along X axis after SCE and lifetime corrections. The non-flat profile is due to the diffusion effect. The red line represents the global MPV value.

corrections in data are not known).

The effect on the X corrections is presented in Figure 7.5. Both distributions have very similar profiles, although data presents larger uncertainties.

Since no specific position dependence can be observed for the uncertainty of the YZ calibration constants, one can take the MPV of the uncertainty in YZ and add it quadratically to the uncertainty in X constants, which do show a clear dependence with the X position. In this way, the systematic uncertainty associated to the $\frac{dQ}{dx}$ as a function of the position of each hit is the one presented in Figure 7.6. As MC uncertainty was slightly lower, the one to be used is the one of the data. As previously commented, this computation has been done exclusively to the beam side of the TPC, as it is where almost all our analysis takes place. Table 7.2 translates this plot into the systematic source to be used when propagating the systematic in the analysis. X position values have been written in absolute values so it can be used for the non-beam side of the TPC too, in case it is necessary.

The obtained systematic uncertainty for the calorimetry calibration is smaller that what was obtained using the MicroBooNE approach ($\sim 1.8\%$) for data, but similar for MC. Further studies of this approach are needed to understand angle dependences and run-by-run variations, so a proper estimation of the calibration uncertainty can be obtained for each data run. Since other ProtoDUNE-SP analysis do not consider the systematic effect on the recombination, the overall error over the $\frac{dE}{dx}$ is assumed to be 3%. However, the recombination effect will be directly studied on this dissertation.

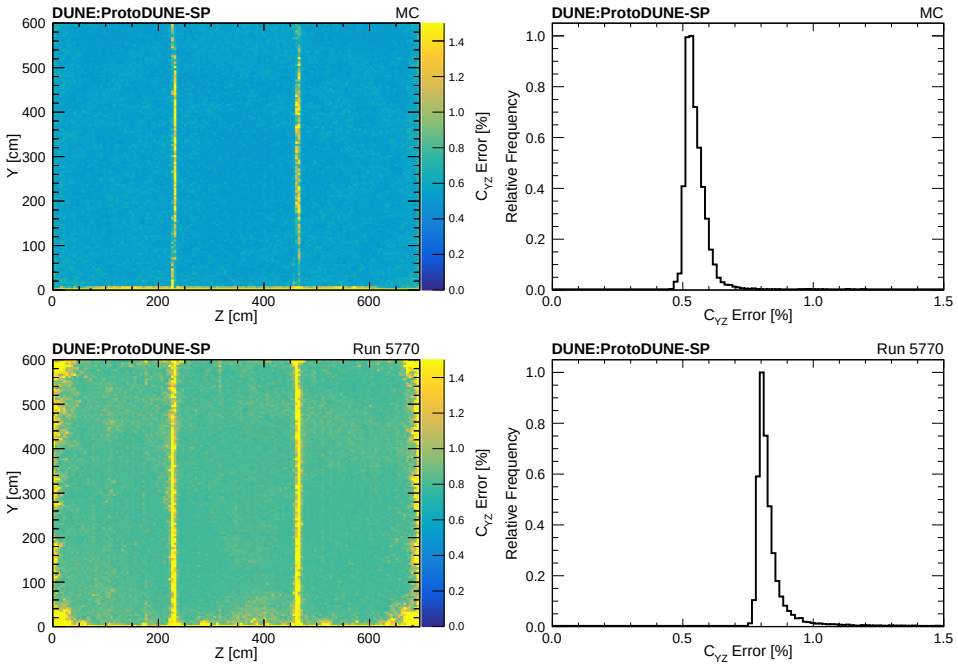

Figure 7.4: Systematic uncertainty propagation of the combined SCE lifetime corrections on the YZ local calibration constants. Top Left: error in YZ corrections for MC simulation. Top right: one-dimensional projection of the plot on the left. Bottom Left: error in YZ corrections for run 5770. Bottom Right: one-dimensional projection of the plot on the left.

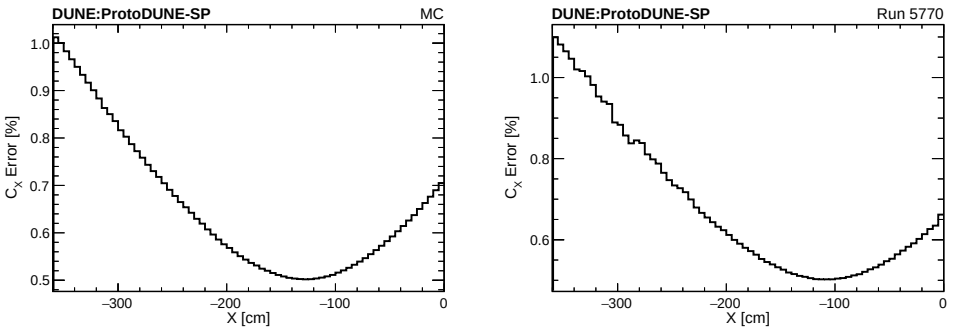

Figure 7.5: Systematic unceratinty propagation of the combined SCE lifetime corrections on the X local calibration constants. Left: MC. Right: Run 5770.

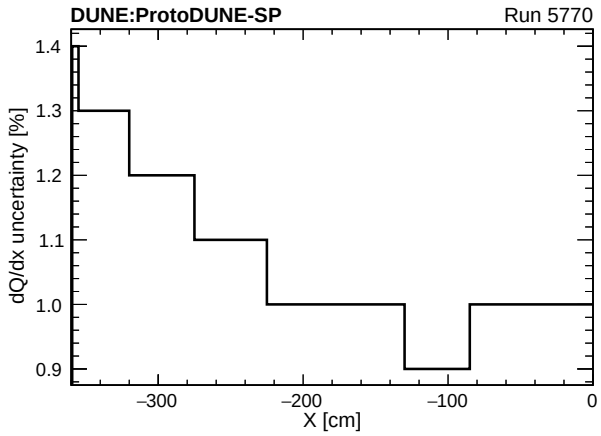

Figure 7.6: Systematic uncertainty on the $\frac{dQ}{dx}$ calibration procedure. Bins size has been computed so the uncertainty to be applied has only one significant digit below 1%.

Table 7.2: Systematic source for the propagation of the calorimetry calibration systematic.

|Hit X position| (cm)	$\sigma_r(dQ/dx)$
0-85	1.0
85-130	0.9
130-225	1.0
225-275	1.1
275-320	1.2
320-355	1.3
355-360	1.4

7.3.4 Error Propagation

This uncertainty source just studied constitutes a clear example of a variation systematic. The $\frac{dQ}{dx}$ of each hit of each track is varied following the source of Table 7.2, generating different $\frac{dE}{dx}$ values for each hit from one toy to another. Derived quantities as χ^2 values are also affected, directly modifying the outcome of the secondary kaon selection. The relative uncertainty for the selection is related with the variation on the number of events passing the selection for the different pseudo-experiments, and it is computed as the RMS of the number of events passing the selection along all toy experiments divided by the by its average value. With this, we can compute a total integrated uncertainty, which in this

Table 7.3: Relative uncertainty of each coherent parameter of the MPV function due to the systematic uncertainty on the calorimetry calibration .

	α	β	γ
σ_r (%)	1.1	0.7	0.2

case is 0.3%. Additionally, we can compute a differential relative uncertainty, as in Figure 7.7, where the uncertainty is represented as a function of χ^2_K. This depends on the observable plotted and on the binning. In this case, the χ^2_K variable is chosen because it is a summary of the $\frac{dE}{dx}$ information, and the binning is chosen so that each bin has a significant amount of entries. The average differential relative uncertainty is approximately 3.5%. The difference between the integrated and the relative uncertainty points out that, even though the final number of events passing the selection suffers a small variation, it exist a significant migration of events between bins from toy to toy.

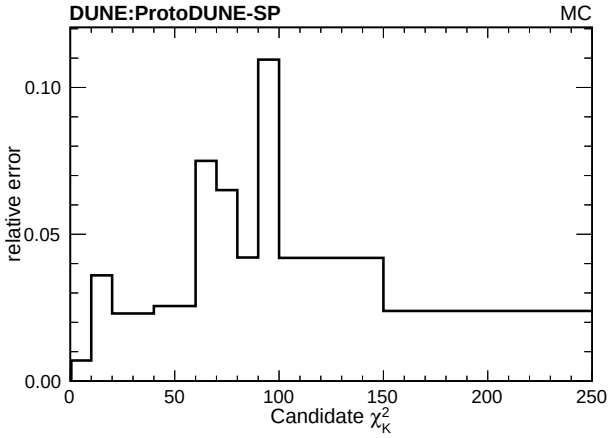

Figure 7.7: Systematic uncertainty of the calorimetric calibration propagated to the selection. The relative error is larger in the regions with lower statistics.

Apart from the selection, the effect over the $\frac{dE}{dx}$ measurement still needs to be evaluated. The fit procedure is repeated for every set of histograms obtained, one per toy, and the different values of the parameters are presented in Figure 7.8. The systematic uncertainty associated to each parameter is computed as the RMS divided by the mean value of the distribution. The results obtained are presented in Table 7.3.

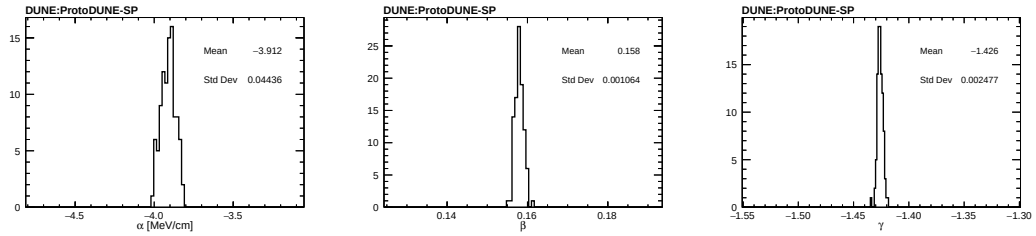

Figure 7.8: Effect of the calorimetry systematic over the coherent parameters.

Table 7.4: Modified Box Model parameters measured in ProtoDUNE-SP. The third row corresponds to the ratio data/MC, and the error is obtained by error propagation from the fitted parameters.

	Data	MC	Ratio
α	0.905 ± 0.015	0.920 ± 0.015	0.98 ± 0.02
β	0.220 ± 0.007	0.212 ± 0.005	1.04 ± 0.04

7.4 Recombination

Once the $\frac{dQ}{dx}$ value of each hit has been calibrated, it still has to be converted into the real energy deposit of the particle, $\frac{dE}{dx}$. The relationship between the energy deposited and the measured charge by the detector is not linear due to the recombination effect, where some of the freed electrons are absorbed again by some of the argon ions. In ProtoDUNE-SP this effect is simulated by the Modified Box Model developed by the ArgoNeuT collaboration [155].

The Modified Box Model has two free parameters, α and β, which can be estimated by comparing the measured deposited charge with the expected energy loss per unit length. The recombination analysis done in ProtoDUNE-SP found a small discrepancy for these parameters between data and MC (see Table 7.4). While MC values are consistent with ArgoNeuT input values, data values are slightly different. This discrepancy can be implemented as a systematic uncertainty by varying the recombination parameters in the MC to match the ones measured in data. This, as in the previous case, is an example of variation systematic, since it affects the $\frac{dE}{dx}$ value of each hit, hence the χ^2 calculation, and the selection has to be redone for each toy experiment.

To propagate the systematic, the MC parameters are multiplied by the ratio data/MC, which has an associated error. From one toy to another, each ratio is varied within this error by random Gaussian throws. Since the α and β parameters are obtained from the same analysis and the same fit, they have a

Table 7.5: Relative uncertainty of each coherent parameter of the MPV function due to the recombination systematic uncertainty.

	α	β	γ
σ_r (%)	4.9	3.1	2.2

correlation matrix (concretely, the correlation coefficient is 0.85) and hence, the throws have to follow this relationship. This can be easily done in the following way: provided a real positive defined matrix M (as in this case, a correlation matrix), it exists a lower triangular matrix L such that

$$M = L \times L^T \,. \tag{7.12}$$

This is known as Cholensky decomposition (particularized for real matrices). Once the matrix L is known, given a vector of uncorrelated random numbers R, another vector of correlated random numbers R' can be computed as

$$R' = L \times R \,. \tag{7.13}$$

Applying the Cholesky decomposition to the correlation matrix of the recombination fit, we obtain:

$$L = \begin{bmatrix} 1 & 0 \\ 0.85 & 1 \end{bmatrix} \,. \tag{7.14}$$

In this way, the parameters α and β can be varied in a correlated way[1].

7.4.1 Error Propagation

The effect of this systematic over the selection can be observed in Figure 7.9. As it can be seen, it has a larger effect than in the previous case. This is probably due to the fact that the relationship between $\frac{dE}{dx}$ and α and β parameters is not lineal, further distorting the larger $\frac{dE}{dx}$ values. This affects much more the calculation of the χ^2 than the previous systematic. The integrated relative error over the selection is 4.7%, whereas the average differential error is 14.0%. As before, the large difference between integrated and relative uncertainty is due to the strong migration of events between bins. Table 7.5 presents the effect over the coherent parameters.

[1] Yes, I agree, that one was easy.

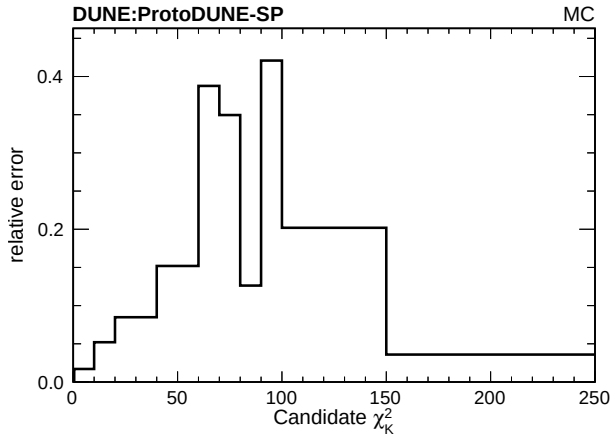

Figure 7.9: Recombination systematic uncertainty propagated to the selection.

7.5 Space charge geometric effect

As previously explained in Section 3.8.1, apart from modifying the $\frac{dQ}{dx}$, the SCE affects the reconstruction process at geometric level. Electrons drifting towards the anode are deviated from what would be their standard trajectories due to the fluctuations of the electric field, meaning that particles' trajectories are not reconstructed as they have originally happened. The effect becomes larger closer to the faces of the detectors, where tracks are heavily shrunken. The SCE correction tries to take care of this effect, modifying the position and the direction of particles' hits.

These modifications have two effects on our analysis (apart from the one in the $\frac{dE}{dx}$ described above). The first one is on the selection, since it depends on the SCE correction:

- varying the absolute length of the tracks (as a consequence, the computation of the momentum by range changes too);
- modifying the initial and end position/direction of the tracks, affecting the cuts that consider the relative position/direction between particles;
- and also modifying the residual range of each hit (affecting to the χ^2 calculations and the cut based on it).

This makes it a variation systematic. The second effect is caused by the variations in the residual range that can generate a migration of events between residual range slices in the fitting algorithm.

Contrary to what was done with the $\frac{dQ}{dx}$, there is no straightforward way to parametrize the SCE at geometric level, so in this case it has to be propagated directly: the analysis loop is repeated in several toy experiments in which the absolute value of the SCE map is varied by throwing random Gaussian numbers with a 5% width. This variation can be done globally (the same variation is applied to all voxels) or locally (a different variation is applied to each voxel). Both approaches had been tried, finding almost no difference in the obtained result. The reason for this is the same as the one aforementioned: the SCE is smoothly parametrized, and the size of the voxels describing it is very large, reducing possible local fluctuations. Consequently, the SCE systematic is propagated by applying global variations of the correction map, since they are less time consuming than the local variations.

7.5.1 Error Propagation

Figure 7.10 shows the differential relative error due to the SCE systematic (globally variated). The effect is lower than before, with an average differential error of 2.4% and an integrated relative error of 0.4%. In the case of the local variations, a differential relative error of 2.6% and an integrated relative error of 0.6% was obtained. Table 7.6 presents the effect over the coherent parameters, which again is small. The uncertainty obtained by the two methods was the same.

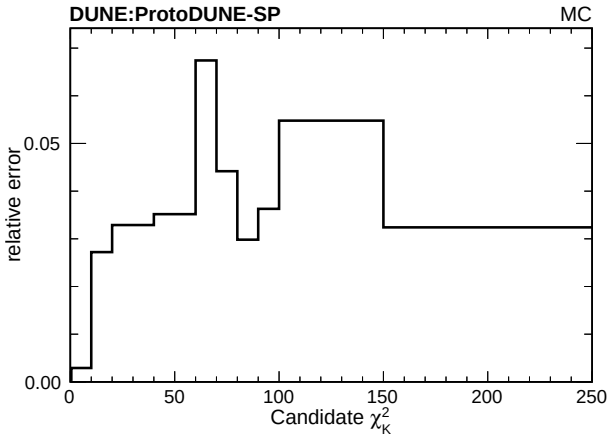

Figure 7.10: SCE systematic uncertainty (at geometric level) propagated to the selection.

Table 7.6: Relative uncertainty of each coherent parameter of the MPV function due to the SCE systematic uncertainty.

	α	β	γ
σ_r (%)	0.4	0.7	0.1

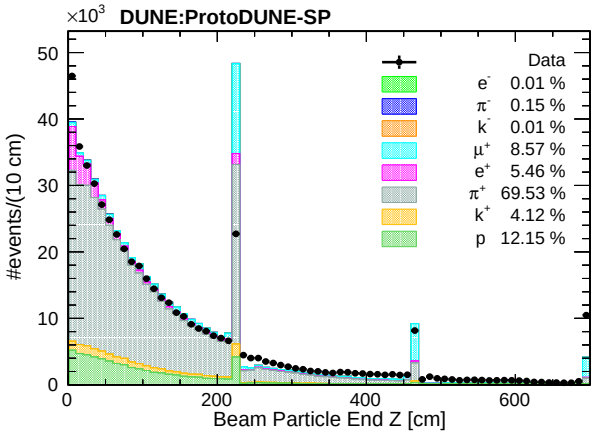

Figure 7.11: Beam particle end position for 6 and 7 GeV sample. The two peaks at 220 and 440 cm correspond to the broken tracks in the region between APAs. This effect is overestimated in MC.

7.6 Broken Tracks on APAs borders

As commented in Chapter 3, due to a problem with the electron diverters located between APAs, particles passing through the detector and passing from one APA to another are very likely to be miss-reconstructed: the track is split in two in the region between the APAs, and the second half is commonly assigned as daughter of the first half. This effect can be seen in Figure 7.11, where the Z end position of the beam particles is represented. Two clear spikes can be seen around 220 and 440 cm, which are the regions between APAs.

It can also be observed the imbalance commented before: the effect of broken tracks between APAs has been simulated in MC, but apparently it is overestimated. This can bias our measurement, and hence has to be propagated as a systematic. The effect on our analysis can be seen in Figure 7.12: the kaon candidates starting in the region between APAs are partially a product of the electron diverters problem, being some broken tracks that have a starting point more upstream than what has been reconstructed. Since this affects more MC than data, the candidates are on average shorter in MC than in data. This

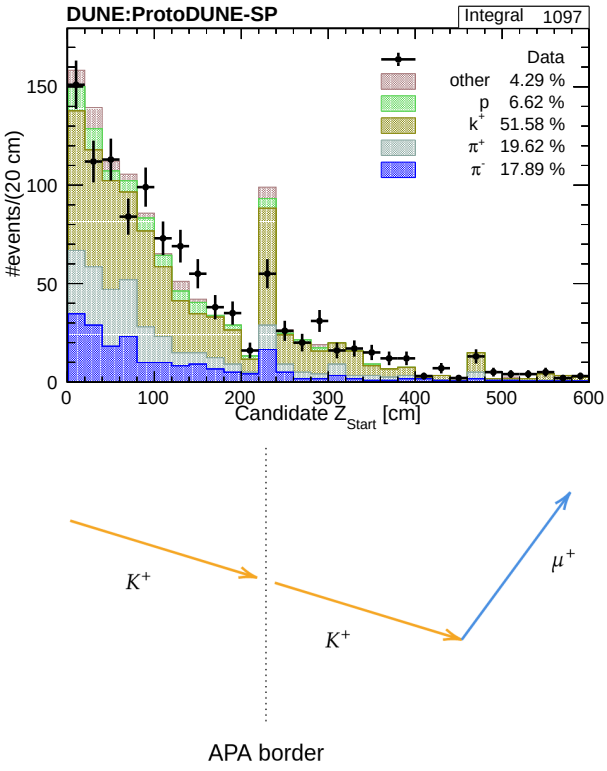

Figure 7.12: Electron diverters effect on the analysis sample. Top: kaon candidate's Z start position. Bottom: schematic view of this effect. The two kaon tracks correspond to a single kaon, so the one selected as the candidate (the second one) is shorter than what it truly is.

implies that, in general, the 1D $\frac{dE}{dx}$ histograms corresponding to larger residual ranges might be less populated in MC than in data.

This effect can be propagated as an efficiency-like systematic. Let's suppose there is a particle coming from the beam going downstream in the detector. When it reaches the region between APAs, there is a probability (or efficiency) ϵ of its trajectory being broken (thus, ending in that region). In the same way, there is a probability $1-\epsilon$ of it being properly reconstructed and ending wherever it is meant to end.

Since we are working with secondary particles, these probabilities have to be properly assigned. In our case, for a true candidate created before the region between APAs and ending after it, there is a probability ϵ of breaking, and hence of the reconstructed candidate **to start** in the region between APAs. In the same way, there is a probability $1-\epsilon$ of the true candidate not breaking, meaning that the reconstructed candidate would start before the breaking region.

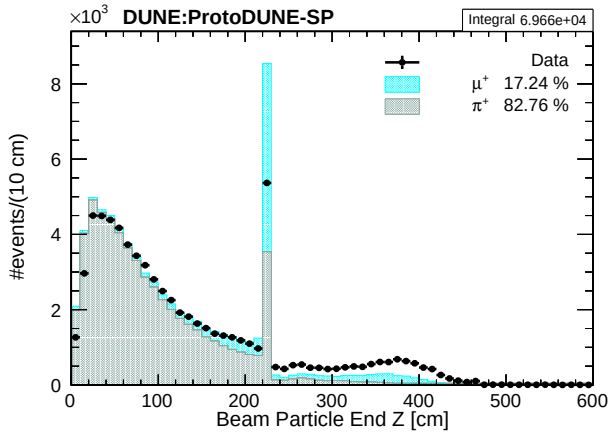

Figure 7.13: Control sample for breaking efficiency measurement. It is formed by 1 GeV/c μ^+ π^+ from the beam.

7.6.1 Efficiency Measurement with a Control Sample

To properly measure this efficiency, a control sample is needed. The control sample chosen is formed by 1 GeV/c μ^+ and π^+ from the beam. This sample is represented in Figure 7.13, where it can be seen how a significant number of tracks reach the electron diverters region. In Figure 7.14-left, it can be observed how, from $Z = 220$ cm to $Z = 234$, there is an excess of ending tracks, which corresponds to the region between APAs. Because of that, the breaking efficiency is defined as

$$\epsilon = \frac{N_{Broken}}{N_{Z>220}}, \tag{7.15}$$

where $N_{Z>220}$ represents the number of tracks reaching, at least, the electron diverters region, and N_{Broken} represents the number of broken tracks. Naturally, not all of the tracks ending in the region between APAs are necessarily broken, so a small selection can be done to maximize the amount of selected broken tracks. From the MC information it is easy to determine which tracks are truly broken: one can simply look at the true Z end position of the track, and check if the track truly stops near the APA region (meaning that it is not broken) or it stops further away from it (meaning that it is broken). Broken tracks are the ones that:

- end between $Z = 220$ cm and $Z = 234$ cm (see Figure 7.14, left), and
- the cosine of the angle formed with respect to the outcoming direction of the daughter is larger than 0.9 (see Figure 7.14, right).

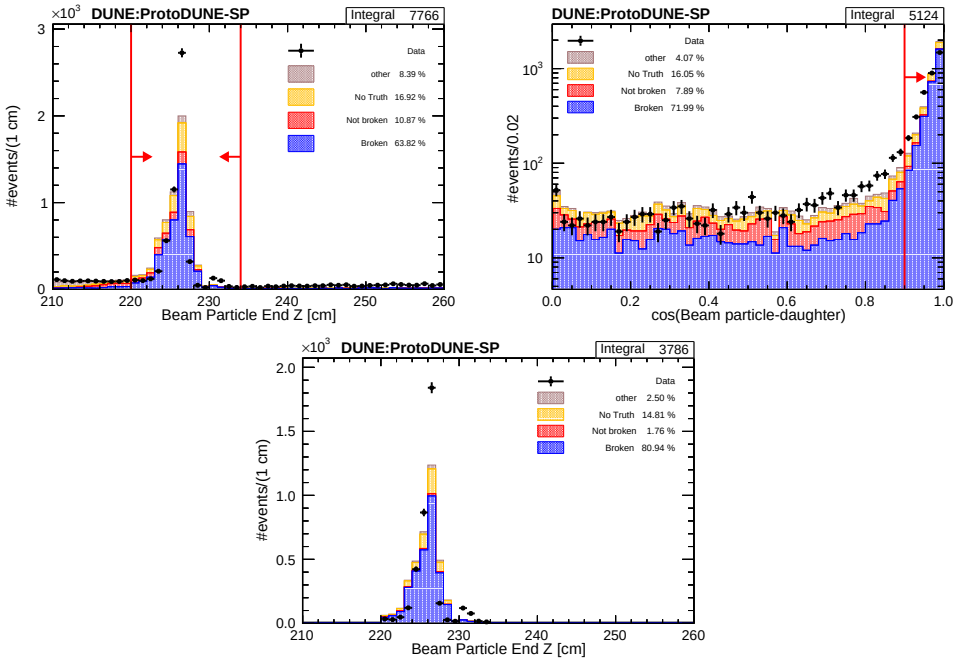

Figure 7.14: Selection of broken tracks. Left: control sample Z end position. Right: cosine between the track and its daughter. Bottom: selection result.

Table 7.7: Broken track efficiency measured with the control sample. The errors shown are statistical. Upper and lower levels of the efficiency are almost symmetric, so the mean value is taken as the error. The error shown for the ratio is computed by error propagation.

	Data	MC	r_{CS}
$N_{Z>220}$	15936	20763	
N_{broken}	3786	9956	
ϵ^{CS}	0.238 ± 0.003	0.480 ± 0.004	0.496 ± 0.007

After this small selection, the control sample has a purity of 80% (see Figure 7.14, bottom). It is important to notice here that the purity is not considering the no-truth information, so it is interesting to see that the amount of truly broken tracks passing the selection is very small. Now, the efficiency ratio between data and MC can be computed. The result of the computation is presented in Table 7.7.

In order to estimate a width for the r_{CS} variation from toy to toy, the control sample just presented can be divided in subsamples based on the θ_{XZ} and θ_{YZ} angles of the track (see Figure 7.15). The θ_{XZ} distribution can be divided above

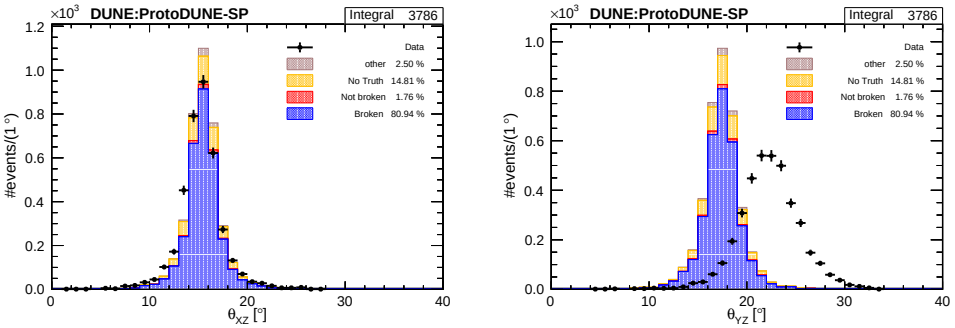

Figure 7.15: Left: θ_{XZ} angle for the selected sample. Right: θ_{YZ} angle for the selected sample. The difference is due to an error in the beam simulation, which enters the detector with a different orientation than data.

Table 7.8: Broken track efficiency measured for different subsamples of the control sample. Errors shown are statistical.

	ϵ^{CS}_{data}	ϵ^{CS}_{MC}	r_{CS}
$\theta^{low}_{XZ}, \theta^{low}_{YZ}$	0.222 ± 0.006	0.465 ± 0.008	0.477 ± 0.016
$\theta^{low}_{XZ}, \theta^{high}_{YZ}$	0.213 ± 0.007	0.475 ± 0.008	0.449 ± 0.018
$\theta^{high}_{XZ}, \theta^{low}_{YZ}$	0.243 ± 0.006	0.472 ± 0.007	0.516 ± 0.015
$\theta^{high}_{XZ}, \theta^{high}_{YZ}$	0.272 ± 0.008	0.492 ± 0.006	0.553 ± 0.017

and below 15° for data and MC, and the θ_{YZ} distribution can be divided above and below 23° for data and above and below 17° for MC. The observed difference between data and MC for the θ_{YZ} distribution is due to a well-known error of the simulation, where the beam orientation with respect to the TPC is not well implemented. The efficiencies and ratios measured for these subsamples are presented in Table 7.8. The maximum deviation between any sample and the main value computed before is 0.057. This value can be taken as the error, so the ratio to be used during the propagation is 0.50 ± 0.06.

Finally, only the ϵ_{MC} on the analysis sample is needed, which can be computed using the true information. The denominator of the efficiency is defined as the number of candidates passing the selection that start above 220 cm and the parents of which start before 220 cm and end after 220 cm. This means that the denominator is formed by tracks broken and tracks that could have been broken. On the other hand, the numerator is formed by the candidates (subsampled from the denominator) that start between 220 and 234 cm but which their true starting position is outside this range, meaning that they are truly broken. Both samples are presented in Figure 7.16. The result obtained is $\epsilon_{MC} = 0.39 \pm 0.04$.

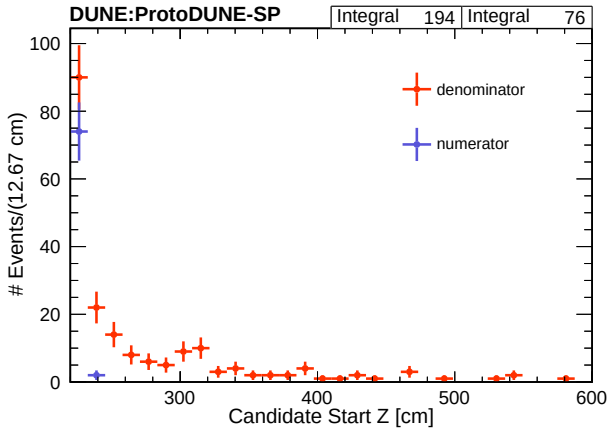

Figure 7.16: Sample and subsample used to compute the true efficiency of the MC in the analysis sample.

7.6.2 Weight Assignment

As previously mentioned, since we are working with secondary particles, efficiency and inefficiency weights have to be properly assigned. Because of how the event selection is developed, only four situations (shown in Figure 7.17) can be considered.

1. A track has been broken, being the first half 'lost' and the second half selected. In this case, the second half starts in the region between APAs and the angle with respect to its parent is above 0.9. This kind of candidates need to be weighted by the efficiency ratio, so that the number of broken tracks is the same in MC and in data.

2. A candidate starts and finishes before the breaking region, meaning that it is not affected by the efficiency or inefficiency, so no weights need to be applied.

3. A candidate starts naturally in the broken track region. No weight is needed since this situation happens equally in data and MC.

4. A candidate passes through the region between APAs without being broken. In this case, the track is part of the inefficiency, thus it has to be weighted by the inefficiency ratio.

Following this weight assignment scheme, we are obtaining a virtual migration of events from the broken track region towards more upstream locations.

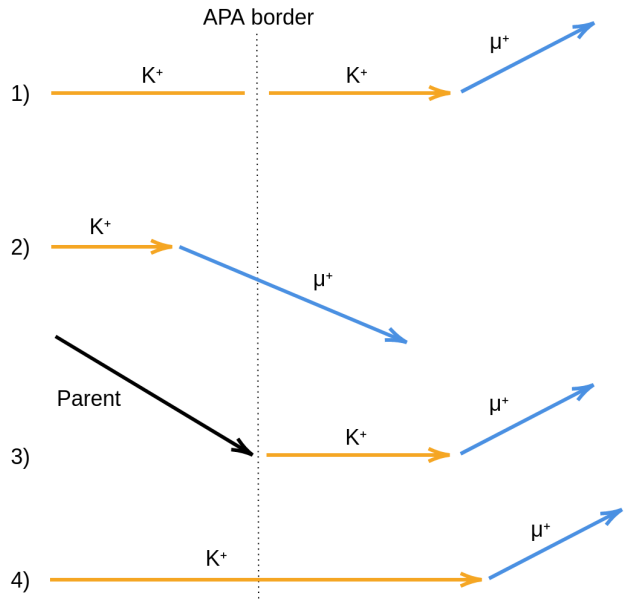

Figure 7.17: Topologies to be considered when assigning efficiency and inefficiency weights in the broken tracks systematic. From top to bottom: broken track that has to be weighted by the efficiency ratio; non broken track that does not have to be weighted; non broken track that starts naturally in the electron diverters regions and does not have to be weighted; and non broken track that has to be weighted by the inefficiency ratio.

Table 7.9: Relative uncertainty of each coherent parameter of the MPV function due to the broken tracks systematic.

	α	β	γ
σ_r (%)	0.1	0.1	0.1

7.6.3 Error Propagation

Figure 7.18-left presents the differential relative uncertainty for the χ^2_K distribution, the average value of which is 0.2 %. The integrated uncertainty is 0.06 %. In addition, the same distribution but for the initial position of the selected candidates is shown in Figure 7.18-right , where it can be clearly seen how the bins in the region between APAs suffer a migration of events towards the bins at their left. Table 7.9 presents the error over the coherent parameters.

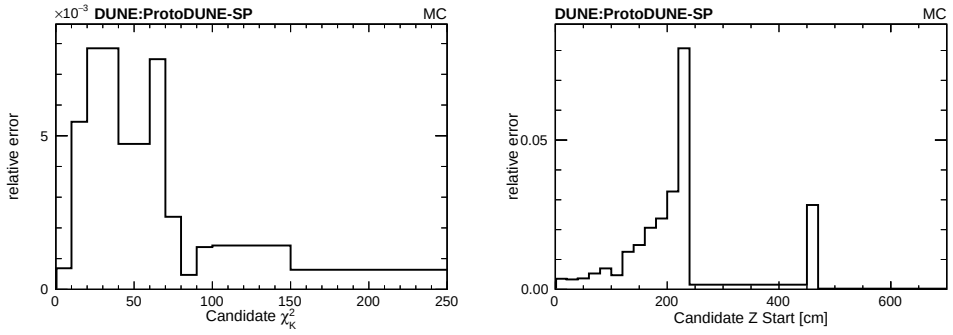

Figure 7.18: Broken tracks on APAs region systematic propagated to the selection. Left: χ^2_K distribution. Right: Start Z distribution. The region between peaks is merged in a single bin due to the low available statistics. The same is done with the region at the right of the second peak.

7.7 Beam Particle Selection Efficiency

Pandora algorithms, apart from reconstructing the different objects inside the TPC (tracks or showers) from lower pieces of information (hits, clusters) to larger ones (tracks/showers, hierarchies), have the responsibility to find the particle thrown at the detector by the beam, namely, selecting one of the reconstructed particles as the beam particle.

An efficiency can be defined for this task as the amount of beam events with an identified beam particle from all the beam events with a reconstructable beam particle. It is worth noticing that this efficiency is not discriminating whether the selected track is the correct one or not, it is only measuring the capability of identifying one of the tracks as the primary particle of the event. These studies were presented in [139], where small discrepancies were found between data and MC depending on the particle specie coming from the beam and its nominal momentum (see Figure 7.19). These differences can be propagated as an efficiency-like systematic uncertainty.

Since at 6 and 7 GeV/c it is not possible to differentiate between pions, muons and positrons, the efficiency was not measured for this sample. Because of that, and in order to be conservative, the efficiencies considered for them are the ones of pions and muons at 3 GeV/c, which are the ones with the largest discrepancy and error. Table 7.10 presents the systematic source for the propagation. The errors on the ratios data/MC are statistical and small, so in addition to these the difference with respect to 1 will be taken as a systematic uncertainty. This allows us to be cautious because we are not interested in measuring any particular characteristic of the beam particle and because the expected error over the kaons'

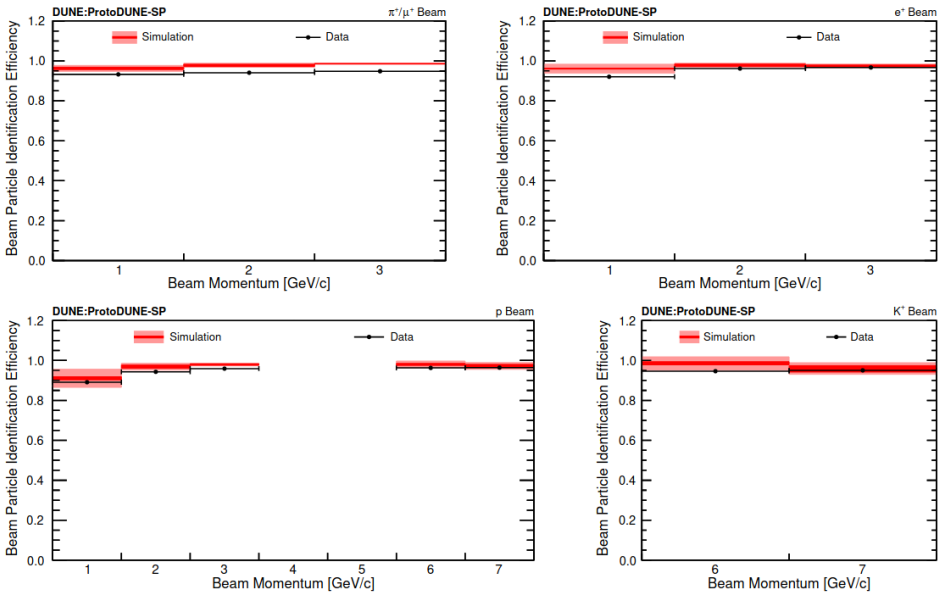

Figure 7.19: Beam particle identification efficiency for different particle species and momenta. Image from [139].

$\frac{dE}{dx}$ is small, since their energy loss does not depend on which particle generated the kaon.

As events with no reconstructed beam particle cannot pass the event selection, no event can be weighted by the inefficiency ratio. Consequently, all the events will be weighted by the corresponding efficiency ratio (depending on the particle specie), so at the end of the day this systematic is simply going to work as a normalisation.

The propagation of this systematic is going to give MC events a weight different from 1 and it will depend on the beam particle momentum and specie. Technically, this should not have a direct effect on our measurement, because the measured $\frac{dE}{dx}$ of stopping kaons is independent on which particle generated the stopping kaons. However, it might be affected secondarily due to the electron diverters systematic propagated above: the number of particles reaching the region between APAs can depend slightly from the particle coming from the beam and originating the secondary particles that we are looking for. For example, protons are usually interacting more upstream inside the detector (further away from the electron diverters) than pions. This implies than we expect a very low effect from this systematic source.

Table 7.10: Ratio data/MC for the beam particle identification efficiency, for different particle species and beam momenta. The true efficiency for the analysis sample is also presented. Errors shown are statistical. Values from [139].

Particle	Momentum (GeV/c)	ϵ_{MC} (%)	r_{CS}
e^+	6	90.9	0.963 ± 0.002
	7	92.1	0.963 ± 0.002
μ^+	6	94.0	0.963 ± 0.002
	7	85.7	0.963 ± 0.002
π^+	6	78.3	0.963 ± 0.002
	7	75.3	0.963 ± 0.002
K^+	6	80.7	0.961 ± 0.011
	7	78.3	0.99 ± 0.02
p	6	78.9	0.983 ± 0.006
	7	73.8	0.993 ± 0.010

Table 7.11: Relative uncertainty of each coherent parameter of the MPV function due to the beam particle identification efficiency systematic.

	α	β	γ
σ_r (%)	0.2	0.3	0.1

7.7.1 Error Propagation

Figure 7.20 presents the differential relative uncertainty, the average value of which is 2.4 %. The integrated uncertainty is 2.4 % too. It is worth noticing than this systematic is mainly affecting the normalization of the selection, since the relative uncertainty profile obtained is almost flat. Table 7.11 presents the effect over the coherent parameters. It is very small, because of the reason just explained; this systematic affects only secondarily to other systematics, and being propagated alone only generates statistical fluctuations.

7.8 Beam Particle Species normalisation

As originally commented, the charged beam used in ProtoDUNE-SP was formed by e^+, π^+, μ^+, K^+ and p (and some residual negative charged particles). At 6 and 7 GeV/c of momentum, the beam instrumentation can distinguish between kaons, protons and others. The proportion of kaons, protons and others are

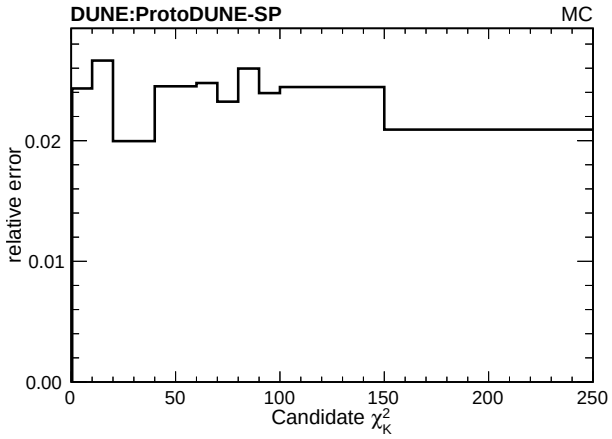

Figure 7.20: Beam particle identification efficiency systematic propagated to the selection.

Table 7.12: Percentage of beam particle species with respect to the total number of beam events as a function of the beam momentum. Errors are computed as Poisson variables and the error on the ratio is computed by error propagation.

Particle	Mom (GeV/c)	% w.r.t. total		Ratio
		Data	MC	
e^+, μ^+, π^+	6	83.0 ± 0.2	85.8 ± 0.2	0.968 ± 0.003
	7	83.0 ± 0.2	85.1 ± 0.3	0.976 ± 0.005
p	6	11.73 ± 0.06	10.68 ± 0.05	1.098 ± 0.007
	7	11.41 ± 0.07	10.86 ± 0.09	1.051 ± 0.011
K^+	6	5.23 ± 0.04	3.56 ± 0.03	1.470 ± 0.016
	7	5.59 ± 0.05	4.09 ± 0.05	1.37 ± 0.02

slightly different in data and MC (depending on the momentum). This small difference, which should not have any direct effect in our measurement, can have an indirect effect for the same reason explained above. Because of that, a normalisation systematic can be propagated here: the MC events are weighted by a normalisation factor such that the proportions of different particle species are the same as in data. In Table 7.12 the proportion of beam events of each particle specie is presented. The ratio presented in the last column is the ratio data/MC, which corresponds to the weight to be applied to the MC events, depending on the particle specie and momentum of the beam particle.

As in the case of the beam particle identification efficiency, this effect is not expected to directly affect the measurement, since the $\frac{dE}{dx}$ of the kaons is

Table 7.13: Relative uncertainty of each coherent parameter of the MPV function due to the beam particle normalisation systematic.

	α	β	γ
σ_r (%)	0.2	0.5	0.1

independent on which particle generated the secondary kaon. Because of that, the variation from toy to toy of the weights that are applied is not significant. Indeed, if we applied the same weight different from 1 to all the events, we would obtain the same result. As a conservative choice, the error of these weights is assumed to be the difference with respect to 1.

7.8.1 Error Propagation

Figure 7.21 presents the differential relative uncertainty, the average value of which is 4.8%. The integrated uncertainty is 4.6%. Even though this effect is a normalisation, we can see that the effect on the distribution is non flat. Beam kaons events are the ones being more affected by this systematic. Since they are the ones that produce secondary kaons more efficiently, the part of the χ^2_K distribution where secondary kaons are located is the one affected the most. Table 7.13 shows the effect over the coherent parameters, which is, as before, small.

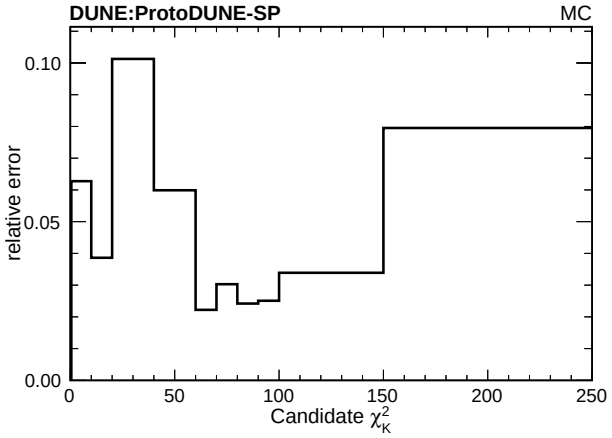

Figure 7.21: Beam species normalisation systematic propagated to the selection.

Table 7.14: Total number of beam events for each beam momentum. Errors are statistical.

	# Events		Ratio Data/MC
	Data	MC	
6 GeV/c	334882	463043	-
7 GeV/c	269317	150477	-
Ratio 7/6	0.804 ± 0.002	0.3250 ± 0.0012	2.475 ± 0.011

7.9 Beam Momentum normalisation

Another normalisation systematic can be propagated from the proportion of beam events at 6 and 7 GeV/c momenta. This proportion is much larger in data than in MC, as it can be seen in Table 7.14. Looking at Figure 7.22, it can be observed how the normalized χ^2_K distribution looks very similar at 6 and 7 GeV/c momenta, for both data and MC. This points out that the different proportion between 6 and 7 GeV/c beam events for data and MC should not directly affect the $\frac{dE}{dx}$ evaluation. However, other effects, as the quantity of tracks reaching the electron diverters region, the beam particle identification efficiency and the beam normalisation by specie, can depend on the initial momentum of the particle. This, as in previous cases, might affect secondarily to our study, so simple normalisation weights could be applied to the MC sample.

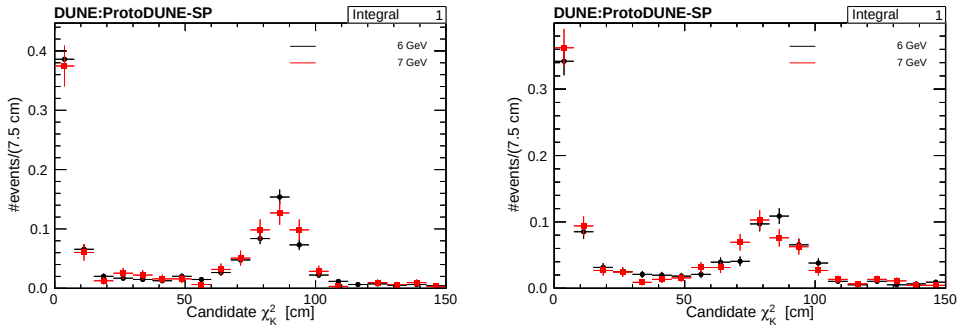

Figure 7.22: χ^2_K distribution normalized for 6 and 7 GeV/c beam events. Left: MC. Right: data.

Nevertheless, it is necessary to be cautious when applying this weights. Since the correction is large ($2.47 \gg 1$), and it is applied to a large fraction of the MC events, we are increasing a lot the available statistics. An option would have been to weight downwards the 6 GeV MC events, but since the overall statistics that we

have are reduced in data and in MC, this would have made impossible to fit the resulting $\frac{dE}{dx}$ distributions in MC. Thus, this option was dismissed, and it was only possible to weight upwards the 7 GeV/c events. As the fit is a likelihood fit and consider this fake inflation of the number events would complicate the evaluation of the errors, we can check instead that this effect has no direct impact over our measurement. In order to accomplish that, the Coherent Fit was repeated by weighting the 7 GeV/c events by 1.5, 2, 2.5, 3, 3.5 and 4 (without propagating any other systematic), and no significant differences were found in the obtained coherent parameters apart from statistical fluctuations (see Figure 7.23). Indeed, it can be observed how the statistical error of the parameters slightly decreases for larger weights due to the inflation of the statistics, previously mentioned. However, since this inflation is not directly affecting the fit result, an in order to be conservative, we can apply the obtained weight with a large error, so that possible correlations with previous systematics are highlighted. Thus, the weight to be applied to the 7 GeV/c MC beam events is 2.5 ± 1

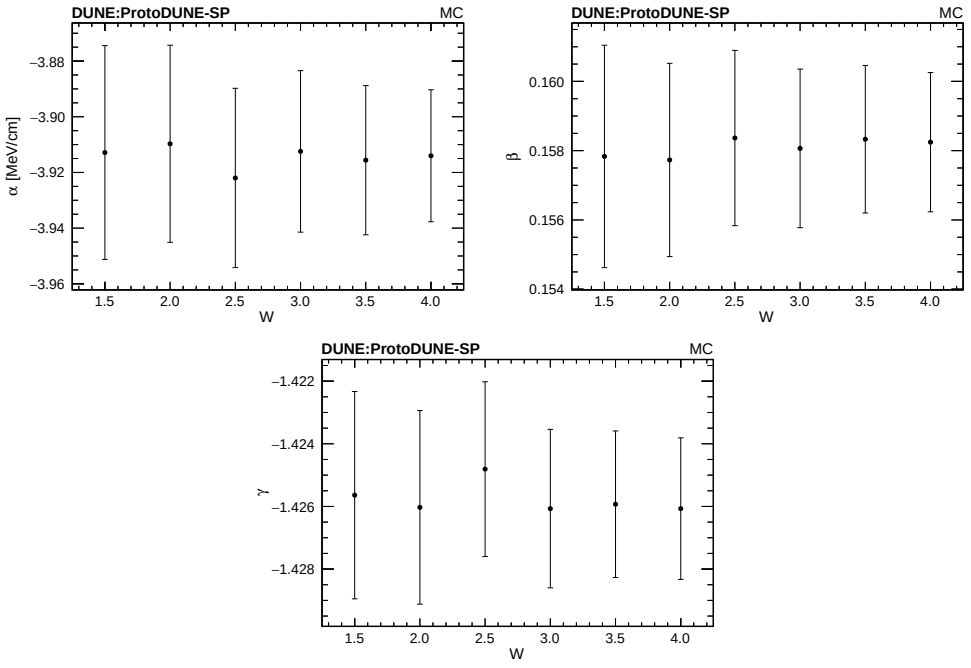

Figure 7.23: Effect of applying different normalisation weights over 7 GeV MC events on the coherent parameters.

Table 7.15: Relative uncertainty of each coherent parameter of the MPV function due to the beam momentum normalisation systematic.

	α	β	γ
σ_r (%)	0.1	0.1	0.0

7.9.1 Error Propagation

Figure 7.24 presents the differential relative uncertainty, the average value of which is 16%. The integrated uncertainty is 16% too. It can be observed a completely flat profile, meaning that this systematic is mostly affecting the normalization. The effect is very large because the assigned uncertainty to the weight is large (of the order of 40%). The small variation obtained for the coherent parameters is shown in Figure 7.15.

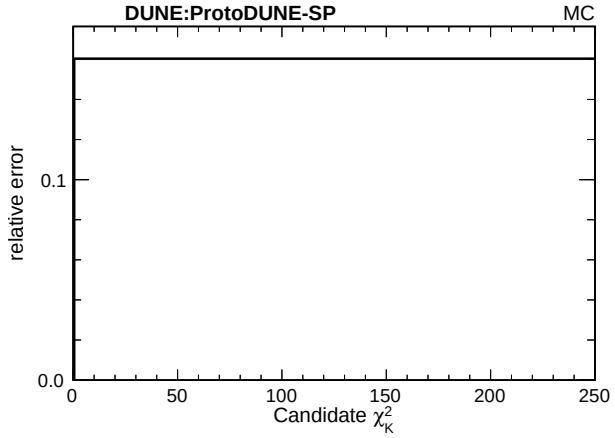

Figure 7.24: Beam momentum systematic propagated to the selection.

8 Results

They say a little knowledge is a dangerous thing, but it's not one half so bad as a lot of ignorance.

— Terry Pratchett, *Equal Rites*

The final results of this dissertation are presented in this Chapter. The resulting kinematic distributions after the event selection considering the effect of systematic uncertainties are presented in Section 8.1. The final evaluation of the kaons's $\frac{dE}{dx}$ is presented in Section 8.2. Section 8.3 closes the chapter with a discussion regarding the next steps to follow with respect to the kaon studies.

8.1 Secondary Kaon Selection

8.1.1 Evaluation of systematic uncertainties

Now that all systematic sources have been evaluated and propagated in Chapter 7, it is time to propagate all of them simultaneously so correlations or anti-correlations can be considered during the event selection. Table 8.1 shows a summary of all the previous systematic uncertainties propagated independently and the result of propagating all of them together. The beam momentum normalization systematic has been excluded of this evaluation, since it was inflated to account for possible secondary effects on the $\frac{dE}{dx}$ evaluation and its error was highly overestimated (on purpose), and it was affecting only the normalization on its own. The differential relative uncertainty for the χ^2_K distribution is presented in Figure 8.1. The integrated uncertainty is 7.9%, whereas the average relative uncertainty is 19.2%. The difference between both values indicates that there is a strong migration of events between bins in the different toy experiments. The systematic uncertainties have been applied to the analysis in such a way than the ones affecting others have been applied first.

Table 8.1: Summary of the propagation of all the systematic uncertainties individually in the event selection. The last two rows represent the quadratic addition of the individual propagations and the fully correlated study. A hyphen means that a particular systematic has not been considered.

Systematic	Integrated Relative Error (%)	Average Differential Relative Error (%)
Calorimetry Calibration	0.3	3.5
Recombination	4.7	15.0
SCE	0.4	2.4
Broken Tracks on APAs	0.1	0.2
Beam PID Efficiency	2.4	2.4
Beam Specie normalisation	4.6	4.8
Beam Momentum normalisation	-	-
Quadratic Sum	7.0	16.5
Total Correlated	7.9	19.2

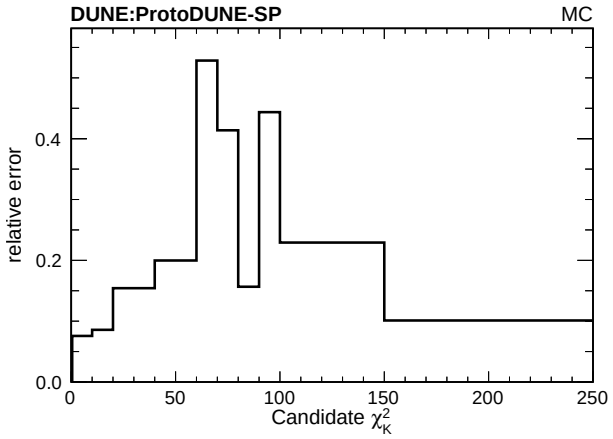

Figure 8.1: All systematic uncertainties propagated to the selection.

8.1.2 Signal and Background Distributions

In Figure 8.2 the χ^2_K, length, Z initial and end position distributions are presented for the whole sample, accounting for both systematic and statistical errors. Several things can be noticed here. First, it can be observed how the systematic uncertainty on the χ^2_K distribution is larger than the uncertainty on the other distributions. This is because the evaluated uncertainties of the calorimetric calibration and the recombination generate a significant migration of events in $\frac{dE}{dx}$ related variables, whereas the migration generated by the Space Charge geometric effect and the breaking tracks is smaller. Second, we can observe a good agreement in the Z starting and ending position of the selected sample, although in the ending position there is a discrepancy in the region between the first and the second APA (Z $\sim$220 cm) that is not present in the starting position. This means that the systematic considering the effect of the broken tracks in the electron diverters region has corrected well the excess of tracks starting in the electron diverters region but is still under-correcting the excess of tracks ending in that region. Third and final, it can be observed how there is a larger accumulation of shorter tracks in data than in MC. This can be also observed in the starting and ending Z distributions: looking at the first three bins of both plots, it can be noticed that MC tracks start before than data tracks, and that data tracks end before MC tracks. This, as a result, generate shorter tracks in the region of the first APA. This is probably related with the SCE. It has the largest effect near the faces of the detector, and the candidates selected are mostly starting in the first meter of the TPC, being heavily shrunken, likely more than MC tracks.

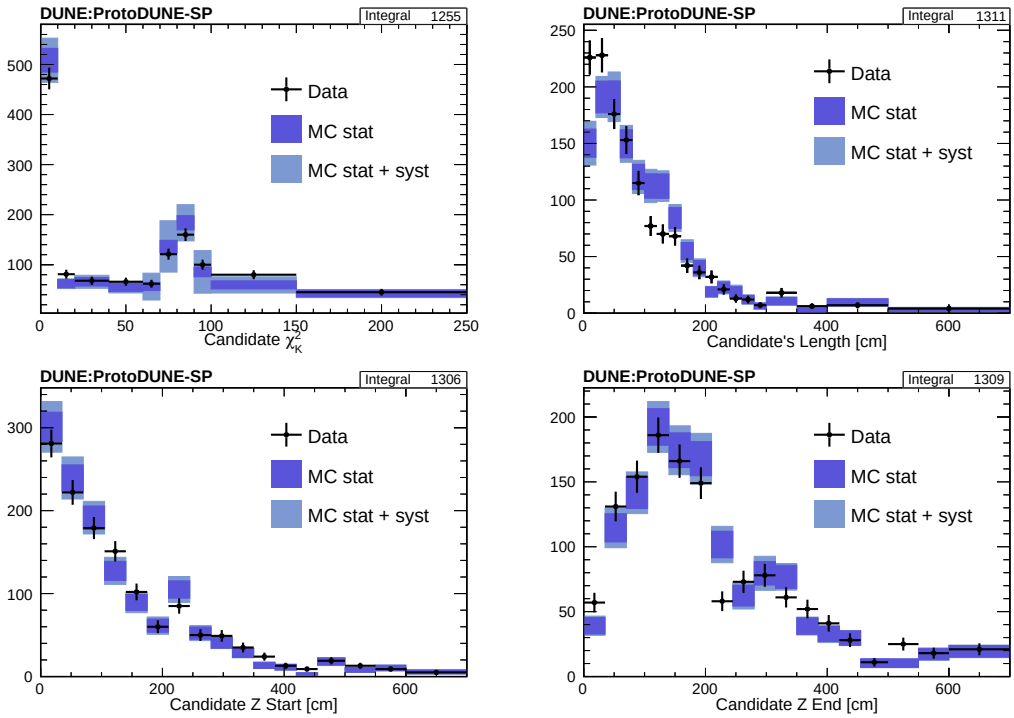

Figure 8.2: Final distributions for the whole sample accounting for statistical and systematic uncertainties. Top left: χ^2_K distribution. Top right: length distribution. Bottom left: Z start position. Bottom right: Z end position.

8.1.3 K^+ Distributions

In Figure 8.3 the initial momentum, length and $\frac{dE}{dx}$ distributions are presented for the kaon sample (by cutting below 50 in the χ^2_K), accounting for both systematic and statistical errors. In the initial momentum distribution it can be seen how data kaons have a slightly lower initial momentum than in MC. This effect can also be observed in the length distribution, in which data events are shorter than MC. It is also visible how the $\frac{dE}{dx}$ is the one more sensitive to the systematic uncertainties.

8.1.4 μ^+ Distributions

In Figure 8.4 the initial momentum and $\frac{dE}{dx}$ distributions are presented for the daughter of the candidates (mostly muons) (by cutting below 50 in the χ^2_K in the candidate distribution), accounting for both systematic and statistical errors. The momentum distribution is narrow due to the momentum by range cut, but not as narrow as the cut, highlighting the worst resolution of the calorimetric

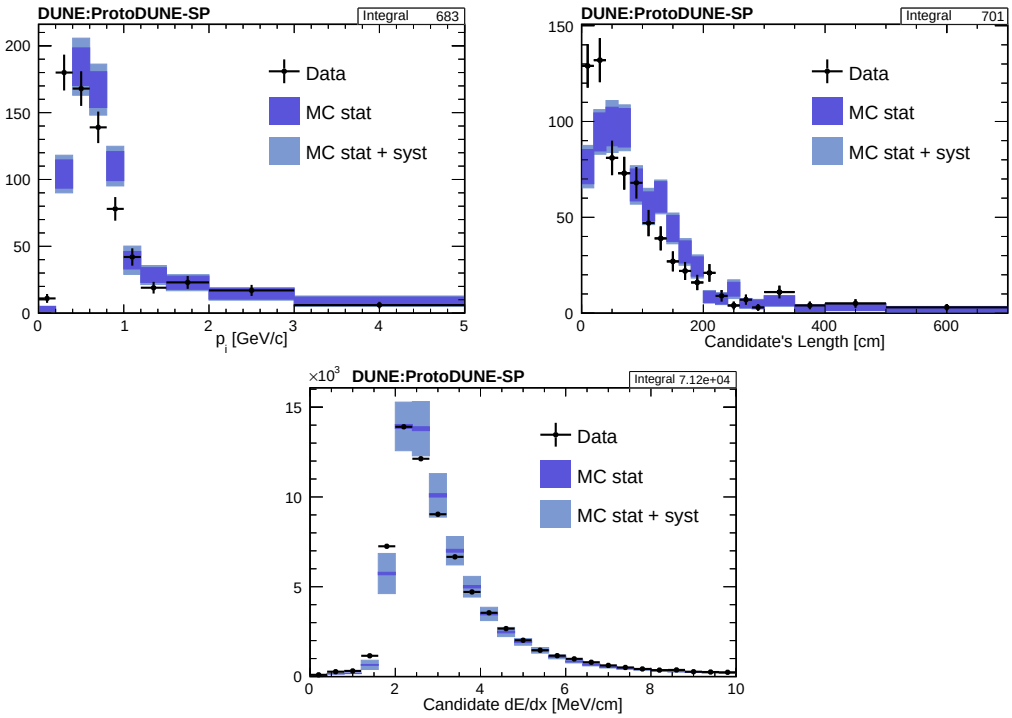

Figure 8.3: Top: initial momentum distribution with statistical and systematic error for the signal sample. Mid: length distribution. Bottom: dE/dx distribution.

reconstruction of the momentum with respect to the length reconstruction. The $\frac{dE}{dx}$ is more sensitive to the systematics, as in the previous case.

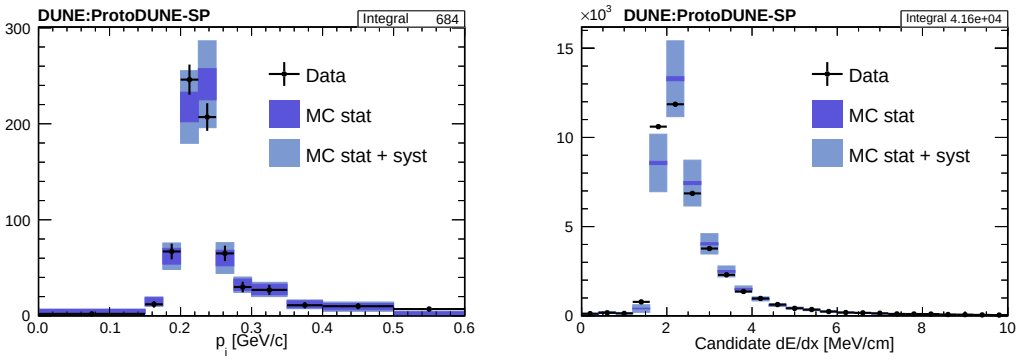

Figure 8.4: Top: initial momentum distribution with statistical and systematic error for the daughters of the signal sample. Bottom: dE/dx distribution.

Table 8.2: Summary of the propagation of all systematic uncertainties individually over the coherent fit parameters. The last two rows represent the quadratic addition of the individual propagations and the fully correlated study.

Systematic	σ_{rel} (%)		
	α	β	γ
Calorimetry Calibration	1.1	0.7	0.2
Recombination	4.9	3.1	2.2
Space Charge Geometric Effect	0.4	0.7	0.1
Broken Tracks on APAs	0.1	0.1	0.1
Beam PID Efficiency	0.2	0.3	0.1
Beam Specie normalisation	0.2	0.5	0.1
Beam Momentum normalisation	0.1	0.1	0.0
Quadratic Sum	5.0	3.3	2.2
Total Correlated	5.3	3.3	2.5

8.2 Results on $\frac{dE}{dx}$ Characterization

8.2.1 Evaluation of Systematic Uncertainties

The result of propagating all of the systematic uncertainties simultaneously in the Coherent Fit parameters that describe the most probable value of the kaons energy loss per unit length is presented in Table 8.2. The final distributions for these parameters are presented in Figure 8.5, along with the results obtained at the end of Chapter 6 (with no systematics considered). It can be observed that the α parameters shows a preference for more negative values when accounting for the systematics uncertainties, even beyond the statistical error. β presents a preference for larger values after the systematics beyond the statistical uncertainty of the result without systematics too. Finally, γ, shows a more similar behaviour.

In Table 8.3 the final results for the Coherent parameters describing the kaon $\frac{dE}{dx}$ MPV are presented for data and MC. Figure 8.6 shows a comparison for the MPV for data and MC. It can be observed how, despite of the systematic uncertainties, it still seems that MC underestimates K^+ energy loss for low residual ranges. Figure 8.7 shows the same plot but the data result has been subtracted to data and MC, so that the differences and the error bars are better comprehended.

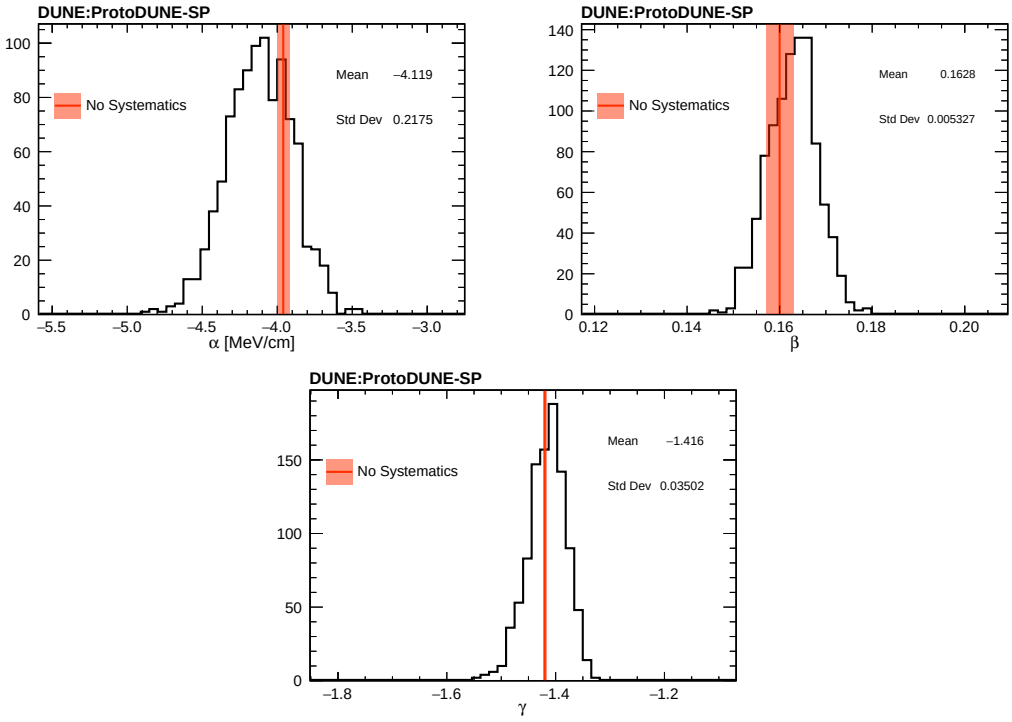

Figure 8.5: Coherent fit parameters for the signal MPV after the propagation of all systematic uncertainties in 1000 toy experiments. The red line represents the results obtained without systematics, and the pale band represents the associated statistical uncertainty.

Table 8.3: Parameters describing the μ_S Coherent function for data and MC. The MC uncertainties shown are first statistical (using MINOS) and second systematic. Data uncertainty is statistical and computed by MINOS.

	α (MeV/cm)	β	γ
MC	$-4.12 \pm 0.04 \pm 0.22$	$0.163 \pm 0.003 \pm 0.005$	$-1.416 \pm 0.003 \pm 0.035$
Data	-4.63 ± 0.08	0.208 ± 0.006	-1.375 ± 0.005

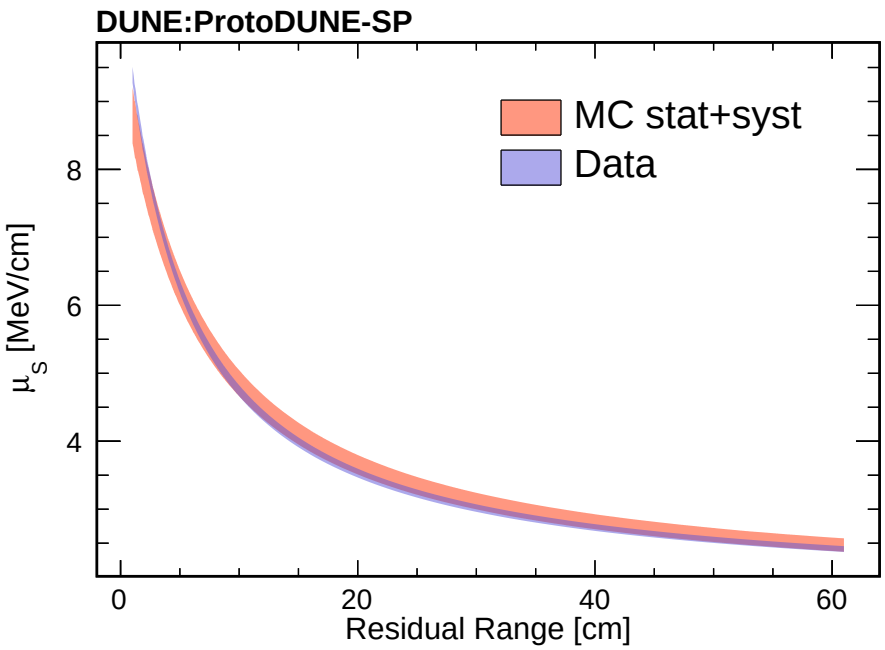

Figure 8.6: K^+ $\frac{dE}{dx}$ MPV comparison for data and MC after systematic uncertainty propagation.

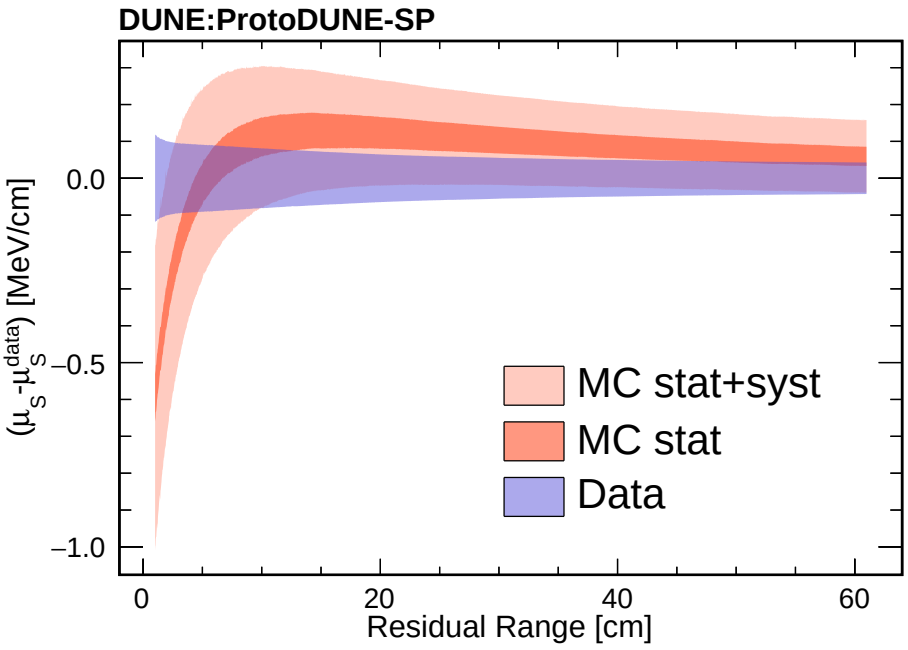

Figure 8.7: K^+ $\frac{dE}{dx}$ MPV minus MPV(data) for data and MC after systematic uncertainty propagation.

8.3 Future Prospects

Although we are reaching the end of this dissertation, the secondary kaon analysis presented here can still be expanded in the near future. The most important thing to do is to further study the observed discrepancy in kaons' $\frac{dE}{dx}$ between data and MC and, in the case of being confirmed, to modify the simulation chain so that this discrepancy is properly considered.

Apart from that, having demonstrated the capability of ProtoDUNE-SP to identify and differentiate kaons from other particle species allows us to think about other analysis involving kaons. One of them is the measurement of the production cross-section of secondary kaons. Using the χ^2_K PID strategy, kaons produced by the beam particle could be isolated from protons or pions, and a measurement of their production rate for the different beam momenta could be obtained. However, this strategy would allow to select only stopping kaons, so an efficiency correction based on the MC would be needed. In order to reduce the dependence in this efficiency correction, it would also be desirable to expand the selection to non-stopping kaons by means of a likelihood fit of their $\frac{dE}{dx}$ versus residual range profile, in which the experimental profile is displaced in the residual range axis by a free parameter to find the point with better agreement with the theoretical profile. A likelihood could be obtained for each particle hypothesis, and they could be dismissed by means of a likelihood ratio test.

Finally, the selection of stopping kaons has allowed to validate DUNE's sensitivity studies regarding proton decay searches. However, even though we have demonstrated the capability to identify low energy kaons, we have also observed than the MC simulation is overestimating the energy resolution of ProtoDUNE-SP. Thus, it is necessary to do a deep study of the systematic differences of the $\frac{dE}{dx}$ and repeat these sensitivity studies for DUNE's FD with more realistic values of energy and position resolution.

9 Conclusions

"Why do you go away? So that you can come back. So that you can see the place you came from with new eyes and extra colors. And the people there see you differently, too. Coming back to where you started is not the same as never leaving."

— Terry Pratchett, *A Hat Full Of Sky*

This thesis has summarized a big part of the work carried out during the last five years regarding different aspects of ProtoDUNE-SP, ProtoDUNE-HD and DUNE FD1[1]. The main result of this dissertation is the demonstration of the kaon PID capabilities of the LArTPC technology using ProtoDUNE-SP data. Understanding the behaviour of low energy kaons in liquid argon is fundamental for DUNE, since the golden decay channel of the proton has a kaon in its final state. Using the 6 and 7 GeV/c momentum beam runs taken during 2018, a selection of secondary stopping kaons produced in hadronic reactions has been presented. As a result, a population of approximately 1200 stopping kaons with a purity of 50% has been obtained. This selection has been developed without using calorimetric information of the kaons or from the PDS, demonstrating the outstanding capabilities of the detector. The selected sample has been compared with other samples of stopping protons and muons, and it has been shown how they can be distinguished and identified by means of a χ^2 test of the energy loss profile. This result is of outmost importance, since it demonstrates the capabilities of the LArTPC detector technology to study this hypothetical proton decay process.

In addition to this, a detailed study of the kaons $\frac{dE}{dx}$ profile as a function of the residual range has been presented. Using the MC truth information, the Coherent Fit approach has been implemented, tested and validated. This has allowed to compare the predicted profile of the simulation with the measured one in the ProtoDUNE-SP detector. After the evaluation of the systematic uncertainties, significant differences have been found for lower residual range values, meaning that *apparently* the simulation is underestimating the kaon energy loss for low

[1] Past, present and future.

momentum. This information can be used now as a new systematic uncertainty to be considered in analysis involving kaons, as in proton decay sensitivity studies or kaon production cross-section measurements; and, naturally, to adjust the simulation after further confirmation.

The analysis presented in this dissertation is only one of the many analyses currently being carried out with ProtoDUNE-SP data, on account of the successful installation, commissioning and operation from Summer 2018 to Summer 2020. During these two years, lessons were learnt and decisions were taken involving the design of the future modules of DUNE's Far Detector. Examples presented in this thesis are the approval of arranging a temperature monitoring system inside the active volume in the FD1, and the selection of the X-ARAPUCA technology as a baseline for the PDS.

The PDS is fundamental for DUNE's physics goals, since it is responsible of providing the t_0 for non-beam events, as for the proton decay. Different R&D lines have been developed in the last three years to optimize the X-ARAPUCA design, aiming one of them to find the best performing photo-sensor according to DUNE's requirements. Several sensor models of two manufacturers (FBK and Hamamatsu) were thoroughly tested in different institutions. The tests done at IFIC for more than a year have been summarized in this work, and in agreement with the results obtained in other laboratories, it was found that HPK models were in general better than FBK's. Furthermore, it has been observed that larger cell pitch models provide better gain and signal to noise ratio with no significant increase of dark current or correlated noise, and that larger quenching resistance models presented lower values of correlated noise. Consequently, the HPK HQR75µm model was selected as a primary SiPM model for DUNE PDS, and the FBK Triple Trench as a secondary one.

The last test for the PDS before the final deployment in South Dakota is the second phase of the ProtoDUNE programme. ProtoDUNE-SP has been replaced by ProtoDUNE-HD, which is a detector hosted by the same cryostat and that will use the final version of all FD1 components prior to their mass production. The installation of this new experiment was recently completed, with substantial IFIC involvement in the cryogenic instrumentation and the PDS. At the time of writing, ProtoDUNE-HD is awaiting at CERN for liquid argon, so that it can be filled and operated in the near future.

All the different topics addressed in this thesis give a sense of the complexity of a project like DUNE. The many details that need to be comprehended and under control require a community effort at every level. However, despite the delays and the funding problems, DUNE keeps gearing up, slowly but steady, so that the first day of data taking will arrive at the beginning of the next decade,

and we will be able to keep studying neutrinos beyond.

A Fits to histograms

In this appendix all residual range slices with their corresponding fits are displayed.

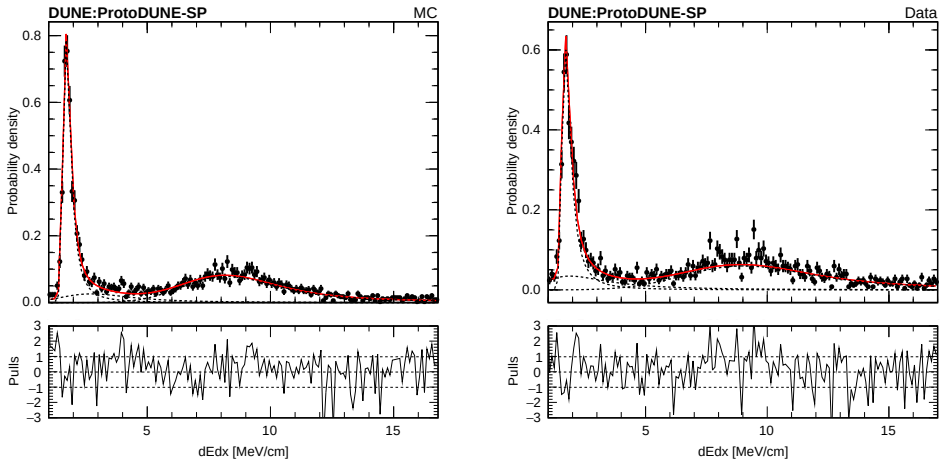

Figure A.1: Coherent Fit result for the slice corresponding to residual ranges between 1 and 3 cm.

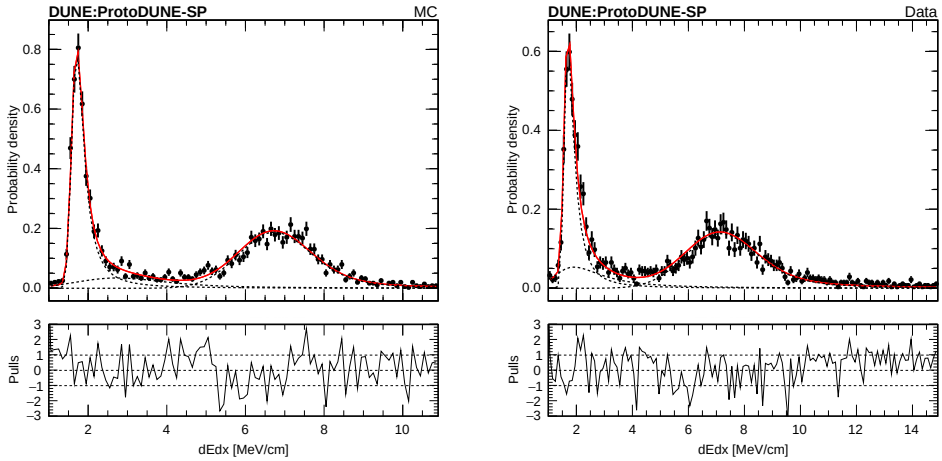

Figure A.2: Coherent Fit result for the slice corresponding to residual ranges between 3 and 5 cm.

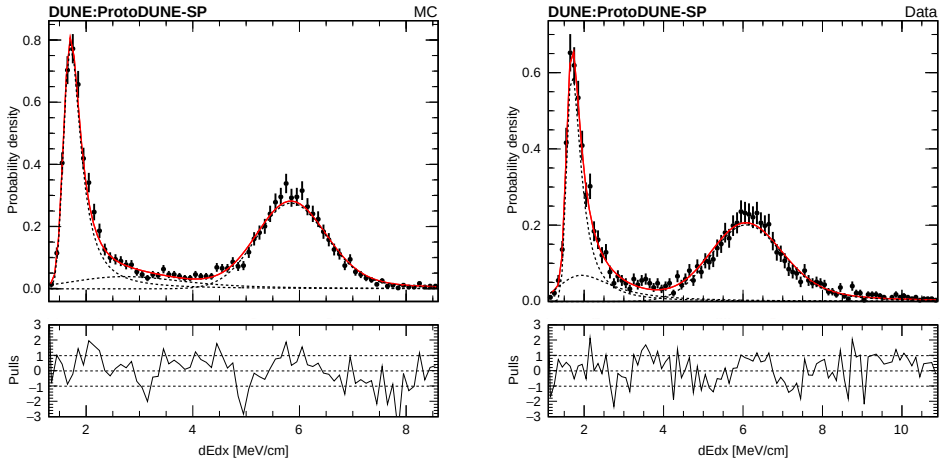

Figure A.3: Coherent Fit result for the slice corresponding to residual ranges between 5 and 7 cm.

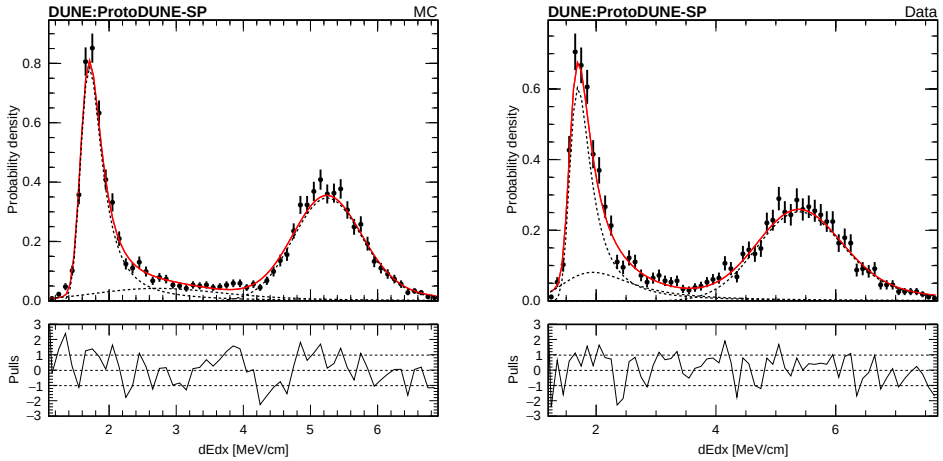

Figure A.4: Coherent Fit result for the slice corresponding to residual ranges between 7 and 9 cm.

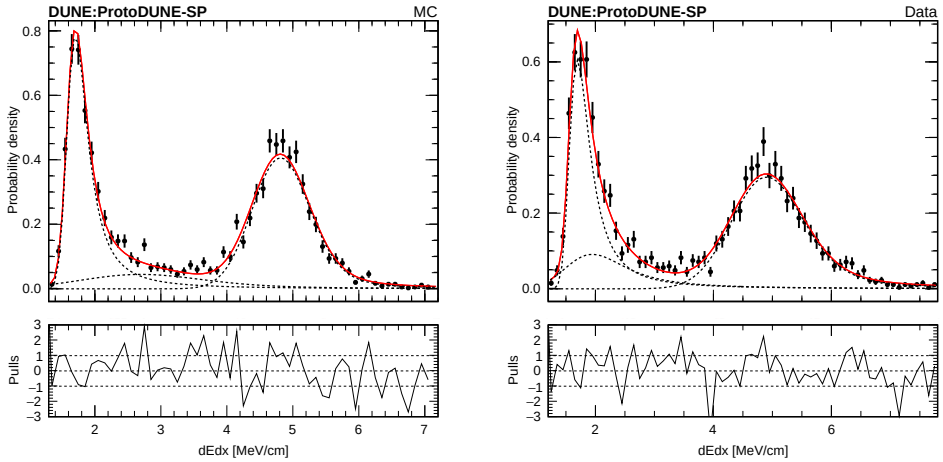

Figure A.5: Coherent Fit result for the slice corresponding to residual ranges between 9 and 11 cm.

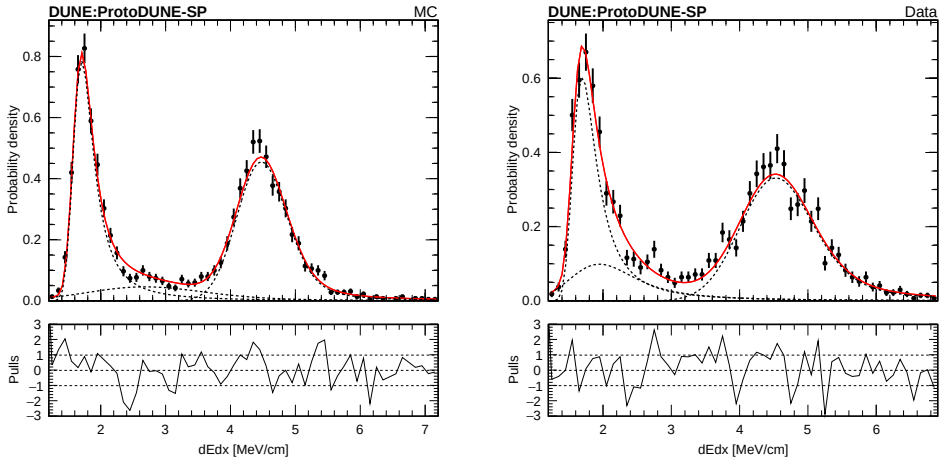

Figure A.6: Coherent Fit result for the slice corresponding to residual ranges between 11 and 13 cm.

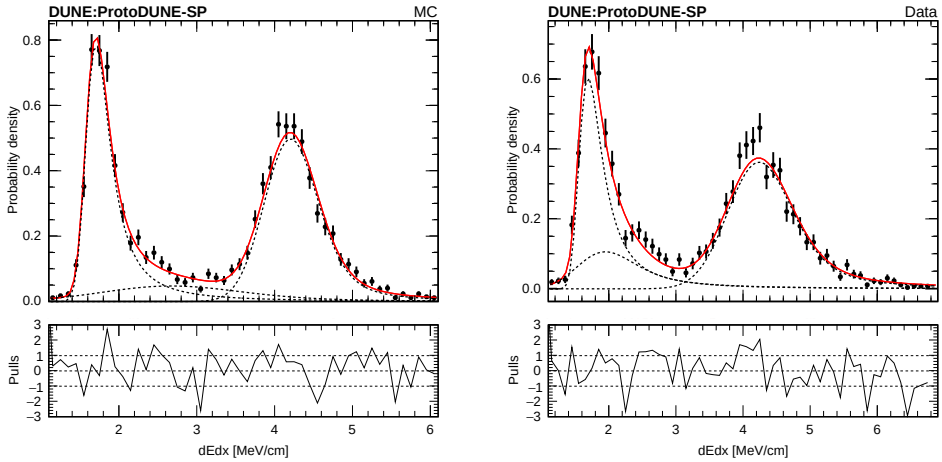

Figure A.7: Coherent Fit result for the slice corresponding to residual ranges between 13 and 15 cm.

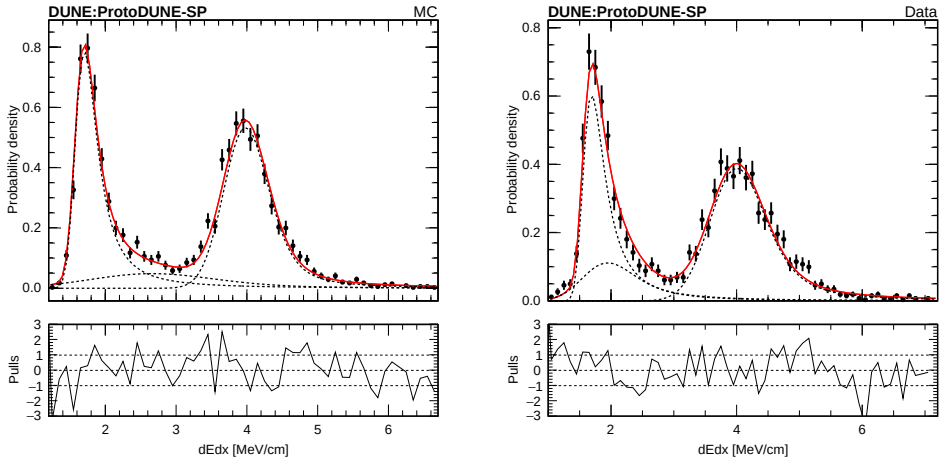

Figure A.8: Coherent Fit result for the slice corresponding to residual ranges between 15 and 17 cm.

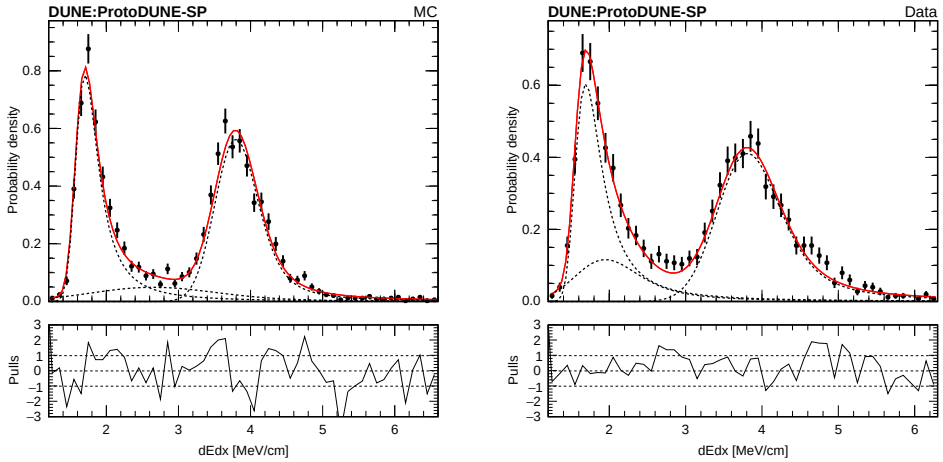

Figure A.9: Coherent Fit result for the slice corresponding to residual ranges between 17 and 19 cm.

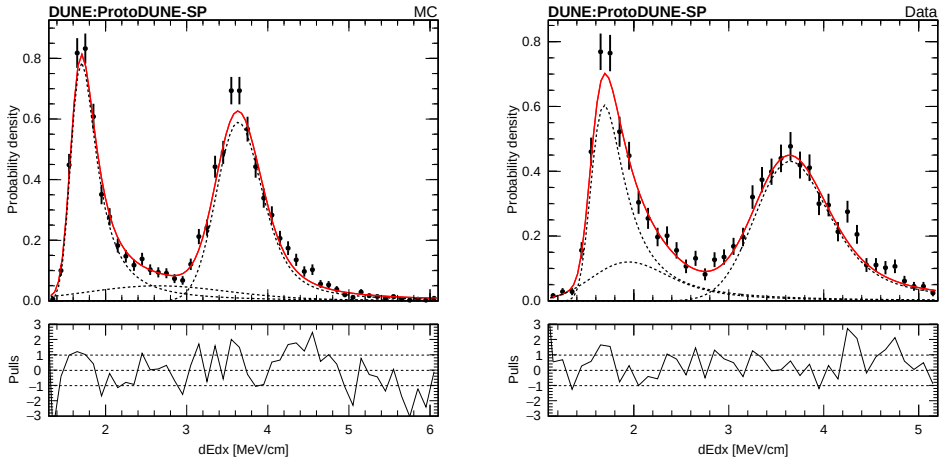

Figure A.10: Coherent Fit result for the slice corresponding to residual ranges between 19 and 21 cm.

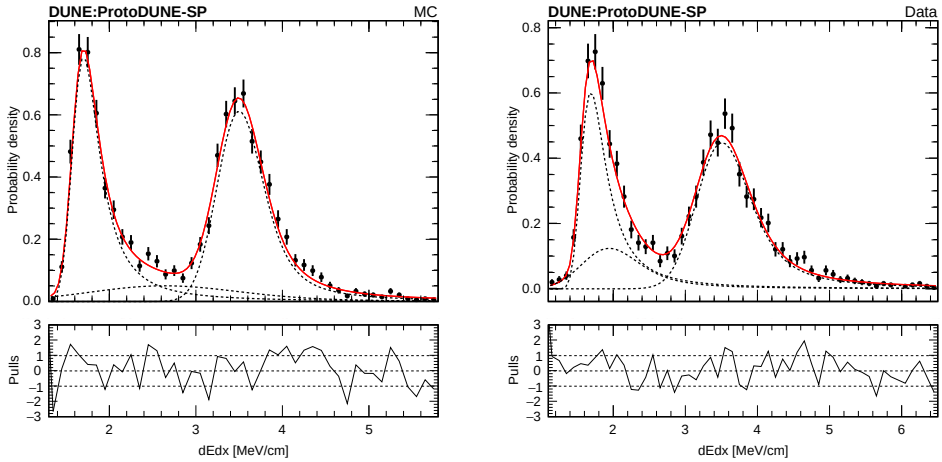

Figure A.11: Coherent Fit result for the slice corresponding to residual ranges between 21 and 23 cm.

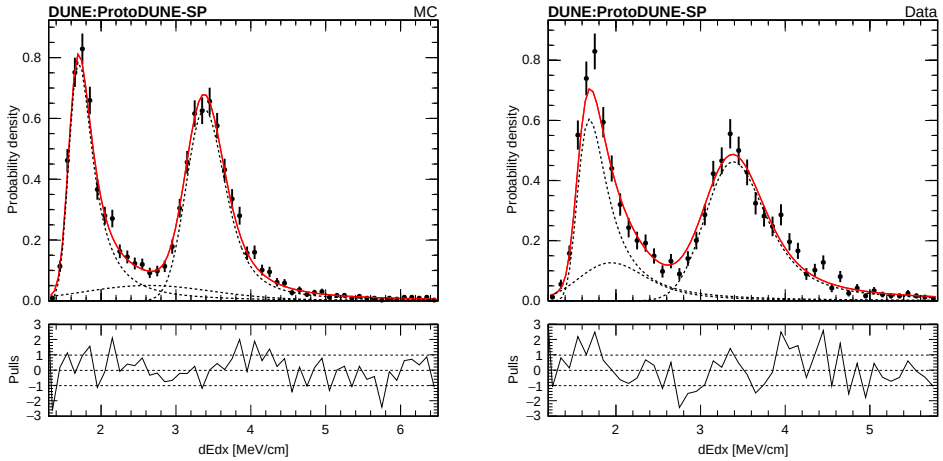

Figure A.12: Coherent Fit result for the slice corresponding to residual ranges between 23 and 25 cm.

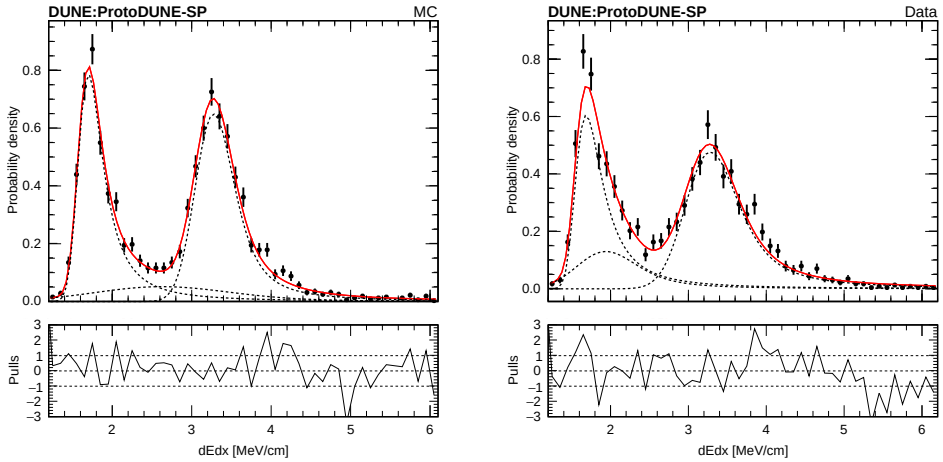

Figure A.13: Coherent Fit result for the slice corresponding to residual ranges between 25 and 27 cm.

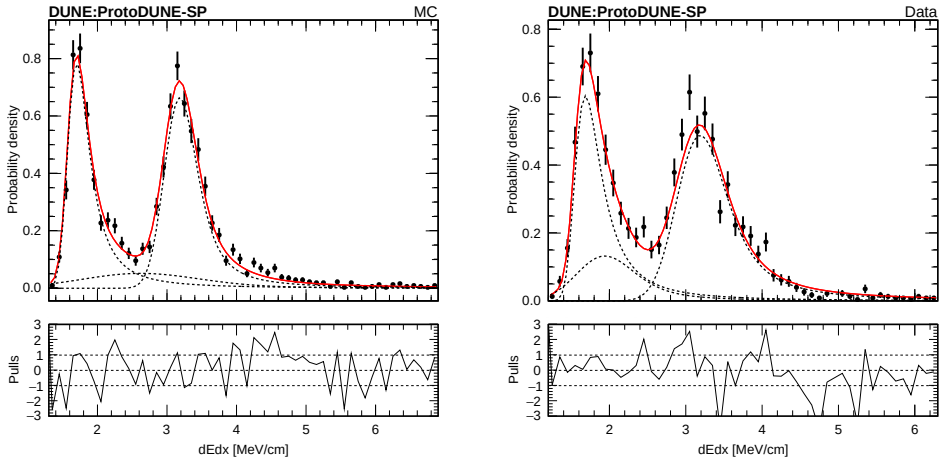

Figure A.14: Coherent Fit result for the slice corresponding to residual ranges between 27 and 29 cm.

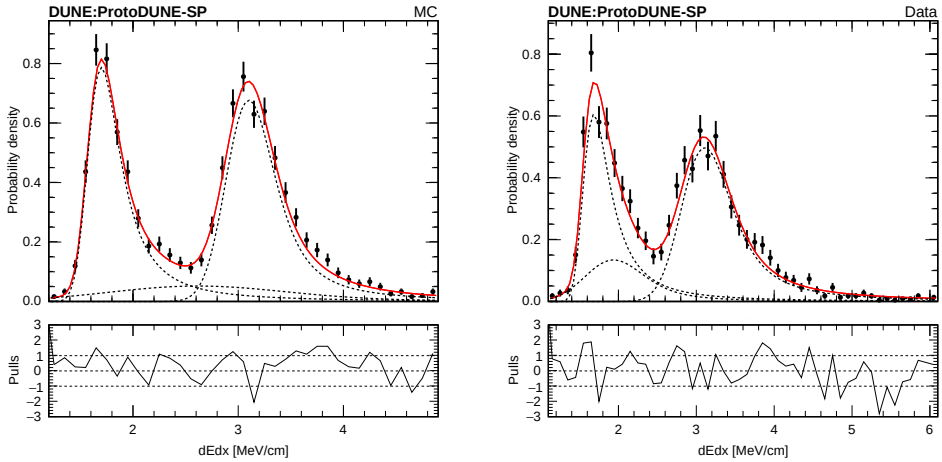

Figure A.15: Coherent Fit result for the slice corresponding to residual ranges between 29 and 31 cm.

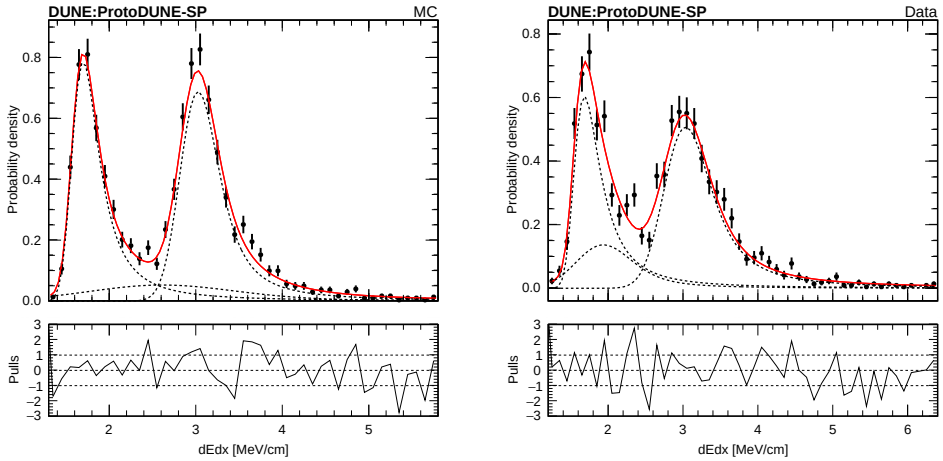

Figure A.16: Coherent Fit result for the slice corresponding to residual ranges between 31 and 33 cm.

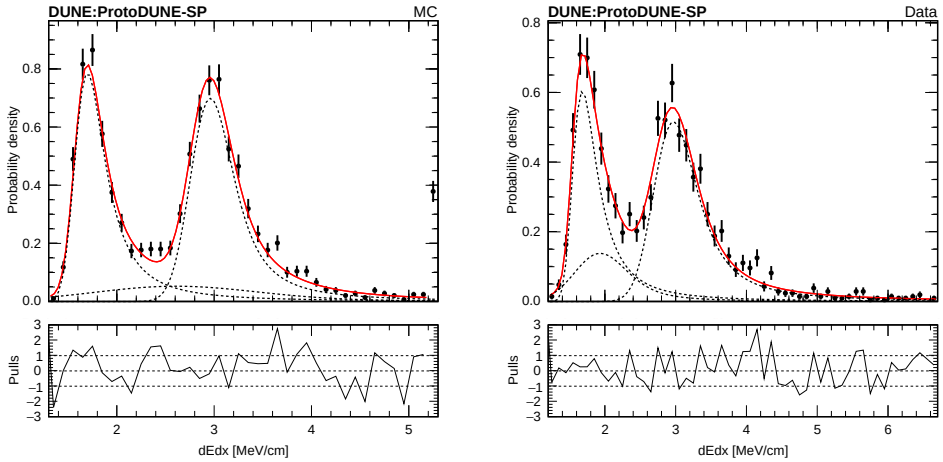

Figure A.17: Coherent Fit result for the slice corresponding to residual ranges between 33 and 35 cm.

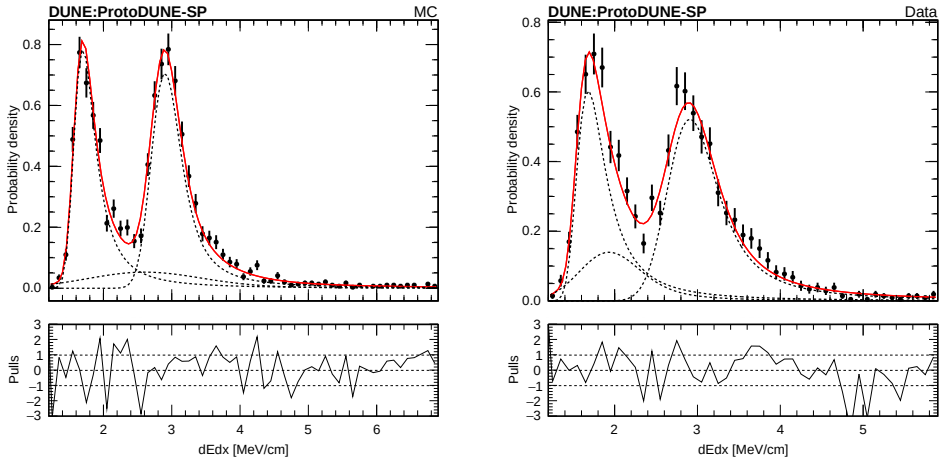

Figure A.18: Coherent Fit result for the slice corresponding to residual ranges between 35 and 37 cm.

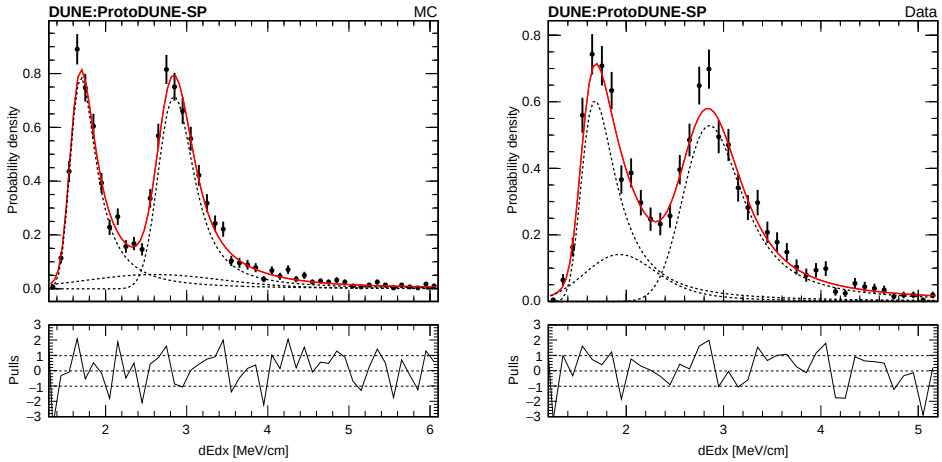

Figure A.19: Coherent Fit result for the slice corresponding to residual ranges between 37 and 39 cm.

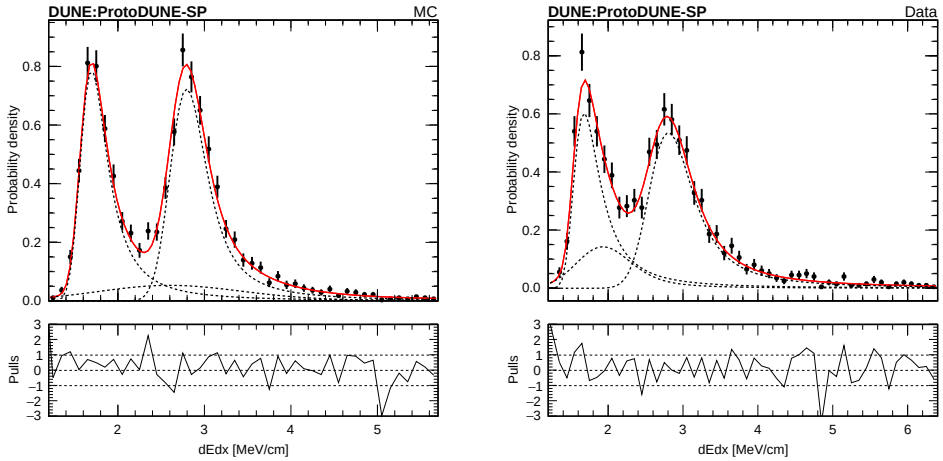

Figure A.20: Coherent Fit result for the slice corresponding to residual ranges between 39 and 41 cm.

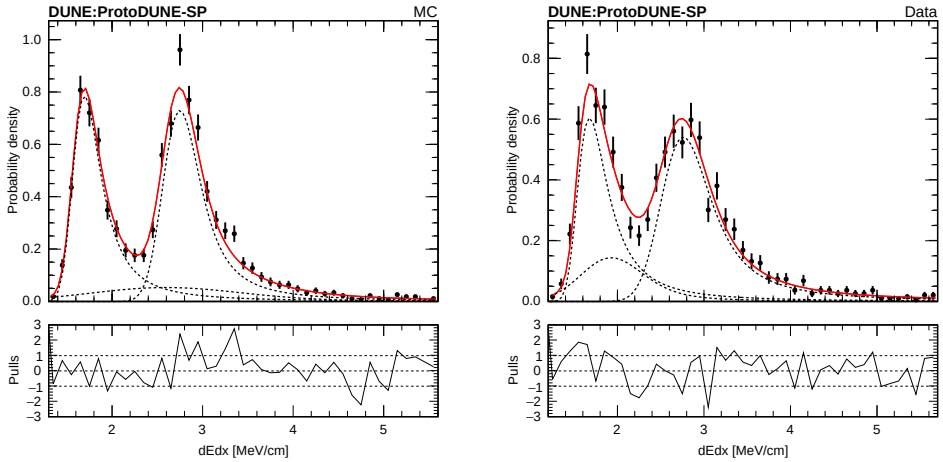

Figure A.21: Coherent Fit result for the slice corresponding to residual ranges between 41 and 43 cm.

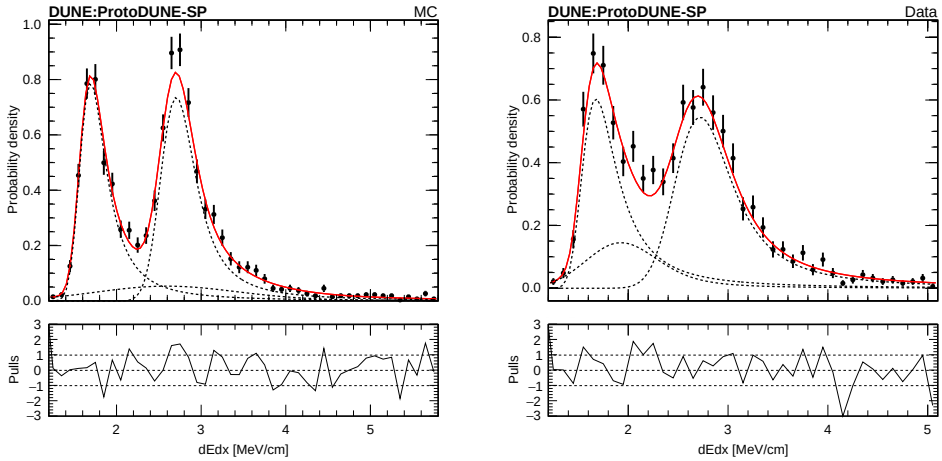

Figure A.22: Coherent Fit result for the slice corresponding to residual ranges between 43 and 45 cm.

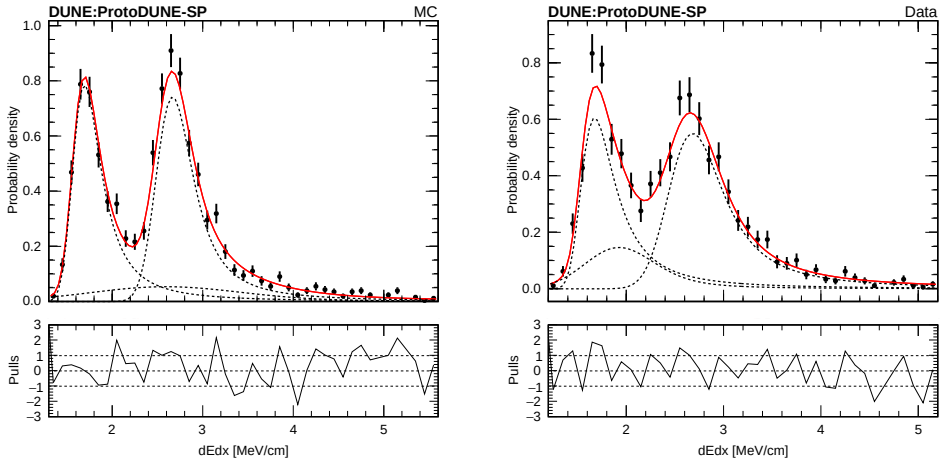

Figure A.23: Coherent Fit result for the slice corresponding to residual ranges between 45 and 47 cm.

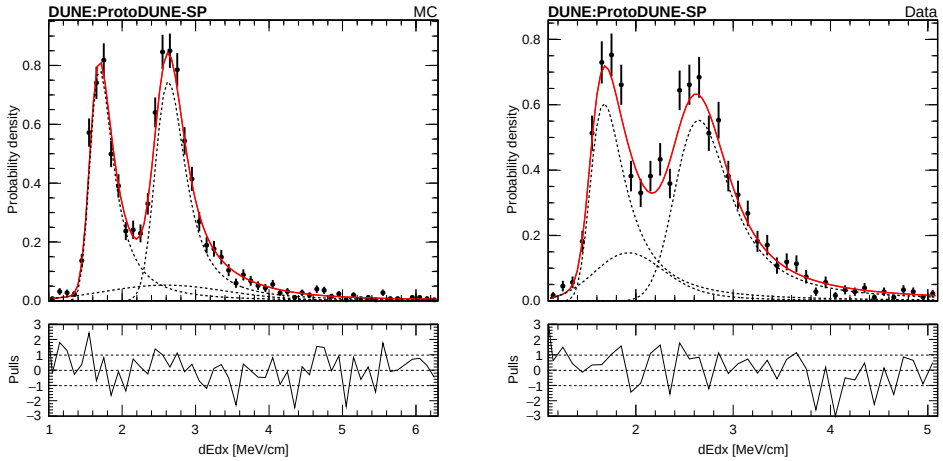

Figure A.24: Coherent Fit result for the slice corresponding to residual ranges between 47 and 49 cm.

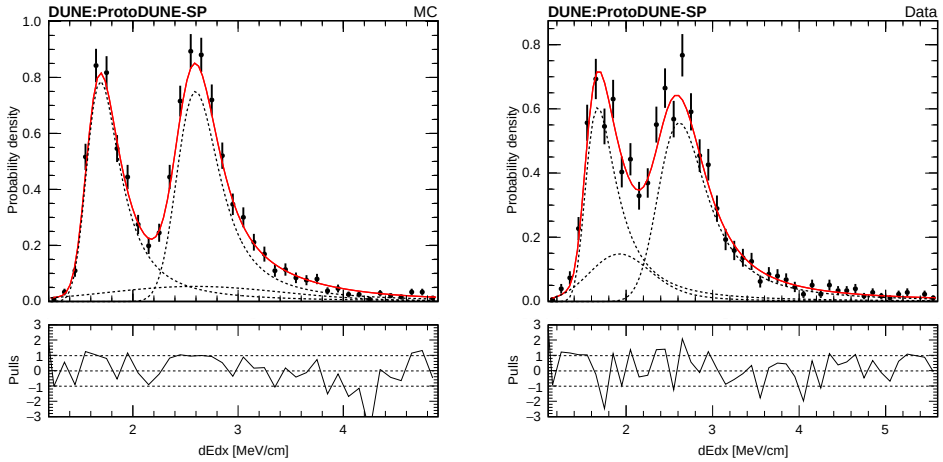

Figure A.25: Coherent Fit result for the slice corresponding to residual ranges between 49 and 51 cm.

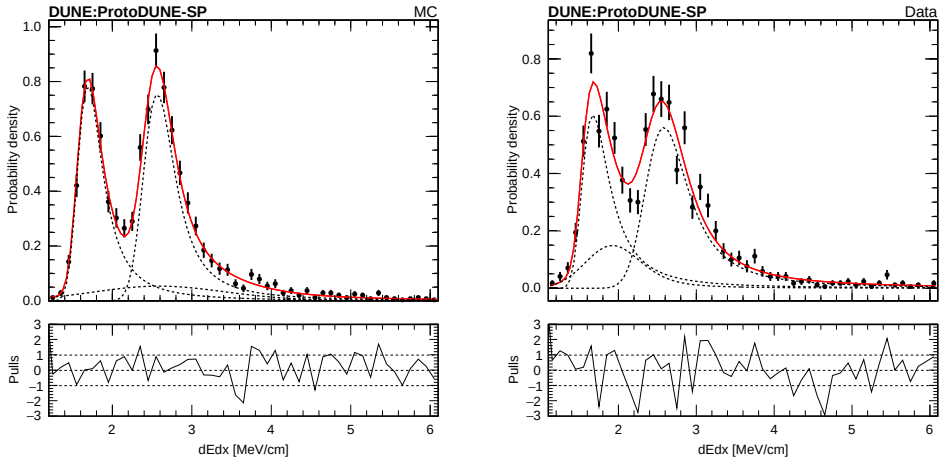

Figure A.26: Coherent Fit result for the slice corresponding to residual ranges between 51 and 53 cm.

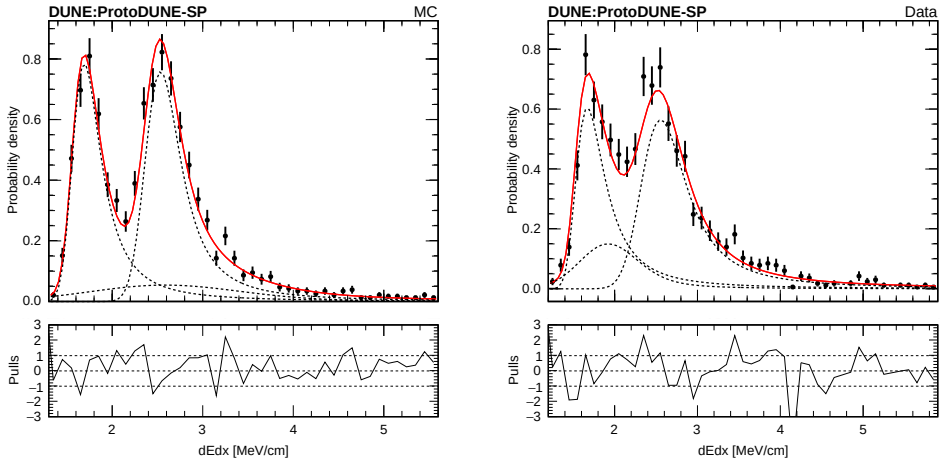

Figure A.27: Coherent Fit result for the slice corresponding to residual ranges between 53 and 55 cm.

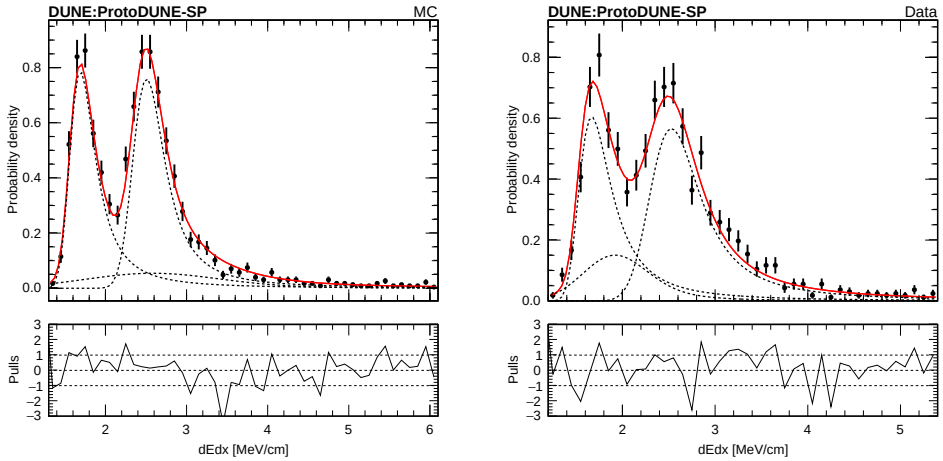

Figure A.28: Coherent Fit result for the slice corresponding to residual ranges between 55 and 57 cm.

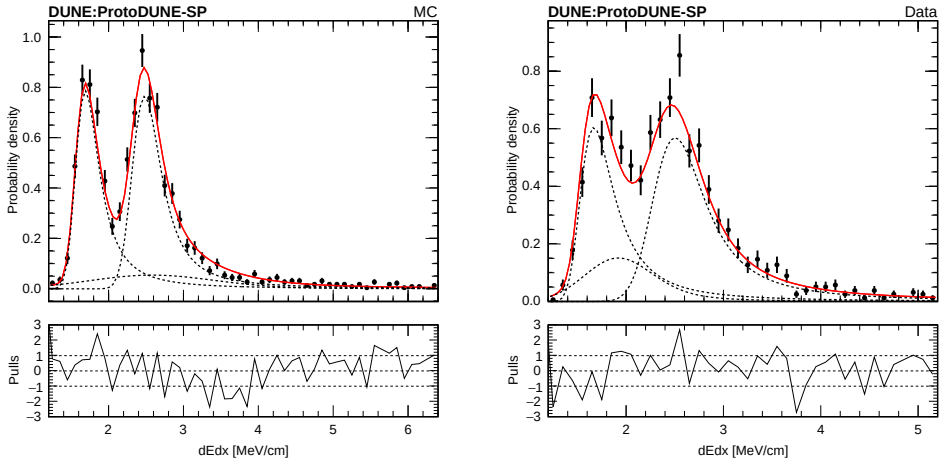

Figure A.29: Coherent Fit result for the slice corresponding to residual ranges between 57 and 59 cm.

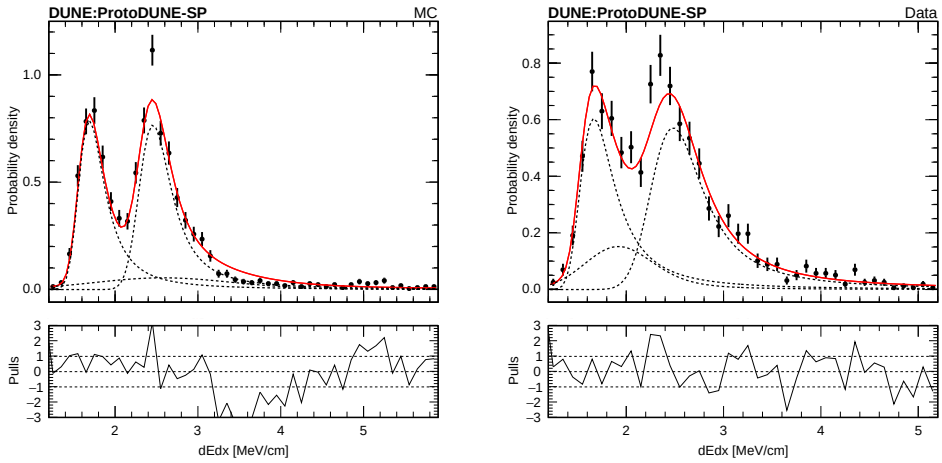

Figure A.30: Coherent Fit result for the slice corresponding to residual ranges between 59 and 61 cm.

Bibliography

[1] J. Chadwick, *The intensity distribution in the magnetic spectrum of beta particles from radium (B + C)*, *Verh. Phys. Gesell.* **16** (1914) 383.

[2] C. D. Ellis and W. A. Wooster, *The average energy of disintegration of radium E*, *Proc. Roy. Soc. Lond. A* **117** (1927) 109.

[3] W. Pauli, "Pauli letter collection: letter to Lise Meitner.".

[4] W. Pauli, *On the Earlier and more recent history of the neutrino*, *Camb. Monogr. Part. Phys. Nucl. Phys. Cosmol.* **1** (1991) 1.

[5] C. L. Cowan, F. Reines, F. B. Harrison, H. W. Kruse and A. D. McGuire, *Detection of the free neutrino: A Confirmation*, *Science* **124** (1956) 103.

[6] S. H. Neddermeyer and C. D. Anderson, *Note on the Nature of Cosmic Ray Particles*, *Phys. Rev.* **51** (1937) 884.

[7] G. Danby, J. M. Gaillard, K. A. Goulianos, L. M. Lederman, N. B. Mistry, M. Schwartz et al., *Observation of High-Energy Neutrino Reactions and the Existence of Two Kinds of Neutrinos*, *Phys. Rev. Lett.* **9** (1962) 36.

[8] ALEPH, DELPHI, L3, OPAL, SLD, LEP Electroweak Working Group, SLD Electroweak Group, SLD Heavy Flavour Group collaboration, *Precision electroweak measurements on the Z resonance*, *Phys. Rept.* **427** (2006) 257 [hep-ex/0509008].

[9] M. L. Perl et al., *Evidence for Anomalous Lepton Production in e+ - e- Annihilation*, *Phys. Rev. Lett.* **35** (1975) 1489.

[10] DONUT collaboration, *Observation of tau neutrino interactions*, *Phys. Lett. B* **504** (2001) 218 [hep-ex/0012035].

[11] M. Walker, *Calibration Hardware Research and Development for SNO+*, Ph.D. thesis, 05, 2014.

[12] J. N. Bahcall, A. M. Serenelli and S. Basu, *New solar opacities, abundances, helioseismology, and neutrino fluxes*, *Astrophys. J. Lett.* **621** (2005) L85 [astro-ph/0412440].

[13] B. T. Cleveland, T. Daily, R. Davis, Jr., J. R. Distel, K. Lande, C. K. Lee et al., *Measurement of the solar electron neutrino flux with the Homestake chlorine detector*, *Astrophys. J.* **496** (1998) 505.

[14] J. N. Bahcall, N. A. Bahcall and G. Shaviv, *Present status of the theoretical predictions for the Cl-36 solar neutrino experiment*, *Phys. Rev. Lett.* **20** (1968) 1209.

[15] SAGE collaboration, *Measurement of the solar neutrino capture rate with gallium metal*, *Phys. Rev. C* **60** (1999) 055801 [astro-ph/9907113].

[16] GALLEX collaboration, *GALLEX solar neutrino observations: Results for GALLEX IV*, *Phys. Lett. B* **447** (1999) 127.

[17] Soudan-2 collaboration, *The Atmospheric neutrino flavor ratio from a 3.9 fiducial kiloton year exposure of Soudan-2*, *Phys. Lett. B* **449** (1999) 137 [hep-ex/9901024].

[18] D. Casper et al., *Measurement of atmospheric neutrino composition with IMB-3*, *Phys. Rev. Lett.* **66** (1991) 2561.

[19] Kamiokande collaboration, *Atmospheric muon-neutrino / electron-neutrino ratio in the multiGeV energy range*, *Phys. Lett. B* **335** (1994) 237.

[20] Super-Kamiokande collaboration, *Study of the atmospheric neutrino flux in the multi-GeV energy range*, *Phys. Lett. B* **436** (1998) 33 [hep-ex/9805006].

[21] P. Harrison, D. Perkins and W. Scott, *Further evidence for threefold maximal lepton mixing and a hierarchical spectrum of neutrino mass-squared differences*, *Physics Letters B* **396** (1997) 186.

[22] B. Pontecorvo, *Neutrino Experiments and the Problem of Conservation of Leptonic Charge*, *Zh. Eksp. Teor. Fiz.* **53** (1967) 1717.

[23] SNO collaboration, *Direct evidence for neutrino flavor transformation from neutral current interactions in the Sudbury Neutrino Observatory*, *Phys. Rev. Lett.* **89** (2002) 011301 [nucl-ex/0204008].

[24] Super-Kamiokande collaboration, *Evidence for oscillation of atmospheric neutrinos*, *Phys. Rev. Lett.* **81** (1998) 1562 [hep-ex/9807003].

[25] J. J. Sakurai, *Modern quantum mechanics; rev. ed.* Addison-Wesley, Reading, MA, 1994.

[26] Z. Maki, M. Nakagawa and S. Sakata, *Remarks on the unified model of elementary particles*, *Prog. Theor. Phys.* **28** (1962) 870.

[27] Particle Data Group collaboration, *Review of Particle Physics*, *PTEP* **2022** (2022) 083C01.

[28] P. F. De Salas, D. V. Forero, S. Gariazzo, P. Martínez-Miravé, O. Mena, C. A. Ternes et al., "Chi2 profiles from Valencia neutrino global fit." http://globalfit.astroparticles.es/, 2021. 10.5281/zenodo.4726908.

[29] KATRIN collaboration, *Improved Upper Limit on the Neutrino Mass from a Direct Kinematic Method by KATRIN*, *Phys. Rev. Lett.* **123** (2019) 221802 [1909.06048].

[30] KamLAND-Zen collaboration, *Search for Majorana Neutrinos near the Inverted Mass Hierarchy Region with KamLAND-Zen*, *Phys. Rev. Lett.* **117** (2016) 082503 [1605.02889].

[31] Topical Conveners: K.N. Abazajian, J.E. Carlstrom, A.T. Lee collaboration, *Neutrino Physics from the Cosmic Microwave Background and Large Scale Structure*, *Astropart. Phys.* **63** (2015) 66 [1309.5383].

[32] Planck collaboration, *Planck 2018 results. VI. Cosmological parameters*, *Astron. Astrophys.* **641** (2020) A6 [1807.06209].

[33] P. De Salas, S. Gariazzo, O. Mena, C. Ternes and M. Tórtola, *Neutrino Mass Ordering from Oscillations and Beyond: 2018 Status and Future Prospects*, *Front. Astron. Space Sci.* **5** (2018) 36 [1806.11051].

[34] S. Gariazzo, M. Archidiacono, P. F. de Salas, O. Mena, C. A. Ternes and M. Tórtola, *Neutrino masses and their ordering: Global Data, Priors and Models*, *JCAP* **1803** (2018) 011 [1801.04946].

[35] L. Wolfenstein, *Neutrino Oscillations in Matter*, *Phys. Rev. D* **17** (1978) 2369.

[36] A. Y. Smirnov, *The MSW effect and matter effects in neutrino oscillations*, *Phys. Scripta T* **121** (2005) 57 [hep-ph/0412391].

[37] SNO collaboration, *The Sudbury neutrino observatory*, *Nucl. Instrum. Meth. A* **449** (2000) 172 [nucl-ex/9910016].

[38] R. Davis, *A review of the Homestake solar neutrino experiment*, *Prog. Part. Nucl. Phys.* **32** (1994) 13.

[39] GALLEX collaboration, *The GALLEX experiment: Status report*, in *2nd International Workshop on Neutrino Telescopes*, 1990.

[40] SAGE collaboration, *SAGE: The Soviet-American gallium solar neutrino experiment*, *Nucl. Phys. B Proc. Suppl.* **28** (1992) 75.

[41] Super-Kamiokande collaboration, *The Super-Kamiokande detector*, *Nucl. Instrum. Meth. A* **501** (2003) 418.

[42] IceCube collaboration, *The Design and Performance of IceCube DeepCore*, *Astropart. Phys.* **35** (2012) 615 [1109.6096].

[43] Double Chooz collaboration, *Double Chooz: A Search for the neutrino mixing angle theta(13)*, hep-ex/0606025.

[44] RENO collaboration, *RENO: An Experiment for Neutrino Oscillation Parameter θ_{13} Using Reactor Neutrinos at Yonggwang*, 1003.1391.

[45] Daya Bay collaboration, *The Detector System of The Daya Bay Reactor Neutrino Experiment*, *Nucl. Instrum. Meth. A* **811** (2016) 133 [1508.03943].

[46] KamLAND collaboration, *First results from KamLAND: Evidence for reactor anti-neutrino disappearance*, *Phys. Rev. Lett.* **90** (2003) 021802 [hep-ex/0212021].

[47] LSND collaboration, *The Liquid scintillator neutrino detector and LAMPF neutrino source*, *Nucl. Instrum. Meth. A* **388** (1997) 149 [nucl-ex/9605002].

[48] MiniBooNE collaboration, *The MiniBooNE Detector*, *Nucl. Instrum. Meth. A* **599** (2009) 28 [0806.4201].

[49] T2K collaboration, *The T2K Experiment*, *Nucl. Instrum. Meth. A* **659** (2011) 106 [1106.1238].

[50] NOvA collaboration, *The NOvA Technical Design Report*, .

[51] MINOS collaboration, *MINOS detectors for neutrino interactions*, *Nucl. Instrum. Meth. A* **461** (2001) 290.

[52] F. Kaether, W. Hampel, G. Heusser, J. Kiko and T. Kirsten, *Reanalysis of the GALLEX solar neutrino flux and source experiments*, *Phys. Lett. B* **685** (2010) 47 [1001.2731].

[53] SNO collaboration, *Combined Analysis of all Three Phases of Solar Neutrino Data from the Sudbury Neutrino Observatory*, in *13th ICATPP Conference on Astroparticle, Particle, Space Physics and Detectors for Physics Applications*, pp. 360–366, 2012, DOI.

[54] Super-Kamiokande collaboration, *Solar neutrino measurements in super-Kamiokande-I*, *Phys. Rev. D* **73** (2006) 112001 [hep-ex/0508053].

[55] Super-Kamiokande collaboration, *Solar neutrino measurements in Super-Kamiokande-II*, *Phys. Rev. D* **78** (2008) 032002 [0803.4312].

[56] Super-Kamiokande collaboration, *Solar Neutrino Measurement at Super-Kamiokande-III*, in *Meeting of the Division of Particles and Fields of the American Physical Society (DPF 2009)*, 9, 2009, 0909.5469.

[57] KamLAND collaboration, *Precision Measurement of Neutrino Oscillation Parameters with KamLAND*, *Phys. Rev. Lett.* **100** (2008) 221803 [0801.4589].

[58] KamLAND collaboration, *Constraints on θ_{13} from A Three-Flavor Oscillation Analysis of Reactor Antineutrinos at KamLAND*, *Phys. Rev. D* **83** (2011) 052002 [1009.4771].

[59] KamLAND collaboration, *Reactor On-Off Antineutrino Measurement with KamLAND*, *Phys. Rev. D* **88** (2013) 033001 [1303.4667].

[60] T2K collaboration, *Improved constraints on neutrino mixing from the T2K experiment with $\mathbf{3.13 \times 10^{21}}$ protons on target*, *Phys. Rev. D* **103** (2021) 112008 [2101.03779].

[61] A. Himmel, *New oscillation results from the nova experiment*, July, 2020. 10.5281/zenodo.3959581.

[62] MINOS collaboration, *Combined analysis of ν_μ disappearance and $\nu_\mu \to \nu_e$ appearance in MINOS using accelerator and atmospheric neutrinos*, *Phys. Rev. Lett.* **112** (2014) 191801 [1403.0867].

[63] Super-Kamiokande collaboration, *Atmospheric neutrino oscillation analysis with external constraints in Super-Kamiokande I-IV*, *Phys. Rev. D* **97** (2018) 072001 [1710.09126].

[64] IceCube collaboration, *Measurement of Atmospheric Neutrino Oscillations at 6–56 GeV with IceCube DeepCore*, *Phys. Rev. Lett.* **120** (2018) 071801 [1707.07081].

[65] RENO collaboration, *Measurement of Reactor Antineutrino Oscillation Amplitude and Frequency at RENO*, *Phys. Rev. Lett.* **121** (2018) 201801 [1806.00248].

[66] Daya Bay collaboration, *Measurement of the Electron Antineutrino Oscillation with 1958 Days of Operation at Daya Bay*, *Phys. Rev. Lett.* **121** (2018) 241805 [1809.02261].

[67] Double Chooz collaboration, *First Measurement of θ_{13} from Delayed Neutron Capture on Hydrogen in the Double Chooz Experiment*, *Phys. Lett. B* **723** (2013) 66 [1301.2948].

[68] T2K collaboration, *Constraint on the matter–antimatter symmetry-violating phase in neutrino oscillations*, *Nature* **580** (2020) 339 [1910.03887].

[69] NOvA collaboration, *First Measurement of Neutrino Oscillation Parameters using Neutrinos and Antineutrinos by NOvA*, *Phys. Rev. Lett.* **123** (2019) 151803 [1906.04907].

[70] P. F. de Salas, D. V. Forero, S. Gariazzo, P. Martínez-Miravé, O. Mena, C. A. Ternes et al., *2020 global reassessment of the neutrino oscillation picture*, *JHEP* **02** (2021) 071 [2006.11237].

[71] K. Abe et al., *Letter of Intent: The Hyper-Kamiokande Experiment — Detector Design and Physics Potential —*, 1109.3262.

[72] JUNO collaboration, *JUNO Conceptual Design Report*, 1508.07166.

[73] DUNE collaboration, *Deep Underground Neutrino Experiment (DUNE), Far Detector Technical Design Report, Volume I Introduction to DUNE*, *JINST* **15** (2020) T08008 [2002.02967].

[74] A. Pich, *The Standard Model of Electroweak Interactions*, in *2010 European School of High Energy Physics*, pp. 1–50, 1, 2012, 1201.0537.

[75] E. Majorana, *Teoria simmetrica dell'elettrone e del positrone*, *Nuovo Cim.* **14** (1937) 171.

[76] J. Hisano, *Proton decay in SUSY GUTs*, *PTEP* **2022** (2022) 12B104 [2202.01404].

[77] P. Nath and P. Fileviez Perez, *Proton stability in grand unified theories, in strings and in branes*, *Phys. Rept.* **441** (2007) 191 [hep-ph/0601023].

[78] Super-Kamiokande collaboration, *Search for proton decay via $p \to e^+\pi^0$ and $p \to \mu^+\pi^0$ in 0.31 megaton $\cdot$ years exposure of the Super-Kamiokande water Cherenkov detector*, *Phys. Rev. D* **95** (2017) 012004 [1610.03597].

[79] Super-Kamiokande collaboration, *Search for proton decay via $p \to \nu K^+$ using 260 kiloton $\cdot$ year data of Super-Kamiokande*, *Phys. Rev. D* **90** (2014) 072005 [1408.1195].

[80] J. A. Formaggio and G. P. Zeller, *From eV to EeV: Neutrino Cross Sections Across Energy Scales*, *Rev. Mod. Phys.* **84** (2012) 1307 [1305.7513].

[81] DUNE collaboration, *Long-Baseline Neutrino Facility (LBNF) and Deep Underground Neutrino Experiment (DUNE): Conceptual Design Report, Volume 1: The LBNF and DUNE Projects*, 1601.05471.

[82] DUNE collaboration, *Deep Underground Neutrino Experiment (DUNE) Near Detector Conceptual Design Report*, *Instruments* **5** (2021) 31 [2103.13910].

[83] DUNE collaboration, *Deep Underground Neutrino Experiment (DUNE), Far Detector Technical Design Report, Volume IV: Far Detector Single-phase Technology*, *JINST* **15** (2020) T08010 [2002.03010].

[84] MicroBooNE collaboration, *Search for an Excess of Electron Neutrino Interactions in MicroBooNE Using Multiple Final-State Topologies*, *Phys. Rev. Lett.* **128** (2022) 241801 [2110.14054].

[85] MicroBooNE collaboration, *First Measurement of Energy-Dependent Inclusive Muon Neutrino Charged-Current Cross Sections on Argon with the MicroBooNE Detector*, *Phys. Rev. Lett.* **128** (2022) 151801 [2110.14023].

[86] ICARUS collaboration, *Design, construction and tests of the ICARUS T600 detector*, *Nucl. Instrum. Meth. A* **527** (2004) 329.

[87] MicroBooNE, LAr1-ND, ICARUS-WA104 collaboration, *A Proposal for a Three Detector Short-Baseline Neutrino Oscillation Program in the Fermilab Booster Neutrino Beam*, 1503.01520.

[88] DUNE collaboration, *Deep Underground Neutrino Experiment (DUNE), Far Detector Technical Design Report, Volume II: DUNE Physics*, 2002.03005.

[89] DUNE collaboration, *Long-baseline neutrino oscillation physics potential of the DUNE experiment*, *Eur. Phys. J. C* **80** (2020) 978 [2006.16043].

[90] DUNE collaboration, *Snowmass Neutrino Frontier: DUNE Physics Summary*, 2203.06100.

[91] K. S. Babu et al., *Working Group Report: Baryon Number Violation*, 1311.5285.

[92] DUNE collaboration, *Prospects for beyond the Standard Model physics searches at the Deep Underground Neutrino Experiment*, *Eur. Phys. J. C* **81** (2021) 322 [2008.12769].

[93] R. M. Bionta et al., *Observation of a Neutrino Burst in Coincidence with Supernova SN 1987a in the Large Magellanic Cloud*, *Phys. Rev. Lett.* **58** (1987) 1494.

[94] Kamiokande-II collaboration, *Observation of a Neutrino Burst from the Supernova SN 1987a*, *Phys. Rev. Lett.* **58** (1987) 1490.

[95] ArgonCube collaboration, *ArgonCube: a Modular Approach for Liquid Argon TPC Neutrino Detectors for Near Detector Environments*, tech. rep., CERN, Geneva, 2017.

[96] W. R. Leo, *Techniques for Nuclear and Particle Physics Experiments: A How to Approach*. 1987.

[97] T. Doke, K. Masuda and E. Shibamura, *Estimation of absolute photon yields in liquid argon and xenon for relativistic (1 MeV) electrons*, *Nucl. Instrum. Meth. A* **291** (1990) 617.

[98] MicroBooNE collaboration, *Design and Construction of the MicroBooNE Detector*, *JINST* **12** (2017) P02017 [1612.05824].

[99] C. Anderson et al., *The ArgoNeuT Detector in the NuMI Low-Energy beam line at Fermilab*, *JINST* **7** (2012) P10019 [1205.6747].

[100] LArIAT collaboration, *LArIAT: Liquid Argon In A Testbeam*, 1406.5560.

[101] ArgoNeuT collaboration, *A Study of Electron Recombination Using Highly Ionizing Particles in the ArgoNeuT Liquid Argon TPC*, *JINST* **8** (2013) P08005 [1306.1712].

[102] LArIAT collaboration, *Calorimetry for low-energy electrons using charge and light in liquid argon*, *Phys. Rev. D* **101** (2020) 012010 [1909.07920].

[103] T. Heindl, T. Dandl, M. Hofmann, R. Krucken, L. Oberauer, W. Potzel et al., *The scintillation of liquid argon*, *EPL* **91** (2010) 62002 [1511.07718].

[104] WARP collaboration, *Measurement of the specific activity of ar-39 in natural argon*, *Nucl. Instrum. Meth. A* **574** (2007) 83 [astro-ph/0603131].

[105] DUNE collaboration, *The Single-Phase ProtoDUNE Technical Design Report*, 1706.07081.

[106] DUNE collaboration, *Design, construction and operation of the ProtoDUNE-SP Liquid Argon TPC*, *JINST* **17** (2022) P01005 [2108.01902].

[107] H. Souza, E. Segreto, A. Machado, R. Sarmento, M. Bazetto, L. Paulucci et al., *Liquid argon characterization of the X-ARAPUCA with alpha particles, gamma rays and cosmic muons*, *JINST* **16** (2021) P11002.

[108] S. Bordoni, *The CERN Neutrino Platform*, *PoS* **EPS-HEP2017** (2017) 483.

[109] DUNE collaboration, *Status of ProtoDUNE Dual Phase*, *PoS* **EPS-HEP2019** (2020) 381 [1910.10115].

[110] DUNE collaboration, *First results on ProtoDUNE-SP liquid argon time projection chamber performance from a beam test at the CERN Neutrino Platform*, *JINST* **15** (2020) P12004 [2007.06722].

[111] DUNE collaboration, *A LArTPC with Vertical Drift for the DUNE Far Detector*, *PoS* **NuFact2021** (2022) 173.

[112] J. M. Ordan, *DUNE Experiment progress Oct 2017*, .

[113] D. Montanari, J. Bremer, A. Gendotti, M. Geynisman, S. Hentschel, T. Loew et al., *Development of membrane cryostats for large liquid argon neutrino detectors*, *IOP Conference Series: Materials Science and Engineering* **101** (2015) 012049.

[114] D. Adams et al., *The ProtoDUNE-SP LArTPC Electronics Production, Commissioning, and Performance*, *JINST* **15** (2020) P06017 [2002.01782].

[115] B. Howard, S. Mufson, D. Whittington, B. Adams, B. Baugh, J. R. Jordan et al., *A Novel Use of Light Guides and Wavelength Shifting Plates for the Detection of Scintillation Photons in Large Liquid Argon Detectors*, *Nucl. Instrum. Meth. A* **907** (2018) 9 [1710.11233].

[116] L. Bugel, J. M. Conrad, C. Ignarra, B. J. P. Jones, T. Katori, T. Smidt et al., *Demonstration of a Lightguide Detector for Liquid Argon TPCs*, *Nucl. Instrum. Meth. A* **640** (2011) 69 [1101.3013].

[117] Z. Moss, J. Moon, L. Bugel, J. M. Conrad, K. Sachdev, M. Toups et al., *A Factor of Four Increase in Attenuation Length of Dipped Lightguides for Liquid Argon TPCs Through Improved Coating*, 1604.03103.

[118] A. A. Machado and E. Segreto, *ARAPUCA a new device for liquid argon scintillation light detection*, *JINST* **11** (2016) C02004.

[119] E. M. Conover, *Muon-induced backgrounds in the Double Chooz neutrino oscillation experiment*, Ph.D. thesis, Chicago U., 2014.

[120] G. Bressi, M. Cambiaghi, G. Carugno, E. Conti, B. Dainese, G. Prete et al., *Argon purification in liquid phase*, *Nucl. Instrum. Meth. A* **292** (1990) 585.

[121] D. L. Adams et al., *Design and performance of a 35-ton liquid argon time projection chamber as a prototype for future very large detectors*, *JINST* **15** (2020) P03035 [1912.08739].

[122] WA105 collaboration, *Performance study of a 3×1×1 m3 dual phase liquid Argon Time Projection Chamber exposed to cosmic rays*, *JINST* **16** (2021) P08063 [2104.08227].

[123] DUNE collaboration, *Cryogenic Instrumentation at ProtoDUNE*, *PoS* **ICHEP2020** (2021) 131.

[124] DUNE collaboration, *Movable Thermometer System in ProtoDUNE*, *PoS* **ICHEP2020** (2021) 197 [2012.10567].

[125] M. A. García-Peris, *ProtoDUNE T-Gradient development and calibration*, Master's thesis, Valencia U., 7, 2018, 10.2172/1780813.

[126] N. Charitonidis and I. Efthymiopoulos, *Low energy tertiary beam line design for the CERN neutrino platform project*, *Phys. Rev. Accel. Beams* **20** (2017) 111001.

[127] A. C. Booth, N. Charitonidis, P. Chatzidaki, Y. Karyotakis, E. Nowak, I. Ortega-Ruiz et al., *Particle production, transport, and identification in the regime of 1−7 GeV/c*, *Phys. Rev. Accel. Beams* **22** (2019) 061003.

[128] I. Ortega Ruiz, *Accurate Profile Measurement of the low Intensity Secondary Beams in the CERN Experimental Areas*, Ph.D. thesis, Ecole Polytechnique, Lausanne, 2018. 10.5075/epfl-thesis-8278.

[129] N. Charitonidis, Y. Karyotakis and L. Gatignon, *Estimation of the R134a gas refractive index for use as a Cherenkov radiator, using a high energy charged particle beam*, *Nucl. Instrum. Meth. B* **410** (2017) 134.

[130] R. Herbst et al., *Design of the SLAC RCE Platform: A general purpose ATCA based data acquisition system*, in *2014 IEEE Nuclear Science Symposium and Medical Imaging Conference and 21st Symposium on Room-Temperature Semiconductor X-ray and Gamma-ray Detectors*, 3, 2016, DOI.

[131] J. Anderson et al., *FELIX: a PCIe based high-throughput approach for interfacing front-end and trigger electronics in the ATLAS Upgrade framework*, *JINST* **11** (2016) C12023.

[132] K. Biery, E. Flumerfelt, J. Freeman, W. Ketchum, G. Lukhanin and R. Rechenmacher, *artdaq: DAQ Software Development Made Simple*, *J. Phys. Conf. Ser.* **898** (2017) 032013.

[133] K. Biery, C. Green, J. Kowalkowski, M. Paterno and R. Rechenmacher, *artdaq: An Event-Building, Filtering, and Processing Framework*, *IEEE Trans. Nucl. Sci.* **60** (2013) 3764 .

[134] B. Baller, *Liquid argon TPC signal formation, signal processing and reconstruction techniques*, *JINST* **12** (2017) P07010 [1703.04024].

[135] MicroBooNE collaboration, *Ionization electron signal processing in single phase LArTPCs. Part I. Algorithm Description and quantitative evaluation with MicroBooNE simulation*, *JINST* **13** (2018) P07006 [1802.08709].

[136] MicroBooNE collaboration, *Ionization electron signal processing in single phase LArTPCs. Part II. Data/simulation comparison and performance in MicroBooNE*, *JINST* **13** (2018) P07007 [1804.02583].

[137] J. S. Marshall and M. A. Thomson, *The Pandora Software Development Kit for Pattern Recognition*, *Eur. Phys. J. C* **75** (2015) 439 [1506.05348].

[138] MicroBooNE collaboration, *The Pandora multi-algorithm approach to automated pattern recognition of cosmic-ray muon and neutrino events in the MicroBooNE detector*, *Eur. Phys. J. C* **78** (2018) 82 [1708.03135].

[139] DUNE collaboration, *Reconstruction of interactions in the ProtoDUNE-SP detector with Pandora*, 2206.14521.

[140] DUNE collaboration, *Separation of track- and shower-like energy deposits in ProtoDUNE-SP using a convolutional neural network*, *Eur. Phys. J. C* **82** (2022) 903 [2203.17053].

[141] A. Reynolds, *Evaluating the low-energy response of the ProtoDUNE-SP detector using Michel electrons*, Ph.D. thesis, Oxford U., 2020.

[142] E. L. Snider and G. Petrillo, *LArSoft: Toolkit for Simulation, Reconstruction and Analysis of Liquid Argon TPC Neutrino Detectors*, *J. Phys. Conf. Ser.* **898** (2017) 042057.

[143] C. Green, J. Kowalkowski, M. Paterno, M. Fischler, L. Garren and Q. Lu, *The art framework*, *Journal of Physics: Conference Series* **396** (2012) 022020.

[144] T. J. Roberts, K. B. Beard, D. Huang, S. Ahmed, D. M. Kaplan and L. K. Spentzouris, *G4Beamline Particle Tracking in Matter-dominated Beam Lines*, *Conf. Proc. C* **0806233** (2008) WEPP120.

[145] T. T. Böhlen, F. Cerutti, M. P. W. Chin, A. Fassò, A. Ferrari, P. G. Ortega et al., *The FLUKA Code: Developments and Challenges for High Energy and Medical Applications*, *Nucl. Data Sheets* **120** (2014) 211.

[146] A. Ferrari, P. R. Sala, A. Fasso and J. Ranft, *FLUKA: A multi-particle transport code (Program version 2005)*, .

[147] "Mad - methodical accelerator design." `https://pdg.lbl.gov/2019/AtomicNuclearProperties/adndt.pdf`.

[148] D. Heck, J. Knapp, J. N. Capdevielle, G. Schatz and T. Thouw, *CORSIKA: A Monte Carlo code to simulate extensive air showers*, .

[149] GEANT4 collaboration, *GEANT4–a simulation toolkit*, *Nucl. Instrum. Meth. A* **506** (2003) 250.

[150] U. Sowada, J. M. Warman and M. P. de Haas, *Hot-electron thermalization in solid and liquid argon, krypton, and xenon*, *Phys. Rev. B* **25** (1982) 3434.

[151] M. Wojcik and M. Tachiya, *Electron thermalization and electronion recombination in liquid argon*, *Chemical Physics Letters* **379** (2003) 20.

[152] T. Doke, A. Hitachi, J. Kikuchi, K. Masuda, S. Tamada, A. Mozumder et al., *Estimation of the fraction of electrons escaping from recombination in the ionization of liquid argon with relativistic electrons and heavy ions*, *Chemical Physics Letters* **115** (1985) 164.

[153] J. Thomas and D. A. Imel, *Recombination of electron-ion pairs in liquid argon and liquid xenon*, *Phys. Rev. A* **36** (1987) 614.

[154] ICARUS collaboration, *Study of electron recombination in liquid argon with the ICARUS TPC*, *Nucl. Instrum. Meth. A* **523** (2004) 275.

[155] ArgoNeuT collaboration, *A Study of Electron Recombination Using Highly Ionizing Particles in the ArgoNeuT Liquid Argon TPC*, *JINST* **8** (2013) P08005 [1306.1712].

[156] MicroBooNE collaboration, *Measurement of space charge effects in the MicroBooNE LArTPC using cosmic muons*, *JINST* **15** (2020) P12037 [2008.09765].

[157] MicroBooNE collaboration, *Calibration of the charge and energy loss per unit length of the MicroBooNE liquid argon time projection chamber using muons and protons*, *JINST* **15** (2020) P03022 [1907.11736].

[158] P. Buzhan et al., *Silicon photomultiplier and its possible applications*, *Nucl. Instrum. Meth. A* **504** (2003) 48.

[159] F. Acerbi and S. Gundacker, *Understanding and simulating SiPMs*, *Nucl. Instrum. Meth. A* **926** (2019) 16.

[160] "Photodiode characteristics and applications." `https://www.osioptoelectronics.com/media/pages/knowledgebase/b954012b64-1675100541/an-photodiode-parameters-and-characteristics.pdf`.

[161] "An introduction to the silicon photomultiplier." `https://www.seti.net/cosmic-rays/SETIPixel/CosmicWatch-Desktop-Muon-Detector-v2-master/Datasheets/Intro_to_SiPMs.pdf`.

[162] P. Carniti, A. Falcone, C. Gotti, A. Lucchini, G. Pessina, S. Riboldi et al., *A low noise and low power cryogenic amplifier for single photoelectron sensitivity with large arrays of SiPMs*, *JINST* **15** (2020) P01008 [1911.06562].

[163] M. Andreotti et al., *Cryogenic Characterization of Hamamatsu HWB MPPCs for the DUNE Photon Detection System*, *in preparation* (2023) .

[164] M. Andreotti et al., *Cryogenic Characterization of FBK SiPMs for the DUNE Photon Detection System*, *in preparation* (2023) .

[165] NA49 collaboration, *Inclusive production of charged kaons in p+p collisions at 158 GeV/c beam momentum and a new evaluation of the energy dependence of kaon production up to collider energies*, *Eur. Phys. J. C* **68** (2010) 1 [1004.1889].

[166] A. Paudel, *A pion-argon cross section measurement in the ProtoDUNE-SP experiment with cosmogenic muon*, Ph.D. thesis, Kansas State U., 2021. 10.2172/1779480.

[167] R. Diurba, *Evaluating the ProtoDUNE-SP Detector Performance to Measure a 6 GeV/c Positive Kaon Inelastic Cross Section on Argon*, Ph.D. thesis, Minnesota U., 2021.

[168] J. Calcutt, *Measurement of π^+ – Argon Absorption and Charge Exchange Interactions Using ProtoDUNE-SP*, Ph.D. thesis, Michigan State U., Michigan State U., 2021.

[169] "Muon stopping power and range tables 10 mev-100 tev." `https://pdg.lbl.gov/2019/AtomicNuclearProperties/adndt.pdf`.

[170] MINERvA collaboration, *Measurement of K^+ production in charged-current ν_μ interactions*, *Phys. Rev. D* **94** (2016) 012002 [`1604.03920`].

[171] X. Lu, *Exploring the performance limits of the ALICE Time Projection Chamber and Transition Radiation Detector for measuring identified hadron production at the LHC*, Ph.D. thesis, 2013.

[172] M. Hatlo, F. James, P. Mato, L. Moneta, M. Winkler and A. Zsenei, *Developments of mathematical software libraries for the lhc experiments*, *IEEE Transactions on Nuclear Science* **52** (2005) 2818.

[173] A. G. Frodesen, O. Skjeggestad and H. Tofte, *Probability and Statistics in Particle Physics*. Universitetsforlaget, Bergen, Norway, 1979.

[174] R. Brun and F. Rademakers, *ROOT: An object oriented data analysis framework*, *Nucl. Instrum. Meth. A* **389** (1997) 81.

[175] B. Murtagh and M. Saunders, *A projected lagrangian algorithm and its implementation for sparse nonlinear constraints*, vol. 16, pp. 84–117, (03, 2009), DOI.

[176] F. James, *Statistical methods in experimental physics*. 2006.